

Investigation on Wire Electro Discharge Machining Characteristics of TiNiCu Shape Memory Alloys

Thesis

Submitted in partial fulfillment of the requirements for the degree of

DOCTOR OF PHILOSOPHY

by

ABHINABA ROY



DEPARTMENT OF MECHANICAL ENGINEERING
NATIONAL INSTITUTE OF TECHNOLOGY KARNATAKA
SURATHKAL, MANGALORE - 575025
JUNE - 2020

DECLARATION

I hereby declare that the Research Thesis entitled "**Investigation on Wire Electro Discharge Machining Characteristics of TiNiCu Shape Memory Alloys**" which is being submitted to the **National Institute of Technology Karnataka, Surathkal** in partial fulfillment of the requirements for the award of the degree of **Doctor of Philosophy in Mechanical Engineering** is a *bonafide report of the research work carried out by me*. The material contained in this Research Synopsis has not been submitted to any other Universities or Institutes for the award of any degree.



ABHINABA ROY

Register No. **155017ME15P01**

Department of Mechanical Engineering

Place: NITK - Surathkal

Date: 20/06/2020

CERTIFICATE

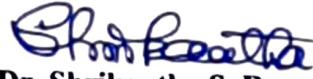
This is to certify that the Research Thesis entitled "**Investigation on Wire Electro Discharge Machining Characteristics of TiNiCu Shape Memory Alloys**" submitted by **Mr. Abhinaba Roy (Register No. 155017ME15P01)** as the record of the research work carried out by him, is accepted as the Research Thesis submission in partial fulfillment of the requirements for the award of the degree of **Doctor of Philosophy.**



Dr. Narendranath S.

Professor & Research Guide

Department of Mechanical Engg.



Dr. Shrikantha S. Rao

Chairman - DRPC

Department of Mechanical Engg.



GururBrahma GururVishnu GururDevo Maheshwaraha
Guru Saakshaat ParaBrahma Tasmai Sri Gurave Namaha

Om Namah Shivaya

I dedicate this thesis to my **Maa and Baba...**
Thank you for this reality and shaping my soul

I dedicate this thesis to my beloved **Wife...**
Thank you for being my Ardhangini and supporting me

I dedicate this thesis to my respected **Guru...**
Thank you for guiding me throughout
Keep your blessings on me forever

I dedicate this thesis to **everyone else...**
Who were with me and those who were not
Because, there is something to learn from everyone

I dedicate this thesis to the **cosmos...**
Because, at the end we are all stardust

Om Tryambakam Yajāmahe Sugandhim Puṣṭi-vardhanam
Urvārukam-iva Bandhanān Mṛtyor Mukṣīya Mā-'mṛtāt

ACKNOWLEDGEMENT

Supreme Lord Shiva annihilates the universe as we know it making it possible for the new life to form. Another way of saying this is "Energy can neither be created nor be destroyed, energy can only be transferred or changed from one form to another". Science and spirituality are all but same. Change is the only truth about this reality, change is permanent. Several changes have led me where I stand now. At first I would like to express my heartfelt gratitude to my supervisor **Dr. Narendranath S.**, Department of Mechanical Engineering for his guidance, supervision and continuous mental and emotional support whenever I needed it. I would like to thank him for critically evaluating my research work in its every stage and encouraging me to think beyond. I am thankful to God for providing him in my life where he helped me in understanding how to lead a dignified life. Now after spending more than four years with him all I want is to become a leader like him. I hope to make him proud not only through my research work but also through passing on his values as a supervisor to my students in future.

I would like to thank **Dr. Shrikantha S. Rao**, Professor and Head, and **Dr. Prasad Krishna**, Professor and former Head, **Dr. M.R. Ramesh** and **Dr. Mrityunjay Doddamani**, Department of Mechanical Engineering for their encouragement, suggestions and for extending departmental facilities which helped in successful completion of my research work.

I would like to thank **Science and Engineering Research Board - Department of Science and Technology (DST)**, Government of India for their financial support under the project reference number **SB/S3/MMER/0067/2013**. Due to their support I was able to carry out research work, pay for required testing facilities outside the Institute and procure important items.

I am extremely thankful to the members of Research Program Assessment Committee (RPAC) **Dr. Subhaschandra Kattimani**, Associate Professor, Department of Mechanical Engineering and **Dr. G.S. Dwarakish**, Professor, Department of Applied Mechanics and Hydraulics for their valuable suggestions and appreciation throughout the research work. Their critical suggestions have helped me refining this research work.

I would like to extend my appreciation for all Teaching and Non-Teaching staff members of the Department of Mechanical Engineering and from other departments, NITK Surathkal for their kind help and support during my tenure as a Junior Research Fellow and Doctoral Fellow.

I would also like to thank **Dr. Udaya Bhat K.**, Professor and former Head, Department of Metallurgical and Materials Engineering for allowing me to use several important facilities like scanning electron microscope and X-ray diffractometer for this research work.

My sincere thanks to all my seniors and friends Dr. Manjaiah M, Dr. Priyaranjan Sharma, Dr. Hargovind Soni, Dr. Mahesh B. Davanageri, Dr. Ravindra I. Badiger, Dr. Gajanan Anne, Dr. Sachin B., Mr. Sachin Kumar, Mr. Jaideep Banik, Mr. Gajanan M. Naik, Mr. Manoj I.V. and Mr. Prithvirajan Sekar for their constant help and support.

Finally, I would like to thank my respected parents, my wife, my sister and brother-in-law for their blessings, encouragement, love and support. I would also like to extend my appreciation to all my immediate family members, cousins and friends who have helped me in keeping my morale high. I consider myself privileged to have such wonderful people in my life.

THANK YOU ALL !

(ABHINABA ROY)

ABSTRACT

Shape memory alloys are well known across academia and industries due to their unique functional capabilities, such as shape memory effect and superelasticity besides other useful properties. They are also known for their toughness, resistance to corrosion, improved fatigue life and damping capabilities. Shape memory effect is exhibited by these group of alloys due to reverse martensitic phase transformation which transforms de-twinned martensites back to twinned martensites. This phase transformation of shape memory alloys occurs without any change in state of the material, which contextually known as diffusionless transformation. Superelasticity, on the other hand is exhibited by these alloys, when the alloy is handled at an operating temperature higher than its austenitic temperature. Ni rich NiTi shape memory alloy for example can be processed to be superelastic at room temperature.

These incredible qualities qualify shape memory alloys as potential materials for smart applications such as sensors and actuators. A vast majority of these alloys exhibit shape memory effect due to thermal load and some of them are also influenced by a magnetic field. Thermally induced shape memory alloys have formed wide applicability due to ease of use and economic factor. Among these alloys, TiNi based shape memory alloys are most widely researched and put into applications compared to Cu-based or Fe-based alloys. Phase transformation temperature of TiNi based shape memory alloys lie within a nominal operating temperature range (60°C-100°C) which makes them more suitable for sensing and actuating applications. However, with addition of a ternary element, phase transformation temperature of these alloys can be tailored to specific needs. Addition of Cu as ternary element in TiNi binary alloy system was found to reduce its phase transformation temperature and narrow transformation hysteresis. Cu addition also facilitates thermal conductivity making it more sensitive to change in thermal flux. Therefore, TiNiCu ternary shape memory alloys could be used for much sensitive applications.

Major challenge these alloys impose is poor machinability with conventional machining techniques. High tool wear, poor machined surface quality and additional post-machining processes compromise finish quality, accuracy of the end product and increase the cost involved. This is where non-conventional machining techniques proved as an added advantage to process these functional alloys and soon became a more popular choice over conventional machining techniques. Non-conventional machining process like laser beam

machining (LBM), water jet machining (WJM), electrochemical machining (ECM) and electrodischarge machining (EDM) result to better machining characteristics compared to conventional machining techniques. due to non-contact nature of the tool-workpiece interface. However, thick recast layer, oxidation, burr formation are some of machining defects that non-conventional machining techniques exhibit. Wire electrodischarge machining (WEDM) is a variant of traditional electrodischarge machine (EDM) where machining is carried out using an wire electrode. Sparking between wire electrode and workpiece results in removal of workpiece material through local melting. Advantage of W-EDM over EDM is that through CNC any desired profile can be cut imposing minimum damage to workpiece material.

Sensors and actuators incorporating shape memory effect are generally micro shaped components which undergoes microscopic shape change. Major aim of this study is to investigate WEDM characteristics of various homologous TiNiCu shape memory alloys and to optimize machining responses so as to produce components without compromising accuracy and quality. Six different TiNiCu shape memory alloys were vacuum melted and characterized in terms of microstructure, phases present, phase transformation temperatures and microhardness. Optical microscope with image analyzer, X-ray diffractometer, differential scanning calorimeter and microhardness tester were used to perform aforementioned characterization. Further, to determine the quality of machining, the following output responses namely material removal rate (MRR), surface roughness (SR), kerf width (KW), recast layer thickness (RLT), machined surface microhardness (MH) and machined surface morphology were studied and reported. $Ti_{50}Ni_{25}Cu_{25}$ exhibited least thermal hysteresis ($\sim 6^{\circ}C$) which indicates its suitability as ideal material for sensor and actuator applications. Due to varying thermal conductivity of vacuum melted homologous TiNiCu shape memory alloys, variation in WEDM responses were observed. Thereafter, prediction of WEDM responses was carried out using Artificial Neural Network (ANN) and optimization of WEDM responses was performed using Genetic Algorithm (GA). After a thorough investigation, WEDM process parameters to machine homologous TiNiCu shape memory alloys were reported and discussed in detail.

Keywords: Wire electro discharge machining; Shape memory alloys; Material removal rate; Surface roughness; Kerf width; Recast layer thickness; Microhardness; Machined surface morphology; Artificial Neural Network; Genetic Algorithm.

CONTENTS

| | |
|---|-------------|
| <i>Declaration</i> | |
| <i>Certificate</i> | |
| <i>Acknowledgements</i> | |
| <i>Abstract</i> | |
| <i>Contents</i> | <i>i</i> |
| <i>List of Figures</i> | <i>viii</i> |
| <i>List of Tables</i> | <i>xiv</i> |
| <i>List of Symbols and Abbreviations</i> | <i>xvi</i> |
| | |
| CHAPTER 1 - INTRODUCTION | 1 |
| 1.1. SHAPE MEMORY ALLOY | 1 |
| 1.1.1 TiNi Based Shape Memory Alloys | 2 |
| 1.1.2 TiNiCu Shape Memory Alloys | 3 |
| 1.1.3 Applications of Shape Memory Alloys | 3 |
| 1.2 MACHINING OF SHAPE MEMORY ALLOYS | 5 |
| 1.2.1 Conventional Machining of Shape Memory Alloys | 5 |
| 1.2.2 Non-Conventional Machining of Shape Memory Alloys | 6 |
| 1.3 WIRE ELECTRO DISCHARGE MACHINING OF SMA | 8 |
| 1.3.1 Introduction of WEDM | 8 |
| 1.3.2 Principle of WEDM | 9 |
| 1.3.3 Process Parameters of WEDM | 9 |
| 1.3.3.1 Pulse on time | 10 |
| 1.3.3.2 Pulse off time | 10 |
| 1.3.3.3 Servo Voltage | 10 |
| 1.3.3.4 Wire Feed | 11 |
| 1.3.3.5 Dielectric Flushing Pressure | 11 |
| 1.3.4 Machining Output Responses of WEDM | 11 |
| 1.3.4.1 Material Removal Rate | 11 |

| | | |
|-------------------------------|--|----|
| 1.3.4.2 | Surface Roughness | 12 |
| 1.3.4.3 | Kerf Width | 12 |
| 1.3.4.4 | Recast Layer Thickness | 13 |
| 1.3.5 | Significance and Implementation of WEDM | 13 |
| 1.4 | DESIGN OF EXPERIMENTS (DOE) | 14 |
| 1.4.1 | Taguchi's Orthogonal Design of Experiments | 15 |
| 1.4.2 | Box-Behnken Design of Experiments | 15 |
| 1.4.3 | Factorial Design of Experiments | 15 |
| 1.5 | PREDICTION AND OPTIMIZATION USING ARTIFICIAL NEURAL NETWORK AND GENETIC ALGORITHM | 15 |
| 1.6 | OUTLINE OF THESIS | 16 |
| CHAPTER 2 - LITERATURE REVIEW | | 19 |
| 2.1 | INTRODUCTION | 19 |
| 2.2 | TiNi BASED SHAPE MEMORY ALLOYS | 19 |
| 2.2.1 | Binary TiNi Alloy | 19 |
| 2.2.2 | Ternary TiNiX Alloy | 21 |
| 2.2.3 | TiNiCu Shape Memory Alloy | 22 |
| 2.3 | CHARACTERIZATION OF TiNiCu SHAPE MEMORY ALLOYS | 24 |
| 2.3.1 | Metallographic Characterization | 24 |
| 2.3.2 | Thermo-analytic Characterization | 25 |
| 2.3.3 | Crystallographic Characterization | 28 |
| 2.4 | MACHINING OF TiNi BASED SHAPE MEMORY ALLOYS | 30 |
| 2.4.1 | Conventional Machining of Shape Memory Alloys | 30 |
| 2.4.2 | Non-conventional Machining of Shape Memory Alloys | 33 |
| 2.5 | WEDM of TiNi BASED SHAPE MEMORY ALLOYS | 37 |
| 2.5.1 | Effect of Peak Current (I_p) | 37 |
| 2.5.2 | Effect of Pulse on Time (T_{on}) | 38 |
| 2.5.2.1 | Effect of T_{on} on MRR and SR | 38 |

| | | |
|---------|--|----|
| 2.5.2.2 | Effect of T_{on} on Surface Morphology | 40 |
| 2.5.2.3 | Effect of T_{on} on Kerf Width | 40 |
| 2.5.2.4 | Effect of T_{on} on Recast layer thickness | 41 |
| 2.5.3 | Effect of Pulse off Time (T_{off}) | 42 |
| 2.5.3.1 | Effect of T_{off} on MRR and SR | 42 |
| 2.5.3.2 | Effect of T_{off} on Surface Morphology | 43 |
| 2.5.3.3 | Effect of T_{off} on Kerf Width | 43 |
| 2.5.3.4 | Effect of T_{off} on Recast Layer Thickness | 44 |
| 2.5.4 | Effect of Servo Voltage (SV) | 45 |
| 2.5.4.1 | Effect of SV on MRR and SR | 45 |
| 2.5.4.2 | Effect of SV on Surface Morphology | 46 |
| 2.5.4.3 | Effect of SV on Kerf Width | 46 |
| 2.5.4.4 | Effect of SV on Recast Layer Thickness | 47 |
| 2.5.5 | Effect of Wire Feed (WF) | 48 |
| 2.5.5.1 | Effect of WF on MRR and SR | 48 |
| 2.5.5.2 | Effect of WF on Surface Morphology | 49 |
| 2.5.5.3 | Effect of WF on Kerf Width | 49 |
| 2.5.5.4 | Effect of WF on Recast Layer Thickness | 50 |
| 2.5.6 | Effect of Flushing Condition | 51 |
| 2.5.6.1 | Effect of flushing conditions on MRR and SR | 51 |
| 2.5.6.2 | Effect of flushing conditions on Surface Morphology | 52 |
| 2.5.6.3 | Effect of flushing conditions on Kerf Width | 53 |
| 2.5.6.4 | Effect of flushing conditions on Recast Layer Thickness | 54 |
| 2.6 | DESIGN AND MODELING OF WEDM PROCESS | 55 |
| 2.7 | PREDICTION OF WEDM RESPONSES | 56 |
| 2.8 | OPTIMIZATION OF WEDM RESPONSES | 58 |
| 2.9 | SUMMARY AND MOTIVATION FROM LITERATURE SURVEY | 59 |

| | | |
|-------------|--|----|
| 2.10 | OBJECTIVES OF CURRENT RESEARCH WORK | 60 |
| | | |
| CHAPTER 3 - | EXPERIMENTAL DETAILS | 61 |
| 3.1 | MATERIAL SELECTION AND PREPARATION | 61 |
| 3.2 | PRELIMINARY CHARACTERIZATION OF TiNiCu ALLOYS | 63 |
| | 3.2.1 Metallographic Characterization | 63 |
| | 3.2.2 Thermo-analytic Characterization | 64 |
| | 3.2.3 Crystallographic Characterization | 65 |
| 3.3 | EXPERIMENTAL SETUP | 66 |
| | 3.3.1 Wire Electro Discharge Machine | 66 |
| | 3.3.2 Surface Roughness Tester | 68 |
| | 3.3.3 Scanning Electron Microscope | 69 |
| | 3.3.4 Microhardness | 70 |
| 3.4 | DESIGN OF EXPERIMENTS AND ARTIFICIAL NEURAL NETWORK | 71 |
| | 3.4.1 Design of Experiments (DOE) and Factor Analysis | 71 |
| | 3.4.2 Response Prediction using Artificial Neural Network | 73 |
| | 3.4.3 Optimization using Genetic Algorithm | 76 |
| 3.5 | SUMMARY | 78 |
| | | |
| CHAPTER 4 - | WEDM ANALYSIS OF TiNiCu SHAPE MEMORY ALLOYS | 79 |
| 4.1 | INTRODUCTION | 79 |
| 4.2 | CHARACTERIZATION OF TiNiCu TERNARY SHAPE MEMORY ALLOYS | 80 |
| | 4.2.1 Microstructure of TiNiCu Shape Memory Alloys | 80 |
| | 4.2.2 Phase analysis of TiNiCu Shape Memory Alloys | 81 |
| | 4.2.3 Calorimetric Analysis of TiNiCu Shape Memory Alloys | 84 |
| | 4.2.4 Microhardness analysis of TiNiCu shape memory alloys | 86 |
| 4.3 | WEDM EXPERIMENTAL RESULTS | 87 |
| 4.4 | FACTOR ANALYSIS | 91 |

| | | |
|---------|--|-----|
| 4.4.1 | Analysis of Variance | 91 |
| 4.4.1.1 | Material Removal Rate | 91 |
| 4.4.1.2 | Surface Roughness | 92 |
| 4.4.1.3 | Kerf Width | 93 |
| 4.4.1.4 | Recast Layer Thickness | 93 |
| 4.4.2 | Taguchi Analysis - Material Removal Rate | 94 |
| 4.4.2.1 | Effect of Pulse on Time | 94 |
| 4.4.2.2 | Effect of Pulse off Time | 95 |
| 4.4.2.3 | Effect of Servo Voltage | 95 |
| 4.4.2.4 | Effect of Wire Feed | 96 |
| 4.4.3 | Taguchi Analysis - Surface Roughness | 97 |
| 4.4.3.1 | Effect of Pulse on Time | 97 |
| 4.4.3.2 | Effect of Pulse off Time | 98 |
| 4.4.3.3 | Effect of Servo Voltage | 98 |
| 4.4.3.4 | Effect of Wire Feed | 99 |
| 4.4.4 | Taguchi Analysis - Kerf Width | 99 |
| 4.4.4.1 | Effect of Pulse on Time | 100 |
| 4.4.4.2 | Effect of Pulse off Time | 101 |
| 4.4.4.3 | Effect of Servo Voltage | 101 |
| 4.4.4.4 | Effect of Wire Feed | 102 |
| 4.4.5 | Taguchi Analysis - Recast Layer Thickness | 103 |
| 4.4.5.1 | Effect of Pulse on Time | 103 |
| 4.4.5.2 | Effect of Pulse off Time | 104 |
| 4.4.5.3 | Effect of Servo Voltage | 105 |
| 4.4.5.4 | Effect of Wire Feed | 106 |
| 4.5 | ANALYSIS OF WEDM RESPONSES - MATERIAL REMOVAL RATE AND SURFACE ROUGHNESS | 106 |
| 4.6 | ANALYSIS OF WEDM RESPONSES - SURFACE MICROHARDNESS AND SURFACE MORPHOLOGY | 108 |
| 4.6.1 | Surface Microhardness | 108 |

| | | |
|---|---|-----|
| 4.6.2 | Surface Morphology | 111 |
| 4.6.2.1 | Effect of Discharge Energy on Surface Morphology | 111 |
| 4.6.2.2 | Effect of Peak current and Peak voltage on Surface Morphology | 113 |
| 4.6.2.3 | Effect of Flushing pressure and Direction on Surface Morphology | 120 |
| 4.7 | ANALYSIS OF WEDM RESPONSES - KERF WIDTH AND RECAST LAYER | 124 |
| 4.8 | VARIATION IN WEDM RESPONSES DUE TO HOMOGENIZATION | 127 |
| 4.8.1 | Effect of homogenization on Material Removal Rate | 127 |
| 4.8.2 | Effect of homogenization on Surface Roughness | 130 |
| 4.8.3 | Effect of homogenization on Kerf Width | 132 |
| 4.8.4 | Effect of homogenization on Recast Layer Thickness | 134 |
| 4.9 | IDENTIFICATION OF OPTIMUM MACHINED SURFACE MORPHOLOGY | 136 |
| 4.9.1 | Identification of suitable machining parameters yielding desirable response | 137 |
| 4.9.2 | Box Behnken - Design of Experiment | 138 |
| 4.9.3 | Surface Morphology of Machined Surface using Box Behnken DOE | 139 |
| 4.10 | SUMMARY | 141 |
| CHAPTER 5 - PREDICTION AND OPTIMIZATION OF WEDM RESPONSES | | 143 |
| 5.1 | INTRODUCTION | 143 |
| 5.2 | DEVELOPMENT OF SUITABLE NEURAL NETWORK | 143 |
| 5.3 | PREDICTION OF WEDM RESPONSES | 150 |
| 5.4 | DEVELOPMENT OF GENETIC ALGORITHM FITNESS FUNCTION | 153 |

| | | |
|---|--------------------------------|-----|
| 5.5 | OPTIMIZATION OF WEDM RESPONSES | 154 |
| 5.6 | SUMMARY | 157 |
| CHAPTER 6 - CONCLUSION AND FUTURE SCOPE | | 159 |
| 6.1 | CONCLUSIONS | 159 |
| 6.2 | FUTURE SCOPE OF WORK | 160 |
| REFERENCES | | 163 |
| LIST OF PUBLICATIONS | | 189 |
| BIO-DATA | | 191 |

LIST OF FIGURES

| FIGURE NO. | DESCRIPTION | PAGE NO. |
|------------|---|----------|
| Figure 1.1 | Different applications of shape memory alloys (Ali et al., 2014) | 4 |
| Figure 1.2 | SMA applications in automotive sector (Jani et al., 2014) | 4 |
| Figure 1.3 | (a) Tool nose damage (b) Abrupt chip formation (Weinert and Petzoldt, 2004) | 5 |
| Figure 1.4 | SEM image of : (a) Grit embedment (b) Parent material detachment by grit (Kong et al., 2011) | 7 |
| Figure 1.5 | SEM image of : (a) kerf profile at upper side and reverse side (b) magnified image of reverse side (Frotscher et al., 2011) | 7 |
| Figure 1.6 | Material removal in WEDM (Hsieh et al., 2009) | 9 |
| Figure 1.7 | Effect of kerf width on machined profile (Roy et al., 2018) | 12 |
| Figure 1.8 | Effect of recast layer thickness of shape recoverability (Roy et al., 2018) | 13 |
| Figure 2.1 | Crystal arrangement of high and low temperature phases and 2D view of (a) Austenite (b) Twinned martensite (c) Detwinned martensite (Falvo, 2008) | 20 |
| Figure 2.2 | DSC plot (a) Ti-50.8Ni (b) Ti-40.8Ni-10Cu (Li et al., 2016) | 23 |
| Figure 2.3 | DSC (a) cooling and (b) heating heat flow curves of 435°C aged Ti ₅₀ Ni ₂₅ Cu ₂₅ ribbons (Chen et al., 2018) | 27 |
| Figure 2.4 | X-ray patterns of rapidly quenched Ti ₅₀ Ni _{50-x} Cu _x (x = 30–38 at.%) alloy ribbons after isothermal | |

| | | |
|-------------|---|----|
| | (dotted curves) and 10 ms electro pulse (solid curves) crystallization. (Shelyakov et al., 2019) | 30 |
| Figure 2.5 | DSC plot of as received, dry machined and cryogenically machined NiTi alloy (Kaynak et al., 2014) | 31 |
| Figure 2.6 | Surface topography NiTi alloy (a) Dry (b) Cryogenic (Kaynak et al. 2014a) | 32 |
| Figure 2.7 | morphology of (a) milled and (b) EDMed NiTi alloy (Guo et al., 2013) | 32 |
| Figure 2.8 | SEM image of part made using (a)CW laser (b)FS laser (Biffi and Tuissi, 2017) | 33 |
| Figure 2.9 | SEM image of : (a) microstructure made using PWJ machining (b) microcracks highlighted with arrows (Frotscher et al., 2011) | 35 |
| Figure 2.10 | Microholes on partially electrochemical machined surface (Lee and Shin, 2011) | 35 |
| Figure 2.11 | Recast layer at (a) $I = 4A$, $f = 10$ kHz (b) $I = 4A$, $f = 5$ kHz and Surface morphology at (c) $I = 2A$ (d) $I = 4$ A (Fu et al., 2016) | 36 |
| Figure 2.12 | MRR and SR vs. Pulse duration at different peak current (Hsieh et al., 2013) | 37 |
| Figure 2.13 | MRR, SR vs. T_{on} for NiAlFe SMA (at various peak current) (Chen et al., 2008) | 39 |
| Figure 2.14 | MRR, SR vs. T_{on} for TiNiZr, TiNiCr and NiAlFe SMA (Hsieh et al., 2009) | 39 |
| Figure 2.15 | SEM micrographs showing surface morphology at T_{on} (a) $36 \mu s$ and (b) $48 \mu s$ (Manjaiah et al., 2016) | 40 |
| Figure 2.16 | Recast layer at T_{on} (a) $3 \mu s$ (b) $12 \mu s$ (c) $25 \mu s$ and (d) $50 \mu s$ (Hsieh et al., 2013) | 41 |
| Figure 2.17 | Recast layer thickness at T_{on} : (a) $112 \mu s$ (b) $116 \mu s$ (c) $120 \mu s$ (d) $124 \mu s$ (e) $128 \mu s$ (Manjaiah et al., 2018) | 42 |

| | | |
|-------------|--|----|
| Figure 2.18 | Effect of T_{off} on MRR and SR (Manjaiah et al., 2018) | 43 |
| Figure 2.19 | Machined surface at T_{off} : (a) 4 μ s (b) 10 μ s (Manjaiah et al., 2016) | 43 |
| Figure 2.20 | RLT vs. T_{off} (Roy and Narendranath, 2018) | 44 |
| Figure 2.21 | MRR and SR vs. Servo voltage during WEDM of TiNiCu (Manjaiah et al. 2018) | 45 |
| Figure 2.22 | Machined surface morphology at SV : (a) 20 V (b) 80 V (Manjaiah et al. 2018) | 46 |
| Figure 2.23 | KW vs. SV and other machining parameters (Roy and Narendranath, 2018) | 47 |
| Figure 2.24 | Recast layer thickness at (a) 20 V (b) 60 V (Soni et al., 2017) | 47 |
| Figure 2.25 | Mean effects plot of MRR vs. WEDM parameters (Manjaiah et al., 2015) | 48 |
| Figure 2.26 | Effects plot showing MRR, SR vs. WF (Roy et al., 2017) | 49 |
| Figure 2.27 | Machined surface morphology at (a,b,c) SV- 15 V, WF - 6,8,10 m/min (d,e,f) SV - 30 V, WF - 6,8,10 m/min (g,h,i) SV - 45 V, WF - 6,8,10 m/min (j,k,l) SV - 60 V, WF - 6,8,10 m/min (Roy and Narendranath, 2018a) | 50 |
| Figure 2.28 | Effect of vacuum assisted flushing on machining time and surface roughness in EDM high depth drilling (Tanjilul et al., 2018) | 52 |
| Figure 2.29 | Machined surface morphology at (a) Downward flow (b) Upward flow (Roy and Sanna Yellappa, 2019) | 53 |
| Figure 2.30 | Effect of wire tension, wire speed, flow rate and servo voltage on kerf width (Habib, 2017) | 54 |
| Figure 2.31 | Comparison of experimental data with prediction data for SR, VMRR and accuracy (Ugrasen et al., 2014) | 57 |
| Figure 3.1 | Vacuum Arc Melting Setup | 62 |
| Figure 3.2 | (a) Optical microscope (b-d) Microstructure of TNC11, TNC12 and TNC13 (e-g) Microstructure of TNC21, TNC22 and TNC23 | 63 |

| | | |
|-------------|--|-----|
| Figure 3.3 | Differential Scanning Calorimeter and DSC curve | 64 |
| Figure 3.4 | X-ray diffraction equipment and XRD plot | 65 |
| Figure 3.5 | Wire electro discharge machining setup | 66 |
| Figure 3.6 | Surface roughness tester | 68 |
| Figure 3.7 | Scanning Electron Microscope | 69 |
| Figure 3.8 | Microhardness Tester | 70 |
| Figure 3.9 | Structure of Genetic Algorithm | 75 |
| Figure 3.10 | Flowchart of the experimental plan | 76 |
| Figure 4.1 | Microstructure of (a)Ti ₅₀ Ni ₄₀ Cu ₁₀ (b)Ti ₄₅ Ni ₄₅ Cu ₁₀ (c)Ti ₄₀ Ni ₅₀ Cu ₁₀ and (d)Ti ₅₀ Ni ₃₅ Cu ₁₅ (e)Ti ₅₀ Ni ₃₀ Cu ₂₀ (f)Ti ₅₀ Ni ₂₅ Cu ₂₅ | 80 |
| Figure 4.2 | XRD plots of (a) TNC11 (b) TNC12 (c) TNC13 | 82 |
| Figure 4.3 | XRD plots of (a) TNC21 (b) TNC22 (c) TNC23 | 83 |
| Figure 4.4 | DSC plots of TNC11, TNC12 and TNC13 | 84 |
| Figure 4.5 | DSC plots of TNC21, TNC22 and TNC23 | 86 |
| Figure 4.6 | As cast microhardness of prepared TiNiCu alloys | 87 |
| Figure 4.7 | Effects plot for Material Removal Rate | 94 |
| Figure 4.8 | Effects plot for Surface Roughness | 97 |
| Figure 4.9 | Effects plot for Kerf Width | 99 |
| Figure 4.10 | Kerf zone at T _{on} (a) 100 μs (b) 110 μs (c) 120 μs (d) 130 μs | 100 |
| Figure 4.11 | Kerf zone at SV (a) 15 V (b) 30 V (c) 45 V (d) 60 V | 102 |
| Figure 4.12 | Effects plot for Recast Layer Thickness | 103 |
| Figure 4.13 | Recast Layer Thickness at T _{off} : (a) 20 μs (b) 30 μs (c) 40 μs (d) 50 μs | 104 |
| Figure 4.14 | Recast Layer Thickness at SV : (a) 15 V (b) 30 V (c) 45 V (d) 60 V | 105 |
| Figure 4.15 | Material Removal Rate of L16 experimental trial for Alloy Set 1 and 2 | 106 |
| Figure 4.16 | Surface Roughness of L16 experimental trial for Alloy Set 1 and 2 | 107 |
| Figure 4.17 | Machined surface microhardness of TNC11, TNC12 and | |

| | | |
|-------------|--|-----|
| | TNC13 | 109 |
| Figure 4.18 | Machined surface microhardness of TNC21, TNC22 and TNC23 | 110 |
| Figure 4.19 | Effect of machined surface microhardness on shape recovery | 111 |
| Figure 4.20 | Surface morphology at (a) 4 th (b) 6 th (c) 11 th and (d) 14 th experimental run | 113 |
| Figure 4.21 | I_p and V_p for all experimental runs | 115 |
| Figure 4.22 | Average surface roughness (R_a) and depth (R_z) | 115 |
| Figure 4.23 | Surface morphology of experimental run 1-9 | 117 |
| Figure 4.24 | Surface morphology of experimental run 10-18 | 117 |
| Figure 4.25 | Spark profile of experimental trial 1 st , 3 rd , 10 th and 12 th | 119 |
| Figure 4.26 | Machined surface morphology at (a) 49.03 (b) 98.06 and (c) 147.1 kPa flushing pressure for experimental run resembling higher discharge energy (22-24) | 120 |
| Figure 4.27 | Machined surface morphology at (a) 49.03 (b) 98.06 and (c) 147.1 kPa flushing pressure for experimental run resembling higher discharge energy (7-9) | 122 |
| Figure 4.28 | Surface morphology at (a) Downward and (b) Upward flushing direction | 123 |
| Figure 4.29 | Kerf Width of L16 experimental trial for Alloy Set 1 and 2 | 124 |
| Figure 4.30 | Effect of Kerf Width on machined profile | 125 |
| Figure 4.31 | RLT of L16 experimental trial for Alloy Set 1 and 2 | 126 |
| Figure 4.32 | Recast layer thickness comparison (a,b) TNC11 (c,d) TNC23 | 127 |
| Figure 4.33 | Kerf width profile | 128 |
| Figure 4.34 | MRR L16 plots for homogenized and non-homogenized samples | 129 |
| Figure 4.35 | SR L16 plots for homogenized and non-homogenized samples | 130 |
| Figure 4.36 | Machined surface morphology of TNC11 (a)As cast (b)Homogenized | 132 |

| | | |
|-------------|---|-----|
| Figure 4.37 | KW L16 plots for homogenized and non-homogenized samples | 133 |
| Figure 4.38 | Kerf width of : (a) As cast and (b) Homogenized sample | 134 |
| Figure 4.39 | RLT L16 plots for homogenized and non-homogenized samples | 135 |
| Figure 4.40 | RLT of 6th experimental run for (a) As cast (b) Homogenized samples | 136 |
| Figure 4.41 | (a) Coral reef surface morphology (b) Optimum surface morphology | 139 |
| Figure 4.42 | Scanning electron micrograph of optimum machined surface morphology | 140 |
| Figure 5.1 | Experimental and prediction of (a-c)MRR (d-f)SR (g-i)KW (j-l)RLT | 147 |
| Figure 5.2 | Training algorithm updating weight and bias to minimize error | 149 |
| Figure 5.3 | Experimental and predicted values of responses of TNC11 | 151 |
| Figure 5.4 | Experimental and predicted values of responses of TNC23 | 151 |
| Figure 5.5 | Weight and bias distribution | 153 |

LIST OF TABLES

| TABLE NO. | DESCRIPTION | PAGE NO. |
|------------|---|----------|
| Table 3.1 | Alloy composition (in at.%) and symbol | 62 |
| Table 3.2 | Taguchi's L16 orthogonal experimental array | 67 |
| Table 4.1 | Taguchi's L16 orthogonal experimental plan | 88 |
| Table 4.2 | Material removal rate (mm^3/min) for TiNiCu shape memory alloys | 89 |
| Table 4.3 | Surface roughness (μm) for TiNiCu shape memory alloys | 89 |
| Table 4.4 | Kerf width (μm) for TiNiCu shape memory alloys | 90 |
| Table 4.5 | Recast layer thickness (μm) for TiNiCu shape memory alloys | 90 |
| Table 4.6 | ANOVA results for MRR | 92 |
| Table 4.7 | ANOVA results for SR | 92 |
| Table 4.8 | ANOVA results for KW | 93 |
| Table 4.9 | ANOVA results for RLT | 93 |
| Table 4.10 | Response table for means of MRR | 94 |
| Table 4.11 | Response table for means of SR | 97 |
| Table 4.12 | Response table for means of KW | 99 |
| Table 4.13 | Response table for means of RLT | 103 |
| Table 4.14 | As cast material microhardness of prepared TiNiCu alloys | 108 |
| Table 4.15 | Experimental Results | 114 |
| Table 4.16 | L27 experimental run | 121 |
| Table 4.17 | MRR of Homogenized and Non-Homogenized samples (in mm^3/min) | 128 |
| Table 4.18 | SR of Homogenized and Non-Homogenized samples (in μm) | 130 |

| | | |
|------------|---|-----|
| Table 4.19 | KW of Homogenized and Non-Homogenized samples (in μm) | 132 |
| Table 4.20 | RLT of Homogenized and Non-Homogenized samples (in μm) | 134 |
| Table 4.21 | Selected parameter and their range for Box Behnken experimentation | 138 |
| Table 4.22 | DOE using Box Behnken technique for surface morphology experiments | 138 |
| Table 4.23 | Input process parameters resulting suitable machined surface morphology | 140 |
| Table 5.1 | Normalized input process parameters | 144 |
| Table 5.2 | Normalized output process responses | 145 |
| Table 5.3 | R-value of different ANN architectures | 146 |
| Table 5.4 | Training performance chart using different transfer functions | 148 |
| Table 5.5 | Input sets chosen for testing | 150 |
| Table 5.6 | Percentage prediction error of TNC11 | 152 |
| Table 5.7 | Percentage prediction error of TNC23 | 152 |
| Table 5.8 | Parameters settings used in GA multi objective optimization | 156 |
| Table 5.9 | Optimized WEDM input parameters for TNC11 | 157 |
| Table 5.10 | Optimized WEDM input parameters for TNC23 | 157 |

LIST OF SYMBOLS AND ABBREVIATIONS

| | |
|-------|---|
| A_f | : Austenitic Finish Temperature |
| ANN | : Artificial Neural Network |
| ANOVA | : Analysis of Variance |
| A_s | : Austenitic Start Temperature |
| B19' | : Monoclinic lattice structure |
| B19 | : Orthorhombic lattice structure |
| B2 | : Cubic lattice structure |
| DOE | : Design of Experiments |
| DSC | : Differential Scanning Calorimeter(ry) |
| DSC | : Differential Scanning Calorimetry |
| EDM | : Electro Discharge Machining |
| GA | : Genetic Algorithm |
| GA | : Genetic Algorithm |
| I_p | : Peak Current |
| k_f | : Kerf width (in mm) |
| KW | : Kerf Width |
| KW11 | : Kerf width for alloy $Ti_{50}Ni_{40}Cu_{10}$ |
| KW12 | : Kerf width for alloy $Ti_{45}Ni_{45}Cu_{10}$ |
| KW13 | : Kerf width for alloy $Ti_{40}Ni_{50}Cu_{10}$ |
| KW21 | : Kerf width for alloy $Ti_{50}Ni_{35}Cu_{15}$ |
| KW22 | : Kerf width for alloy $Ti_{50}Ni_{30}Cu_{20}$ |
| KW23 | : Kerf width for alloy $Ti_{50}Ni_{25}Cu_{25}$ |
| L16 | : 16 experimental trial obtained through Taguchi's DOE |
| M_f | : Martensitic Finish Temperature |
| MH | : Micro Hardness |
| MRR | : Material Removal Rate (in mm^3/min) |
| MRR11 | : Material removal rate for alloy $Ti_{50}Ni_{40}Cu_{10}$ |
| MRR12 | : Material removal rate for alloy $Ti_{45}Ni_{45}Cu_{10}$ |
| MRR13 | : Material removal rate for alloy $Ti_{40}Ni_{50}Cu_{10}$ |

| | |
|-------------------------|---|
| MRR21 | : Material removal rate for alloy Ti ₅₀ Ni ₃₅ Cu ₁₅ |
| MRR22 | : Material removal rate for alloy Ti ₅₀ Ni ₃₀ Cu ₂₀ |
| MRR23 | : Material removal rate for alloy Ti ₅₀ Ni ₂₅ Cu ₂₅ |
| M _s | : Martensitic Start Temperature |
| MSD | : Mean Square Deviation |
| P | : Process parameter to be normalized |
| P _{max} | : Maximum value of process parameter |
| P _n | : Normalized process parameter |
| R _a | : Average surface roughness (in μm) |
| R _{dn} | : De-normalized response |
| R _{ik} | : k th response of i th experiment |
| RLT | : Recast Layer Thickness |
| RLT11 | : Recast layer thickness for alloy Ti ₅₀ Ni ₄₀ Cu ₁₀ |
| RLT12 | : Recast layer thickness for alloy Ti ₄₅ Ni ₄₅ Cu ₁₀ |
| RLT13 | : Recast layer thickness for alloy Ti ₄₀ Ni ₅₀ Cu ₁₀ |
| RLT21 | : Recast layer thickness for alloy Ti ₅₀ Ni ₃₅ Cu ₁₅ |
| RLT22 | : Recast layer thickness for alloy Ti ₅₀ Ni ₃₀ Cu ₂₀ |
| RLT23 | : Recast layer thickness for alloy Ti ₅₀ Ni ₂₅ Cu ₂₅ |
| R _{max} | : Maximum response in training data |
| R _{min} | : Minimum response in training |
| R _{testing} | : Testing coefficient |
| R _{train} | : Training coefficient |
| R _{validation} | : Validation coefficient |
| R _z | : Average surface depth (in μm) |
| SEM | : Scanning Electron Microscope |
| SR11 | : Surface Roughness for alloy Ti ₅₀ Ni ₄₀ Cu ₁₀ |
| SR12 | : Surface Roughness for alloy Ti ₄₅ Ni ₄₅ Cu ₁₀ |
| SR13 | : Surface Roughness for alloy Ti ₄₀ Ni ₅₀ Cu ₁₀ |
| SR21 | : Surface Roughness for alloy Ti ₅₀ Ni ₃₅ Cu ₁₅ |
| SR22 | : Surface Roughness for alloy Ti ₅₀ Ni ₃₀ Cu ₂₀ |
| SR23 | : Surface Roughness for alloy Ti ₅₀ Ni ₂₅ Cu ₂₅ |

| | |
|-----------|--|
| SV | : Servo voltage (in Volts) |
| T | : Time taken (in minutes) |
| t_h | : Workpiece thickness (in mm) |
| TiNi | : Binary Titanium Nickel Shape Memory Alloy |
| TiNiCu | : Ternary Titanium Nickel Copper Shape Memory Alloy |
| t_l | : Travel length (in mm) |
| TNC11 | : $Ti_{50}Ni_{40}Cu_{10}$ |
| TNC12 | : $Ti_{45}Ni_{45}Cu_{10}$ |
| TNC13 | : $Ti_{40}Ni_{50}Cu_{10}$ |
| TNC21 | : $Ti_{50}Ni_{35}Cu_{15}$ |
| TNC22 | : $Ti_{50}Ni_{30}Cu_{20}$ |
| TNC23 | : $Ti_{50}Ni_{25}Cu_{25}$ |
| T_{off} | : Pulse off time (in μs) |
| T_{on} | : Pulse on time (in μs) |
| V_p | : Peak Voltage |
| WEDM | : Wire Electro Discharge Machine(ing) |
| WF | : Wire feed (in m/min) |
| x(1) | : Symbol for pulse on time during ANN-GA optimization |
| x(2) | : Symbol for pulse off time during ANN-GA optimization |
| x(3) | : Symbol for servo voltage during ANN-GA optimization |
| x(4) | : Symbol for wire feed during ANN-GA optimization |
| XRD | : X-ray Diffractometer(ry) |
| y(1) | : Symbol for MRR of TNC11 during ANN-GA optimization |
| y'(1) | : Symbol for MRR of TNC23 during ANN-GA optimization |
| y(2) | : Symbol for SR of TNC11 during ANN-GA optimization |
| y'(2) | : Symbol for SR of TNC23 during ANN-GA optimization |
| y(3) | : Symbol for KW of TNC11 during ANN-GA optimization |
| y'(3) | : Symbol for KW of TNC23 during ANN-GA optimization |
| y(4) | : Symbol for RLT of TNC11 during ANN-GA optimization |
| y'(4) | : Symbol for RLT of TNC23 during ANN-GA optimization |

CHAPTER 1

INTRODUCTION

Shape memory alloys (SMAs) belong to the smart material family which are widely known because they can "memorize" their parent shape when heated post deformation. Pseudoelasticity is another characteristics of these alloys usually exhibited in austenitic phase. Due to such intriguing properties of these alloys, they are exploited in various fields like aerospace, biomedical, automobile etc. In a study based on the usability of SMAs, it has been found that TiNi based SMAs are the most practical group of SMAs due to their enhanced mechanical properties as compared to other group of SMAs (Otsuka and Ren, 2005). Due to superior mechanical properties such as high hardness, high toughness etc. conventional machining techniques yield poor surface finish on machined components and also causes high tool wear and low profile accuracy for these alloys (Weinert et al., 2004). Such detrimental influence of conventional machining techniques on shape memory component affect its operational performance. On the other hand non-conventional machining techniques yield results suitable to produce shape memory component as it addresses most of the issues raised by conventional machining techniques. Hence, conventional machining techniques are not suitable to machine these materials. Therefore, wire electro discharge machining (WEDM), a widely used non-conventional machining technique has been explored to machine TiNi based shape memory alloys in this study. Effect of process parameters on machining responses have been evaluated while machining of TiNiCu shape memory alloys using WEDM.

1.1 SHAPE MEMORY ALLOYS

Shape memory alloys can be used as actuators and sensors in various fields due to some of its remarkable advantages such as high power-to-weight ratio, minimal thermal load requirement, miniaturization of conventional components and fatigue resistance. Shape memory actuators and sensors can also be used for aerospace applications due to their unhindered spark-free, quiet operating nature. First ever account of shape memory effect was recorded by Arne Ölander in 1932 while

experimenting with a Gold-Cadmium alloy. Specifically there are few distinctive types of shape memory alloys which are classified as Cu-based (Ahlers; 1986, Wu; 1990), Fe-based (Maki; 1998, Kajiwara; 1999), TiNi based (Knowles and Smith, 1981; Middleton et al., 1985) and other alloys (Humbeeck and Stalmans, 1998; James and Hane, 2000). Among them binary TiNi gained most recognition due to its characteristics like superior power-to-weight ratio, fatigue resistance, damping capacity and excellent biocompatibility. After NITINOL (binary TiNi alloy) was discovered at Naval Ordnance Laboratory its application surged across all domains followed by extensive research (Buehler et al., 1963). Shape memory alloys are also known for superelasticity or pseudoelasticity which is exhibited by this alloy at its austenitic phase (Buehler et al., 1963). Further discussion on TiNi shape memory alloys are carried out in upcoming section.

1.1.1 TiNi Based Shape Memory Alloys

Binary TiNi alloy exhibit shape memory effect through non-diffusive thermoelastic phase transformation between low temperature phase martensite and high temperature phase austenite. When TiNi alloy is deformed under fully martensitic state, twinned martensites transforms into detwinned martensites at deformation zone unlike dislocation slip that occurs in conventional steel alloys (Saburi 1998; Wei et al., 1998). Mechanical properties and microstructures of TiNi thin films have been examined in order to apply TiNi to microelectromechanical systems (Walker et al., 1990; Busch et al., 1990; Ishida et al., 1993). There are several typical martensitic transformations in Ti–Ni-based SMAs. The martensitic transformation in solution-treated near equiatomic Ti–Ni SMAs takes place from the B2 to the B19' structure (Nakayama et al., 2001), while $B2 \rightarrow R \rightarrow B19'$ two stage transformation always happens in Ti–Ni–Fe SMAs and aged Ni-rich Ti–Ni SMAs (Hwang et al., 1983; Kim et al., 2004). Ti–Ni–Cu SMAs with different compositions experience three kinds of martensitic transformations (Lee et al., 2006), including $B2 \rightarrow B19'$, $B2-B19-B19'$ and $B2 \rightarrow B19'$. One of the basic issue related to binary TiNi alloy is its uncontrollable actuation frequency and large hysteresis, which are not useful for actuation or sensing applications. Addition of Cu decreases the hysteresis width of the

SMA response. This results in the decrease of transformation strain, reduction in pseudoelastic hysteresis and also reduces the sensitivity of the martensitic start temperature to composition. The small hysteresis associated with the transformation makes TiNiCu an ideal choice for actuators.

1.1.2 TiNiCu Shape Memory Alloys

Phase transformation temperatures of TiNiCu shape memory alloys are sensitive to percentage composition. Among different compositions of TiNiCu, 5 to 10 at.% Cu are preferred. Addition of Cu greater than 10 at.% is most preferred (Saburi et al., 1989). However, above 10 at.% addition of Cu, the alloy becomes brittle. A group of researcher studied the effect of Cu content on the shape memory behavior of the ternary alloy thin films containing various Cu contents where Ti is maintained at around 50 at.%. They confirmed that the films containing less than 10 at.% Cu show both martensitic phases of B19 and B19'. But in case of films containing more than 10 at.% Cu, only B19 martensite phase was observed. Therefore, this has been concluded that the transformation behavior of Ti-Ni-Cu films depends on Cu content. It has been concluded that films containing higher than 15 at.% Cu showed very narrow transformation hysteresis ($\sim 13^{\circ}\text{C}$) and perfect shape memory effect even when the applied stress was as high as ~ 400 MPa. These characteristics are preferable for the ternary Ti-Ni-Cu thin films to be used as important elements of high performance micro-actuators (Hori et al., 2010). Melting of these alloys are very difficult due to high reactivity of Ti and Ni. Inert atmosphere is required during their melting. Therefore, Vacuum Arc Melting has been adopted in the current research to develop these alloys.

1.1.3 Applications of Shape Memory Alloys

Shape memory alloys are implemented in several fields to transform thermal energy into mechanical movement. Jani et al. (2014) conducted a literature survey on outreach, contribution and applications in the field of "shape memory alloys" and found that majority of US patents filed between 1990-2013 direct to biomedical applications of shape memory alloys. From several studies it was acknowledged that

NiTi shape memory alloys are suitable materials for medical applications due to superior biocompatibility they exhibit along with shape memory effect and pseudoelasticity (Hoh; 2009, Machado; 2003). They can be used as stents (Figure 1.1a) and as sensors and actuators (Figure 1.1b). Aerospace applications of shape memory alloys have gained much attention after they were first used as couplers in hydraulic tubing in F-14 aircraft in 1971 (Melton, 1999).

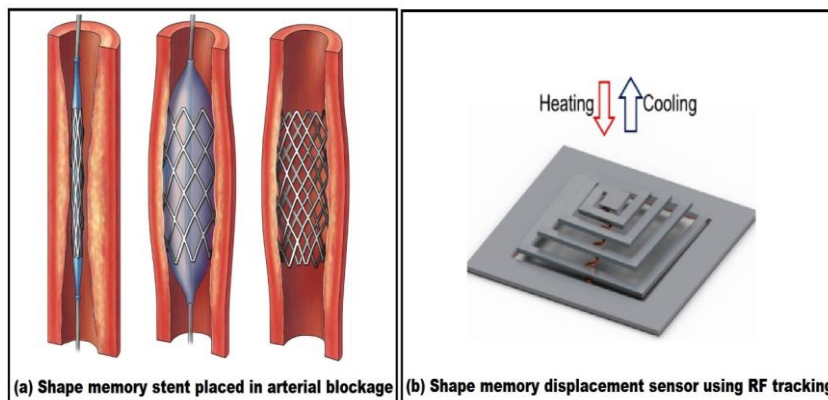


Figure 1.1 Different applications of shape memory alloys (Ali et al., 2014)

Recent advances in aerospace applications of shape memory alloys contain wing and shape morphing which have led to development of variable geometry aircraft components such as inlet cowl of F-15 engine (Wax et al., 2003) and chevron of Boeing engine to reduce noise (Mabe et al., 2005). Figure 1.2 comprehensively depicts several existing and potential shape memory applications in automotive sector as depicted by Jani et al., 2014. Since shape memory alloys can reduce the robustness of conventional components they are highly favored in automotive industry.

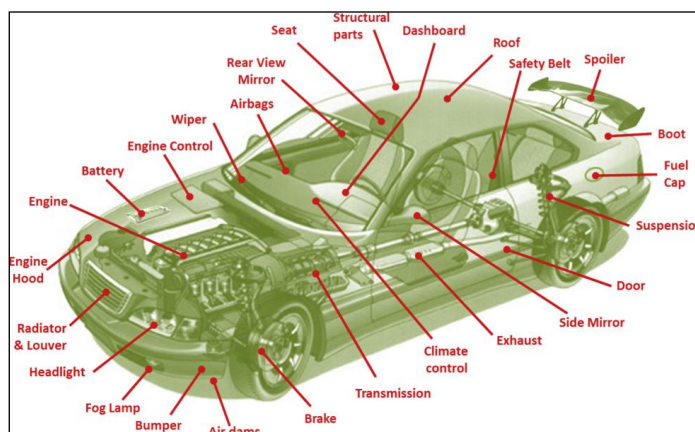


Figure 1.2 SMA applications in automotive sector (Jani et al., 2014)

1.2 MACHINING OF SHAPE MEMORY ALLOYS

Shape memory alloys are smart functional materials whose properties are result of its unique metallurgical configurations. Shape memory applications demand components having intricate shape and structure for successful implementation of shape memory effect. Therefore, machining of these alloys into required components require precision in terms of profile and metallurgical viewpoint. In other words, manufacturer should proceed with extreme caution while machining shape memory alloys as metallurgical or profile damage may hinder shape memory ability of the material. Selection of proper machining technique for shape memory alloys is critical since the end product is expected to bear necessary qualities of a smart material. Hence, this section confers about conventional and non-conventional machining of shape memory alloys and presents different standpoint regarding this matter.

1.2.1 Conventional Machining of Shape Memory Alloys

Abrupt chip formation, burr formation, high tool wear, poor machined surface quality, imperfect end profile and metallurgical surface damage are some disadvantages of conventional machining. Weinert and Petzoldt (2004) found similar results while turning binary NiTi shape memory alloy. Figure 1.3a indicates nose of tool which suffered severe damage while turning NiTi shape memory alloy, whereas Figure 1.3b indicates adverse chip formation due to pseudoelastic nature and thus resulting in poor surface finish.

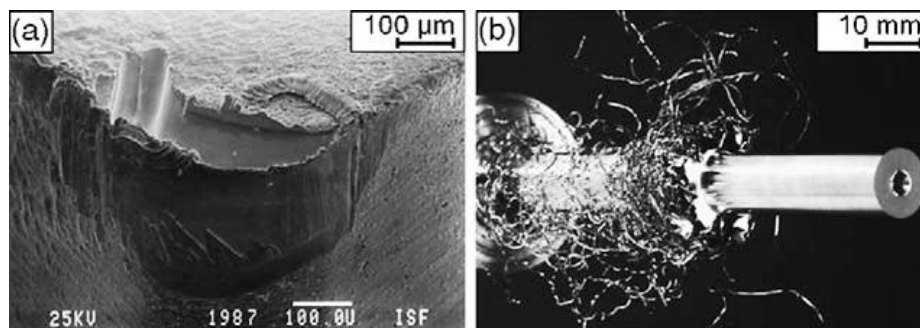


Figure 1.3 (a) Tool nose damage (b) Abrupt chip formation (Weinert and Petzoldt, 2004)

In another report the group of authors suggested that use of coated cemented carbide yields better results compared to traditional turning tools (Weinert et al., 2004). However, outcome of conventional machining is more or less same for shape memory alloys. Manjaiah et al. (2014) concluded in their study that non-conventional machining techniques are more suitable for shape memory alloys as damage inflicted on workpiece material by such techniques are negligible compared to conventional machining techniques. Non-conventional machining techniques include laser beam machining, water jet machining, electrochemical machining, electro-discharge machining etc.

1.2.2 Non-Conventional Machining of Shape Memory Alloys

Non-conventional machining techniques such as laser beam machining (LBM), water jet machining (WJM), electro-chemical machining (ECM) and electro-discharge machining (EDM) have several advantages over conventional machining techniques. Since it is a non-contact process no damage occurs to workpiece material due to shear deformation and tool wear is either negligible or absent compared to conventional machining techniques. Biffi and Tuissi (2017) performed a comparative study where a thin superelastic nitinol plate was machined to form a diamond shaped microelement using femtosecond (FS) and continuous wave (CW) laser machine. It was found that continuous wave laser machining led to formation of heat affected zone as wide as 250 μ m whereas this was avoided using femtosecond laser equipment. Similar results were also reported by Li et al. (2006) and Tung et al. (2008). Kong et al. (2011) implemented plain water jet (PWJ) machining and abrasive water jet (AWJ) machining to mill NiTi shape memory alloy. They found that AWJ milling resulted in better depth control compared to PWJ but results in several machining defects such as grit embedment, striation marks, debris attachment, burr formation etc. Figure 1.4 indicates grits attached to the machined surface after AWJ machining.

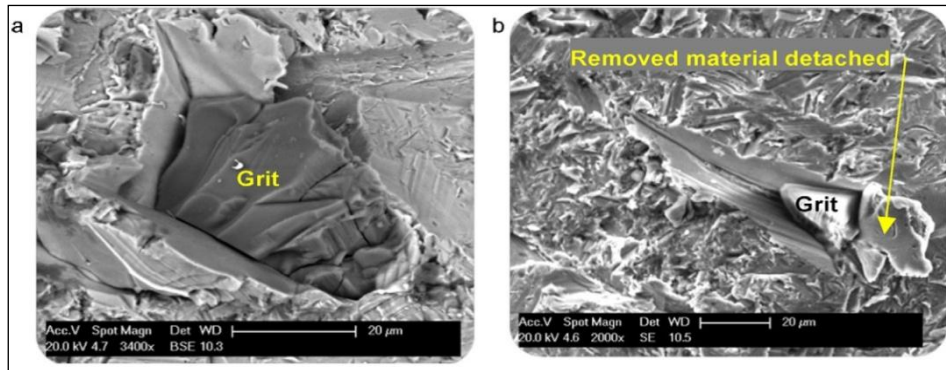


Figure 1.4 SEM image of : (a) Grit embedment (b) Parent material detachment by grit
(Kong et al., 2011)

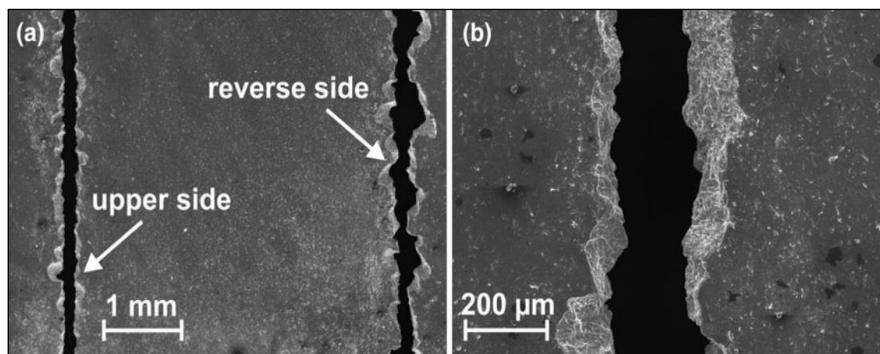


Figure 1.5 SEM image of : (a) kerf profile at upper side and reverse side (b)
magnified image of reverse side (Frotscher et al., 2011)

Frotscher et al. (2011) in their study observed that kerf profile of NiTi plates at upper and reverse side are dissimilar due to characteristic nature of the jet geometry which tend to blow away chunk of material. Figure 1.5 indicates the kerf profile and resulting geometrical inaccuracy caused by AWJ machining. Lee and Shin (2011) investigated electrochemical polishing (ECP) of nitinol using neutral as well as acidic electrolyte. They reported that high duty factor and current value increase material removal rate but deteriorate machined surface quality and they have recommended this operation mostly for finishing operations. Limitations of aforementioned non-conventional machining techniques can be addressed by electrodischarge machining (EDM). Through this technique precise components could be manufactured and machining defects like striation, burr formation, profile accuracy, debris attachment etc. can be minimized (Manoj et al., 2019a). EDM generates thinner recast layer compared to LBM and better surface finish compared to other non-conventional

machining techniques. Due to ionization of dielectric medium oxidation of machined surface can be observed on EDMed surface which leads to higher machined surface hardness compared to bulk material (Müller et al., 2000). Wire electrodischarge machining (WEDM) is another variant of EDM where the traditional "mirror" tool is replaced by a thin brass wire using which any desirable profile can be cut with reduced recast layer. Forthcoming section discusses in detail about various aspects of WEDM absolutely necessary to comprehend this research work.

1.3 WIRE ELECTRO DISCHARGE MACHINING OF SMA

WEDM can be considered far more flexible and economically preferable compared to traditional EDM. High tool wear of EDM leads to reduced end profile accuracy over a period of time and needs to be replaced. WEDM on the other hand uses thin brass wire electrode which can be easily recycled and reduces tooling cost. Sharp profiles with high accuracy and thinner recast layer can be achieved with WEDM irrespective of the hardness of the workpiece. Only requirements of WEDM process is that workpiece material needs to be electrically conductive and must possess fair thermal conductivity. Shape memory alloys exhibit their unique material characteristics due to special crystal arrangement of constituent elements. Recast material does not possess that arrangement and hence is detrimental to our cause. In this study WEDM is used to machine TiNiCu shape memory alloys and upcoming sections discuss in details about WEDM and its aspects.

1.3.1 Introduction of WEDM

WEDM is a electro-thermal process where material removal is done by short repetitive electrical sparks in presence of a dielectric fluid which impinges on workpiece (anode) from the wire electrode (cathode) and causes local melting. Pressurized dielectric fluid dislodges the melted workpiece material and makes way for the sparks to remove more material. Principle of WEDM process is discussed briefly in the upcoming section.

1.3.2 Principle of WEDM

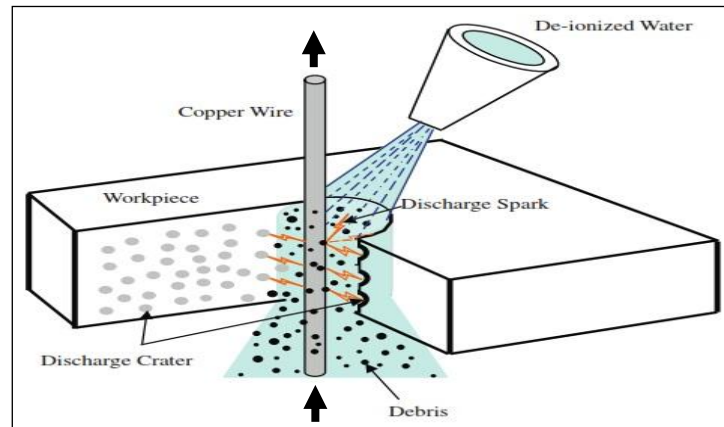


Figure 1.6 Material removal in WEDM (Hsieh et al., 2009)

Figure 1.6 is a graphical representation of working principle of WEDM process. Copper wire shown in the image acts as cathode which is continuously fed to the machining zone and workpiece acts as the anode. Machining zone is filled with a dielectric medium (de-ionized water) at high pressure. A RC circuit is employed to convert AC to pulsed DC current in order to generate high energy sparks between a suitable gap maintained between cathode and anode using a servo mechanism. These sparks impinge on the workpiece surface and causes local heating. Due to high temperature localization on a single point, workpiece material melts and is carried away by flushing dielectric. El-Hofy et al (2005) estimated that temperature may rise to about 10,000°C at the spark impingement zone which causes instant vaporization of workpiece material. Integration of this process with a CNC unit helps to perform profile cutting. There are few machining parameters of WEDM which directly or indirectly affect the material removal mechanism. Major process parameters are discussed in the subsequent section.

1.3.3 Process Parameters of WEDM

In any generic WEDM unit there are certain process parameters which directly or indirectly control the material removal mechanism. It is imperative for any manufacturer to select appropriate level of WEDM parameters to perform optimized

machining. Optimized machining comprises of factors like high material removal rate, superior integrity of machined surface, high profile accuracy etc.

1.3.3.1 Pulse on time

Pulse on time is the duration for which sparking continues for a given pulse cycle. A pulse cycle consists of two distinct phenomenon: a duration for which sparking continues and duration for which sparking is halted (for the sake of debris removal). This process parameter determines the period of time for which material is being removed through melting by sparking. For a fixed pulse cycle, higher pulse on time results in more material removal but have disadvantages like frequent wire breakage and poor surface finish. Frequent wire breakage at longer pulse on time is caused by heat generation and accumulation on the wire electrode as spark generates from it. Longer pulse on time ensures larger and deeper crater caused by the impinging spark discharge which in turn contributes to higher machined surface roughness.

1.3.3.2 Pulse off time

Pulse off time is the duration for which sparking is halted for a given spark cycle. Generally this halt duration is lesser than pulse on time and helps in debris removal which generates in the machining zone immediately after sparking is halted. For a fixed pulse cycle, higher pulse off time results in low material removal rate and superior surface finish.

1.3.3.3 Servo Voltage

Servo voltage is another process parameter which controls the sparking gap during machining by varying the voltage between wire electrode and workpiece surface induced through servo mechanism. Increase in servo voltage widens the gap between wire electrode and workpiece, hence lowers the material removal rate and improves surface quality. On the other hand lower servo voltage reduces the gap which results in more severe sparking conditions, hence high material removal rate and poor machined surface quality.

1.3.3.4 Wire Feed

Fresh wire electrode is being fed continuously to the machining zone from a spool of wire. The rate at which wire electrode is fed to the machining zone determines the speed and quality of machining. Higher wire feed rate ensures breakage free seamless machining and improved productivity. Lower wire feed rate may lead to frequent wire breakage due to melting of the wire during sparking.

1.3.3.5 Dielectric Flushing Pressure

Dielectric fluid is supplied with a specific flushing pressure which can be controlled based on machine capability. High dielectric flushing pressure facilitates efficient removal of molten debris from machining zone but may cause issues like poor surface finish and low accuracy parts due to vibration of wire electrode.

1.3.4 Machining Output Responses of WEDM

WEDM responses like material removal rate (MRR), surface roughness (SR), kerf width (KW), recast layer thickness (RLT) determine productivity of the machining and quality of a part being produced by this process. For shape memory alloys, it is imperative to produce parts with superior surface integrity and profile accuracy. Aforementioned machining responses are investigated in this research work and optimized to determine suitable process parameter levels in order to produce shape memory components having suitable characteristics.

1.3.4.1 Material Removal Rate

Material removal rate determines the productivity of a machining process. Higher material removal rate indicates better productivity. Material removal rate can be determined by amount of material removed during machining for a unit period of time.

1.3.4.2 Surface Roughness

Craters formed during sparking in WEDM process largely contribute in surface roughness and are directly controlled by parameters like pulse on time and servo voltage. A part produced using WEDM having high surface roughness will not be suitable for sensitive applications. High surface roughness indicates deeper and larger crater along with more amount of resolidified debris present in the surface.

1.3.4.3 Kerf Width

Kerf width is the width of cut in WEDM process which directly affects the accuracy of the produced part. Kerf width is the overcut (generally 25-40 μm) on both sides of the wire electrode summed up with diameter of wire electrode (250 μm in our case) and is strongly influenced by WEDM parameters. This machining response can be optimized (reduced in this case) with proper selection of process parameters which in turn will improve part accuracy. Higher kerf width results in undersized part whereas lower kerf width indicates a more accurate part. Figure 1.7 signifies the effect of kerf width on profile to be machined. Larger kerf results in poor profile accuracy whereas smaller kerf provides a more accurate profile.

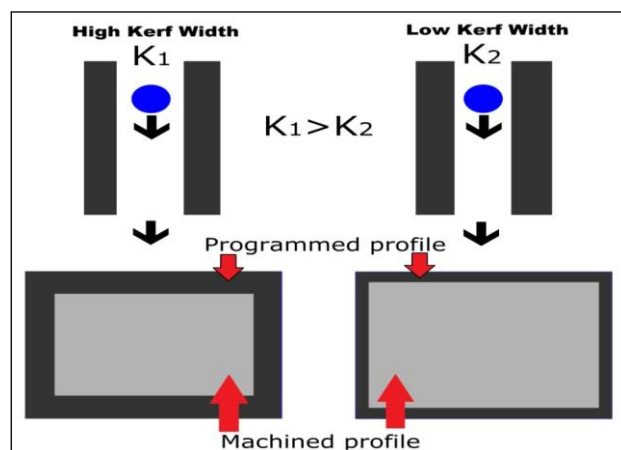


Figure 1.7 Effect of kerf width on machined profile (Roy et al., 2018)

1.3.4.4 Recast Layer Thickness

Resolidified debris which still remains on the machined surface is widely known as "recast" layer. This recast material consists mostly oxides which contribute to higher material hardness compared to bulk workpiece material. Thicker recast layer indicates that shape recovery of a WEDMed component will be restricted and hence selection of process parameters should be done carefully to minimize recast layer thickness. Figure 1.8 depicts the effect of recast layer thickness on shape recoverability of a component machined using WEDM.

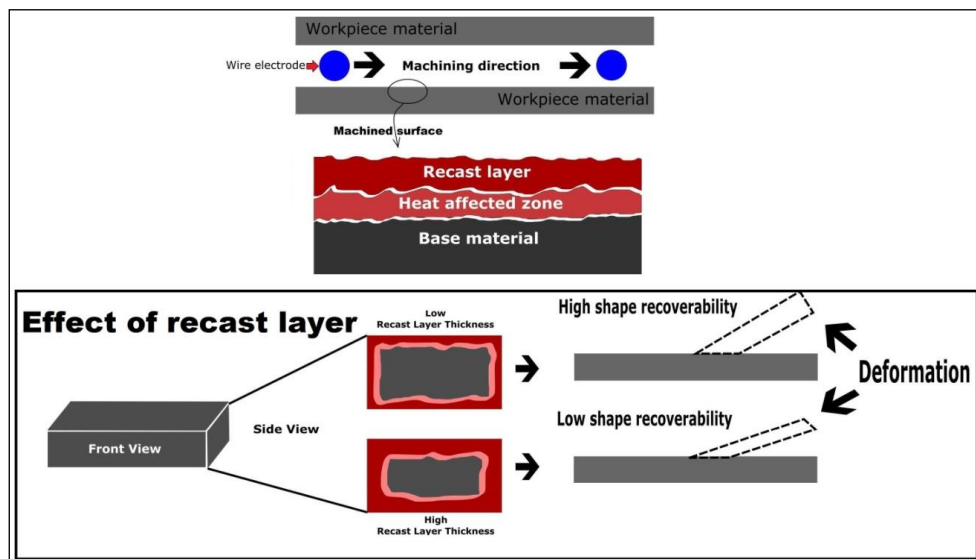


Figure 1.8 Effect of recast layer thickness of shape recoverability (Roy et al., 2018)

1.3.5 Significance and Implementation of WEDM

Performance of WEDM process is quantified by output machining responses material removal rate, surface roughness, kerf width and recast layer thickness. These output responses of WEDM process depends on the input process parameters namely pulse on time, pulse off time, servo voltage and wire feed as used in this study. Depending on the level of these parameters implemented during machining, quality of the component being machined is determined. WEDM is favored when intricate profiles are to be machined possessing higher accuracy. When superior accuracy is required, efforts are to be made to minimize KW in order to achieve a more accurate machined profile. As discussed earlier RLT has to be minimized to reduce metallurgical damage

caused to the material due to spark machining. Since damage caused to workpiece material during WEDM is least compared to other machining techniques it has become the choice for automobile, aerospace, tool and die making and even for biomedical applications. Shape memory components are incorporated in design to minimize weight and size of a conventional machine or instrument where a certain kind of displacement is vital to its functioning. Shape memory alloys reduce movable parts in such conventional machines or instruments as such displacements can be carried out with thermal loading and constrained motion or a combination of both. One of the most favored applications of TiNiCu shape memory alloys are sensors and actuators. Such design comprises of miniature parts which react to thermal load and hence shape change occurs. Smart design such as shown in Figure 1.1b, have complex shapes which can be machined using WEDM with ease. Due to intrinsic capability of WEDM to produce such detailed profiles, it is used to study the effect of WEDM input process parameters on output machining responses. In this study six different TiNiCu shape memory alloys were investigated in terms of MRR, SR, KW and RLT. Other aspects like machined surface morphology and machined surface microhardness were also investigated. Furthermore, detailed investigation on effect of other less studied aspects of WEDM process such as flushing pressure, flushing direction, peak current and peak voltage on machined surface quality were also investigated. To realize this vast experimental investigation in an efficient manner, several design of experiments techniques were incorporated to minimize machining time and avoid repetitive experimental runs.

1.4 DESIGN OF EXPERIMENTS (DOE)

Design of experiments (DOE) help in understanding the relationship between factors and output response of a particular process, in our case WEDM. Through DOE it is possible to understand the extent of variation in WEDM responses caused due to varying process parameters. In this research work three different DOE were used based on requirement.

1.4.1 Taguchi's Orthogonal Design of Experiments

Taguchi's L16 orthogonal array was used to perform machining of TiNiCu shape memory alloys. Material removal rate, surface roughness, kerf width and recast layer thickness were noted for each experimental run. Taguchi's design of experiment efficiently helps to determine degree of influence on machining responses by machining process parameters through effects plot and statistical analysis like ANOVA, ANOM etc.

1.4.2 Box-Behnken design of experiments

Box-Behnken design of experiment of response surface methodology was used to perform few WEDM experiments to optimize surface morphology features. Due to rotatable nature of this methodology, fewer design points and varying levels are enough to formulate an experimental plan.

1.4.3 Factorial design of experiments

Factorial design of experiments allow combinations of all possible experimental run using the provided level of process parameters. This experimental methodology was used to investigate effect of flushing pressure, flushing direction, peak current and peak voltage on surface morphology.

1.5 PREDICTION AND OPTIMIZATION USING ARTIFICIAL NEURAL NETWORK AND GENETIC ALGORITHM

Artificial neural network (ANN) has been implemented in this research work to learn the WEDM process. Based on design of experiments (DOE), machining responses MRR, SR, KW and RLT for each experimental run were established. ANN mapped the relation between levels of WEDM process parameters with obtained machining responses via a process known as training. 75% of the machining data was fed to the ANN for neural mapping and rest 25% was used for testing and validation process. After a low error neural mapping was achieved, the trained neural network was used to predict MRR, SR, KW and RLT. Prediction of output machining responses was

carried out to establish the feasibility of reducing machining time and achieving suitable process modeling which helps to develop a relation between input variables and output responses of machining process. ANN maps the relation between input process parameters and output machining responses in terms of neural weights. These neural weights are assigned to each neuron based on non-linear relation between input and output of WEDM process. Furthermore, these neural weights were used to establish suitable functions to perform optimization of input process parameters based on experimental results obtained during WEDM process. Optimization of machining responses were carried out using Genetic Algorithm (GA) based optimization technique. Fitness function for GA optimization was obtained from equations consisting of weights and biases assigned to ANN based on mapped input and output of WEDM process. Finally, optimization of WEDM process parameters were carried out to define suitable process parameter levels to obtain suitable MRR, SR, KW and RLT in accordance with requirements of a TiNiCu shape memory alloy component such as actuators and sensors.

1.6 OUTLINE OF THESIS

CHAPTER 1

In this chapter background of shape memory alloys, their types and extent of applications have been introduced. This chapter also discussed about suitability of WEDM for machining of SMAs. Principle, process parameters and DOE implemented in WEDM process were discussed along with machining responses which determine the quality of machining.

CHAPTER 2

This chapter presents an extended literature review on binary and ternary TiNi shape memory alloys. Findings by other researchers on effect of WEDM process parameters on machining responses are also reported. Prediction and optimization techniques incorporating artificial neural network as adopted by other researchers are also

discussed in this chapter. Based on literature, motivation and objective of current research work are presented in this chapter.

CHAPTER 3

This chapter deals with experimental setups used for development, characterization and machining of TiNiCu shape memory alloys. Methodology used for conducting machining experiments and other setups used for measuring various machining responses are also discussed in this chapter.

CHAPTER 4

In this chapter results obtained after characterization and quantified data of WEDM responses like material removal rate, surface roughness, kerf width, recast layer thickness, machined surface microhardness etc. are reported. Suitable level of WEDM process parameters for developed TiNiCu shape memory alloys are also reported. Reason and degree of variation in machining responses due to difference in composition of developed TiNiCu shape memory alloys are also reported in this chapter.

CHAPTER 5

In this chapter artificial neural network was used to map the responses of WEDM process with WEDM process parameters. Finally after suitable neural network was established it was trained with the machining data and prediction of responses were carried out. Furthermore, optimization of WEDM responses were carried out using multi objective genetic algorithm technique and detailed discussions are presented in this chapter.

CHAPTER 6

In this chapter conclusions derived from the current research study are presented. Along with systematic presentation of conclusions based on research objectives, this chapter also addresses several future scopes on this broad topic.

CHAPTER 2

LITERATURE REVIEW

2.1 INTRODUCTION

This chapter presents the review of research work which were inspired by excellent properties exhibited by shape memory alloys and their wide range of applications. Due to the difficulty in machining of these group of alloys, non-conventional machining is adopted to process these materials. WEDM is the most accepted machining process due to its versatility to machine efficiently and form intricate parts having complex geometries with ease. Most suitable experimental methodology in terms of design of experiments and optimization techniques were identified from works of various researchers. The literature survey is based upon the effect of WEDM process parameters on the output responses such as material removal rate, surface integrity etc.

2.2 TiNi BASED SHAPE MEMORY ALLOYS

Among different shape memory alloys TiNi based shape memory alloys were found to be most useful because of their superior mechanical properties and suitable phase transformation temperatures. Besides automobile and aerospace domains TiNi based shape memory alloys are also used widely in biomedical sector. It was observed that phase transformation temperatures can be tailored with ease either by changing percentage composition or appropriate heat treatment. After binary TiNi alloy was discovered, researchers conducted studies on several aspects of shape memory and pseudoelastic phenomenon to comprehend its behavior and implement them for suitable applications.

2.2.1 Binary TiNi Alloy

After around three long decades of discovery of shape memory effect in the 1930s, Buehler et al. (1963) discovered the shape memory effect in the early 1960s in near

equiatomic NiTi alloy. They have discovered a maximum A_f (austenitic finish) temperature of 120°C for equiatomic NiTi alloy (i.e. 50 at.% of Ni and 50 at.% Ti). Diffusionless transformation from austenite to martensite or vice versa leads to shape memory effect. Austenite to martensite transformation can be carried out in NiTi alloy either by reducing temperature (thermally induced) or by applying a mechanical stress (stress induced). During cooling austenite starts transforming into martensite and the temperature at which this phase change occurs is known as martensitic start temperature (M_s). The temperature at which entire austenite is converted back into martensite is known as martensitic finish temperature (M_f). Similarly, when martensite is heated to form austenite, temperature at which austenite starts to appear is known as austenitic start temperature (A_s) and the temperature at which entire martensite is converted to austenite is known as austenitic finish temperature (A_f) (Duerig and Pelton, 1994). When thermal load is applied post deformation, shape memory material such as binary NiTi alloy receives the heat and its temperature rises. Desired shape of a shape memory component is set at its austenitic phase which does not revert back to deformed shape when thermal load is withdrawn. Therefore, when detwinned martensite starts transforming into austenite, parent shape gets recovered and when thermal load is withdrawn it cools down to form twinned martensite. It has to be noted that shape of the component at its austenitic state and twinned martensite state are similar. Entire shape recovery cycle is characterized by difference between austenitic finish and martensitic start temperature ($A_f - M_s$), also known as transformation hysteresis. Smaller the thermal hysteresis, faster will be the actuation rate. For binary NiTi alloy transformation hysteresis is typically $30-50^{\circ}\text{C}$ as reported by Gallardo et al. (2002), which indicates slower actuation rate. It has been observed that decreasing the Nickel atomic percentage from the equiatomic composition does not change the transformation temperature. However, if the composition of Nickel is increased above 50 at.%, the transformation temperature begins to decrease, with A_f becoming as low as -40°C for 51 at.% Nickel (Otsuka et al., 2005). Another reason NiTi alloy exhibit shape memory effect is that martensite can exist in 24 different variants or "twins" which reorient themselves into a single "detwinned" variant under mechanical load (Otsuka et al, 2005). Figure 2.1 roughly depicts two dimensional

view of three dimensional shape of austenite, martensite and two dimensional representation of twinned and detwinned martensite (martensite variants).

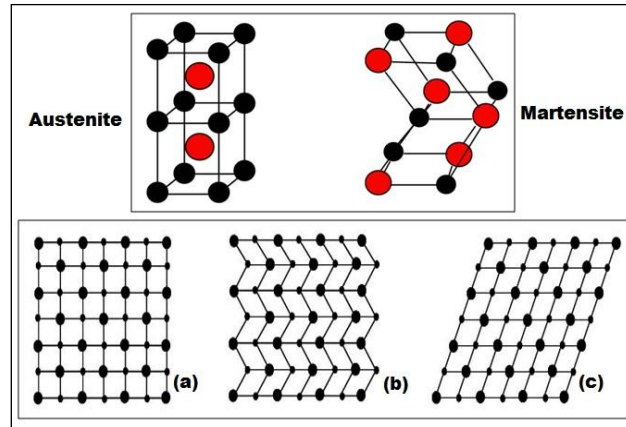


Figure 2.1 Crystal arrangement of high and low temperature phases and 2D view of (a) Austenite (b) Twinned martensite (c) Detwinned martensite (Falvo, 2008)

However, several applications of shape memory alloys demand either a transformation temperature beyond binary NiTi alloy system or narrower transformation hysteresis. This can be solved by addition of a third element in NiTi binary alloys system, also known as ternary TiNi shape memory alloys.

2.2.2 Ternary TiNiX Alloy

Addition of a third element in binary NiTi alloy system could help in controlling transformation temperatures either by reducing or increasing M_s or A_f . Ternary alloys such as TiNiPd, TiNiPt, TiNiHf, TiNiZr, TiNiAu and TiNiAl are high temperature shape memory alloys mostly used at high temperature working environment. Martensitic start temperature (M_s) of TiNiPd and TiNiPt could vary from -26°C (for 10 at.% Pd) to 563°C (for 50 at.% Pd) and from -10°C (for 10 at.% Pt) to 1040°C (for 50 at.% Pt) respectively as reported by Lo et al. (1990). Phase transformation temperatures (M_s and A_s) up to 240°C was reported for up to 30 at.% Zr NiTiZr shape memory alloys (Gao et al., 1997). In case of $\text{Ni}_{49}\text{Ti}_{36}\text{Hf}_{15}$ alloy 10% elongation was observed at room temperature and about 30% at 237°C . Reason for such behavior was attributed to transformation induced plasticity (Wang et al., 1999). This could also

result in narrow transformation hysteresis and improved mechanical properties (Gallardo et al., 2002). Addition of Iron in NiTi alloy system drastically reduces phase transformation temperature and exhibit R-phase transformation (Karthik et al., 2017). Naresh et al. (2017) reported that M_s temperature increases from -61°C to -6°C when 2% Fe is added and then decreases gradually if Fe content is increased. Even though suitable phase transformation temperature was obtained for NiTiFe shape memory alloys, it was found that this alloy exhibits very high hardness which is not suitable for certain actuator applications. However, it was found that for micro components, addition of Cu makes a more suitable material for actuator applications (Shelyakov et al., 2019).

2.2.3 TiNiCu Shape Memory Alloy

Copper being a close neighbor of Nickel in the periodic table, addition of Cu in binary TiNi alloy brings tremendous change in its properties. One of the notable property of these alloys is that addition of Cu reduces the hysteresis of the SMA response. However, this also results in a decrease in the transformation strain. Addition of Cu greater than 10 at.% makes the alloy brittle thus affecting the formability of the alloy as reported by Saburi et al. (1989). At 10 at.% Cu, the transformation hysteresis is much smaller than for the binary alloy at the expense of the total transformation strain which is reduced around 4.0% as observed by Nam et al. (1990). The addition of Cu also reduces the pseudoelastic hysteresis. The width of the pseudoelastic hysteresis is cut down to half at less than 100 MPa for $\text{Ti}_{50}\text{Ni}_{40}\text{Cu}_{10}$ when compared to binary NiTi alloy. In a study conducted on the phase transformation behavior by Matveeva et al. (1997) it has been observed that for TiNiCu alloys system, at composition % between 7.5-10 at.% Cu, the material undergoes a clear three stage cubic to orthorhombic to monoclinic transformation where small hysteresis associated with the transformation makes TiNiCu an ideal choice for actuators. Also, it has been found that among different composition of TiNiCu alloy system, Cu content between 5-10 at.% is most preferred. Transformation hysteresis (A_f-M_s) for TiNi and TiNiCu alloys are approximately 26°C and 16°C respectively. Such narrower transformation hysteresis is what makes TiNiCu a more suitable material for actuator applications

compared to binary TiNi alloy. Similar results were also reported by Wang et al. (2003). Gil et al. (2004) evaluated microstructural, mechanical and cytotoxicity of different NiTi and NiTiCu SMAs. They have found out that the addition of copper was effective to narrow the stress hysteresis and to stabilize the superelasticity characteristics. It has been deduced that although M_s is insensitive to the substitution of Ni by Cu, M_s decreases as Cu substitutes Ti which leads to the fact that the presence of Cu makes the M_s temperature less sensitive to variations in the Ni-Ti ratio. After conducting a calorimetric study, they have found out that alloys with Cu have substantially more narrow hysteresis as compared to binary NiTi alloy. Hori et al. (2010) studied the effect of Cu content on the shape memory behavior of the ternary alloy thin films containing different % of Cu contents where Ti is maintained constant at around 50 at.%. They confirmed that the films containing less than 10 at.% Cu show both martensitic phases of B19 and B19'. It has been concluded that films containing higher than 15 at.% Cu showed very narrow transformation hysteresis ($\sim 13^\circ\text{C}$) and perfect shape memory effect even when the applied stress was as high as ~ 400 MPa. Recent developments reported by Li et al. (2016) indicates that vacuum arc melted TiNiCu shape memory alloys are excellent material for biomedical implants as Cu ions have good antibacterial properties. Figure 2.2 depicts DSC plots obtained for binary TiNi and TiNiCu shape memory alloys in their study. Effect of Cu addition on transformation hysteresis can be clearly observed from DSC plots.

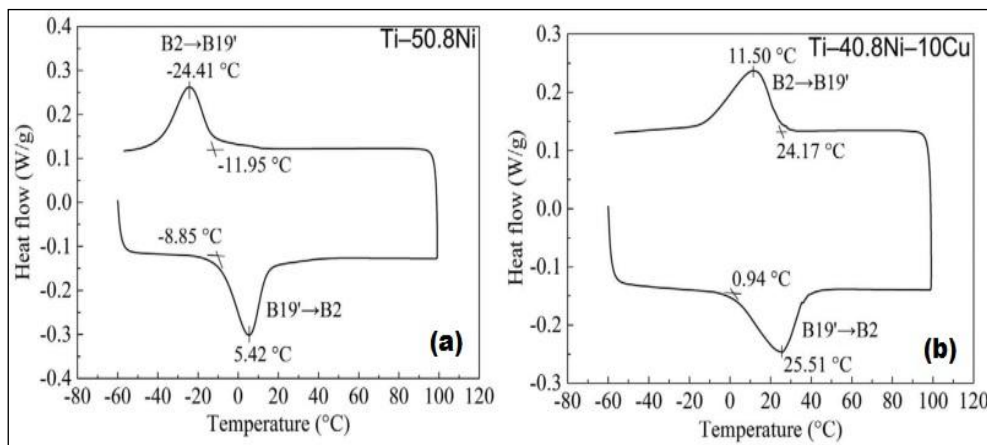


Figure 2.2 DSC plot (a) Ti-50.8Ni (b) Ti-40.8Ni-10Cu (Li et al., 2016)

2.3 CHARACTERIZATION OF TiNiCu SHAPE MEMORY ALLOYS

Shape memory alloys exhibit such unique properties due to special crystal arrangement of martensite and austenite and diffusionless transformation between them. Before a developed shape memory alloy could be used for its shape memory characteristics, it needs to be inspected in terms of microstructure and thermal qualities such as existing martensite and austenite phases, their orientation and phase transformation temperatures. This section discusses about available literature on characterization of TiNiCu shape memory alloys.

2.3.1 Metallographic Characterization

It was confirmed by Sutou et al. (2005) that shape memory effect is strongly influenced by relative grain size (d/D ; d is grain size and D is wire diameter) in polycrystalline shape memory alloys. It was observed that yield stress, work hardening after yielding and stress hysteresis decreases with increasing relative grain size and leads to transformation strain and maximum pseudoelastic strain. Kim et al. (2007) also observed that grain refinement happened in melts having higher Cu content due to higher undercooling. Ishida et al. (2008) prepared $\text{Ti}_{51.6}\text{Ni}_{36.8}\text{Cu}_{11.6}$ and annealed them at three different temperatures (500°C , 600°C and 700°C) and found that grain size was not largely affected by annealing temperature. However, at higher annealing temperature (700°C) disk-shaped precipitates were absent but resulted in spherical and plate like precipitates largely identified as Ti_2Ni and Ti_2Cu phases respectively. He et al. (2009) emphasized that most of the research work until their intervention was carried out on TiNiCu alloys having equal molar ratio of Ti to Ni+Cu and hence carried out investigation on Ti rich high Cu content $\text{Ti}_{52}\text{Ni}_{23}\text{Cu}_{25}$ alloy. They reported that proper crystallization technique should be adopted to obtain suitable martensite and austenite phases or else the prepared alloy will fail to exhibit any shape memory behavior due to amorphous microstructure. Morakabati et al. (2010) reported in their study that increase in Cu content of TiNiCu shape memory alloys subsequently increases critical stress of the material. The reason for happening so was mainly attributed to formation of Cu containing precipitates. They identified a complex compound $\text{Ti}_2(\text{Ni,Cu})$ through microstructure analysis which contributed to

increase in hardness and critical stress of the material. They concurred that increase in Cu content also increased volume fraction of Cu containing precipitates and content of solid solution. It was also observed by them that grain growth occurs during deformation at higher temperatures. In a study of Ti rich and Ni rich TiNiCu shape memory alloys by Zarnetta et al. (2011) it was found that $\text{Ti}(\text{Ni,Cu})_2$ precipitates appear bright due to high Cu content and Ti rich phases appear dark due to high Ti content. It was found that increase in Ti content leads to increased grain size and reduced hardness. In another study it was found that grain size decreases with increasing Cu content (Ishida et al., 2013). Similar results were reported again in another study by Ishida et al. (2014). Formation of coherent $\text{Ti}(\text{Ni,Cu})_2$ phases have reportedly led to increased critical stress for slip. Haenschke et al. (2013) reported different precipitate morphology of similarly prepared TiNiCu shape memory alloy which was due to difference in ingot size. They reported that bigger as cast ingot size (40 kg) results in coarser and more clustered precipitate formation whereas finer and homogenous precipitation was observed for smaller ingot size (10 kg). They have observed precipitates which were partly at the grain boundaries and partly within the grain. Gargarella et al. (2013) obtained both B2 and B19 microstructure in TiNiCu melt which were characterized as dendritic and lamellar structure respectively and inferred that variation in grain size also results in variation of phase transformation temperatures.

2.3.2 Thermo-analytic Characterization

Shape memory effect of TiNiCu shape memory alloys, which occurs due to martensitic phase transformation between its low temperature phase martensite and high temperature phase austenite. It is imperative to study the nature of phase transition in shape memory alloys as transformation of its phases are temperature specific. Differential scanning calorimetry (DSC) technique facilitates identification of temperature at which a material undergoes phase transition. As shown in Figure 2.2, martensitic start, martensitic finish, austenitic start and austenitic finish temperature can be easily identified using DSC graphs. After Nam et al. (1990) signified the addition of Cu in binary TiNi alloy system several researchers

investigated the effect of Cu content on phase transformation temperature and one such instance is the study by Murty et al. (1995). They investigated effect of Cu rich and Ni rich composition on phase transformation behavior of TiNiCu shape memory alloys. It was observed by them that Cu rich composition tend to produce TiCu phase leading to amorphous behavior of such alloys. They found sharp DSC peaks for $\text{Ti}_{50}\text{Ni}_{40}\text{Cu}_{10}$ compared to $\text{Ti}_{50}\text{Ni}_{10}\text{Cu}_{40}$ which was attributed to the presence of TiCu phase. This aspect was confirmed by X-ray diffraction results. Wang et al. (2005) studied the effect of heating and cooling rate on phase transformation characteristics of TiNiCu shape memory alloys. They procured a sample subjected to two different annealing conditions and tested them for varying scanning rate in a DSC. They found that M_f and A_f increases with increasing scanning rate whereas M_s and A_s are not sensitive. Nam et al. (2005) also reported similar behavior while studying shape memory characteristics of $\text{Ti}_{50}\text{Ni}_{25}\text{Cu}_{25}$ ribbons. Ishida et al. (2006) were investigating on shape memory behavior of six different TiNiCu thin films of Ti rich and Ni,Cu rich composition. During calorimetric analysis it was revealed that M_s temperature increases with increasing Cu content and higher annealing temperature results in significant increase in M_s temperature. Ni,Cu rich TiNiCu thin films subjected to similar annealing conditions had lower M_s temperature compared to their Ti rich counterparts. Kim et al. (2007) and Gao et al. (2015) also reported similar transformation characteristics with arc melted and sputtered TiNiCu samples. Hori et al. (2008) investigated effect of Cu addition on shape memory behavior of TiNiCu thin films. They reported that TiNiCu alloys containing more than 15 at.% Cu exhibited very narrow transformation hysteresis and increasing Cu content reduces A_f temperature and saturated at around 70°C for 5 at.% Cu addition. They found during their investigation that TiNiCu alloy having 5 at.% Cu had transformation hysteresis of around 13°C which is one-third of binary TiNi alloy. Similar transformation hysteresis was also reported by Mineta et al. (2011). Jiang et al (2013) prepared porous TiNiCu alloy through powder metallurgical process having different Cu concentration. They found sharper peaks and one step phase transformation for $\text{Ti}_{50}\text{Ni}_{30}\text{Cu}_{20}$ shape memory alloy whereas a two step transformation having wider peaks was observed for $\text{Ti}_{50}\text{Ni}_{40}\text{Cu}_{10}$ shape memory alloy. The reason for such behavior was due to concentration of precipitates and their distribution. Similar reason

was cited by Haenschke et al. (2013). In another study it was found that increasing Cu content leads to increased M_s temperature and saturates until around 22 at.% Cu (Ishida et al., 2013). Chen et al. (2018) prepared melt spun ribbons of TiNiCu shape memory alloy and annealed them for different durations. They observed significant change in phase transformation characteristics where no peaks were observed for 150 min aged ribbon due to near amorphous grain conditions. However, sharper and broader transformation peaks were recorded during DSC analysis at ageing temperature ranging from 180-800 min. Transformation temperatures (heating and cooling) of aged ribbons are depicted in Figure 2.3. In another study by Shelyakov et al. (2019) it was found that Cu rich TiNiCu melt spun ribbons were unable to crystallize with conventional isothermal annealing and hence failed to exhibit any transformation peak for alloys having 38 at.% Cu. Therefore, it has become apparent that phase transformation behavior can be widely influenced by microstructure of TiNiCu shape memory alloys which is governed by parameters that define them like phases present, crystal arrangement etc. which drives this study to the upcoming section about findings related to crystallographic characterization of TiNiCu shape memory alloys.

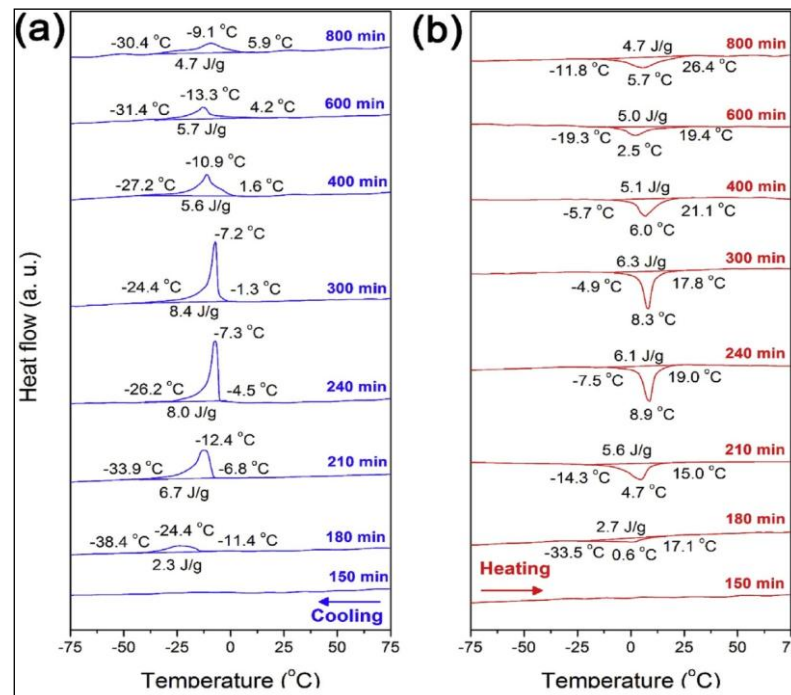


Figure 2.3 DSC (a) cooling and (b) heating heat flow curves of 435°C aged $Ti_{50}Ni_{25}Cu_{25}$ ribbons (Chen et al., 2018)

2.3.3 Crystallographic Characterization

Shape memory effect being a result of diffusionless martensitic transformation is mostly influenced by nature of crystallographic orientation of its constituent elements. High temperature austenitic phase (B2) of shape memory alloys exist as cubic whereas low temperature martensitic phase (B19 or B19') exists in either monoclinic or orthorhombic orientation. These phases present in the alloy determine and confirm the nature of shape memory behavior. X-ray diffraction technique helps in determining the phases present in a given sample. Lo et al. (1993) conducted a preliminary study on two stage martensitic transformation of $Ti_{50}Ni_{40}Cu_{10}$ shape memory alloy. They noted the X-ray diffraction peaks during heating and cooling the shape memory sample to characterize the B2 and B19/B19' peaks. It was reported that an intense peak indicates strong presence of a particular phase in a given sample. B19 and B19' phases can co-exist and can be identified as slight diffusion in peak size and intensity. Murty et al. (1995) investigated glass forming ability of melt spun TiNiCu shape memory alloy with Cu rich and Ni rich compositions. From X-ray diffraction peaks it was observed that Cu rich alloy exhibited an amorphous phase with very little crystallinity whereas low Cu % alloys exhibited peaks representing fairly crystalline phase presence. Major crystalline peak observed for Cu rich phase was for TiCu precipitates. Intermediate TiNiCu alloy exhibited several such intermetallic precipitates which were absent for Ni rich compositions. Ren et al. (2000) prepared RF magnetron sputtered TiNiCu thin films and found that as deposited films were mostly amorphous but proper annealing crystallizes the film which was apparent from sharp peaks in X-ray diffraction plots. Similar observations were reported by Fu et al. (2003), He et al. (2009) and Shelyakov et al. (2013). Craciunescu et al. (2003) also studied martensitic transformation behavior of TiNiCu thin films sputtered at different temperatures. They found a weak 111 (B19) + 020 (B2) peak at room temperature which intensified to a sharp and prominent 110 (B2) peak upon heating at 100°C. Du et al. (2004) prepared three different TiNiCu thin films with increasing Cu content from 4.5at% to 15at.%. They conducted XRD test at various temperatures to note phase change in these alloys. At room temperature, it was found that increasing Cu content leads to more prominent orthorhombic martensites as compared to monoclinic

martensite at lower Cu content alloy. Ishida et al. (2006) found similar results while investigating shape memory behavior of TiNiCu thin films annealed at 973 K. Kim et al. (2014) investigated effect of Cu addition on martensitic transformation of powder metallurgically prepared TiNi alloy. They found that B2 and B19 phase co exists at room temperature. However, Liu et al. (2006) warned that excessively higher annealing temperature may lead to formation of needle like TiCu precipitates which hinders formation of appropriate martensites required for shape recovery and was further re-confirmed by another study by Xie et al. (2007). While investigating phase transformation behavior of porous $Ti_{50}Ni_{40}Cu_{10}$ and $Ti_{50}Ni_{30}Cu_{20}$ shape memory alloys, Jiang et al. (2013) found that $Ti(Ni,Cu)$, $Ti_2(Ni,Cu)$ and $Ti(Ni,Cu)_2$ are primary phases present in them. Ghadimi et al. (2013) concluded from XRD plot obtained in their study that diffusion of Cu and Ti into Ni lattice led to broadening and decrease in intensity of Ni peaks. They also observed decrease in B2 peak intensity and peak widening which was correlated to crystalline refinement and lattice strain enhancement. Abbasi et al. (2015) were investigating on nanostructured TiNiCu shape memory alloy. They prepared nano grained TiNiCu alloy through hot rolling and upto 70% cold rolling. XRD plots revealed that homogenized cast samples had sharp B2 and B19 peaks for grains whose size ranged from 30-50 μm . Those sharp peaks were broadened and peak intensities were reduced which was correlated to nanostructured grain formation. In a recent study by Shelyakov et al. (2019) it was reported that increase in Cu content leads to decrease in intensity of characteristic peaks (B2 or B19) and appearance of B11 reflection peaks (TiCu precipitates). They addressed this issue by incorporating electro pulse crystallization rather than isothermal annealing. Figure 2.4 clearly depicts the X-ray diffraction plots of alloys prepared by melt spinning having varying Cu content. Dotted curves and solid curves indicate X-ray diffraction plots of isothermal crystallization and electro pulse crystallization respectively. Reduction in B19 martensitic phases due to excessive addition of Cu affected the martensitic phase transformation behavior of these alloys by shifting martensitic transformation to higher temperature along with high enthalpy of phase change, reason being the presence of detrimental B11-TiCu phases.

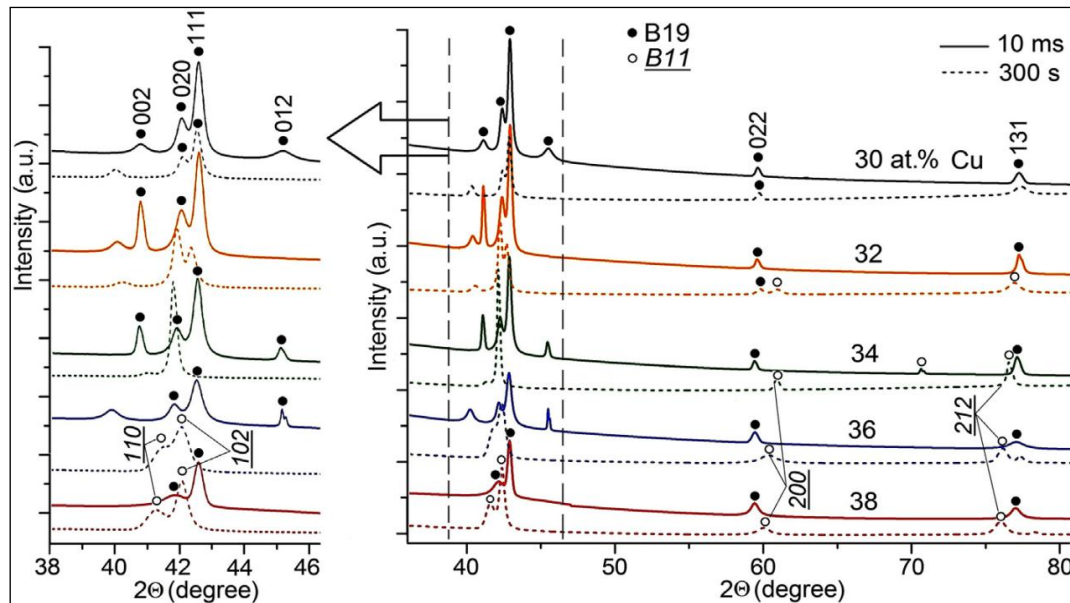


Figure 2.4 X-ray patterns of rapidly quenched $\text{Ti}_{50}\text{Ni}_{50-x}\text{Cu}_x$ ($x = 30\text{--}38$ at.%) alloy ribbons after isothermal (dotted curves) and 10 ms electro pulse (solid curves) crystallization. (Shelyakov et al., 2019)

2.4 MACHINING OF TiNi BASED SHAPE MEMORY ALLOYS

2.4.1 Conventional Machining of Shape Memory Alloys

Conventional machining techniques like turning, drilling, milling and grinding uses a harder tool to perform material removal. Machining of TiNi based alloys using conventional techniques has proved to be inefficient as quality of machined product does not meet satisfactory standards and damages caused to tool are high (Weinert et al., 2002). In another study Weinert et al. (2004) attempted to obtain a bushing through turning and drilling NiTi and TiNiNb shape memory alloy. They concluded that multi layer coated (TiCN/TiAlN or TiCN/TiN) tool can produce better results but machining defects pertaining to conventional techniques cannot be eradicated completely. The group of author also investigated feasibility of machining micro components through milling TiNi alloy using TiAlN coated solid carbide tool (Weinert and Petzoldt, 2008). They recommended minimum quantity lubrication using ester oil to minimize tool wear and generate suitable surface characteristics of machined workpiece. However, possibility of damage to functionality of shape memory alloys due to reaction of oil compound with metallic surfaces owing to

generation of high temperature at tool-workpiece contact point was not addressed in this study. Kaynak et al. (2013, 2013a) proposed cryogenic machining using LN₂ and compared the machined surface integrity with MQL (minimum quantity lubrication) and dry machining condition. Although tool wear was reduced through cryogenic machining, machined surface and subsurface (upto 500 μm) was affected by this technique leading to retarded martensitic phase transformation (Kaynak et al., 2014). Figure 2.5 illustrates phase transformation behavior of samples taken from machined surface upto 500 μm for dry and cryogenically turned NiTi shape memory alloy compared to as received sample. Such retardation in cryogenically machined samples occurred due to severe twinning deformation of NiTi alloy.

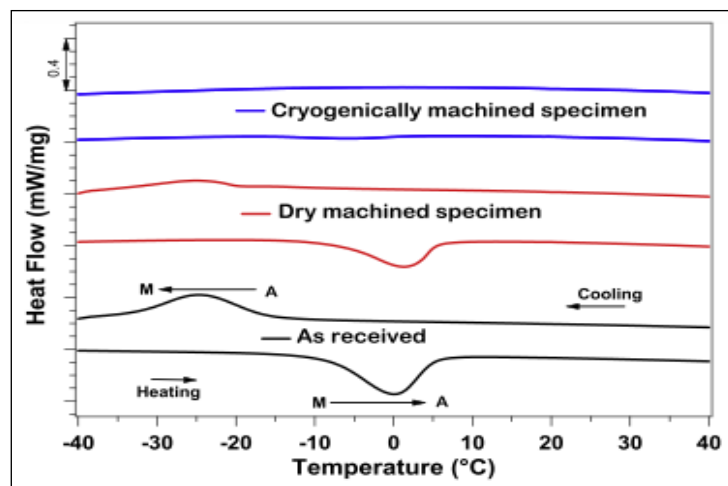


Figure 2.5 DSC plot of as received, dry machined and cryogenically machined NiTi alloy (Kaynak et al., 2014)

It was further established that for short machining time cryogenic machining yielded suitable tool wear behavior and surface roughness but for long machining time similar results were observed for cryogenic, dry and MQL machining conditions (Kaynak et al., 2014a, 2015). Similar results were reported by Khalil et al. (2018) while machining NiTi alloy using MQnL (minimum quantity nano lubrication). Figure 2.6 represents difference in surface topography of NiTi alloy machined in dry and cryogenic conditions.

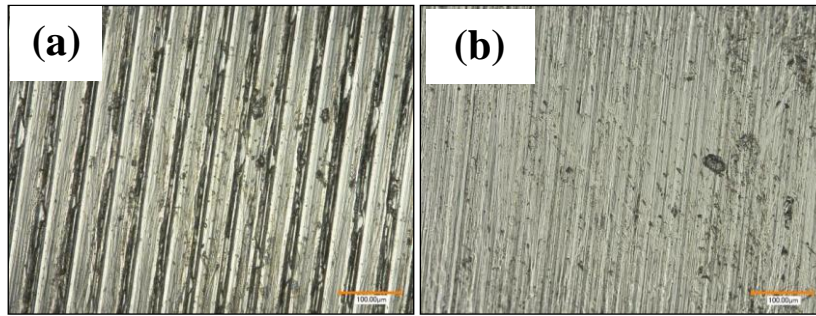


Figure 2.6 Surface topography NiTi alloy (a) Dry (b) Cryogenic (Kaynak et al. 2014a)

In a study by Guo et al. (2013) machinability of NiTi shape memory alloy using milling and EDM was investigated. They reported that burr free surface can be produced using EDM but surface roughness was more due to coral reef morphology of EDMed surface compared to finish milling. Machined surface through both conventional and non-conventional machining techniques lead to formation of a white oxidized layer due to thermal exposure (Liu et al., 2016). This white layer has significantly higher hardness compared to parent material and is devoid of parent material's intrinsic properties. Formation of white layer was found unavoidable in both the cases however, lower white layer thickness was recorded for EDM. Inset images in Figure 2.7 indicates machined surface morphology of milled and EDMed surface of NiTi shape memory alloy (lowest surface roughness marked in white arrows). In a detailed review by Kaya and Kaya (2019) it was concluded that conventional machining of NiTi shape memory alloys causes unfavorable results whereas non-conventional machining techniques prove to be more useful. Hence, from the discussion it is quite evident that conventional machining of TiNi based shape memory alloys do not produce suitable results and are detrimental for shape memory applications. Hence, aspects of non-conventional machining of TiNi based shape memory alloys are discussed in upcoming section.

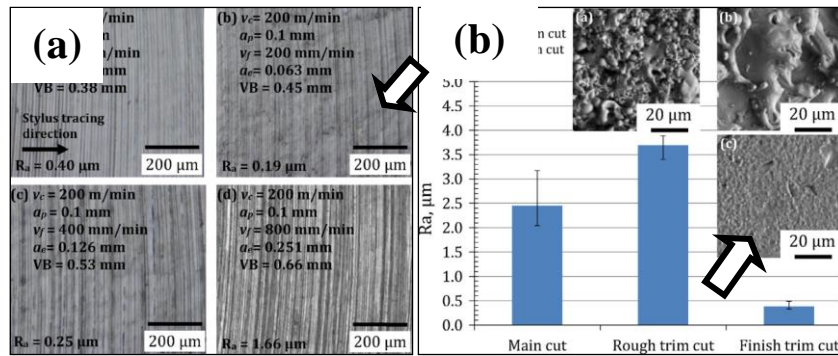


Figure 2.7 Surface morphology of (a) milled and (b) EDMed NiTi alloy (Guo et al., 2013)

2.4.2 Non-conventional machining of shape memory alloys

Non-conventional machining techniques consist of laser beam machining (LBM), water jet machining (WJM), electro-chemical machining (ECM) and electro-discharge machining (EDM). These machining techniques are invented fairly recently compared to most of conventional machining techniques and have numerous advantages over them. Non-conventional machining techniques do not have a tool which makes a physical contact with the workpiece to be machined and hence damage caused to workpiece due to shear deformation is nonexistent. In initial studies by Müller and Monaghan (2000; 2001) it was found that EDM could be a suitable alternative to machine SiC particle reinforced aluminium alloy matrix composite which would be very difficult using conventional machining techniques. While comparing EDM with LBM and WJM they concluded that WJM is suitable for rough cut applications but yielded geometrical errors in specimens. LBM generated fast machining rates compared to EDM but machined surface was not upto the mark as it contained several defects like striation marks, burrs at the exit end etc. Li et al. (2006) investigated machining capability of a femtosecond laser cutting machine while fabricating miniature devices out of NiTi shape memory alloy. Similar methodology was adopted by Hung et al. (2015) to machined NiTi shape memory alloy for biomedical applications. Their findings set a benchmark for researchers who were investigating on machining of difficult-to-machine materials like titanium alloys and shape memory alloys.

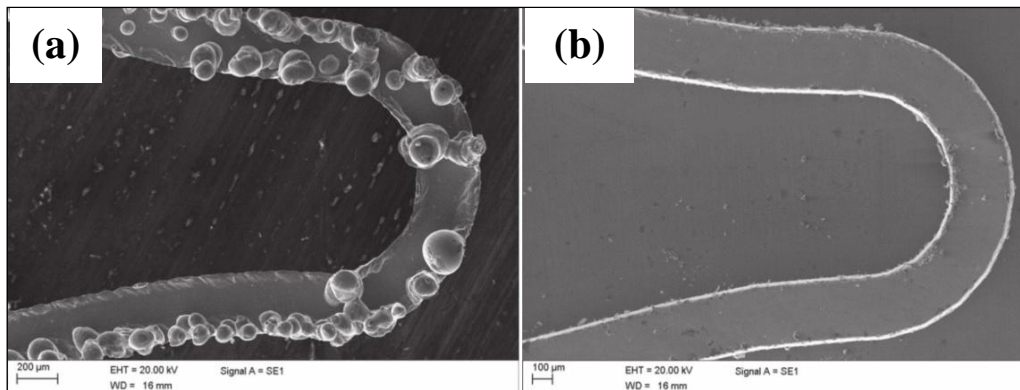


Figure 2.8 SEM image of part made using (a)CW laser (b)FS laser (Biffi and Tuissi, 2017)

Superiority of femtosecond laser cutting process was further justified by Biffi and Tuissi (2017) while comparing machined surface generated by continuous wave laser machine. Figure 2.8 indicates difference between machined surface using femtosecond and continuous wave laser equipment. Similar results were reported by Tung et al. (2008). Waterjet machining has been favored by several researchers due to reduced mechanical and thermal damage caused to workpiece material (Kong et al., 2011; Frotscher et al., 2011). One of the most adopted application of this technique is preparation of shallow pockets which require masking of surface not to be machined to avoid over erosion (Kong et al., 2011a). In another study the group of researcher have proposed several modes to overcome such issues regarding intricate profile cutting using abrasive water jet machining (Kong et al., 2013). Figure 2.9 depicts a microstructure formed by PWJ (plain water jet) machining. Even though abrasive particles were not used, machined surface were not upto the mark and presence of microcracks were recorded throughout the machined surface. They have also recorded grit embedment in NiTi parent material. Therefore, neither PWJ and AWJ machining could be implemented to produce intricate structures using this machining technique which indicates need for more suitable non-conventional machining process. Ma et al. (2007) proposed incorporation of confined-etchant-layer technique to produce 3D structures using electrochemical machining technique. They concluded that structures having high aspect ratio (L/D) would be difficult to machine due to over erosion. Lee and Shin (2011) performed electrochemical polishing of NiTi shape memory alloy

with multiple electrolyte medium and found that formation of a porous machined surface is unavoidable which could be detrimental for certain applications and in a previous study they observed that quality of machined surface can be improved by applying a moderate duty factor, low current and long machining time (Lee et al., 2010).

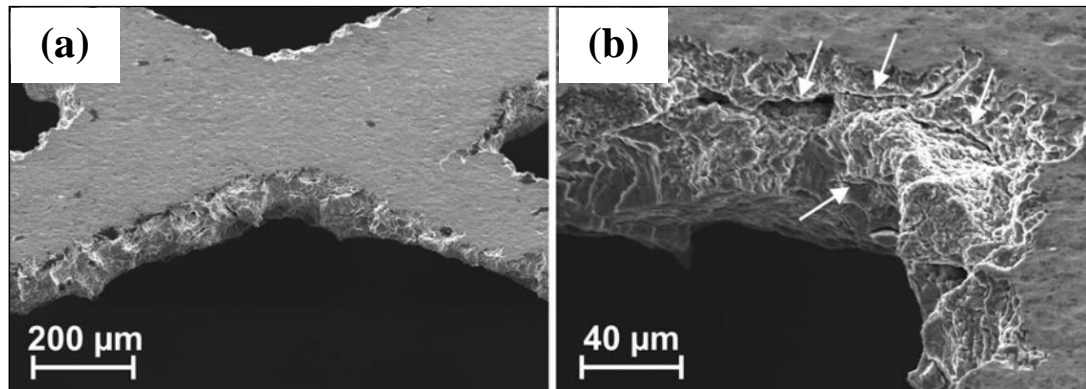


Figure 2.9 SEM image of : (a) microstructure made using PWJ machining (b) microcracks highlighted with arrows (Frotscher et al., 2011)

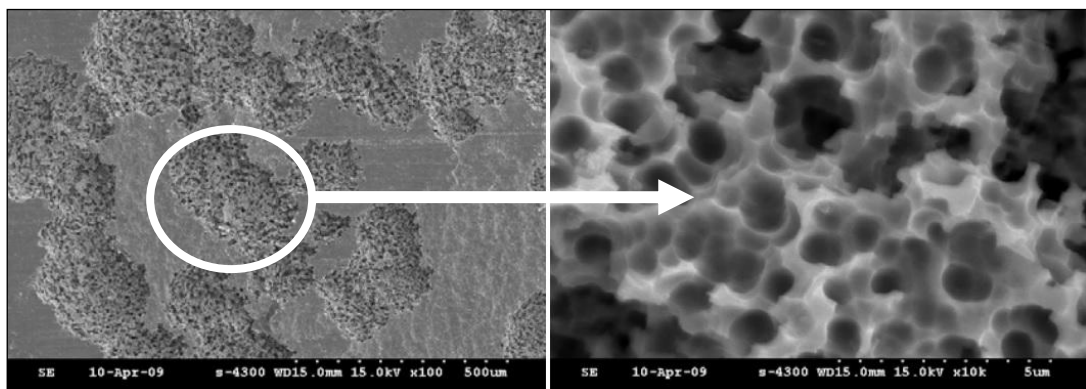


Figure 2.10 Microholes on partially electrochemical machined surface (Lee and Shin, 2011)

Since electrochemical polishing is already a slow machining process such long machining hours add to machining cost and recommended this operation for finishing operations. Figure 2.10 depicts the microholes on a partially machined nitinol surface. Theisen and Schuermann (2004) performed electro discharge machining of NiTi shape memory alloy. It was concluded from their study that material removal rate and surface roughness depends on the machining parameters which unavoidably created craters and re-melted drops on the machined surface. Surface roughness varied from

10-30 μm which can be considered pretty high for finished machined surface. White layer depth also reached a maximum of 22 μm which showed no shape memory behavior.

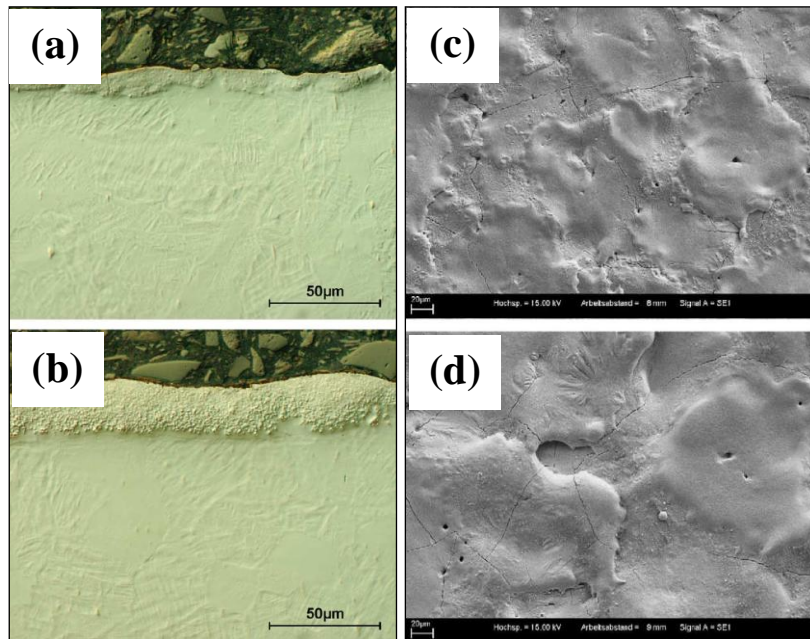


Figure 2.11 Recast layer at (a) $I = 4\text{A}$, $f = 10\text{ kHz}$ (b) $I = 4\text{A}$, $f = 5\text{ kHz}$ and Surface morphology at (c) $I = 2\text{A}$ (d) $I = 4\text{ A}$ (Fu et al., 2016)

Fu et al. (2016) performed a comparative analysis of white layer formed between laser cut and EDMed NiTi shape memory alloy shown in Figure 2.11. It was found that EDMed machined surface shows much lower surface roughness compared to laser cut machined surface and hardness of white layer formed due to laser cut was low compared to EDM which was attributed to different quenching rates of the processes. However, major limitation of EDM is to prepare the tool electrode which requires to be geometrically exact with the profile to be machined. Therefore, geometrically complicated and intricate profiles could not be machined without having significant error in them which in turn affects the profile to be machined. WEDM on the other hand can be used to machine intricate profiles which will be difficult to process with either EDM or any other non-conventional machining process (Hsieh et al., 2009; Li et al., 2014; Manoj et al., 2019). Such superior capability of WEDM is a influencing factor to employ this technique in the current study. Upcoming section discusses in

detail about various aspects of WEDM absolutely necessary to comprehend this research work.

2.5 WEDM of TiNi BASED SHAPE MEMORY ALLOYS

Wire electro discharge machining works on the same principle as that of traditional EDM with only exception of the electrode which is a thin wire compared to a profiled tool in EDM process. WEDM facilitates material removal through several primary process parameters, namely peak current (I_p), peak voltage (V_p), pulse on time (T_{on}), pulse off time (T_{off}), servo voltage (SV) and wire feed (WF). However, there are also several other parameters which influence material removal in some degree or the other like servo feed (SF), flushing pressure (F_p), flushing direction (F_d), dielectric material etc. Following sections present findings by researchers who have worked on effect of significant primary WEDM process parameters on various machining responses.

2.5.1 Effect of Peak Current (I_p)

Higher peak current and peak voltage though helps in boosting MRR they cause serious surface and subsurface damage in workpiece material (Hsieh et al., 2013). Material removal rate and surface roughness at different peak current while performing EDM of TiNiZr and NiAlFe shape memory alloy are shown in Figure 2.12.

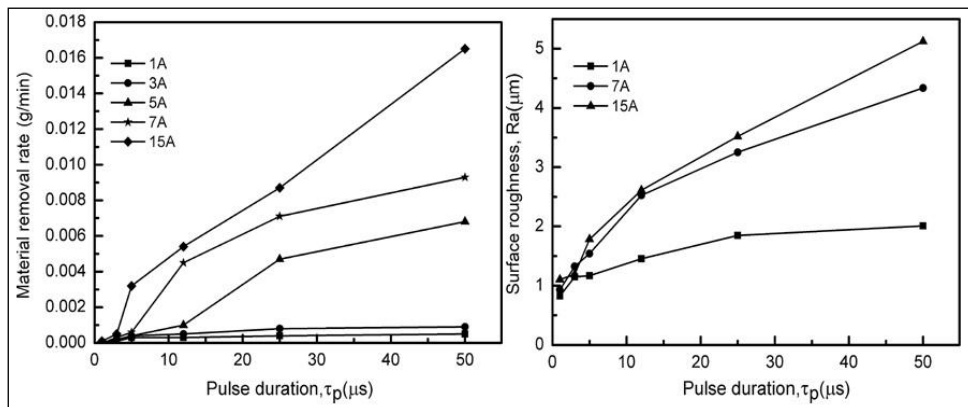


Figure 2.12 MRR and SR vs. Pulse duration at different peak current (Hsieh et al., 2013)

Since lower peak current and peak voltage generates better machined surface, these two parameters were kept low and constant based on machine capability and nature of influence. T_{on} , T_{off} , SV, WF and flushing conditions (F_p and F_d) were selected in the current study and relevant surveys while machining various shape memory alloys and their effect on machining output responses are reported in the forthcoming sections.

2.5.2 Effect of Pulse on Time (T_{on})

Pulse on time (T_{on}) is the duration for which spark discharge continues for a given pulse cycle and machining speed increases with the increase in pulse on time as discharge energy increases with increasing T_{on} (Tarng et al., 1995). However, high discharge energy results in poor surface finish.

2.5.2.1 Effect of T_{on} on MRR and SR

Liao et al. (2004) performed a study to achieve a fine surface finish in WEDM and found a shallow crater along with large diameter leads to a better surface roughness. To obtain flat craters, it is important to control the electrical discharge energy at a lower level by setting a short T_{on} since discharge energy is proportional to T_{on} . A higher discharging energy will cause violent sparks and results in a deeper erosion crater on the surface. They have concluded that a small voltage and a large resistance can be used so as to provide a small discharging energy and hence a good surface can be produced. Similar results were reported by Zinelis (2007). Chen et al. (2008) in their study of machining of NiAlFe and TiNiZr ternary shape memory alloys observed that MRR and SR increases with the increase in pulse on time. Longer discharge duration (T_{on}) results in higher erosion of material and higher surface roughness. From Fig.2.13 it can be seen that MRR and SR increases with the increase in pulse on duration at different peak current levels. Overall trend at various peak current is similar for both MRR and SR.

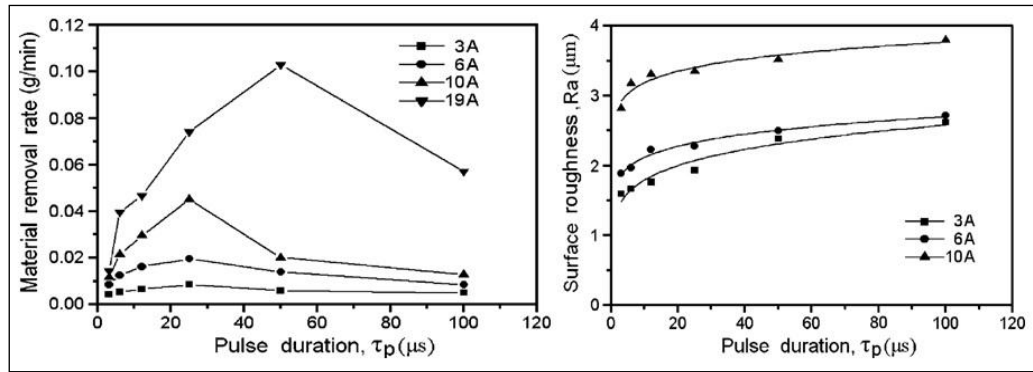


Figure 2.13 MRR, SR vs. T_{on} for NiAlFe SMA (at various peak current) (Chen et al., 2008)

From the studies by Chen et al. (2008) and Hsieh et al. (2009) it was found that MRR and SR varies for the given workpiece where NiAlFe suffered higher MRR and SR compared to TiNiCr and TiNiZr for similar T_{on} . Rationale for such behavior was established by the group of researchers as difference in thermal conductivity and melting temperature of the studied shape memory alloys. It was observed that due to higher melting temperature of the material, the heat generated during sparking is not enough to melt the material and evaporate it. On the other hand higher thermal conductivity of the material causes more energy transfer to the nearby matrix leading to lower MRR. Figure 2.14 illustrates the variation in MRR and SR for TiNiZr, TiNiCr and NiAlFe shape memory alloys, where NiAlFe have higher MRR and SR value than TiNiCr followed by TiNiZr shape memory alloy.

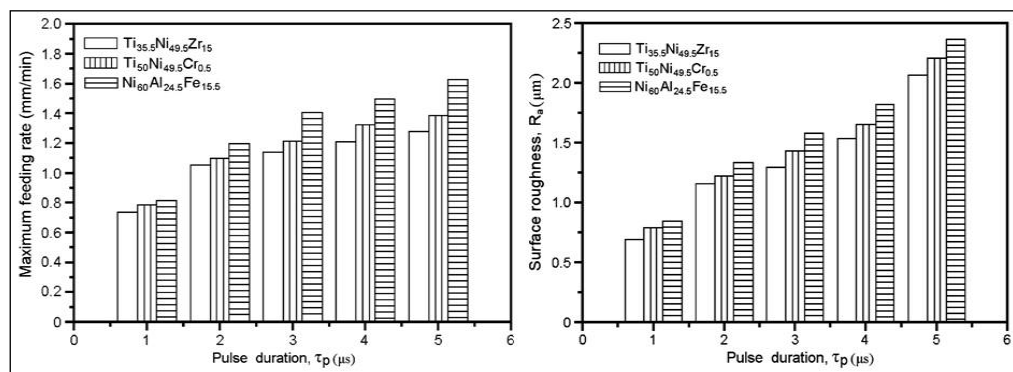


Figure 2.14 MRR, SR vs. T_{on} for TiNiZr, TiNiCr and NiAlFe SMA (Hsieh et al., 2009)

2.5.2.2 Effect of T_{on} on Surface Morphology

Manjaiah et al. (2016) performed WEDM of $Ti_{50}Ni_{45}Cu_5$ shape memory alloy at 36 μs and 48 μs pulse on duration. Figure 2.15 depicts surface morphology of WEDMed workpiece using scanning electron micrographs where deeper craters and rough surface is evident for higher T_{on} value and better surface features for lower T_{on} value. Similar observation for such surface morphology due to variation in pulse on time was also done by Hsieh et al. (2013).

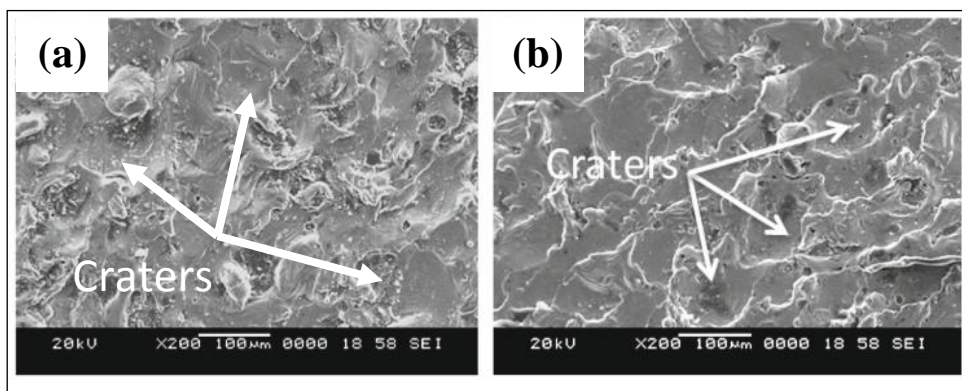


Figure 2.15 SEM micrographs showing surface morphology at T_{on} (a) 36 μs and (b) 48 μs (Manjaiah et al., 2016)

2.5.2.3 Effect of T_{on} on Kerf Width

Tosun et al. (2004) and Ikram et al. (2013) while investigating kerf formation and material removal rate in wire electro discharge machining using Taguchi technique. Kerf width or width of cut in WEDM process determines the accuracy of profile being machined which is greatly influenced by T_{on} (Parashar et al., 2010). Muniappan et al. (2017) observed an increase in kerf width from 292 μm to 327 μm with an increase in T_{on} from 108 μs to 126 μs . Similar trend in results was also reported by Inset image of Figure 2.23 indicates effect of T_{on} on kerf width. For three different alloys Roy and Narendranath (2018) observed similar trend in results.

2.5.2.4 Effect of T_{on} on Recast layer thickness

Pulse on time also influences white layer or recast layer formation during EDM or WEDM process. Hsieh et al. (2013) EDMed TiNiZr shape memory alloy at 3 μs , 12 μs , 25 μs and 50 μs T_{on} duration. They observed growing recast layer thickness with longer T_{on} duration and SEM micrograph of the machined surface cross section is shown in Figure 2.16. With increasing T_{on} duration more amount of discharge energy was released to the workpiece surface to be machined and hence net volume of molten workpiece was also increased which was eventually frozen due to rapid dielectric quenching.

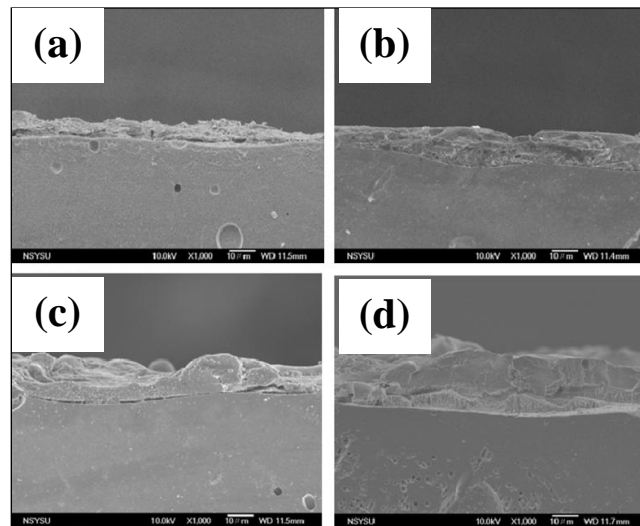


Figure 2.16 Recast layer at T_{on} (a) 3 μs (b) 12 μs (c) 25 μs and (d) 50 μs (Hsieh et al., 2013)

Similar observation was also noticed by Liu et al. (2014) where wide variation in recast layer thickness was observed for rough cut and trim during WEDM process. In trim cut modes of WEDM process very short pulse on duration is implemented compared to rough cut modes and Manjaiah et al. (2018) varied the pulse on duration for a mere 16 μs . However, recast layer thickness was found to grow from 8.3 μm to 23.4 μm as shown in Figure 2.17.

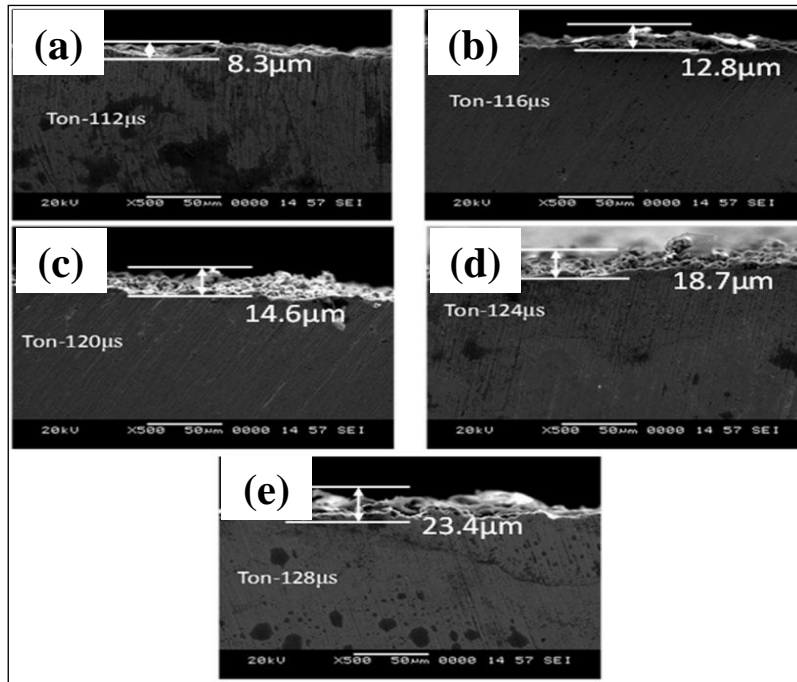


Figure 2.17 Recast layer thickness at T_{on} : (a) 112 μ s (b) 116 μ s (c) 120 μ s (d) 124 μ s (e) 128 μ s (Manjaiah et al., 2018)

2.5.3 Effect of Pulse off Time (T_{off})

Pulse on time (T_{on}) and pulse off time (T_{off}) together constitutes the pulse cycle in WEDM process. For a given fixed pulse cycle increase in pulse off time indicates shrinking T_{on} which further leads to lesser discharge spark impinging on the workpiece. Upcoming sections discuss about effect of T_{off} on various WEDM responses.

2.5.3.1 Effect of T_{off} on MRR and SR

Growing T_{off} leads to reduced MRR and improve machined surface quality by lowering surface roughness (Manjaiah et al., 2018). Figure 2.18 depicts reduction in MRR and surface roughness with increasing pulse off duration while machining two different TiNiCu shape memory alloys. Reason for deterioration of MRR due to increasing T_{off} is decreased discharge sparking leading to reduced melting per unit time which is also the reason for lowered surface roughness.

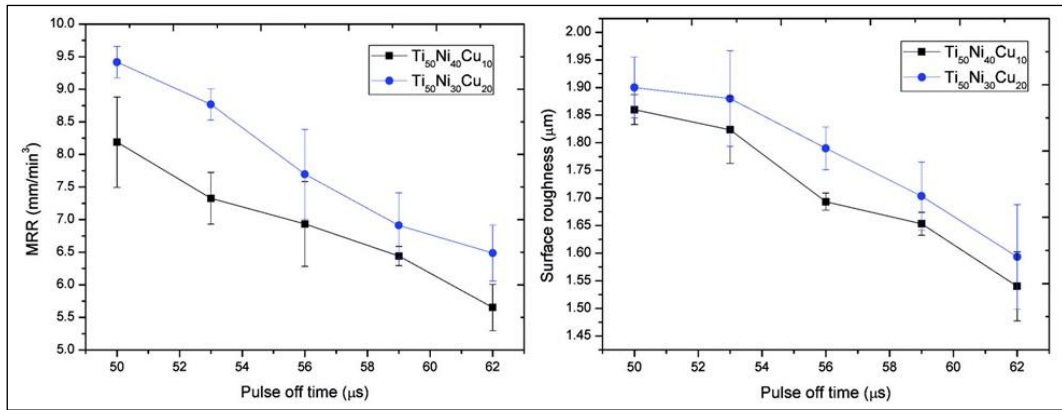


Figure 2.18 Effect of T_{off} on MRR and SR (Manjaiah et al., 2018)

2.5.3.2 Effect of T_{off} on Surface Morphology

In a study by Manjaiah et al. (2016) it was found that increasing T_{off} leads to smaller diameter craters as shown in Figure 2.19 where machined surface morphology at T_{off} : 4 μs and 10 μs are illustrated. Deeper and larger craters are visible in SEM micrograph representing 4 μs T_{off} whereas more molten debris are present in the latter. More uneven flushing pock marks and waviness can be observed for lower T_{off} value.

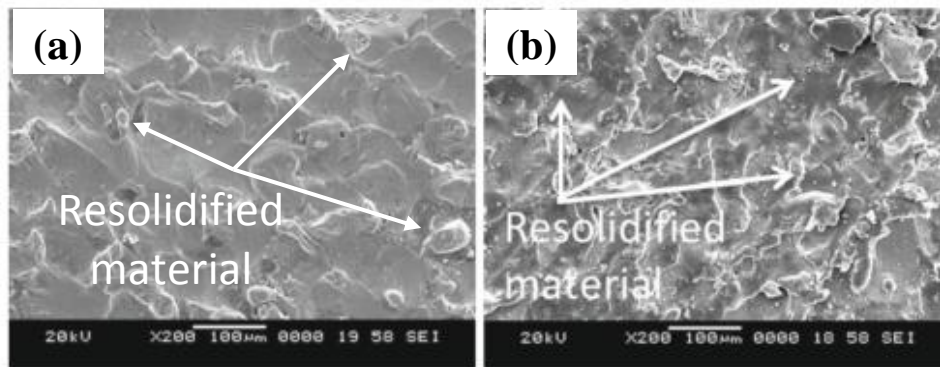


Figure 2.19 Machined surface at T_{off} : (a) 4 μs (b) 10 μs (Manjaiah et al., 2016)

2.5.3.3 Effect of T_{off} on Kerf width

Kerf width was found to have not influenced much from ANOVA studies conducted by Muniappan et al. (2017) and Roy and Narendranath (2018). However, effects plot given in inset image of Figure 2.23 shows an initial decreasing trend which again spikes slightly at higher T_{off} due to longer duration available for flushing of debris

material from the machining zone. Servo voltage on the other hand was found to have significant influence on widening of kerf during WEDM of TiNiCu shape memory alloys although T_{on} exhibited good influential significance. But influential factors was found to be varying while machining homologous TiNiCu shape memory alloys (Roy and Narendranath, 2018).

2.5.3.4 Effect of T_{off} on Recast layer thickness

It has been established by several researchers that recast layer thickness is mostly influenced by pulse on time and servo voltage (Soni et al., 2017, Manjaiah et al., 2018). T_{on} has a significant influence due to rapid change in discharge energy with increasing value. However, Roy and Narendranath (2018) concluded that T_{off} also has significant influence as observed while machining homologous TiNiCu shape memory alloys under similar machining conditions as shown in Figure 2.20.

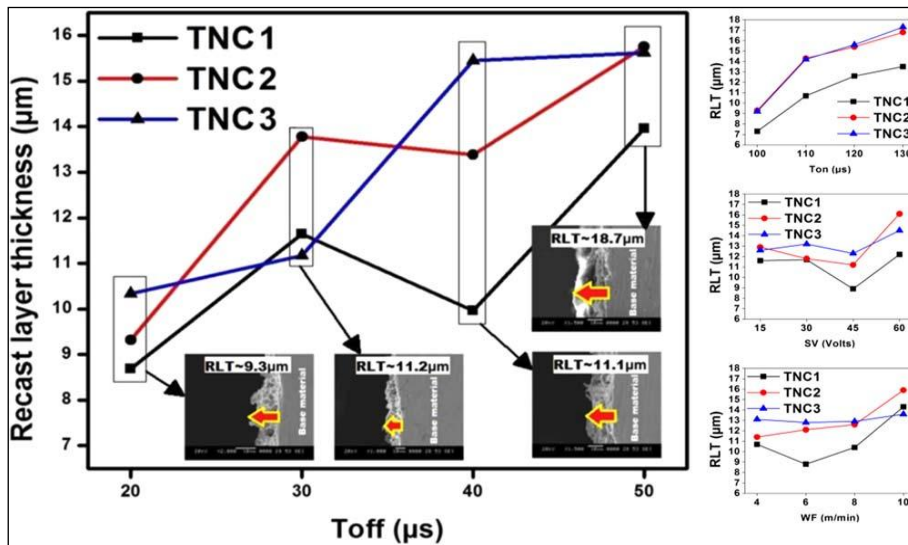


Figure 2.20 RLT vs. T_{off} (Roy and Narendranath, 2018)

The reason for such alteration in response behavior was attributed to change in workpiece material property. It was found that $Ti_{45}Ni_{45}Cu_{10}$ and $Ti_{40}Ni_{50}Cu_{10}$ had higher thermal conductivity compared to $Ti_{50}Ni_{40}Cu_{10}$ which resulted in faster transfer of heat to the nearby matrix of workpiece material and hence thinner recast layer formation. Therefore, for these two alloys namely $Ti_{45}Ni_{45}Cu_{10}$ and $Ti_{40}Ni_{50}Cu_{10}$, T_{on}

was not much significant it was for $Ti_{50}Ni_{40}Cu_{10}$ and hence longer T_{off} facilitated more time for deposition and quenching by dielectric fluid.

2.5.4 Effect of Servo Voltage (SV)

Servo voltage in WEDM process determines the gap maintained between wire electrode and workpiece through a servo mechanism during machining and it greatly influences the material removal and machined surface morphology. Effect of servo voltage on various WEDM responses are listed below.

2.5.4.1 Effect of SV on MRR and SR

Lower servo voltage implies shorter spark gap whereas higher servo voltage value indicates wider spark gap during machining. Shorter spark gap leads to more intense discharge spark impingement on the workpiece surface hence high MRR compared to wider spark gap at high servo voltage. Therefore, increase in servo voltage results in reduced MRR and lower machined surface roughness (Manjaiah et al. 2015). Figure 2.21 represents the effect of servo voltage on MRR and SR during a study by Manjaiah et al. (2018). It can be seen that for both TiNiCu shape memory alloys, MRR and SR reduced due to increasing servo voltage.

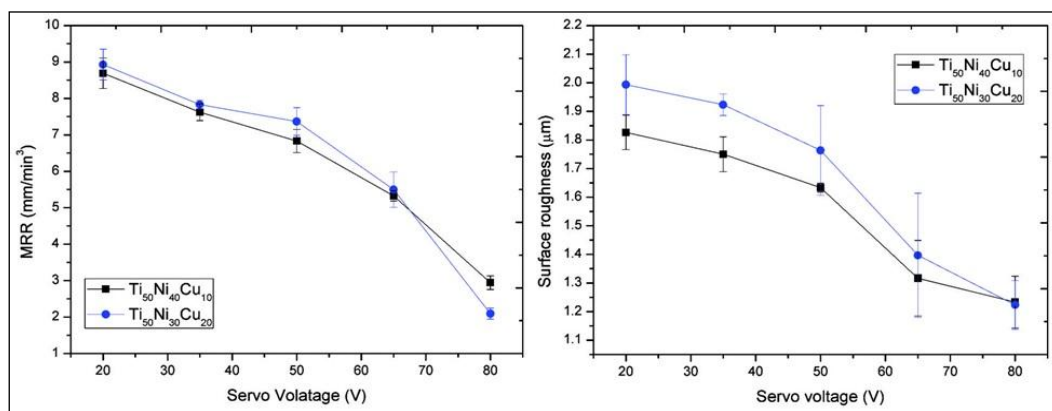


Figure 2.21 MRR and SR vs. Servo voltage during WEDM of TiNiCu (Manjaiah et al. 2018)

2.5.4.2 Effect of SV on Surface Morphology

Since higher servo voltage results in decreased spark intensity that impinges on workpiece surface, a more even machined surface is obtained. This happens primarily due to better flushing conditions due to wider gap conditions at higher servo voltage. Manjaiah et al. (2018) presented in their study that due to high pulse energy at low servo voltage value larger craters are formed and causes deterioration of machined surface as can be observed from Figure 2.22. Lesser resolidified debris can be found at higher servo voltage value of 80 Volts (Figure 2.22b) whereas more amount of resolidified material can be observed at low servo voltage of 20 Volts.

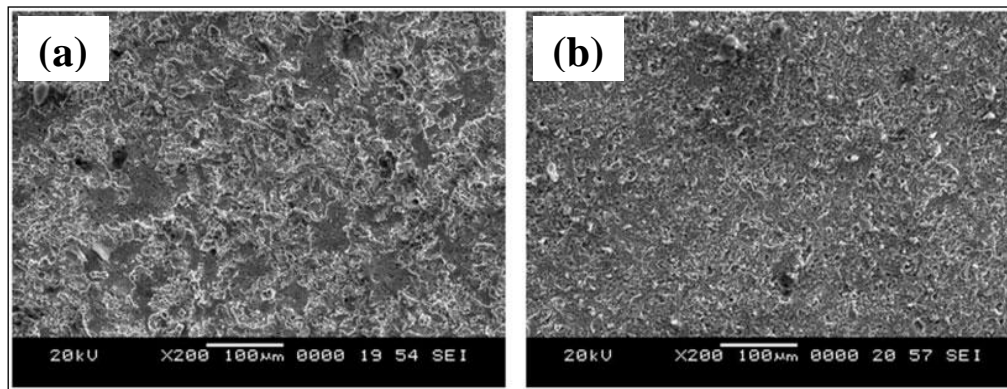


Figure 2.22 Machined surface morphology at SV : (a) 20 V (b) 80 V (Manjaiah et al. 2018)

2.5.4.3 Effect of SV on Kerf width

Since higher MRR is associated with low servo voltage values, wider kerf is observed by Roy and Narendranath (2018) at low servo voltage value. It was found from this investigation that low servo voltage leads to more severe sparking conditions leading to more erosion of material from the workpiece. Figure 2.23 illustrates the change in kerf width with variation in servo voltage in four levels. Maximum kerf was noted for 15 V servo voltage (350 μm) and lowest kerf was recorded for 60 V servo voltage (315 μm).

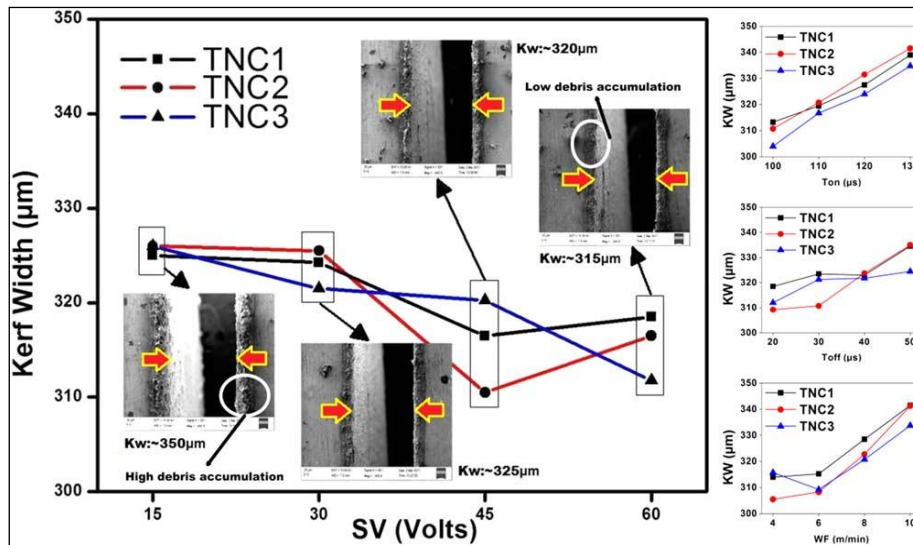


Figure 2.23 KW vs. SV and other machining parameters (Roy and Narendranath, 2018)

2.5.4.4 Effect of SV on Recast Layer Thickness

Low servo voltage value indicates shorter spark gap resulting in more intense spark impingement. Such intense spark impingement creates deeper and wider craters, a behavior similar to long T_{on} duration along a short T_{off} . Therefore, effect of servo voltage on recast layer thickness bear similar trend with that of kerf width. It was found by Soni et al. (2017) that recast layer thickness is more when lower value of servo voltage is applied during machining. Severe sparking condition of low servo voltage leads to more melting of material than it happens at higher servo voltage. Figure 2.24(a-b) shows recast layer thickness at 20 V and 60 V respectively. Average recast layer thickness of 40 µm was observed for 20 V servo voltage compared to 7 µm for 60 V servo voltage.

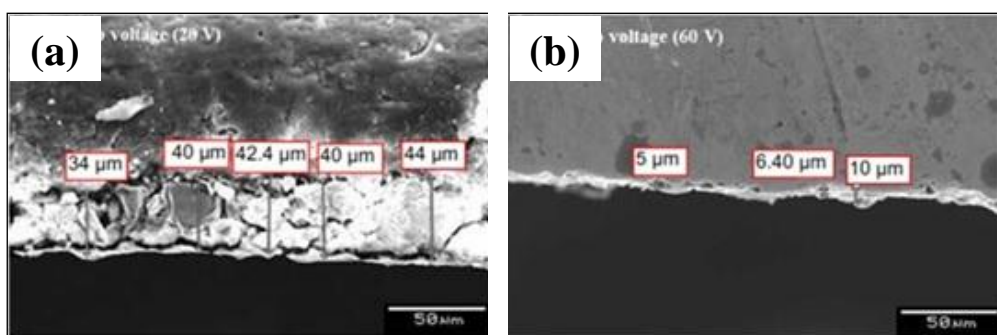


Figure 2.24 Recast layer thickness at (a) 20 V (b) 60 V (Soni et al., 2017)

2.5.5 Effect of Wire Feed (WF)

Wire electrode is fed to the machining zone continuously to carry out machining without breakage of wire in WEDM process. Continuous feeding of wire and its rate affects the efficiency of debris removal from the machining zone. A faster wire feed rate also ensures minimization of secondary electrical discharges which have no effect of material removal mechanism which takes place between wire electrode and loosened debris.

2.5.5.1 Effect of WF on MRR and SR

In the study by Manjaiah et al. (2014) it was established that wire feed rate does not have significant influence on MRR and SR. However, small changes are observed in these responses. In another study by Manjaiah et al. (2015) investigated effect of wire electrode material on MRR and SR during machining of TiNiCu shape memory alloys. They concluded that zinc coated brass wire produces better machined surface characteristics while machining TiNiCu shape memory alloys but WF was not a significant factor. However, over a wide increment in WF it was found that MRR increases which was due to better flushing of debris from machining zone which reduced secondary sparks. Secondary sparks take place between wire electrode and loose debris and is considered not useful for material removal in WEDM process. Figure 2.25 represents mean effects plot of MRR vs. several WEDM parameters. Effects plot of MRR vs. WF are marked with an arrow for two different TiNiCu shape memory alloys.

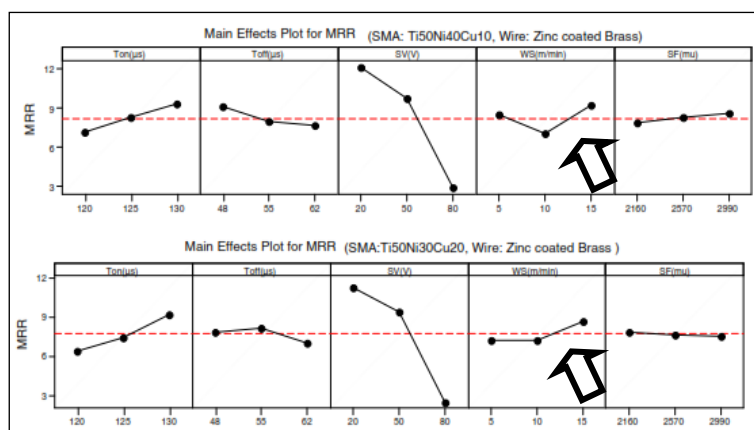


Figure 2.25 Mean effects plot of MRR vs. WEDM parameters (Manjaiah et al., 2015)

Roy et al. (2017) also performed WEDM of three different TiNiCu shape memory alloys under similar machining conditions and found that increasing WF do not has significant impact on MRR and SR but at very high WF (10 m/min), slight improvement in MRR and subsequent degradation in SR was observed. Similar observation was done for surface roughness in studies by other group of authors (Manjaiah et al., 2015, Soni et al., 2017, Hargovind et al., 2019). Figure 2.26 depicts the effects plot of MRR and SR vs. WF.

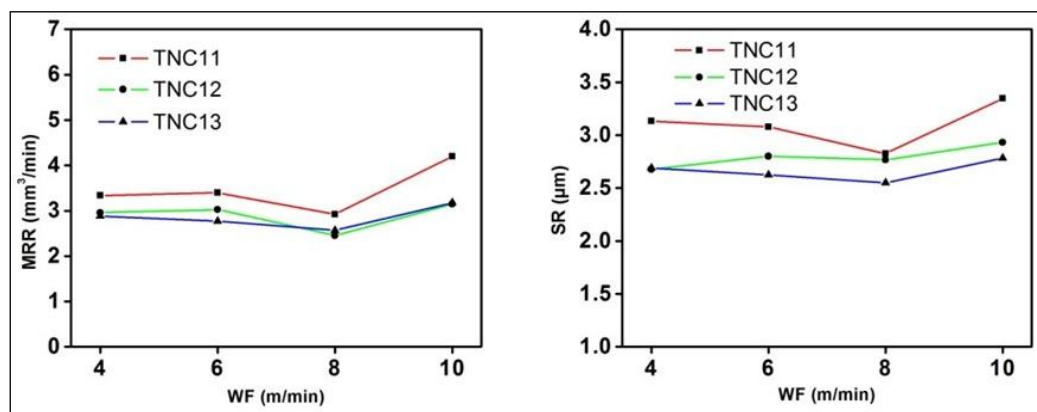


Figure 2.26 Effects plot showing MRR, SR vs. WF (Roy et al., 2017)

2.5.5.2 Effect of WF on Surface Morphology

In another study by Roy and Narendranath (2018a), effect of SV and WF on surface morphology was investigated. It was found from the investigation that higher WF generates better surface finish as more melt free zones were available and recommended to use high servo voltage and high wire feed rate to obtain better machined surface finish. Figure 2.27 illustrates in detail about change in machined surface morphology at different SV and WF levels.

2.5.5.3 Effect of WF on Kerf Width

Roy and Narendranath (2018) concluded from their investigation of variation in kerf width that increasing WF leads to widening of kerf as better removal of debris from machining zone facilitated uniform sparking on the workpiece and resulted in more melting of material. Inset image of Figure 2.23 represents effects plot of kerf width variation with respect to increasing wire feed rate.

2.5.5.4 Effect of WF on Recast Layer Thickness

Since higher WF facilitates uniform sparking due to reduced secondary discharges, more heat energy per spark was dissipated on the workpiece and hence a slightly increased recast layer thickness was observed by Roy and Narendranath (2018) as illustrated in Figure 2.20. Overall, effect of WF on WEDM machining parameters were found to be insignificant. However, it is evident that under similar machining conditions homologous alloys like ternary TiNiCu alloys behave differently and therefore machining parameter level shall be chosen with greater interest.

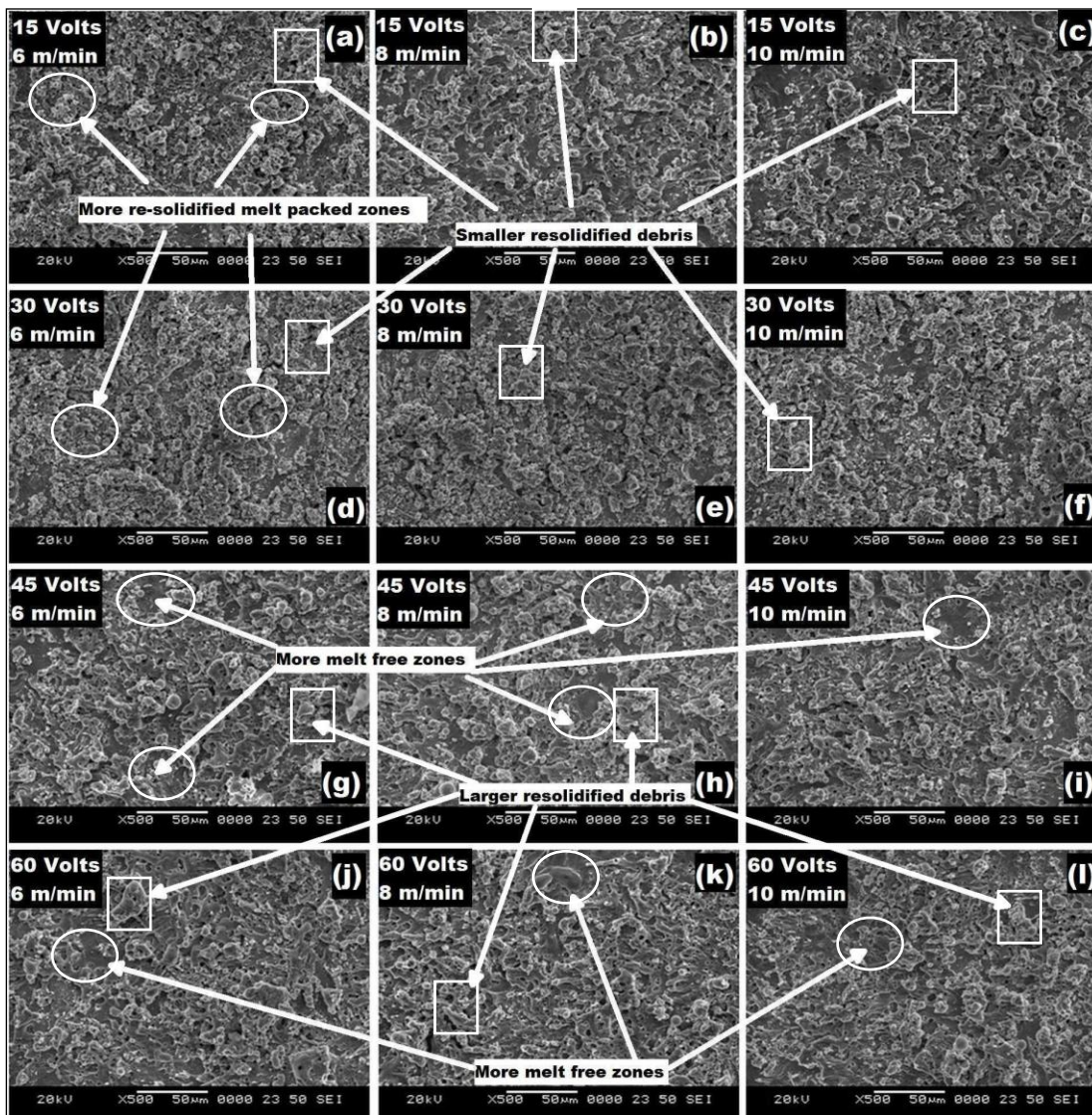


Figure 2.27 Machined surface morphology at (a,b,c) SV- 15 V, WF - 6,8,10 m/min (d,e,f) SV - 30 V, WF - 6,8,10 m/min (g,h,i) SV - 45 V, WF - 6,8,10 m/min (j,k,l) SV - 60 V, WF - 6,8,10 m/min (Roy and Narendranath, 2018a)

2.5.6 Effect of Flushing Condition

Dielectric fluid in EDM and WEDM process envelops the machining zone viz. the gap between electrode and workpiece where sparking takes place. Ionization of dielectric fluid due to application of large potential difference between electrode and workpiece leads to formation of an electrical bridge which carries out the sparking process via establishment of a plasma channel (Wong et al., 1995). Flushing conditions of the dielectric fluid such as flushing pressure, flow rate, flushing direction, nature of dielectric fluid etc. have certain degree of influence over different machining responses. Few relevant works by various researchers are discussed in upcoming sections.

2.5.6.1 Effect of flushing conditions on MRR and SR

Contamination of spark gap with debris material was stated as the main reason for reduced MRR at high discharge conditions and hence proper flushing is required (Schulze and Schätzing, 2013). Efficient removal of debris from machining zone is done by jet flushing which has become a popular technique in both EDM and WEDM processes (Makenzi et al., 2014). Dielectric fluid also facilitates in cooling the machining zone and removal of debris (Singh et al., 2018). It was confirmed in a study that proper selection of dielectric flushing is necessary to ensure optimal machining performance as material removal rate decreases with increasing flushing pressure and becomes constant at high flushing pressure levels whereas even though surface roughness reduces for increasing flushing pressure, it again surges at high flushing pressure levels (Lee and Li, 2001). Similar observation was done by Goodlet and Koshy (2015) where acoustic emission during EDM was utilized to quantify response behavior. Tanjilul et al. (2018) addresses the difficulty in flushing dislodged debris during deep hole EDM drilling. They proposed a novel simultaneous flushing and vacuum assisted EDM drilling with a specially designed tool electrode having inner slots for flushing. It was found that vacuum assisted EDM drilling reduced machining time and surface roughness. Figure 2.28 indicates the variation in machining time and average surface roughness with and without vacuum assisted EDM deep hole drilling.

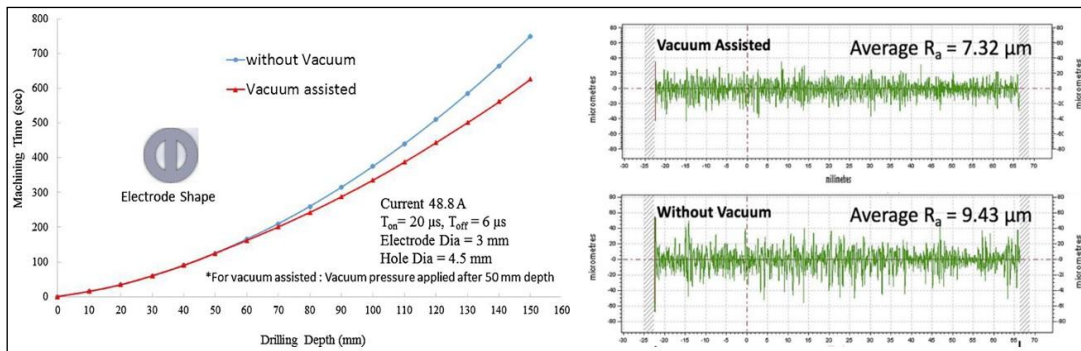


Figure 2.28 Effect of vacuum assisted flushing on machining time and surface roughness in EDM high depth drilling (Tanjilul et al., 2018)

Since insufficient cooling of wire electrode at fast machining rates causes rupture of wire, Haas et al. (2013) proposed different nozzle design, passage of wire electrode through the wire guide at the center of the nozzle causes insufficient cooling effect. However, they manufactured a 3D printed nozzle which provided 20% more efficient cooling than the original design that provided better dielectric flushing conditions.

2.5.6.2 Effect of flushing conditions on Surface Morphology

Bobbili et al. (2013) investigated effect of flushing pressure on MRR and SR and found this to be insignificant process parameters however, a slight variation was observed in SR in effects plot. Chakraborty et al. (2015) conducted a survey on effect of different dielectric fluid on material removal and machined surface quality during EDM and WEDM process. It was found that water based dielectrics produced better machined surface characteristics compared to hydrocarbon based or powder mixed dielectrics. Roy and Sanna Yellappa (2019) found that higher flushing pressure results in fewer machined surface defects and downward direction dielectric flow results in more efficient surface characteristics. Figure 2.29 represents machined surface morphology as observed by Roy and Sanna Yellappa (2019). Figure 2.29a have fewer resolidified debris which indicates better flushing conditions compared upward direction flow as shown in Figure 2.29b.

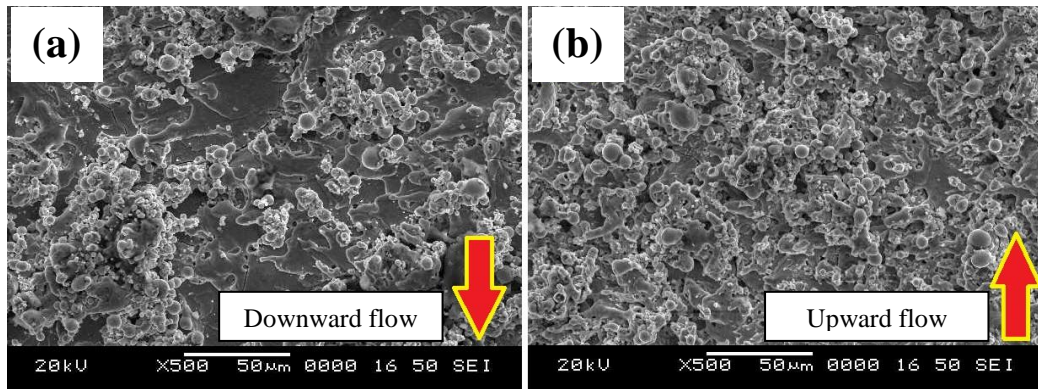


Figure 2.29 Machined surface morphology at (a) Downward flow (b) Upward flow
(Roy and Sanna Yellappa, 2019)

2.5.6.3 Effect of flushing conditions on Kerf Width

Konishi et al. (2015) examined the effect of nozzle tilting angle on MRR, kerf shape and wire deflection in WEDM process. They found that positive nozzle tilting angle is suitable compared to normal and negative nozzle angle orientation as it produced higher MRR, better surface characteristics, lesser wire deflection and uniform kerf. Positive nozzle tilting angle led to suitable dielectric flow behavior which helped in efficient decontamination of working zone and hence higher machining speeds could be attained. Kawata et al. (2017) conducted CFD analysis to track debris movement along the machining zone and found that most of the debris gets flushed away from machining zone through the bottom exit even though bottom nozzle actively flushed dielectric upwards. Habib (2017) carried out WEDM experiments regarding variation in wire vibration amplitude and kerf width at varying wire tension, wire speed and dielectric flow rates. It was observed that kerf width increases at high flow rates and low wire tension and wire speed. He recommended to maintain lower flow rates and higher wire tension to avoid kerf widening. Figure 2.30 shows the effect of process parameters used in this study on kerf width. Kerf width directly influences dimensional accuracy of the part to be produced using WEDM technique. In that regard Ebisu et al. (2018) studied influence of jet flushing in corner accuracy in WEDM process. They concluded from their study that flow and pressure fields around the wire changes significantly after changing direction during corner cutting.

They also found that debris residence time at the middle of the workpiece is more because of vortex flow caused due to bidirectional dielectric flow in WEDM process.

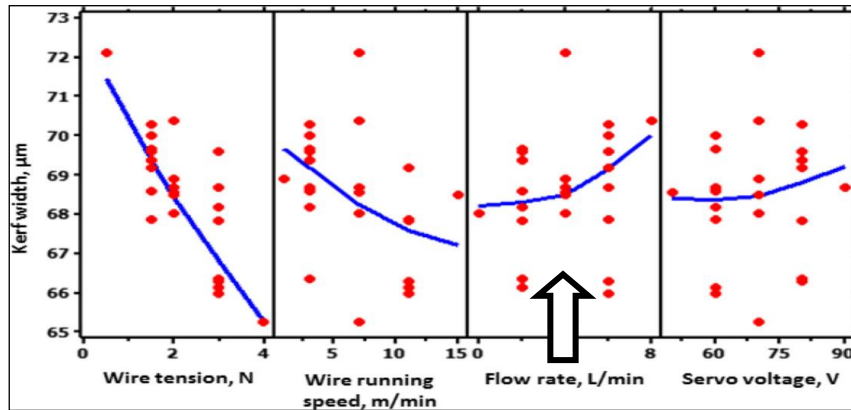


Figure 2.30 Effect of wire tension, wire speed, flow rate and servo voltage on kerf width (Habib, 2017)

2.5.6.4 Effect of flushing conditions on Recast Layer Thickness

Munz et al. (2013) investigated feed rate, surface roughness, electrode wear ratio and recast layer thickness at a wide range of dielectric flow rate (5l/h-25l/h) during EDM drilling. Higher flow rate indicates higher flushing pressure. It was found that for every set of discharge settings there exists a optimum flow rate beyond which feed rate drops due to abrupt wire vibration and spark interruption. Recast layer thickness was found to minimize with increasing flow rate whereas surface roughness was found to increase at higher dielectric flow rate. Higher hydraulic pressure at higher flow rate should be avoided at all cost to minimize undesirable process behavior. Similar observation on recast layer formation was reported by Wegener et al. (2018). Pramanik and Basak (2018) concluded from their investigation that low dielectric flushing pressure at high discharge energy settings lead to wire breakage which is undesirable in WEDM process. They have recommended that spark gap should be flushed properly to avoid unwanted sparks between debris and wire which eventually leads to more heat generation, softening of wire and breaking at higher wire tension. Higher heat generation is an indirect inference towards thicker recast layer formation. It was confirmed in another study that zinc coated brass wire is most suitable wire electrode for WEDM process owing to lower boiling point of zinc coating leading to

more severe sparking conditions (Yue et al., 2018). However, literature on effect of dielectric flushing pressure and flushing direction on machined surface morphology during WEDM process was found to be very rare. Therefore, in this investigation effect of dielectric flushing pressure and direction have been chosen while machining TiNiCu shape memory alloys using WEDM.

2.6 EXPERIMENTAL DESIGN AND MODELING OF WEDM PROCESS

Wire electro discharge machining is a non conventional machining process where several input process parameters influence the material removal mechanism. Process responses of WEDM consist of material removal rate, surface roughness, kerf width, recast layer thickness, machined surface microhardness, residual stress etc. Relation between input process parameters and output responses of WEDM process are not linear in nature. To establish the effect of various parameters on process responses proper experimentation planning is required. This section discusses about several techniques adopted by researchers while conducting WEDM experiments. Puri and Bhattacharyya (2005) also performed modeling and analysis of white layer depth in a wire-cut EDM process through response surface methodology. Ramakrishnan and Karunamoorthy (2008) performed a study of WED machining of Inconel 718. During their study, they have used Taguchi's L9 orthogonal array to design the experiments and used a multilayer perception ANN technique for optimizing the results by the help of multi response Signal to Noise (MRSN) ratio which is obtained by transforming the total loss function obtained. Nourbakhsh et al. (2013) also used Taguchi's DOE to perform WEDM of titanium alloy in order to investigate cutting speed, surface roughness and wire rupture along with machined surface characteristics. Manjaiah et al. (2014) used Taguchi L18 approach to study five parameters of the WEDM process which are peak current, pulse on time, pulse off time, servo voltage and wire feed. Obtained S/N ratio has been evaluated using ANOVA to identify the effect of individual factors. Saravanan et al. (2017) used Taguchi's L8 orthogonal array to perform WEDM experimentation and incorporated grey relational analysis to optimize WEDM process parameters in order to improve accuracy of the parts produced. Soni et al. (2018) proposed a hybrid approach using

response surface methodology (RSM) and grey relational analysis (GRA) coupled with principal component analysis (PCA) to perform optimization of parameters while machining Ti₅₀Ni₄₅Co₅ shape memory alloys. They emphasized on using Taguchi orthogonal experimental array as it provided methodical experiment levels to determine the effect of each parameters on WEDM responses. It was found that Taguchi's design of experiments was most widely used due to its simple yet robust methodology combined with its ability to produce results when experimental data were analyzed using ANOVA. Hence, these techniques were adopted in the current study.

2.7 PREDICTION OF WEDM RESPONSES

From the literature survey regarding machining of TiNi based shape memory alloys, it is evident that different input parameters like pulse on time, pulse off time, servo voltage, wire feed, discharge current, dielectric pressure etc. significantly influences the MRR and surface roughness, which are regarded as the most common output responses in WED machining. Researchers have suggested that it is advantageous to reduce experimental work and emphasize more on process modeling which helps to develop a relation between input variables and responses of machining process. This can be done by using mathematical and soft computing techniques. It has been found that ANN (Artificial Neural Network) is most suitable to model any process which is based on experimental results. ANN is one of the computational approaches that suits well when the physical phenomenon of the process is not well understood, mathematical form defining the process is not available but reasonable experimental data is available. Taguchi based experimental study was carried out by Çaydaş and Hascalık (2008) while abrasive water jet machining of AlZnMgCu1.5 alloy where ANN was implemented to predict suitable process parameters that could generate desired surface roughness. They also formulated a regression model of the machining process to predict output response and found that ANN is a more reliable prediction tool as prediction errors were less compared to prediction through regression model. Assarzadeh and Ghoreishi (2008) efficiently predicted MRR and SR of EDM process where BD3 steel and copper were used as workpiece and tool electrode respectively.

Ugrasen et al. (2014) predicted accuracy, surface roughness and volumetric material removal rate using ANN after performing WEDM of stavax material by varying four process parameters in a Taguchi's L16 orthogonal experimental array. They established accurate prediction using ANN and have recommended inclusion of 70% data in testing set for more accurate predictability of WEDM responses. Figure 2.31 demonstrates the accuracy of predicted values in their study. Similar results were reported by Surya et al. (2017).

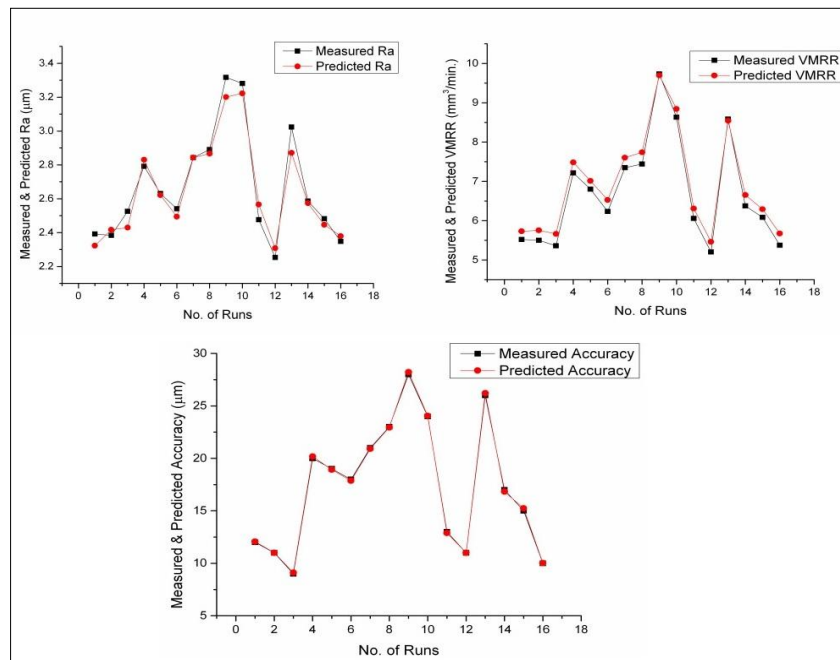


Figure 2.31 Comparison of experimental data with prediction data for SR, VMRR and accuracy (Ugrasen et al., 2014)

Ability of ANN to correlate highly non linear processes has been confirmed in the study by Conde et al. (2018). Soni et al. (2018) concluded from their investigation that ANN based predictions are more accurate compared to RSM prediction technique. As it was reported by numerous researchers that ANN has higher superiority compared to other models in understanding the WEDM process, this technique was adopted in this study to predict WEDM responses. Due to superior mapping capability of ANN, function in terms of weights and biases obtained from trained neural network can be used as objective function for genetic algorithm based optimization. Literature indicating suitability of genetic algorithm to optimize WEDM process are discussed in the upcoming section.

2.8 OPTIMIZATION OF WEDM RESPONSES

Since WEDM is a complex material removal process lacking specific numerical model, it is difficult to optimize output responses using conventional optimization techniques based on judgment. Researchers have suggested that implementation of a well planned experimental chart helps statistical techniques to optimize output responses. Kuriakose and Shunmugam (2005) optimized WEDM parameters using non dominated sorting genetic algorithm for titanium alloys. Pradhan (2012) proposed a new combination of response surface methodology (RSM), grey relational analysis (GRA) and entropy measurement method for the determination of optimum process parameters that maximizes the productivity without compromising the surface quality. Mathew and Babu (2014) performed a multiple process parameter optimization of WEDM on AISI304 using Taguchi Grey Relational Analysis where they have used a L27 orthogonal array for the design of experiments. The model developed is then processed for multi-objective optimization of three responses namely MRR, SR and kerf width using desirability approach and genetic algorithm. Similar results were reported by Ramakrishnan and Karunamoorthy (2008). Chen et al. (2010) performed optimization of WEDM parameter while manufacturing pure tungsten profile using neural network integrated simulated annealing algorithm. Specimens were prepared using Taguchi's L18 orthogonal experimental array. It was concluded from their study that back propagation neural network efficiently predicted WEDM responses. In another study, Rao et al. (2014) investigated machining performance of SiC_p reinforced Al7075 using WEDM where a non dominated sorting genetic algorithm was used to obtain optimized parameter levels. Genetic algorithm (GA) integrated with neural network modelling was found to perform good optimization with less than 3% error as confirmed from validity experimentation. Sahu et al. (2019) also performed ANN backed multi objective genetic algorithm where three different GA optimization techniques were used. They optimized material removal rate and electrode rate to increase productivity through this technique.

2.9 SUMMARY AND MOTIVATION FROM LITERATURE SURVEY

Shape memory alloys are becoming increasingly relevant in special applications across several domains due to superior properties they exhibit along with shape memory effect. It was found from extensive literature survey that TiNiCu ternary shape memory alloys are suitable for both actuator and biomedical applications. However, literature survey conducted in this study indicates that sputter deposition have been the most preferred technique to prepare TiNiCu shape memory alloys for actuator applications. Crystallization and machining of sputter deposited TiNiCu thin films still remains a challenge and does not address requirements of biomedical applications. Based on available literature vacuum arc melting has been adopted in this study to prepare homologous TiNiCu shape memory alloys and machined using wire electro discharge machining technique. Literature on bulk prepared TiNiCu alloys machined using Wire EDM is limited. Since Wire EDM can machine thin structures owing to its quarter-millimeter (250 μm) wire electrode, both micro and macro sized TiNiCu profiles can be machined. Literature on WEDM of homologous TiNiCu shape memory alloys are limited to WEDM responses like material removal rate and surface roughness only. Literature on WEDM responses like kerf width, recast layer thickness, machined surface microhardness of homologous TiNiCu shape memory alloys are not available. Taguchi's design of experiment has been implemented to machine different homologous TiNiCu shape memory alloys in this study. Material removal mechanism of WEDM is a complex non linear process and hence most of the researchers have adopted several detailed design of experiment along with implementation of artificial neural network to map the effect of WEDM process parameters on machining responses.

It was also observed that optimized process parameter varies from material to material and literature on optimized parameters of homologous TiNiCu shape memory alloys are nonexistent. Heat treatment of shape memory alloys is found to be crucial for its operational performance. Researchers have used different heat treatment routes to obtain shape memory alloys having suitable transformation characteristics. Homogenization heat treatment is a prerequisite for any functional material and is must for shape memory alloys. However, literature on effect of homogenization heat

treatment of WEDM responses are also not found. Dielectric flushing in WEDM process is very important as it helps in maintaining stable machining conditions and flushes away molten debris from the machining zone. Even though literature survey reveals few papers on effect dielectric flushing pressure on WEDM responses, effect of dielectric flushing direction are limited and considered in this study. Similarly, literature on WEDM parameters peak current and peak voltage simultaneously on WEDM responses are limited and hence addressed in this study. Detailed objectives of this research work are listed in the upcoming section.

2.10 OBJECTIVES OF CURRENT RESEARCH WORK

Based on literature survey and research gaps observed regarding machining characteristics, prediction and optimization of WEDM responses regarding TiNiCu shape memory alloys, following objectives are derived for this research work.

1. To develop six different homologous $Ti_xNi_{90-x}Cu_{10}$ ($x=50,45,40$) and $Ti_{50}Ni_{50-x}Cu_x$ ($x=15,20,25$) shape memory alloys using Vacuum Arc Melting (VAM) and to investigate grain structure, constituent phases, transformation temperatures and as cast microhardness of shape memory alloys.
2. To study the effect of pulse-on time, pulse-off time, wire feed and servo voltage on material removal rate, surface roughness, kerf width, recast layer thickness, machined surface microhardness and machined surface morphology using Taguchi's L16 orthogonal experimental array.
3. To find out WEDM response specific influential parameters using factor analysis, viz. ANOVA and Taguchi analysis.
4. To study the effect of peak current, peak voltage, dielectric flushing pressure and flushing direction on machined surface morphology and evaluation of variation in WEDM responses due to compositional variation and homogenization heat treatment of TiNiCu shape memory alloys.
5. To perform prediction and optimization of WEDM process responses using Artificial Neural Network (ANN) and Genetic Algorithm (GA) respectively.

CHAPTER 3

EXPERIMENTAL DETAILS

This chapter presents detailed experimental procedures adopted to conduct this research work such as preparation of workpiece material, characterization, design of experiments, machining and analysis. Setups used to perform characterization, machining and analysis required for this experimental research are also illustrated in upcoming sections.

3.1 MATERIAL SELECTION AND PREPARATION

It is evident from literature survey that TiNiCu ternary shape memory alloys are suitable materials for both actuator and biomedical applications. From inferences drawn by the researchers, compositional variation of TiNiCu shape memory alloy leads to shift in phase transformation temperatures. Since phase transformation temperatures of TiNiCu alloys are sensitive to nickel and copper content, two different sets of TiNiCu shape memory alloys namely $\text{Ti}_{50}\text{Ni}_{40}\text{Cu}_{10}$, $\text{Ti}_{45}\text{Ni}_{45}\text{Cu}_{10}$, $\text{Ti}_{40}\text{Ni}_{50}\text{Cu}_{10}$ and $\text{Ti}_{50}\text{Ni}_{35}\text{Cu}_{15}$, $\text{Ti}_{50}\text{Ni}_{30}\text{Cu}_{20}$, $\text{Ti}_{50}\text{Ni}_{25}\text{Cu}_{25}$ are prepared to investigate the effect of nickel rich and copper rich content respectively on phase transformation temperatures and wire electro discharge machining responses. These alloys are prepared using vacuum arc melting equipment as shown in Figure 3.1. Vacuum environment is preferred over other techniques due to high reactivity of titanium, nickel and copper with oxygen which contaminates and disturbs the original intended composition. The unique feature of these group of alloy is exhibited due to specific crystal orientation which could be easily disrupted due to presence of impurities and especially due to oxygen, nitrogen, carbon and other potential contamination. By the help of vacuum arc melting pure ingots of TiNiCu shape memory alloys can be prepared. Before melting, the pure elements were weighed in a high precision weighing balance (CONTECH CA-3102) and placed into copper crucible button pits as shown in inset image of Figure 3.1.

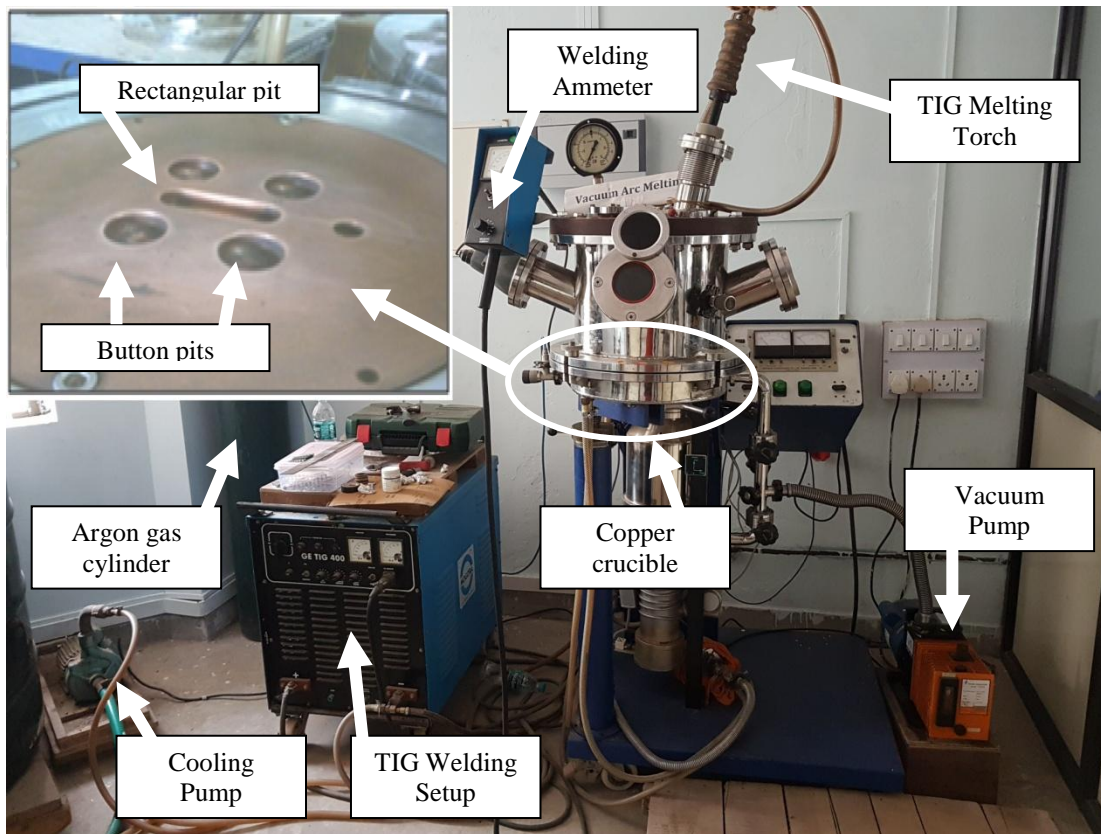


Figure 3.1 Vacuum Arc Melting Setup

Melting was carried out using tungsten plasma torch retrofitted in the vacuum chamber at 10^{-5} mbar vacuum. Before melting was carried out argon gas was purged in the vacuum chamber to create an inert atmosphere. After the melt buttons were obtained, they were re-melted to form a bar specimen which was melted six times on each side to maintain homogeneity. The bar specimens were then used for machining using Wire EDM equipment. Table 3.1 represents the alloy composition and symbol used in this study. TNC11, TNC12 and TNC13 represent fixed Cu (10 at.%) content TiNiCu shape memory alloys whereas TNC21, TNC22 and TNC23 represent fixed Ti (50 at.%) content TiNiCu shape memory alloys.

Table 3.1. Alloy composition (in at.%) and symbol

| Alloy | Ti ₅₀ Ni ₄₀ Cu ₁₀ | Ti ₄₅ Ni ₄₅ Cu ₁₀ | Ti ₄₀ Ni ₅₀ Cu ₁₀ | Ti ₅₀ Ni ₃₅ Cu ₁₅ | Ti ₅₀ Ni ₃₀ Cu ₂₀ | Ti ₅₀ Ni ₂₅ Cu ₂₅ |
|--------|--|--|--|--|--|--|
| Symbol | TNC11 | TNC12 | TNC13 | TNC21 | TNC22 | TNC23 |

3.2 PRELIMINARY CHARACTERIZATION OF TiNiCu ALLOYS

Before machining experimentations were carried out of prepared TiNiCu shape memory alloys, some basic characterization tests were carried out to confirm functionality of these alloys. Confirmation of requisite properties of prepared TiNiCu shape memory alloys further validated that WEDM experimentations were carried out on scientifically proven material exhibiting shape memory effect. Therefore, metallographic, thermo-analytic and crystallographic characterizations were performed which are basic characterization regime for shape memory alloys. Details regarding aforementioned characterization processes are discussed in detail in upcoming sub-sections.

3.2.1 Metallographic Characterization

As cast TiNiCu shape memory alloys were cut into approximately 1cm² flat specimens and mounted using cold acrylic resin for the ease of polishing. Polishing were done using a metallographic polisher using emery papers of progressive grades namely 100, 500, 800, 1200, 2000 followed by mirror polishing using diamond paste. In order to obtain a more visible microstructure all polished samples were etched using an etchant containing two parts hydrofluoric acid (2 ml HF) and ten parts nitric acid (10 ml HNO₃) mixed with twenty parts of distilled water (20 ml H₂O). The etchant was applied using a cotton swab until a matte surface finish was obtained. Required time for appropriate etching has been optimized and samples were washed with distilled water immediately after etching to avoid over etching. Figure 3.2 shows the optical microscope used in this study and microstructure of polished TiNiCu samples.

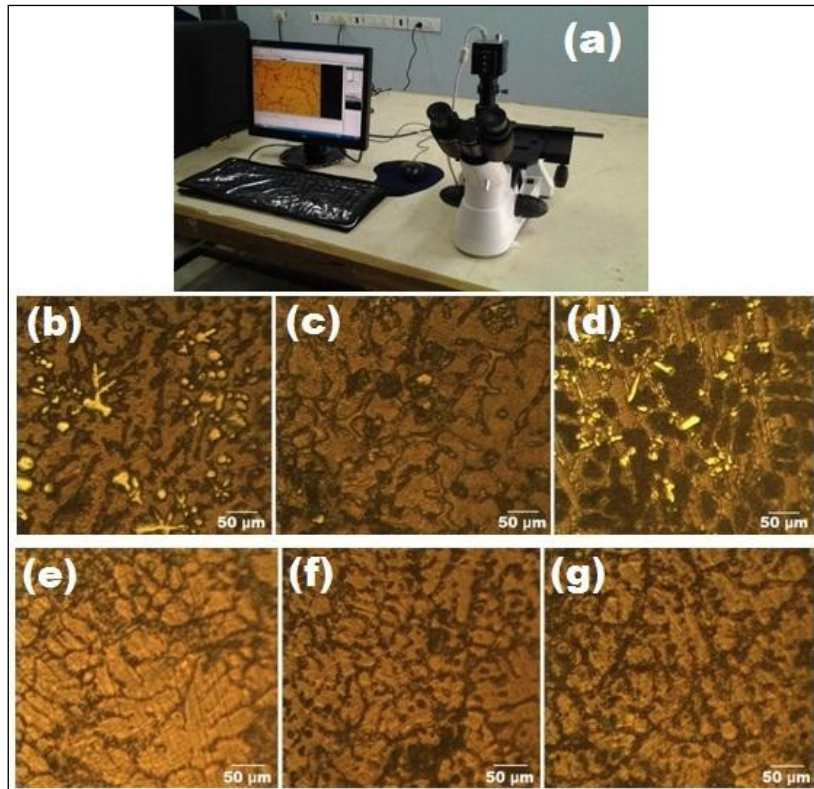


Figure 3.2. (a) Optical microscope (b-d) Microstructure of TNC11, TNC12 and TNC13 (e-g) Microstructure of TNC21, TNC22 and TNC23

3.2.2 Thermo-analytic Characterization

Transformation behavior of prepared TiNiCu shape memory alloys were investigated using Perkin Elmer DSC6000 as shown in Figure 3.3. For the preparation of calorimetric analysis samples were cut weighing few micrograms and polished to remove oxide layer. These samples were sealed and crimped in aluminium thermal pans before put into sample furnaces. All samples were scanned from -40°C to 400°C at a scanning rate of $5^{\circ}\text{C}/\text{min}$ under atmospheric pressure. Phase transformation temperatures were determined using slope line extension method. Figure 3.3 indicates equipment used in this study and system generated graph. Along with graph file data points were also obtained in XLS format which were used later to plot line graphs having better resolution.

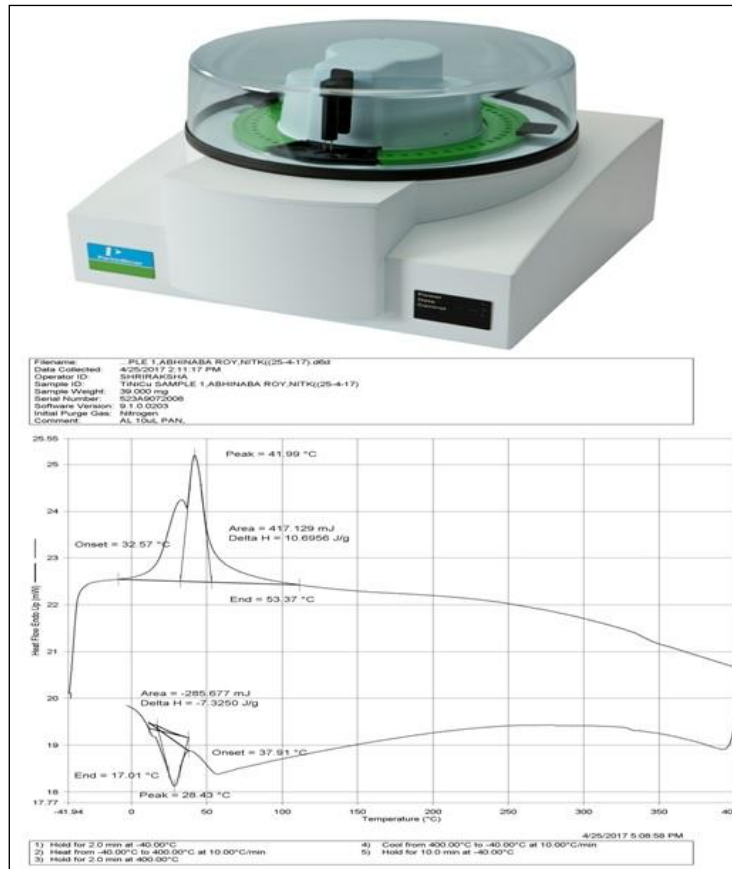


Figure 3.3. Differential Scanning Calorimeter and DSC curve

3.2.3 Crystallographic Characterization

Constituent phases of prepared TiNiCu ternary shape memory alloys were investigated using Rigaku Miniflex 600 XRD equipment as shown in Figure 3.4 emanating CuK α radiation. Scanning range was set for 5⁰-110⁰ at a scanning speed of 2⁰/min for all the alloys. Before testing, the samples were polished, cleaned and heat treated at 100⁰C for 10 minutes to remove residual stresses and to avoid disruption of phase identification. Obtained XRD plots were analyzed using X-pert High Score Plus software. This software can sort background signals, perform smoothing and identify significant peaks and match those peaks with ICDD database. By the help of ICDD database, obtained peaks in this study were narrowed down. Figure 3.4 depicts XRD equipment used in this study and system generated graph. Miniflex software also provides data points in XLS format which were used to generate custom line graphs having higher resolution.

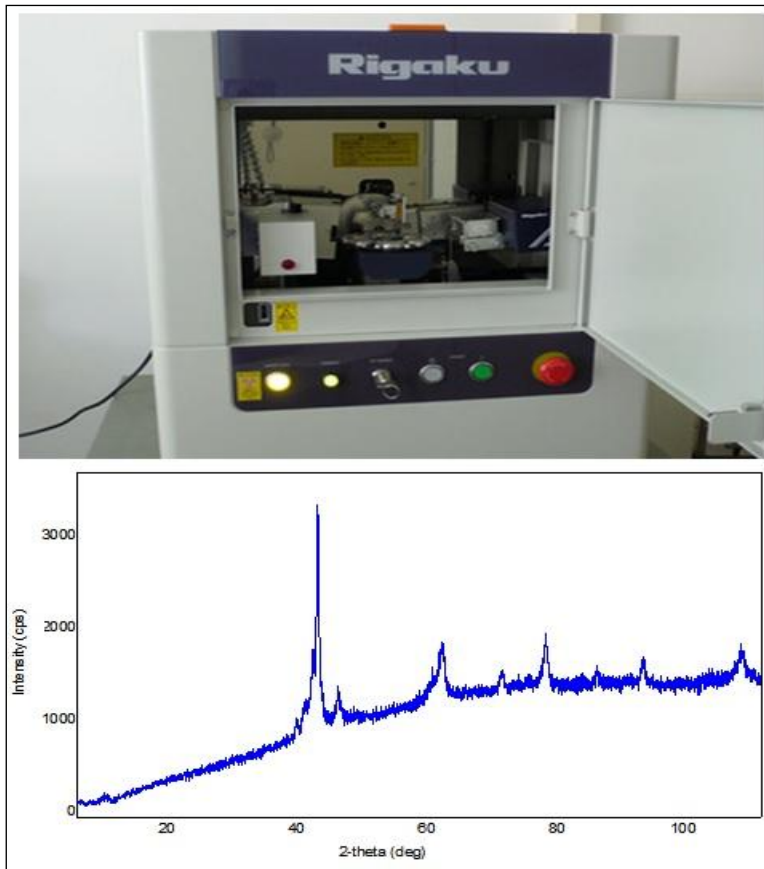


Figure 3.4. X-ray diffraction equipment and XRD plot

3.3 EXPERIMENTAL SETUP

3.3.1 Wire Electro Discharge Machine

All machining experiments were carried out on a wire electro discharge machining unit namely Ecocut - ELPULS15 made by Electronica India Pvt. Ltd as shown in Figure 3.5. The machine consists of a CNC bed where the workpiece is attached. Fresh wire electrode having diameter of 250 μm is fed from the wire spool to the machining zone through a setup of automated power pulleys. Several input process parameters can be controlled in this machine namely, pulse on time, pulse off time, servo voltage, wire feed, servo feed, spark voltage, spark current, corner dwell time, cutting speed override factor, flushing pressure etc. Based on literature most influential process parameters were selected and other parameters were kept constant for this investigation.



Figure 3.5. Wire electro discharge machining setup

Pulse on time (T_{on}), pulse off time (T_{off}), servo voltage (SV) and wire feed (WF) were found to be most influential parameters to control WEDM output responses like material removal rate (MRR), surface roughness (SR), kerf width (KW) and recast layer thickness (RLT). Based on machine capability these parameters were varied at four levels to investigate their effect on chosen machining responses. Henceforth, it was found that Taguchi's L16 orthogonal experimental array can provide enough experimental results at the expense of minimum possible trials for all six prepared TiNiCu shape memory alloys, i.e. 96 experimental trials in total. Zinc coated brass wire was used as the wire electrode in this investigation. 16 experimental trials used in this investigation to carry out machining of TiNiCu shape memory alloys as per Taguchi's method has been tabulated in Table 3.2.

Table 3.2. Taguchi's L16 orthogonal experimental array

| Trial No. | T _{on} (μs) | T _{off} (μs) | SV (Volts) | WF (m/min) |
|-----------|-------------------------|--------------------------|---------------|---------------|
| 1. | 100 | 20 | 4 | 15 |
| 2. | 100 | 30 | 6 | 30 |
| 3. | 100 | 40 | 8 | 45 |
| 4. | 100 | 50 | 10 | 60 |
| 5. | 110 | 20 | 6 | 45 |
| 6. | 110 | 30 | 4 | 60 |
| 7. | 110 | 40 | 10 | 15 |
| 8. | 110 | 50 | 8 | 30 |
| 9. | 120 | 20 | 8 | 60 |
| 10. | 120 | 30 | 10 | 45 |
| 11. | 120 | 40 | 4 | 30 |
| 12. | 120 | 50 | 6 | 15 |
| 13. | 130 | 20 | 10 | 30 |
| 14. | 130 | 30 | 8 | 15 |
| 15. | 130 | 40 | 6 | 60 |
| 16. | 130 | 50 | 4 | 45 |

Material removal rate during WEDM was measured via "weight loss" technique where weight of the samples before and after machining were noted using a scientific weighing scale having 0.001gm least count and divided by time taken by the machine to complete cutting and theoretical density of the prepared alloys as per equation 3.1 given below.

$$\text{MRR} = \frac{w_f - w_i}{\rho \times t} \times 1000 \quad (3.1)$$

MRR = Material Removal Rate (in mm³/min)

w_i = initial weight (in gm, before machining)

w_f = final weight (in gm, after machining)

ρ = density of the alloy (in gm/c.c)

t = time taken (in minutes)

3.3.2 Surface Roughness Tester

Surface roughness (R_a) of wire electro discharge machined samples were measured using surface roughness tester SURFTTEST SJ-301 by Mitutoyo, Japan and is depicted in Figure 3.6. The probe of the roughness tester contains a diamond tip having a radius of $2\ \mu\text{m}$ which scans the surface to be inspected. In this investigation 4 mm was used as evaluation length based on samples size at five different regions for each sample and the average value is used. Stylus speed is maintained constant at 0.25 mm/s for all WEDMed samples.



Figure 3.6. Surface roughness tester

3.3.3 Scanning Electron Microscope

Machined surface morphology, kerf width, recast layer and other intricate details of WEDMed samples were investigated using scanning electron microscope (JEOL JSM-638OLA) developed by Japan Electron Optics Laboratory as shown in Figure 3.7. In the current study 20kV acceleration voltage at high vacuum was used to obtain secondary electron images from the scanning electron microscope (SEM).

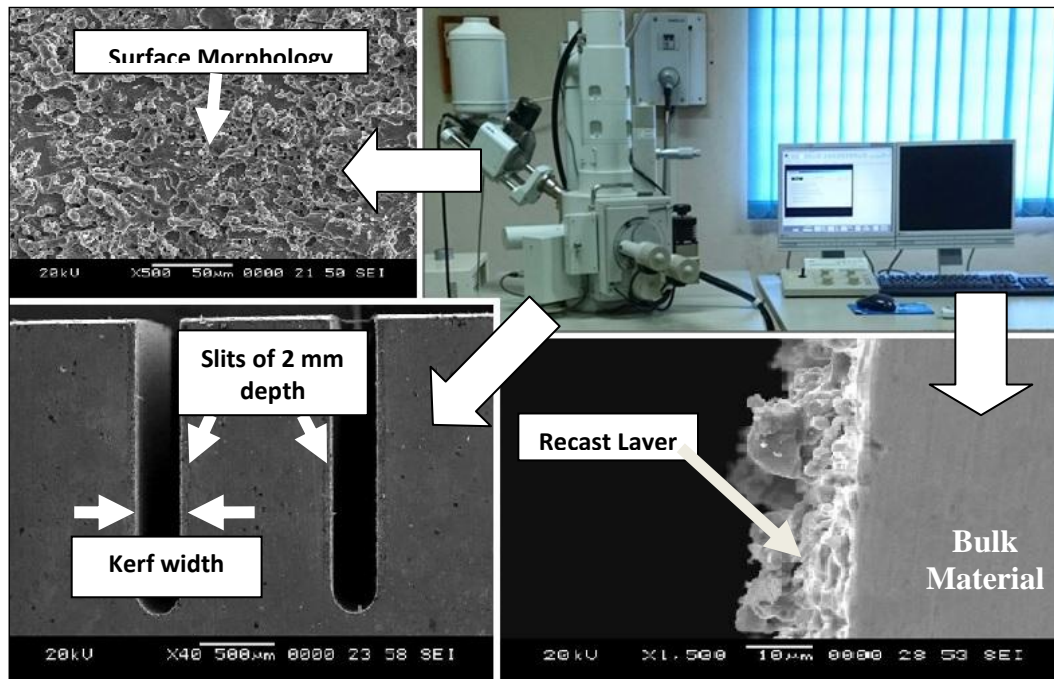


Figure 3.7. Scanning Electron Microscope

Spark erosion mechanism of WEDM produces a complex machined surface morphology as shown in Figure 3.7 and depends on input process parameters used during machining. Defects caused due to machining like micro-cracks, micro-voids etc, can be investigated using SEM micrographs. Kerf width was measured by conducting all 96 experimental trials where 2 mm depth slits (see Figure 3.7) were cut and width of cut for each slits were measures using SEM. Similarly, cross section of machined surfaces were polished, etched and observed under SEM to measure recast layer thickness as shown in Figure 3.7.

3.3.4 Microhardness

In this investigation machined surface microhardness have been investigated for the TiNiCu shape memory alloys for all 96 experimental trials using Omni Tech MVHS-Auto Microhardness tester at 50gf load for 15s dwell time and is shown in Figure 3.8. Inset image represents recast layer and parent material and trend of microhardness.

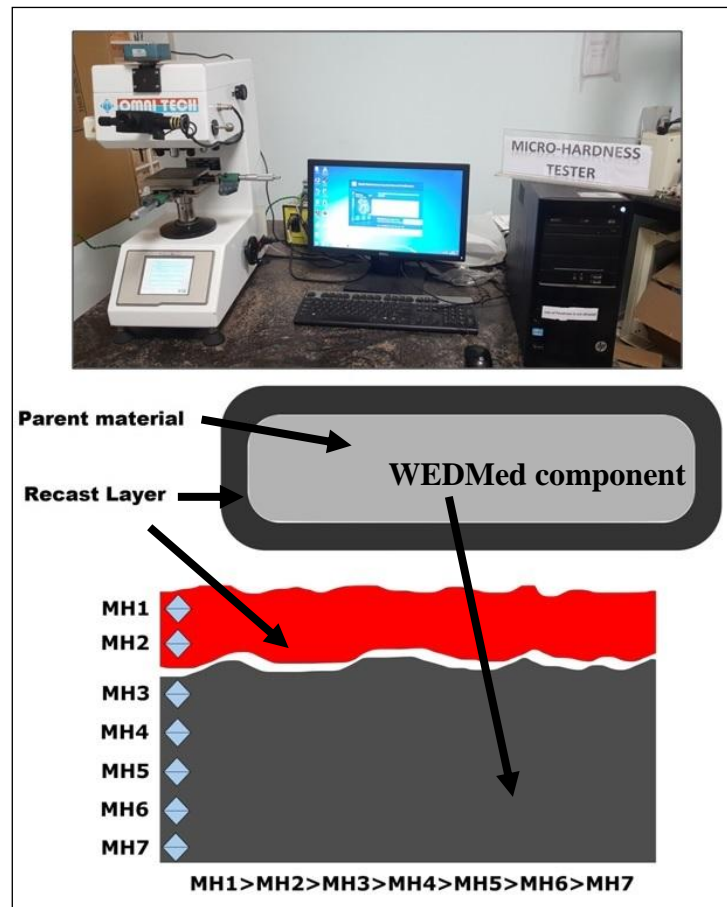


Figure 3.8. Microhardness Tester

3.4 DESIGN OF EXPERIMENTS AND ARTIFICIAL NEURAL NETWORK

3.4.1 Design of Experiments (DOE) and Factor Analysis

Design of experiments (DOE) is a systematic approach to plan experimental trials in such a manner that most of the aspects of involved input process parameters are covered within minimum number of trials. There are several DOE techniques such as Taguchi's method, factorial design, response surface methodology etc. However, it was found from literature in previous chapter that Taguchi technique is most accepted due to its simple yet robust and practical methodology (Tosun et al., 2004; Ramakrishnan and Karunamoorthy, 2008; Nourbakhsh et al., 2013). From Taguchi technique it was found that for four input process parameters varying at four levels, L16 orthogonal experimental array was most suitable and the same is adopted in this study. Further, Taguchi analysis was carried out to find most influential parameter

based on responses obtained. In other words, for a specific WEDM response, the process parameter to have highest influence on that response was identified. Based on Taguchi experimental trials as tabulated in Table 3.2, TiNiCu shape memory alloys were machined. After required WEDM responses were obtained, Taguchi analysis was carried out to determine the extent of variation of WEDM responses due to applied input process parameters. In Taguchi analysis optimal parametric combination is found after selected responses are categorized as "higher-the-better" or "lower-the-better" type. Material removal rate can be categorized as "higher-the-better" type whereas surface roughness, kerf width and recast layer thickness can be categorized as "lower-the-better" type. Taguchi method utilizes signal-to-noise ratio obtained from equation 3.2 and 3.3 which represent mean square deviation (MSD) values based on "higher-the-better" and "lower-the-better" responses respectively where n is number of experimental trials.

$$\text{MSD}_{\text{MRR}} = \frac{1}{n} \sum_{i=1}^n \frac{1}{\text{MRR}_i^2} \quad (3.2)$$

$$\text{MSD}_{\text{SR, KW, RLT}} = \frac{1}{n} \sum_{i=1}^n (\text{SR}, \text{KW}, \text{RLT})_i^2 \quad (3.3)$$

Secondly, variation of WEDM responses namely, material removal rate, surface roughness, kerf width and recast layer thickness due to varying levels of WEDM input process parameters were graphically plotted using mean effects plot. Analysis of variance (ANOVA) was also carried out to determine most influential process parameter for a given WEDM response using statistical analysis software Minitab 17. Through F-test using 95% confidence level most influential input process parameters for MRR, SR, KW and RLT were identified. Box Behnken design of experiment was also implemented to determine optimal machined surface morphology within a narrow range of most influential WEDM process parameters as obtained from ANOVA studies. From ANOVA results it was found that pulse on time, pulse off time and servo voltage have significant influence on surface roughness hence resulting machined surface morphology. Based on Box Behnken design, low and high parameter levels of these three aforementioned parameters resulted in 15 experimental plans which were conducted to study the effect of significant parameters on machined surface morphology. Box Behnken methodology was adopted because range of WEDM parameters to be investigated were narrow and degree of freedom was

limited. In case of such limitations, Box Behnken generates list of experimental trials where impact of WEDM parameters on targeted responses can be evaluated in least number experimental trials. Based on process parameters and machine capability further experimentations to evaluate effect of peak current and peak voltage on machined surface morphology were conducted using factorial design of experiments. Input values of peak current and peak voltage was provided in terms of bit values such as 00, 01, 02 etc. Combination of bit values for peak current and peak voltage yields distinctive parameter values, since each of these WEDM parameters has certain number of possible combinations (six for peak current and 3 for peak voltage), factorial experimental plan was undertaken.

3.4.2 Response Prediction using Artificial Neural Network

Artificial neural network is a powerful soft computing tool which fits well for modeling complex physical phenomenon like wire electro discharge machining in this work. Material removal process in Wire EDM is a non-linear phenomenon which is dependent on several process parameters. Due to varying impact or influence of each of these parameters on Wire EDM process, it is a complex phenomenon which cannot be comprehended in term of regression models alone. ANN however, due to its biologically inspired design, respond well when reasonable experimental data is available. Experimental data in this work was collected through Taguchi's DOE (L16) for all prepared TiNiCu shape memory alloys. Pulse on time (T_{on}), pulse off time (T_{off}), servo voltage (SV) and wire feed (WF) are four parameters of Wire EDM technique which were considered to map their influence on output response material removal rate (MRR), surface roughness (SR), kerf width (KW) and recast layer thickness (RLT). Before these experimental data can be fed into neural network they need to be normalized as normalized data is better understood by ANN since normalization distributes the data in values ranging from 0-1. By doing this different units and levels are scaled to similar values which makes it easier for neural network to understand the data better and establish better R-value during training process. To normalize experimental parameter equation 3.4 was used.

Input parameters were normalized as:

$$P_n = \frac{P}{P_{\max}} \quad (3.4)$$

Where,

P_{\max} = Maximum value of process parameter

P_n = Normalized process parameter

P = Process parameters to be normalized

Output responses were normalized as:

$$\text{For lower-the-better criteria (LB) : } R_n = \frac{\max R_{ik} - R_{ik}}{\max R_{ik} - \min R_{ik}} \quad (3.5)$$

$$\text{For higher-the-better criteria (HB) : } R_n = \frac{R_{ik} - \min R_{ik}}{\max R_{ik} - \min R_{ik}} \quad (3.6)$$

Where,

R_{ik} = k^{th} response of i^{th} experiment

R_n = Normalized response

Machining responses where maximum value is desirable (like material removal rate), higher-the-better criteria was used as shown in equation 3.5, whereas for surface roughness (for which minimum value is desirable), lower-the-better criteria was used as shown in equation 3.6. In general 70% of the experimental data (normalized) is used for training the neural network and rest is used for testing and validation. However, in this study 75% data was used for training (12 experimental results out of each L16 experimental array) and rest was used for testing and validation (2 each for testing and validation). After simulated results were obtained they have to be de-normalized to obtain the actual values. De-normalization of normalized responses obtained after ANN prediction were performed using equation 3.7 and 3.8.

$$\text{For lower-the-better criteria (LB) : } R_{dn} = R_{\max} - R_n(R_{\max} - R_{\min}) \quad (3.7)$$

$$\text{For higher-the-better criteria (HB) : } R_{dn} = R_n(R_{\max} - R_{\min}) + R_{\min} \quad (3.8)$$

Where,

R_{dn} = De-normalized response

R_{\max} = Maximum response in training data

R_{\min} = Minimum response in training data

In this study attempt has been made to map effect of four Wire EDM parameters (pulse on time, pulse off time, servo voltage and wire feed) on four specific machining responses (material removal rate, surface roughness, kerf width and recast layer thickness) and subsequent prediction of machining responses using artificial

neural network. Since Wire EDM process parameters interact non-linearly with consequent machining responses it is imperative to select proper network architecture for efficient training of the parameter-response set. It was found from literature that feed forward back propagation neural networks are most likely to generate suitable mapping results (Thillaivanan et al., 2010). Hence in this study feed forward back propagation neural network was used to map behavior of selected Wire EDM parameters on selected machining responses for prepared TiNiCu shape memory alloys. Input and output data has to be fed into neural network to start the training process. These experimental data after being normalized were supplied to the neural network to start the training of network. Equation 3.9 represents the input process parameters used in this study where X denotes the input vector in a transpose arrangement whereas Y represents output machining responses given in equation 3.10.

$$X = \{T_{on}, T_{off}, SV, WF\}^T \quad (3.9)$$

$$Y = \{MRR, SR, KW, RLT\}^T \quad (3.10)$$

Where,

T_{on} = Pulse on time (μs), T_{off} = Pulse off time (μs)

SV = Servo voltage (Volts), WF = Wire feed (m/min)

MRR = Material removal rate (mm^3/min), SR = Surface roughness (μm)

KW = Kerf width (μm), RLT = Recast layer thickness (μm)

Each neuron in input and output layer of ANN model represent Wire EDM process parameters and investigated machining responses respectively. Therefore, in this study input layer consists of four neurons and output layer consists of four neurons (representing four parameters and four responses accordingly). However, number of neurons in hidden layers depend on the complexity of the neuron model which is generally limited by equations 3.11 and 3.12. In this work, it was found that two hidden layers are sufficient to achieve good correlation.

$$\text{Minimum neuron} = (\text{Input} + \text{Output}) / 2 \quad (3.11)$$

$$\text{Maximum neuron} = 2 (\text{Input}) + 1 \quad (3.12)$$

Although more number of layer could help in building a complex network structure that does not necessarily indicates that good fitting conditions can be obtained. Over-fitting has been reported by many researchers which leads to poor correlation and

hence poor prediction results containing significant error (Hill and Minsker, 2010). After several trials it was found that two hidden layers and one output layer is sufficient to achieve good correlation and hence 4-9-9-4-4 network architecture was used in this study. After successful training of the artificial neural network suitable prediction results were obtained. In this study, four input sets were selected based on duty factor. Duty factor is the ratio of discharge duration to discharge cycle. This factor represents energy dissipation factor during sparking in Wire EDM process. In this case duty factor ranges from 0.66 to 0.86. These four input parameter sets were chosen based on four intermediate values between the range, which are 0.75, 0.78, 0.81 and 0.84.

3.4.3 Optimization using Genetic Algorithm

Genetic algorithm are computer programs which are inspired by Charles Darwin's theory of natural evolution. Through this algorithm fittest outputs are identified through the process of natural selection in order to find out parameters that influence it. Genetic algorithm due to its capability of increasing productivity while performing multi objective optimization (Sahu et al., 2019) was considered in this study in collaboration with neural network mapping. At first the algorithm creates a random initial population using the fitness function provided (obtained from ANN). Then a sequence of new population is created using inputs from the current population to create the next population. To create new population or solutions, genetic algorithm uses three basic genetic operators like selection, crossover and mutation. Figure 3.9 represents generalized structure of genetic algorithm.

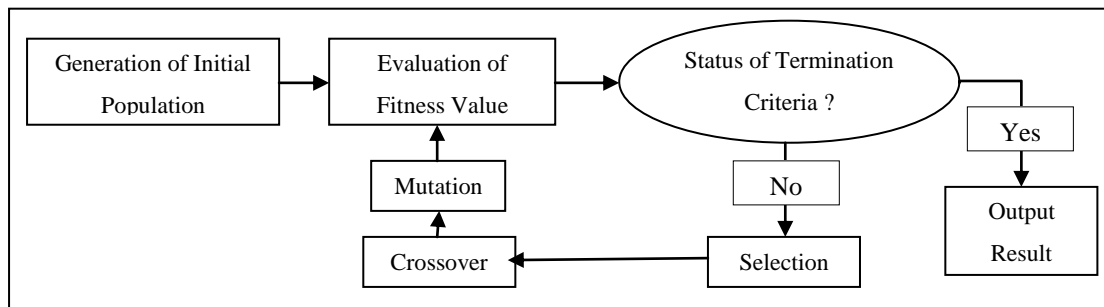


Figure 3.9. Structure of Genetic Algorithm

Fitness value of the new population indicates suitability with the optimized conditions, which is evaluated through objective function. New population is created for many generation until solution criteria is met, in this case optimized conditions. In this study, fitness function obtained through ANN weights and biases were treated as objective function and criteria was set to maximize MRR, minimize SR, KW and RLT. To evaluate optimized parameters, multi objective genetic algorithm was performed through *optimtool* function in MATLAB. Flowchart of detailed experimental plan discussed in previous sections is shown in Figure 3.10 and the entire research work is carried out with maximum care and close observation to get the best results.

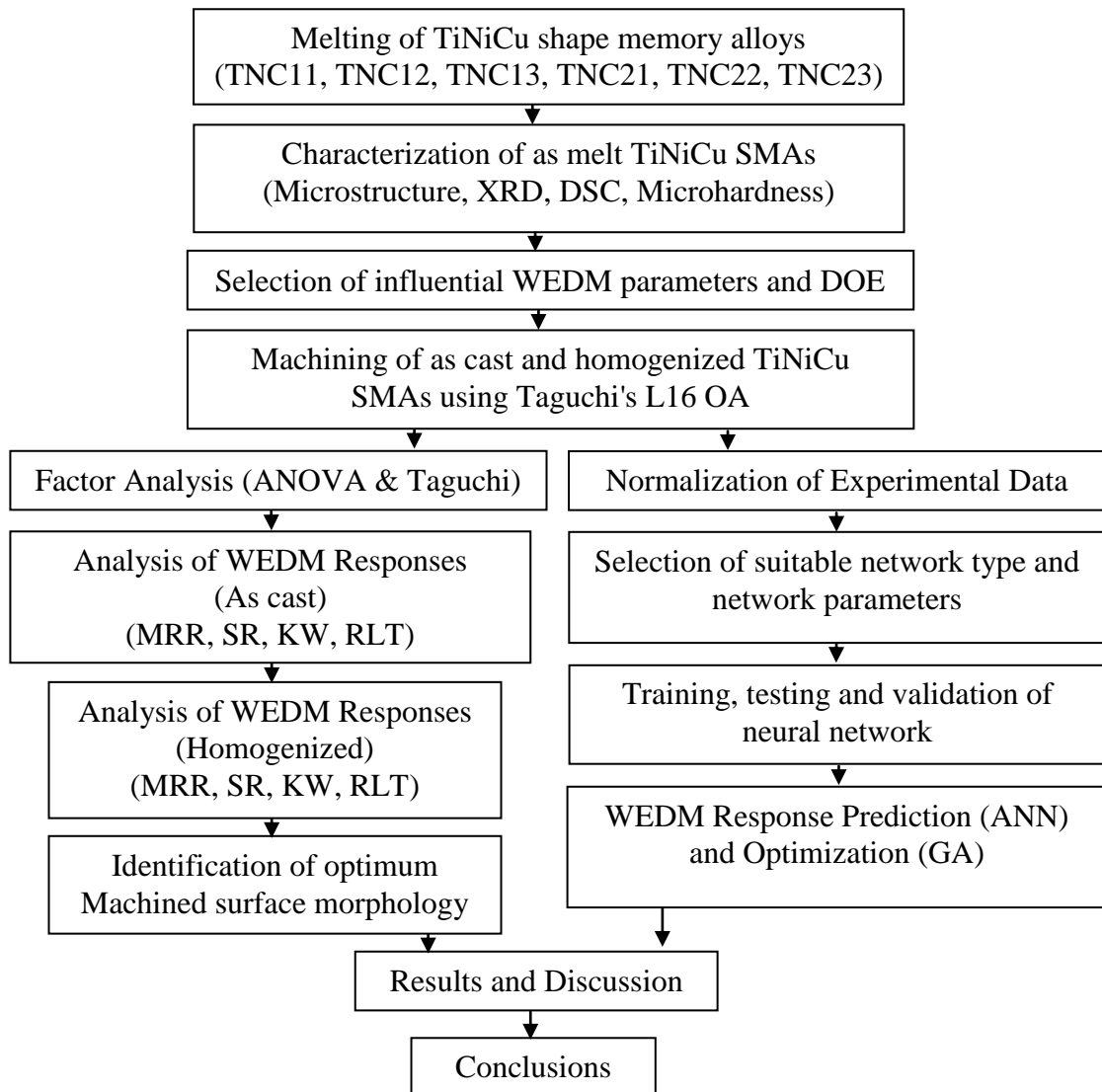


Figure 3.10. Flowchart of the experimental plan

3.5 SUMMARY

In this chapter techniques adopted for preparation of the TiNiCu alloys and wire electro discharge machining of TiNiCu shape memory alloys are discussed. Taguchi's design of experiment (L16) was implemented to conduct machinability study of all TiNiCu alloys. Factor analyses were carried out using Taguchi analysis and ANOVA. Further experimental plans to study change in surface morphology due to significant factors were done using Box Behnken design and factorial design. Material removal rate, surface roughness, kerf width and recast layer thickness were recorded for all 96 experimental trials. Characterization of machined surface in terms of phases present and nature of surface morphology were carried out using XRD plots and scanning electron micrographs. Microhardness of machined surfaces were measured using microhardness tester. Phase transformation temperature of TiNiCu shape memory alloys were determined using differential scanning calorimetry. Finally, artificial neural network was employed to map selected WEDM responses with used input process parameters in order to predict and optimize WEDM responses.

CHAPTER 4

WEDM ANALYSIS OF TiNiCu SHAPE MEMORY ALLOYS

4.1 INTRODUCTION

Six different TiNiCu ternary shape memory alloys were prepared in a vacuum environment (10^{-5} mbar) under argon atmosphere. First group of alloy (alloy set 1) have fixed Cu content (10at%) and another group of alloy have fixed Ti content (50at%). Characterization of prepared TiNiCu shape memory alloys were carried out which revealed differences in properties in terms of microstructure, constituent phases, phase transformation temperatures and microhardness.

Furthermore, pulse-on time (T_{on}), pulse-off time (T_{off}), servo voltage (SV) and wire feed rate (WF) were selected as major WEDM input process parameters. Four major machining responses have been selected namely, material removal rate (MRR), surface roughness (SR), kerf width (KW) and recast layer thickness (RLT). To understand the effect of WEDM process parameters on machining responses, Taguchi's L16 orthogonal experimental design was implemented. Taguchi analysis and ANOVA analysis were carried out to identify most significant parameters for a chosen WEDM responses. Another set of experimentation was carried out to identify the variation in selected machining responses due to homogenization heat treatment of TiNiCu shape memory alloy.

Machined surfaces were characterized in terms of constituent phases, microhardness and surface morphology. Furthermore, WEDM experimentation were carried out using Box Behnken and factorial design of experiments to investigate the effect of dielectric flushing pressure, flushing direction, peak current and pulse peak voltage on machined surface characteristics. Obtained WEDM responses were used to train a feed forward back propagation neural network in order to predict and optimize WEDM responses.

4.2 CHARACTERIZATION OF TiNiCu TERNARY SHAPE MEMORY ALLOYS

Characterization of TiNiCu shape memory alloys were carried out in order to investigate the effect of compositional variation on microstructure, constituent phases, microhardness and phase transformation temperatures. All specimens for aforementioned characterizations were prepared using WEDM technique as this technique results in negligible metallurgical change due to very low thermal impact.

4.2.1 Microstructure of TiNiCu Shape Memory Alloys

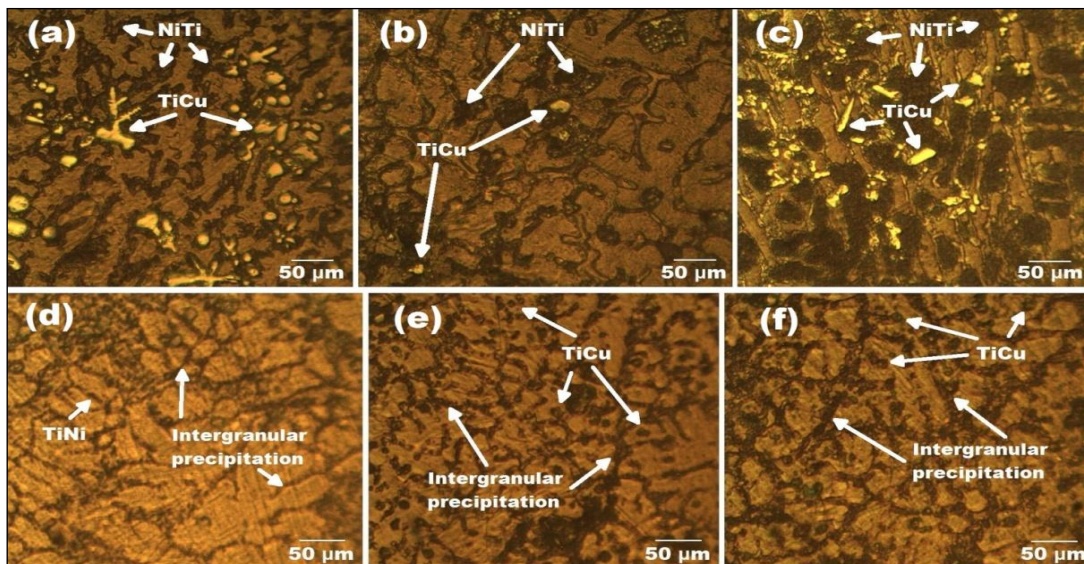


Figure 4.1 Microstructure of (a)Ti₅₀Ni₄₀Cu₁₀ (b)Ti₄₅Ni₄₅Cu₁₀ (c)Ti₄₀Ni₅₀Cu₁₀ and (d)Ti₅₀Ni₃₅Cu₁₅ (e)Ti₅₀Ni₃₀Cu₂₀ (f)Ti₅₀Ni₂₅Cu₂₅

Figure 4.1(a-c) corresponds to microstructure of fixed Cu content TiNiCu shape memory alloys where Ti and Ni content were varied. Figure 4.1(d-f) represents microstructure of fixed Ti content shape memory alloy where Ni and Cu content were varied to understand the effect of compositional variation on microstructure of prepared alloys. NiTi phases are quite common in TiNiCu alloys and with increasing Ni content, it can be seen that NiTi phases have grown which is evident from the dark region as depicted in Figure 4.1c, which were smaller in size for Ti₅₀Ni₄₀Cu₁₀ as seen in Figure 4.1a. It should be noted that bright secondary phases obtained in Ti₅₀Ni₄₀Cu₁₀ shape memory alloy are larger in size which appear to disperse in smaller

sized grains. Morakabati et al. (2010) reported Ti-rich TiNi and TiCu precipitates in $Ti_{50.4}Ni_{49.6-x}Cu_x$ prepared using vacuum induction melting. Zarnetta et al. (2011) also observed similar characteristics in their study of thin film characterization of TiNiCu shape memory alloys. He et al. (2009) supported that equal molar ratio of Ti to Ni+Cu is desirable to avoid formation of secondary phases. Such Cu rich secondary phases are not observed in fixed Ti content TiNiCu shape memory alloys as none of them can be observed in microstructure of $Ti_{50}Ni_{35}Cu_{15}$, $Ti_{50}Ni_{30}Cu_{20}$ and $Ti_{50}Ni_{25}Cu_{25}$ shape memory alloy as depicted in Figure 4.1(d-f). Instead they form complex $Ti_2(Ni, Cu)$ precipitates which exists in nominal quantity and exhibit higher lattice structural configuration which is evident from spherical and plate like structure as observed in Figure 4.1(d-f). It can be observed from Figure 4.1(d-f) that grain size decreases with increasing Cu content which therefore contributes in grain refinement. Formation of precipitates are unavoidable even though molar ratio of Ti to Ni+Cu is maintained at 1:1. As can be seen in Figure 4.1d, plate like precipitates are more abundant in $Ti_{50}Ni_{35}Cu_{15}$ and as Cu content is increasing, spherical precipitates are rising. Ishida et al. (2008) concluded in their study that such plate and spherical precipitates can be attributed to TiNi and TiCu phases respectively. As Cu content increases, formation of TiCu phase also increases and is evident from the density of spherical precipitates as indicated in Figure 4.1(d-f). Even though TiCu phase is present in $Ti_{50}Ni_{35}Cu_{15}$, average size is more and in $Ti_{50}Ni_{25}Cu_{25}$ alloy they are smaller in size and exist in a dispersed manner. Equiaxial nature of $Ti_{50}Ni_{35}Cu_{15}$ supports the reason behind higher hardness of this alloy which will be discussed in subsequent section. It should also be noted that intergranular precipitation also increases with increasing Cu content which is evident from Figure 4.1f.

4.2.2 Phase analysis of TiNiCu Shape Memory Alloys

Figure 4.2(a-c) represents X-ray diffraction patterns of vacuum melted TiNiCu alloys having fixed Cu-content. $Ti_{50}Ni_{40}Cu_{10}$ alloy shows Ti-rich phases due to abundance of Ti (represented by Ti^*). As Ti content was reduced and was at its minimum ($Ti_{40}Ni_{50}Cu_{10}$), reflection of NiTi phases were observed at multiple diffraction angle as evident in Figure 4.2c.

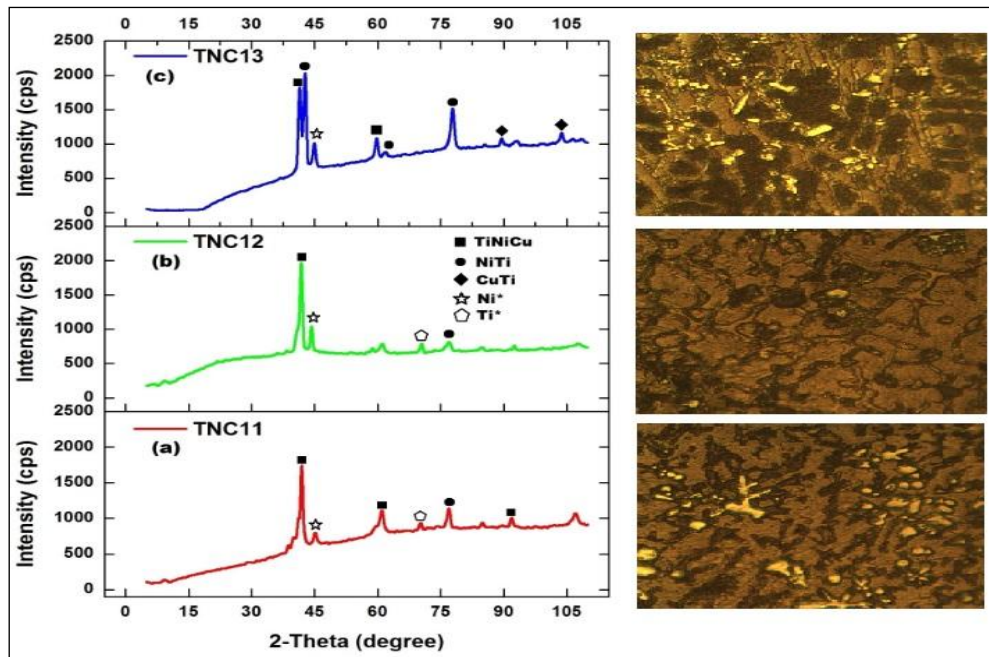


Figure 4.2. XRD plots of (a) TNC11 (b) TNC12 (c) TNC13

TiNiCu phases were observed throughout all the samples as expected due to elemental composition of the prepared alloys. It is interesting to note that number of peaks were reduced as Ni-content increased and the peaks exhibited sharper feature and intense diffraction intensity which also indicates higher volume fraction of Ni-rich phases are present. But that does not necessarily indicates suitability of the material as preferred crystallographic orientation could also be a result of crystallites having sufficiently long range order such that each crystallite diffracts strongly. However, functionality of shape memory alloy being critical to its martensitic structure, could face drastic change due to compositional variation. It is shown in next section that Ni-rich $Ti_{45}Ni_{45}Cu_{10}$ and $Ti_{40}Ni_{50}Cu_{10}$ exhibits amorphous behavior. Even though crystal structure is evident from the XRD plots of Figure 4.2(a-c), with increasing Ni content the alloy becomes more amorphous which is a result of disordered crystallites. This can be related to unequal molar ratio of Ti to Ni+Cu as discussed during analysis of microstructure of the prepared alloys. Due to unequal molar ratio, Ni-rich precipitates were formed due to decreasing Ti-content. Also, due to formation of secondary phases, a reduction in crystalline nature of the alloy occurred due to discontinuity in the alloy matrix and resulted in amorphous grain generation. This would be further established in subsequent section during calorimetric analysis. Presence of γ -CuTi

phases in Ni-rich alloy ($\text{Ti}_{40}\text{Ni}_{50}\text{Cu}_{10}$) confirms the higher hardness (527 Hv) of the alloy as established in the next section during microhardness analysis. Due to higher Ni-content, formation of NiTi phase was more probable and it is evident from the sudden growth at around 41° at $\text{Ti}_2(\text{Ni}, \text{Cu})$ peak region. Such Ti_2Ni (represented by Ti^*) precipitates found at around 68° diffraction angle are absent in Ni-rich alloy as can be seen in Fig. 4.2(a-c). It has been reported by Morakabati et al. (2010) that Cu containing precipitates decreases the plasticity of the alloy and hence contributes in higher yield strength compared to Ti_2Ni precipitates but also reduces the workability of the alloy. This could be the main reason for these alloys are not attracted enough. But, poor workability conditions can be resolved by advanced machining techniques (Manjaiah et al. 2014).

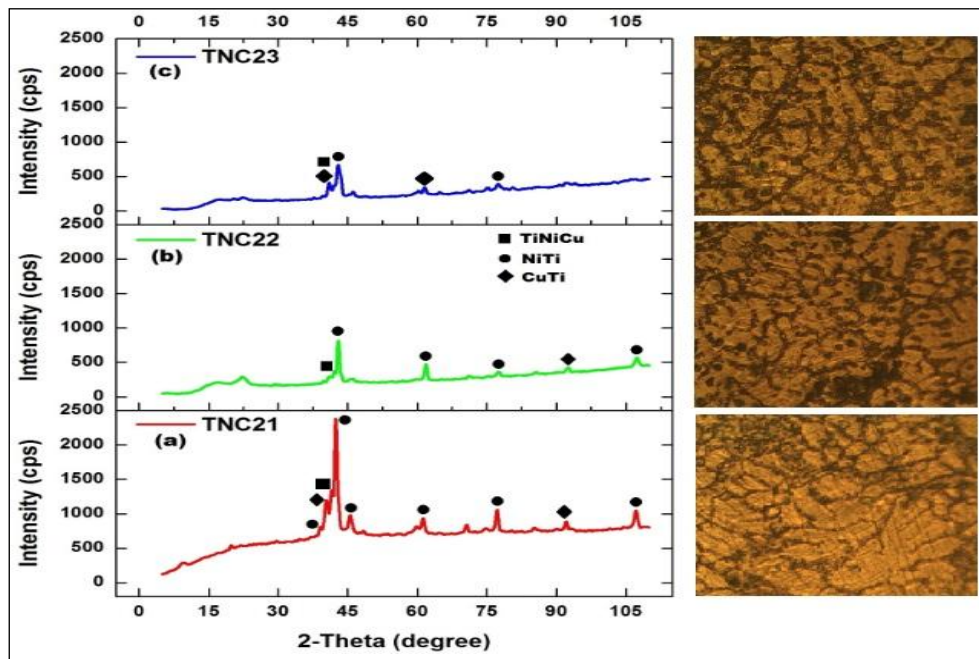


Figure 4.3. XRD plots of (a) TNC21 (b) TNC22 (c) TNC23

XRD plots of fixed Ti content TiNiCu shape memory alloys are represented in Figure 4.3(a-c). In case of these alloys, with increasing Cu content, reflection peaks have reduced as seen in Figure 4.3c. Lobel et al. (2008) investigated sputter deposited TiNiCu thin films with both Ti and Ni rich compositions. XRD peaks observed during their study shows that Ti_2Ni precipitates were observed in Ti-rich compositions due to abundance of Ti and presence of martensitic phases were more in Ni-rich

compositions. It was also observed that intensity of the Ni-rich precipitate composition is higher which describes the crystal regularity and is also observed in our study.

4.2.3 Calorimetric analysis of TiNiCu shape memory alloys

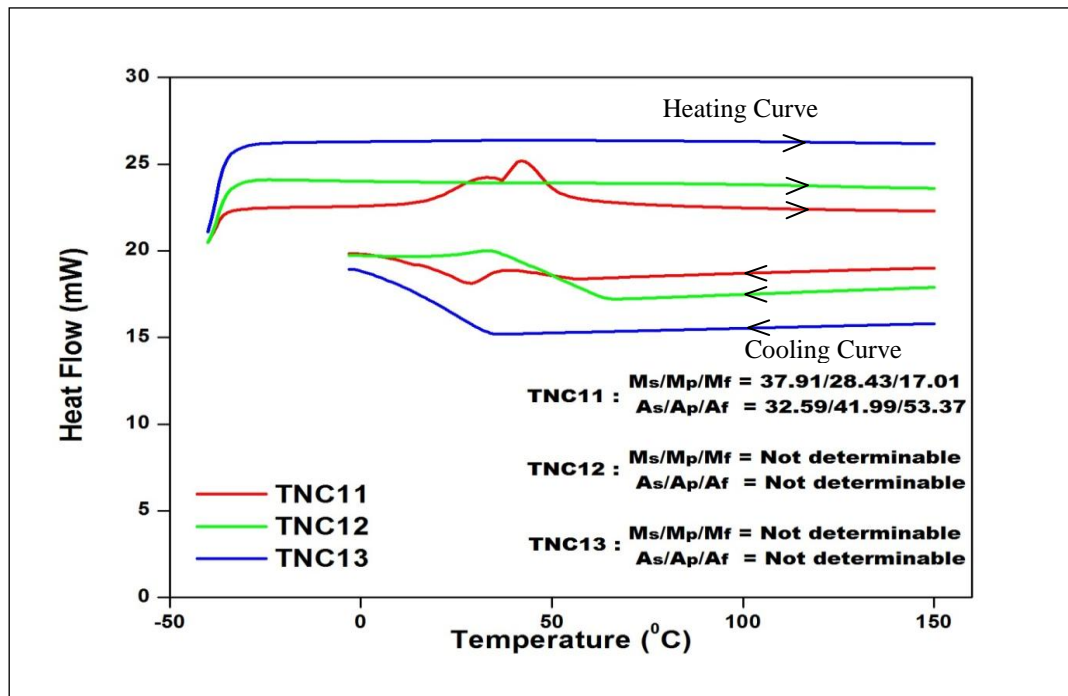


Figure 4.4. DSC plots of TNC11, TNC12 and TNC13

Differential scanning calorimetry facilitates in indentifying the transformation temperatures of a material. In this study phase transformation temperature of six different TiNiCu shape memory alloys (TNC11, TNC12, TNC13, TNC21, TNC22, TNC23) were investigated. In Figure 4.4, DSC plot of TNC11, TNC12 and TNC13 is represented. Plots on top represent heating curve and the ones on below represent cooling curve (indicated in Figure using arrows). Heating and cooling were carried out at 5°C/min at ambient atmosphere. During heating, the alloy begins transforming from martensite in room temperature to austenitic phase and while cooling it transforms back from austenitic to martensitic phase. It can be observed from Figure 4.4 that distinct peaks were observed for TNC11 whereas broad and weak peaks were observed for TNC12 and TNC13. This indicate that TNC12 and TNC13 have largely amorphous grain nature compared to TNC11. Transformation of constituent phase is a

gradual nature which requires adequate heat energy. But rupture in grain nature due to defects or distorted lattice results in incapability to transform. It is evident that only crystalline material would transform with distinct peaks. In our case TNC11 exhibited such characteristics and for TNC12 and TNC12, it behaved as such because of presence of secondary phases which distorted the crystal structure by accumulating intergranular space. The results obtained could be justified with the findings of Zheng et al. (2008). Kim et al. (2008) and He et al. (2009) during their study observed flat, featureless DSC curves for non-annealed TiNiCu melt spun ribbons. Only after crystallization sharp peaks were observed in TiNiCu melt spun ribbons. In case of fixed Ti content TiNiCu shape memory alloys i.e. TNC21, TNC22 and TNC23, sharp distinct peaks were observed as depicted in Figure 4.5. It can be observed that with increasing Ni content in fixed Cu content TNC11, TNC12 and TNC13 alloys, DSC peaks became increasingly blunt. Whereas for fixed Ti content TNC21, TNC22 and TNC23, with increasing Cu content, martensitic start temperature increased and austenitic start temperature decreases, thus reducing transformation hysteresis (A_f-M_s) which is a crucial criteria for actuator applications. When $Ti_{50}Ni_{35}Cu_{15}$ and $Ti_{50}Ni_{25}Cu_{25}$ shape memory alloys were compared, it was observed that with increasing Cu content, both martensitic start (M_s) and austenitic start (A_s) temperature increased although a drop was observed for $Ti_{50}Ni_{30}Cu_{20}$ shape memory alloy. Such increment and drop in transformation start temperature is in accordance with findings of Otsuka and Ren (2005) where M_s temperature reduces at 7.5 at% Cu content compared to 5 and 10 at% Cu content. It was established by Ishida et al. (2013) that transformation temperature is affected by Ni concentration and insensitivity to Ti content is likely due to the small lattice deformation of B2-B19 transformation and the small coherency strain of the precipitates. Also, sensitivity of Cu content to martensitic transformation can be further justified by the findings of Sheliyakov et al. (2013) where they established that most significant changes in local crystal structure of $Ti_{50}Ni_{25}Cu_{25}$ alloy under martensitic transformation occur in Ni-Cu sublattice. In addition to that, transformation hysteresis ($\Delta T=A_s-M_f$) which concludes the net temperature difference required for one complete transformation cycle reduces with increasing Cu content. Transformation hysteresis of $Ti_{50}Ni_{35}Cu_{15}$, $Ti_{50}Ni_{30}Cu_{20}$ and $Ti_{50}Ni_{25}Cu_{25}$ shape memory alloys are 11.82⁰C, 7.53⁰C, 6.61⁰C and 15.58⁰C for

Ti₅₀Ni₄₀Cu₁₀ shape memory alloy. Such reduction in transformation hysteresis with increasing Cu content is in accordance with previous findings (Goryczka et al., 2006). Tomozawa et al. (2010) suggested that in order to increase actuation speed of a microactuator it is necessary to reduce the transformation temperature hysteresis ($\Delta T = A_s - M_f$) and increase the transformation temperature. In their study they concluded to use TiNiCu microactuator heat treated at 973K which showed highest M_s temperature. In this study, Ti₅₀Ni₂₅Cu₂₅ shape memory alloy qualify for being an ideal material for actuator applications as it has highest M_s temperature ($\sim 37^\circ\text{C}$) and narrow transformation hysteresis ($\sim 6^\circ\text{C}$).

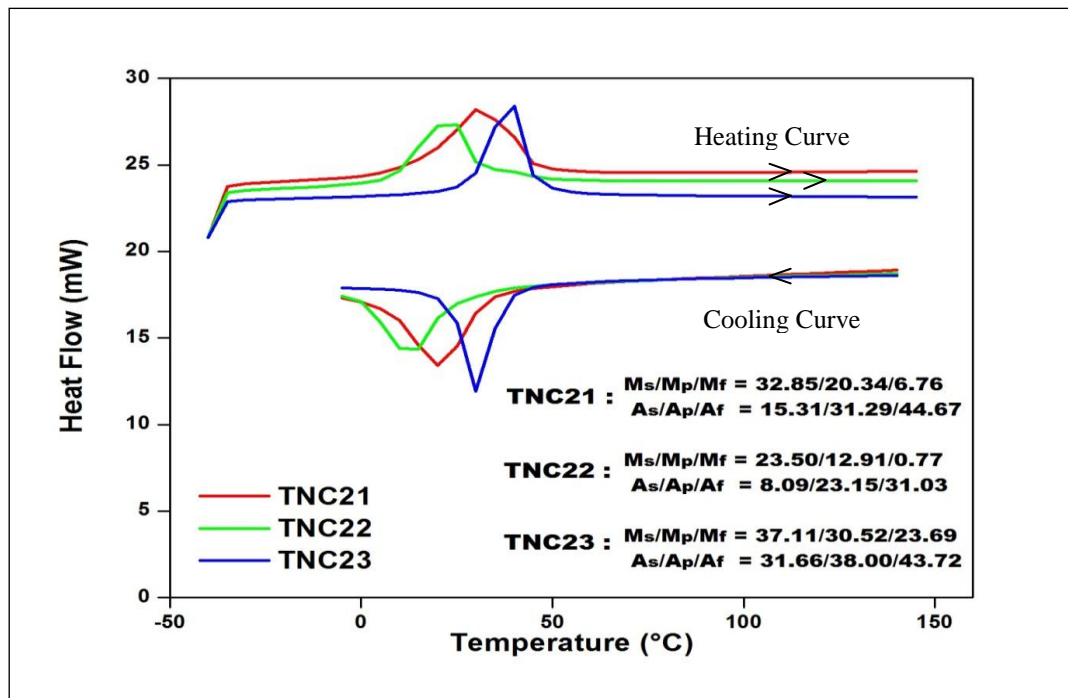


Figure 4.5. DSC plots of TNC21, TNC22 and TNC23

4.2.4 Microhardness analysis of TiNiCu shape memory alloys

Microhardness of TiNiCu shape memory alloys are recorded and shown in Figure 4.6. It was observed that for alloys having fixed Cu content (TNC11, TNC12 and TNC13), hardness gradually increases with increasing Ni content. In the previous section it was confirmed that presence of secondary phases (γ -CuTi, NiTi) is prominent in TNC13 which resulted in higher hardness of this alloy. El-Bagoury et al. (2013) confirmed that

due to presence of Ni-rich Ni_3Ti precipitate in Ni-Fe-Ga-Ti alloy, hardness increases which is also observed in our case. Similar observation was reported by Zarnetta et al. (2011) where increasing Ni % lead to improved young's modulus and higher hardness. On the other hand, for fixed Ti content shape memory alloys (TNC21, TNC22 and TNC23) a similar behavior was observed. Although it is arguable that hardness should decrease with decreasing Ni content (and subsequent increase in Cu content) for these alloys, study of Nam et al. (1990) showed that higher hardness value of TNC23 compared to TNC21 can be attributed to formation of brittle intermetallics that forms from the reaction of Ti and Cu during slow solidification process of vacuum arc melting method. They also confirmed that this is true when Cu content is more than 10 at% in TiNiCu alloys. In a recent study by Chen et al. (2018), it was confirmed that Ti depletes from TiNiCu matrix and affect overall composition. Therefore, with increasing Cu content, formation of TiCu precipitates is more likely and such precipitates leads to hardening of matrix of the material which is evident in this case.

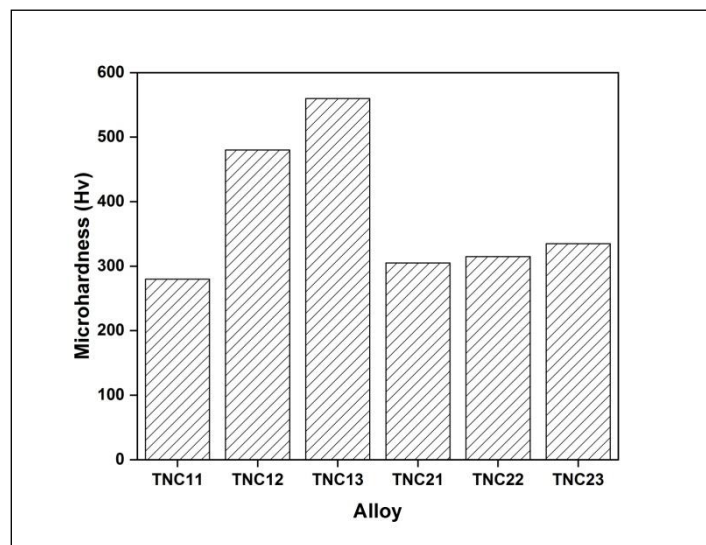


Figure 4.6. As cast microhardness of prepared TiNiCu alloys

4.3 WEDM EXPERIMENTAL RESULTS

Machining of TiNiCu shape memory alloys were performed using wire electro discharge machining. Design of experiments(DOE) was carried out using Taguchi's orthogonal technique. By this DOE technique, for four parameters varied at four levels, 16 experimental trials (L16) was found to well suit the need of the current

study. Table 4.1 indicates Taguchi's L16 orthogonal experimental plan. Experimental values of material removal rate, surface roughness, kerf width and recast layer thickness are tabulated in Table 4.2-4.5 respectively.

Table 4.1. Taguchi's L16 orthogonal experimental plan

| Experimental Run | Pulse-on time (µs) | Pulse-off time (µs) | Servo voltage (Volts) | Wire feed rate (m/min) |
|-------------------------|---------------------------|----------------------------|------------------------------|-------------------------------|
| 1 | 100 | 20 | 15 | 4 |
| 2 | 100 | 30 | 30 | 6 |
| 3 | 100 | 40 | 45 | 8 |
| 4 | 100 | 50 | 60 | 10 |
| 5 | 110 | 20 | 45 | 6 |
| 6 | 110 | 30 | 60 | 4 |
| 7 | 110 | 40 | 15 | 10 |
| 8 | 110 | 50 | 30 | 8 |
| 9 | 120 | 20 | 60 | 8 |
| 10 | 120 | 30 | 45 | 10 |
| 11 | 120 | 40 | 30 | 4 |
| 12 | 120 | 50 | 15 | 6 |
| 13 | 130 | 20 | 30 | 10 |
| 14 | 130 | 30 | 15 | 8 |
| 15 | 130 | 40 | 60 | 6 |
| 16 | 130 | 50 | 45 | 4 |

Table 4.2. Material removal rate (mm³/min) for TiNiCu shape memory alloys

| Experimental Run | Ti ₅₀ Ni ₄₀ Cu ₁₀ | Ti ₄₅ Ni ₄₅ Cu ₁₀ | Ti ₄₀ Ni ₅₀ Cu ₁₀ | Ti ₅₀ Ni ₃₅ Cu ₁₅ | Ti ₅₀ Ni ₃₀ Cu ₂₀ | Ti ₅₀ Ni ₂₅ Cu ₂₅ |
|------------------|--|--|--|--|--|--|
| 1 | 0.53 | 0.31 | 0.33 | 0.45 | 0.28 | 0.44 |
| 2 | 0.4912 | 0.61 | 0.72 | 0.68 | 0.35 | 0.42 |
| 3 | 0.52 | 0.54 | 0.47 | 0.56 | 0.64 | 0.46 |
| 4 | 0.38 | 0.18 | 0.17 | 0.25 | 0.26 | 0.32 |
| 5 | 3.07 | 2.95 | 2.86 | 2.69 | 3.53 | 3.55 |
| 6 | 1.35 | 1.29 | 1.26 | 1.51 | 1.55 | 1.61 |
| 7 | 3.18 | 3.07 | 2.89 | 3.07 | 2.97 | 3.15 |
| 8 | 1.91 | 1.69 | 1.68 | 1.89 | 2.07 | 2.13 |
| 9 | 4.59 | 3.84 | 3.88 | 4.38 | 4.53 | 4.55 |
| 10 | 6.29 | 5.18 | 4.53 | 5.37 | 5.64 | 6.09 |
| 11 | 5.94 | 5.11 | 5.21 | 5.51 | 5.32 | 5.64 |
| 12 | 5.61 | 4.46 | 3.65 | 5.23 | 3.47 | 5.06 |
| 13 | 6.94 | 4.16 | 5.09 | 5.11 | 3.12 | 4.89 |
| 14 | 4.69 | 3.74 | 4.24 | 4.21 | 3.82 | 4.19 |
| 15 | 4.42 | 4.09 | 3.86 | 4.45 | 3.47 | 4.45 |
| 16 | 5.56 | 5.13 | 4.74 | 5.08 | 5.75 | 6.09 |

Table 4.3. Surface roughness (µm) for TiNiCu shape memory alloys

| Experimental Run | Ti ₅₀ Ni ₄₀ Cu ₁₀ | Ti ₄₅ Ni ₄₅ Cu ₁₀ | Ti ₄₀ Ni ₅₀ Cu ₁₀ | Ti ₅₀ Ni ₃₅ Cu ₁₅ | Ti ₅₀ Ni ₃₀ Cu ₂₀ | Ti ₅₀ Ni ₂₅ Cu ₂₅ |
|------------------|--|--|--|--|--|--|
| 1 | 1.85 | 1.63 | 1.53 | 1.54 | 1.61 | 1.82 |
| 2 | 1.31 | 1.34 | 1.31 | 1.77 | 1.86 | 1.57 |
| 3 | 1.06 | 1.48 | 1.46 | 1.91 | 2.01 | 1.92 |
| 4 | 2.32 | 2.26 | 2.13 | 2.12 | 2.78 | 2.23 |
| 5 | 3.05 | 3.19 | 2.71 | 2.83 | 3.33 | 2.99 |
| 6 | 2.59 | 2.27 | 2.89 | 2.16 | 1.86 | 1.96 |
| 7 | 3.48 | 3.23 | 2.72 | 3.21 | 3.33 | 3.35 |
| 8 | 3.09 | 3.36 | 2.65 | 3.05 | 3.38 | 3.03 |
| 9 | 3.61 | 2.99 | 3.02 | 3.45 | 3.66 | 3.39 |
| 10 | 3.62 | 3.04 | 2.99 | 3.81 | 3.66 | 3.69 |
| 11 | 3.89 | 3.48 | 3.14 | 3.88 | 3.79 | 4.02 |
| 12 | 3.99 | 3.16 | 3.34 | 3.83 | 3.69 | 4.09 |
| 13 | 3.97 | 3.19 | 3.28 | 3.77 | 3.57 | 3.84 |
| 14 | 3.54 | 3.24 | 3.08 | 3.61 | 3.61 | 3.73 |
| 15 | 3.96 | 3.51 | 3.15 | 4.01 | 3.59 | 3.99 |
| 16 | 4.19 | 3.32 | 3.19 | 4.06 | 4.23 | 4.11 |

Table 4.4. Kerf width (μm) for TiNiCu shape memory alloys

| Experimental Run | Ti ₅₀ Ni ₄₀ Cu ₁₀ | Ti ₄₅ Ni ₄₅ Cu ₁₀ | Ti ₄₀ Ni ₅₀ Cu ₁₀ | Ti ₅₀ Ni ₃₅ Cu ₁₅ | Ti ₅₀ Ni ₃₀ Cu ₂₀ | Ti ₅₀ Ni ₂₅ Cu ₂₅ |
|------------------|--|--|--|--|--|--|
| 1 | 300 | 300 | 303 | 292 | 290 | 293 |
| 2 | 297 | 300 | 297 | 295 | 295 | 295 |
| 3 | 305 | 303 | 301 | 293 | 301 | 295 |
| 4 | 351 | 343 | 315 | 320 | 317 | 322 |
| 5 | 319 | 317 | 312 | 310 | 303 | 313 |
| 6 | 333 | 333 | 332 | 323 | 326 | 330 |
| 7 | 311 | 310 | 307 | 295 | 303 | 301 |
| 8 | 315 | 323 | 316 | 306 | 315 | 313 |
| 9 | 325 | 336 | 331 | 330 | 320 | 325 |
| 10 | 342 | 329 | 323 | 308 | 315 | 313 |
| 11 | 319 | 329 | 322 | 325 | 320 | 315 |
| 12 | 324 | 332 | 320 | 323 | 312 | 315 |
| 13 | 330 | 284 | 302 | 320 | 313 | 318 |
| 14 | 321 | 280 | 333 | 310 | 292 | 308 |
| 15 | 357 | 353 | 357 | 340 | 330 | 345 |
| 16 | 348 | 342 | 347 | 333 | 335 | 332 |

Table 4.5. Recast layer thickness (μm) for TiNiCu shape memory alloys

| Experimental Run | Ti ₅₀ Ni ₄₀ Cu ₁₀ | Ti ₄₅ Ni ₄₅ Cu ₁₀ | Ti ₄₀ Ni ₅₀ Cu ₁₀ | Ti ₅₀ Ni ₃₅ Cu ₁₅ | Ti ₅₀ Ni ₃₀ Cu ₂₀ | Ti ₅₀ Ni ₂₅ Cu ₂₅ |
|------------------|--|--|--|--|--|--|
| 1 | 2.87 | 4.16 | 5.52 | 3.64 | 4.71 | 9.17 |
| 2 | 4.33 | 7.81 | 8.05 | 4.16 | 4.41 | 10.64 |
| 3 | 6.41 | 6.77 | 9.02 | 8.79 | 6.07 | 17.49 |
| 4 | 15.88 | 18.81 | 14.24 | 7.59 | 14.18 | 35.22 |
| 5 | 9.56 | 9.72 | 12.08 | 11.67 | 11.61 | 9.93 |
| 6 | 18.02 | 17.18 | 10.77 | 9.25 | 8.25 | 28.93 |
| 7 | 8.53 | 15.88 | 18.96 | 14.88 | 14.03 | 15.84 |
| 8 | 6.89 | 14.57 | 15.28 | 11.95 | 9.72 | 16.57 |
| 9 | 9.36 | 12.53 | 13.49 | 19.34 | 19.41 | 16.04 |
| 10 | 11.29 | 18.88 | 14.36 | 20.48 | 21.02 | 19.82 |
| 11 | 11.12 | 15.44 | 17.88 | 16.78 | 20.24 | 23.72 |
| 12 | 18.71 | 14.61 | 16.68 | 20.02 | 18.22 | 20.04 |
| 13 | 12.96 | 10.86 | 10.24 | 23.61 | 32.29 | 20.92 |
| 14 | 12.94 | 11.24 | 11.53 | 21.52 | 19.48 | 22.81 |
| 15 | 13.81 | 15.44 | 15.92 | 21.49 | 22.17 | 21.08 |
| 16 | 14.33 | 15.04 | 16.26 | 23.61 | 22.97 | 23.37 |

4.4 FACTOR ANALYSIS

In this section Analysis of Variance (ANOVA) and Taguchi analysis were carried out to find out the effect of individual parameters on WEDM responses. Taguchi analysis revealed the delta value from mean value of responses for chosen parameter levels through which most significant parameters were identified, whereas ANOVA results also indicate similar results. However, ANOVA can identify the most significant parameter with consideration of a 95% confidence level, Taguchi analysis helps in determining the rank of effect of each parameter for a given WEDM response. Upcoming sections help in determining most significant parameters and rank for material removal rate, surface roughness, kerf width and recast layer thickness.

4.4.1 Analysis of Variance

Analysis of variance for the WEDM responses has been used to identify the influential parameters and percentage contribution of the chosen process parameters that influences selected WEDM responses. ANOVA results for the chosen responses are depicted in Tables presented in subsequent sections. For ease of understanding, we have chosen one alloy from each set and performed ANOVA analysis for the chosen responses for that particular alloy instead of checking the results for all the alloys. As similar characteristics was observed for the machining of alloys, based on the previous results, $Ti_{50}Ni_{40}Cu_{10}$ (TNC11) and $Ti_{50}Ni_{25}Cu_{25}$ (TNC23) exhibited suitable behavior and were chosen for ANOVA analysis. The results for MRR, SR, KW and RLT are given below.

4.4.1.1 Material Removal Rate

From the P-test values in Table 4.6, it is evident that for both the alloys, pulse-on time (T_{on}) and servo voltage (SV) are influential parameters as their values didn't exceed 0.05. However, for TNC23, it can be seen that SV is not as influential compared to TNC11. This is due to varying physical property of these alloys.

Table 4.6. ANOVA results for MRR

| TNC11 | | | | | |
|------------------------|-----------|---------------|---------------|----------------|----------------|
| Source | DF | Adj SS | Adj MS | F-value | P-value |
| T_{on} | 3 | 74.01 | 24.67 | 330.25 | 0.012 |
| T_{off} | 3 | 0.70 | 0.23 | 3.14 | 0.186 |
| WF | 3 | 3.40 | 1.13 | 15.19 | 0.226 |
| SV | 3 | 3.54 | 1.18 | 15.81 | 0.024 |
| TNC23 | | | | | |
| Source | DF | Adj SS | Adj MS | F-value | P-value |
| T_{on} | 3 | 62.18 | 20.73 | 93.75 | 0.002 |
| T_{off} | 3 | 0.31 | 0.10 | 0.47 | 0.726 |
| WF | 3 | 1.38 | 0.46 | 2.07 | 0.282 |
| SV | 3 | 3.55 | 0.18 | 5.35 | 0.101 |

4.4.1.2 Surface Roughness

It is evident from the ANOVA results shown in Table 4.7 that in case of surface roughness, pulse-on time (T_{on}) plays a crucial role as it has highest significance which is clear from its low P-test values for both the chosen alloys. Trend of these results will be further established in upcoming sections

Table 4.7. ANOVA results for SR

| TNC11 | | | | | |
|------------------------|-----------|---------------|---------------|----------------|----------------|
| Source | DF | Adj SS | Adj MS | F-value | P-value |
| T_{on} | 3 | 13.11 | 4.37 | 63.45 | 0.003 |
| T_{off} | 3 | 0.82 | 0.27 | 3.95 | 0.145 |
| WF | 3 | 0.55 | 0.18 | 2.65 | 0.223 |
| SV | 3 | 0.12 | 0.04 | 0.56 | 0.676 |
| TNC23 | | | | | |
| Source | DF | Adj SS | Adj MS | F-value | P-value |
| T_{on} | 3 | 10.83 | 3.61 | 63.42 | 0.003 |
| T_{off} | 3 | 1.04 | 0.35 | 6.09 | 0.086 |
| WF | 3 | 0.23 | 0.08 | 1.36 | 0.404 |
| SV | 3 | 0.28 | 0.09 | 1.66 | 0.344 |

4.4.1.3 Kerf Width

Findings of Table 4.8 confirms that pulse-on time (T_{on}) and servo voltage (SV) are influential parameter that control kerf width and can also be proved from the P-test values.

Table 4.8. ANOVA results for KW

| TNC11 | | | | | |
|-----------------------------|-----------|---------------|---------------|----------------|----------------|
| Source | DF | Adj SS | Adj MS | F-value | P-value |
| T_{on} | 3 | 1481.7 | 493.90 | 8.25 | 0.058 |
| T_{off} | 3 | 557.7 | 185.90 | 3.10 | 0.189 |
| WF | 3 | 579.7 | 193.23 | 3.23 | 0.181 |
| SV | 3 | 2001.7 | 667.23 | 11.14 | 0.039 |
| TNC23 | | | | | |
| Source | DF | Adj SS | Adj MS | F-value | P-value |
| T_{on} | 3 | 1233.69 | 411.23 | 81.23 | 0.002 |
| T_{off} | 3 | 201.19 | 67.06 | 13.25 | 0.081 |
| WF | 3 | 137.19 | 45.73 | 9.03 | 0.152 |
| SV | 3 | 1522.69 | 507.56 | 100.26 | 0.002 |

4.4.1.4 Recast Layer Thickness

In case of recast layer thickness (as seen from Table 4.9), no significant parameters were found in terms of P-test values. But as per previous argument, lower P-test values of pulse-off time (T_{off}) and servo voltage (SV) for both the alloys converge to the fact that even though statistical significance cannot be observed with 95% confidence interval from the machining data, their significance is higher compared to pulse-on time (T_{on}) and wire feed rate (WF).

Table 4.9. ANOVA results for RLT

| TNC11 | | | | | |
|-----------------------------|-----------|---------------|---------------|----------------|----------------|
| Source | DF | Adj SS | Adj MS | F-value | P-value |
| T_{on} | 3 | 88.59 | 29.53 | 1.12 | 0.463 |
| T_{off} | 3 | 62.20 | 20.73 | 0.79 | 0.575 |
| WF | 3 | 25.86 | 8.62 | 0.33 | 0.808 |
| SV | 3 | 63.23 | 21.08 | 0.80 | 0.570 |

| TNC23 | | | | | |
|------------------|----|--------|--------|---------|---------|
| Source | DF | Adj SS | Adj MS | F-value | P-value |
| T _{on} | 3 | 45.47 | 15.16 | 0.33 | 0.807 |
| T _{off} | 3 | 198.77 | 66.26 | 1.44 | 0.385 |
| WF | 3 | 133.41 | 44.47 | 0.97 | 0.510 |
| SV | 3 | 184.19 | 61.40 | 1.34 | 0.409 |

4.4.2 Taguchi Analysis - Material Removal Rate

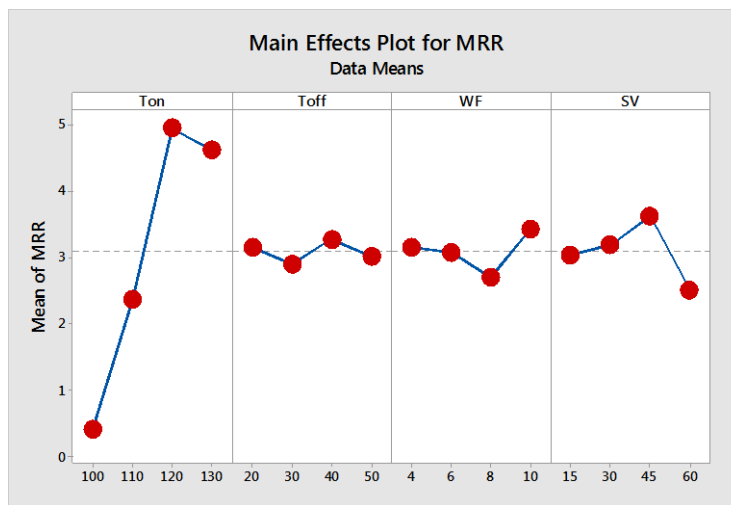


Figure 4.7. Effects plot for Material Removal Rate

Table 4.10. Response table for means of MRR

| Level | T _{on} | T _{off} | WF | SV |
|-------|-----------------|------------------|------|------|
| 1 | 0.43 | 3.17 | 3.16 | 3.04 |
| 2 | 2.37 | 2.91 | 3.09 | 3.19 |
| 3 | 4.96 | 3.29 | 2.72 | 3.64 |
| 4 | 4.64 | 3.03 | 3.43 | 2.53 |
| Delta | 4.53 | 0.38 | 0.71 | 1.11 |
| Rank | 1 | 4 | 3 | 2 |

4.4.2.1 Effect of Pulse on Time

In wire electro discharge machining, effect of pulse on time on MRR is quite consistent which can be justified from Figure 4.7. With an increase in pulse on time duration, MRR gradually increases upto 120 μ s for all the alloys and then attains a constant behavior upto 130 μ s as can be seen from the effects plot. The results are

similar with the findings of other researchers working with WEDM productivity and surface integrity (Mahapatra and Patnaik, 2007; Manjaiah et al. 2014) where they have studied its effect upto three levels of pulse on time. This characteristic drop in MRR at the fourth level (130 μ s) is due to increased vibration of wire electrode which affects the net spark gap and eventually lowers the MRR. Formation of gas bubble due to spark formation, hydraulic forces due to dielectric flushing and impact force due to spark impingement are some of the reasons for transverse vibration of wire electrode (Andhare and Jithin, 2015). At higher wire vibration, the wire electrode becomes incapable of maintaining uniform spark gap at given period of time causing multiple spark generation sites and therefore discharge sparks become uneven which lead to lesser melting of material resulting in lower material removal rate (Guo et al. 1997). From response table for means of MRR as tabulated in Table 4.10, higher delta value also indicates higher influence of pulse on time on MRR.

4.4.2.2 Effect of Pulse off Time

During wire electro discharge machining, pulse off time signifies the duration for which spark discharge does not take place. It can be observed from Figure 4.7 that MRR value rises and drops periodically with increasing pulse off duration. Similar trend in results have been reported by Bobbili et al. (2013) which can be explained by the fact that with increasing pulse off time, the time available for spark discharge per cycle is reduced that lowers the MRR, which is evident from the effects plot as depicted in Figure 4.7. For all the alloys, MRR seems to be optimum during shorter pulse off duration of 20 μ s which is due to increased number of discharges in a single spark cycle of 120-150 μ s. These results match with the findings of Liao et al. (1997) and Ramakrishnan and Karunamoorthy (2008).

4.4.2.3 Effect of Servo Voltage

Servo voltage applied as one of the major input parameters in wire electro discharge machining, helps in maintaining an uniform spark gap between the workpiece and the wire electrode during machining process. Lower spark gap results in more intense spark energy per unit time and hence high MRR. As this can be seen from Figure 4.7,

with increasing servo voltage, material removal rate eventually decreases. But it can also be noted that there is a small increment of MRR between 30V and 45V which has happened due to higher discharge energy per spark which is also observed by Mathew et al. (2014) but after 45V upto 60V, MRR reduces drastically due to lower discharge spark energy caused due to higher spark gap. The net drop in material removal rate for TNC11, TNC12 and TNC13 are 23%, 18% and 17% respectively. For TNC21, TNC22 and TNC23, these variations follow similar trend which verifies that servo voltage is such a machining parameter that is fairly independent of material nature and the trend of overall pattern is similar in nature and match with the findings of Tarnag et al. (1995).

4.4.2.4 Effect of Wire Feed

Effect of wire feed on output responses during wire electro discharge machining seems to have more intensity at higher wire feed rate for all the alloys investigated. Even though material removal rate and surface roughness seems to be in proportion, as observed in Figure 4.7, there is a characteristic drop in their behavior at wire feed rate of 8 m/min as compared to 4 m/min which accounts for around 12%, 17% and 10% drop in material removal rate for TNC11, TNC12 and TNC13 shape memory alloy. Similar trend in results was also observed for TNC21, TNC22 and TNC23. This steady decrement in material removal rate for wire feed rate upto 8 m/min is observed due to rise in uneven sparking at the machining zone caused due to higher wire feed rate and hence lower material removal rate, thereafter a sudden rise is observed.

However, the net increment in MRR for TNC11, TNC12 and TNC13 at wire feed rate of 10 m/min considering the entire range of input parameter are 25%, 6% and 10% respectively. This increase in material removal rate is caused due to better flushing of the molten material from the machining zone by the fast moving wire electrode which previously tend to accumulate due to lower wire feed rate. This happens due to increased wire tension at higher wire feed rate as confirmed by Goswami and Kumar (2014). Such increase in MRR was also observed for TNC21, TNC22 and TNC23 which confirms that higher wire feed rate has analogous effect on all the selected alloys.

4.4.3 Taguchi Analysis - Surface Roughness

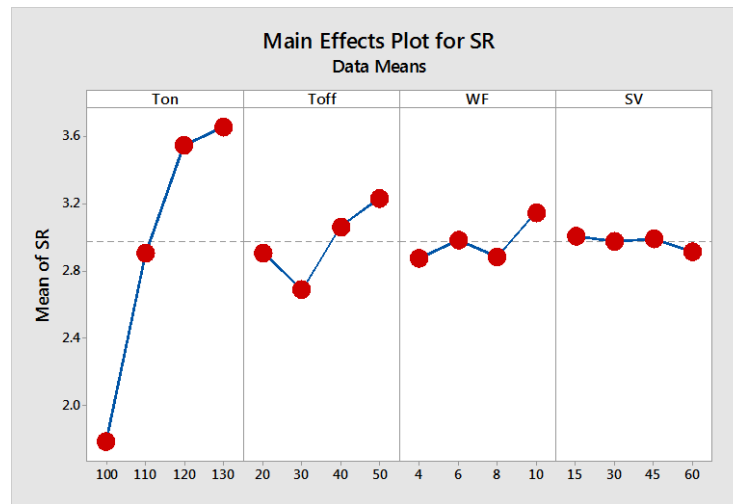


Figure 4.8. Effects plot for Surface Roughness

Table 4.11. Response table for means of SR

| Level | T _{on} | T _{off} | WF | SV |
|-------|-----------------|------------------|------|------|
| 1 | 1.78 | 2.91 | 2.88 | 3.01 |
| 2 | 2.91 | 2.69 | 2.98 | 2.98 |
| 3 | 3.55 | 3.07 | 2.89 | 2.99 |
| 4 | 3.66 | 3.23 | 3.15 | 2.91 |
| Delta | 1.87 | 0.55 | 0.27 | 0.09 |
| Rank | 1 | 2 | 3 | 4 |

4.4.3.1 Effect of Pulse on Time

The trend of surface roughness in all these alloys is similar to the findings of other researchers who emphasized these output responses considering same parameters at hand (Manjaiah et al. 2014) but only at three levels. They also reported a rise in surface roughness with increasing pulse on time caused due to increase in discharge energy of each spark creating larger craters which contributes to increased roughness of machined surfaces. According to the findings of Hsieh et al. (2009), under similar machining conditions for two different material one exhibiting higher material removal rate is due to lower thermal conductivity of the material which makes it easy to melt off the material from the surface compared to its counterparts which adds to surface roughness which is also observed in the current investigation. The net increment in surface roughness for TNC11, TNC12 and TNC13 starting from 110 μ s to 130 μ s are 28%, 9% and 15% respectively. In case of TNC21, TNC22 and TNC23,

similar trend in results have been observed for pulse on duration which finally suggests that surface roughness increases with increasing pulse on duration irrespective of material property but minor difference in response can be observed because materials having dissimilar property will respond differently. Higher influence of pulse on time on SR as compared to other WEDM parameters can also be justified from higher delta value as indicated in Table 4.11.

4.4.3.2 Effect of Pulse off Time

Effect of pulse off time on the selected alloys can be seen in Figure 4.8. With an increase in discharge less period i.e. pulse off time, surface roughness increases for both Cu-fixed and Ti-fixed alloys. However, the surface roughness is least affected by pulse off time for upto 40 μ s. Although, beyond 40 μ s, surface starts to exhibit an increment in roughness which is evident from Figure 4.8 that can be explained by the contribution of longer dielectric quenching time that eventually re-solidifies more molten material at its surface. The net change in surface roughness due to variation in pulse off time for alloys TNC11, TNC12 and TNC13 are 8.9%, 7.5% and 7.3% respectively which proves that pulse off time as a process parameter have least effect on surface quality of the machined samples. It should also be noted that drop in surface roughness vales at 30 μ s pulse off duration is similar for all the selected alloys. However, the variation in behavior of the surface roughness of the chosen alloys is due to the difference in their thermal conductivity and melting temperature which is justified by considering the findings of the researchers (Hsieh et al. 2009, Ramachandran et al. 2013, 2015).

4.4.3.3 Effect of Servo Voltage

The variation in surface quality of wire electro discharge machined samples with respect to varying servo voltage is almost consistent in nature for both the alloy sets. It can be seen from the effects plot that along the entire range of servo voltage applied, surface roughness of the machined samples do not exhibit any major fluctuations as evident from Figure 4.8. At low servo voltage, spark gap is minimum which results in intense spark discharge due to which machined surface suffers heavy

degradation due to formation of larger craters which generally decreases with increasing servo voltage. As discussed earlier and inferred by the researchers (Manjaiah et al., 2014, Goswami and Kumar, 2014), the results obtained in the current investigation is in accordance with the published data.

4.4.3.4 Effect of Wire Feed

A few researchers have investigated the effect of Wire EDM parameters on output responses based on three levels of input parameters (Bobbili et al., 2013; Ramakrishnan and Karunamoorthy, 2008; Mathew et al., 2014; Goswami and Kumar, 2014; Manjaiah et al., 2015). Therefore, a detailed study regarding the further implications of wire feed rate is inevitable and it is attempted in the current investigation. The net change in surface roughness for TNC11, TNC12 and TNC13 are 6.7%, 9.5% and 3.5% respectively. This increase in surface roughness beyond 8 m/min is due to increased wire vibration caused due to higher wire feed rate that leads to uneven sparking and crater formation that eventually leads to higher surface roughness and have yielded similar results for TNC21, TNC22 and TNC23.

4.4.4 Taguchi Analysis - Kerf Width

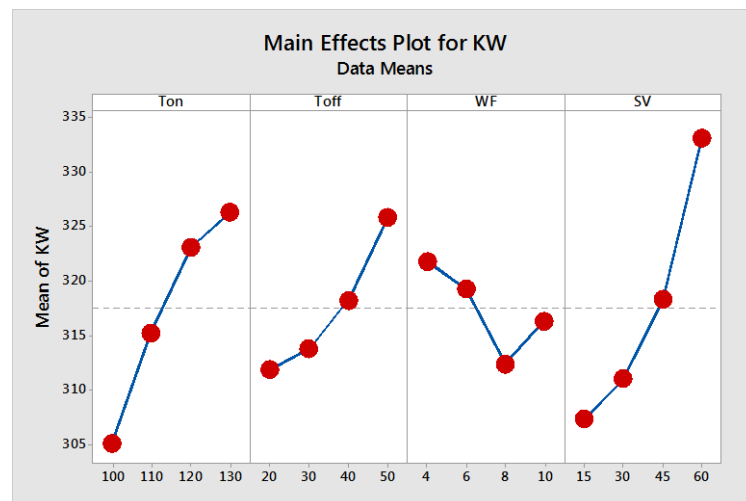


Figure 4.9. Effects plot for Kerf Width

Table 4.12. Response table for means of KW

| Level | T _{on} | T _{off} | WF | SV |
|-------|-----------------|------------------|-------|-------|
| 1 | 305.1 | 311.9 | 321.8 | 307.3 |

| | | | | |
|-------|-------|-------|-------|----------|
| 2 | 315.3 | 313.8 | 319.2 | 311.0 |
| 3 | 323.0 | 318.2 | 312.4 | 318.3 |
| 4 | 326.3 | 325.8 | 316.3 | 333.1 |
| Delta | 21.1 | 13.9 | 9.4 | 25.8 |
| Rank | 2 | 3 | 4 | 1 |

4.4.4.1 Effect of Pulse on Time

It can be seen from Figure 4.9 that for all the selected TiNiCu alloys kerf width increases with increasing pulse on duration. Similar to the case of MRR, with increasing pulse on duration, more amount of material was melted within stipulated time around the wire electrode periphery and hence resulted in wider kerf length. It is evident from the effects plots that kerf width widens abruptly at higher pulse on duration. Figure 4.10(a-d) represents kerf boundary zone at varying pulse on duration and clearly establishes the effect of increasing pulse on duration on kerf width due to increasing explosive nature of the molten material caused due to high energy electrical discharges. Tosun et al. (2004) also investigated variation in kerf based on Taguchi method and reported similar characteristics.

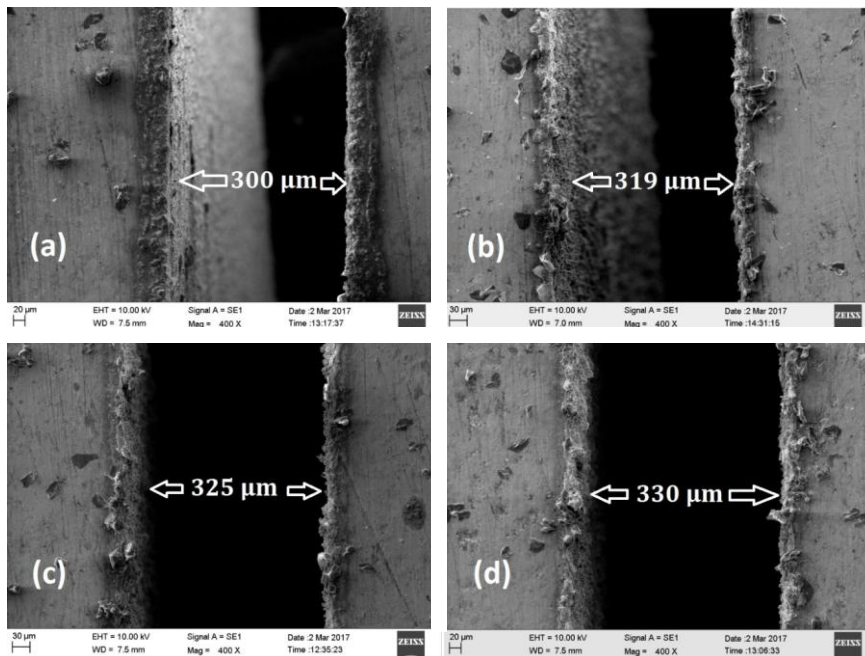


Figure 4.10 Kerf zone at T_{on} (a) 100 μs (b) 110 μs (c) 120 μs (d) 130 μs

4.4.4.2 Effect of Pulse off Time

Kerf width increases with the extension of pulse off duration as noted in Figure 4.9, which signifies that due to extended duration of discharge-less period, more molten metal was flushed out and the trend of results is same as established by Ikram et al. (2013). Widening of kerf at higher pulse off duration happens due to the fact that at higher discharge less period, more amount of material was able to flush out of the kerf zone which eventually contributed in wider kerf.

4.4.4.3 Effect of Servo Voltage

Effect of servo voltage in Fig 4.9 clearly indicates that lower value of servo voltage yields minimum kerf width. Beyond 30 V, kerf width widens abruptly which is due to large ionization of dielectric fluid present between the working gap which is in accordance with the findings of Di et al. (2009). Collectively it is evident that effect of servo voltage is influential like it was in case of pulse on duration and can be observed from the effects plot as shown in Figure 4.9. Also, larger amount of re-solidified molten debris at kerf boundary can be observed at higher value of servo voltage which establish the effect of larger ionization of dielectric fluid resulting in more molten material as can be seen in Figure 4.11. From the findings it is evident that lower value of servo voltage should implemented to maintain narrow kerf width which directly influences profile cutting accuracy. From Table 4.12 it is also evident that servo voltage have higher delta value which indicates higher degree of influence on kerf width.

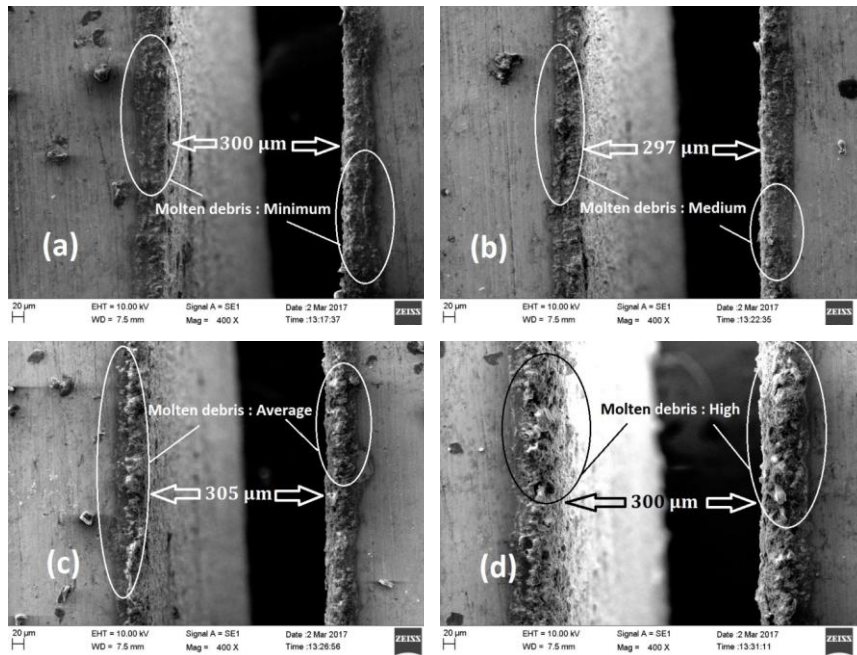


Figure 4.11 Kerf zone at SV (a) 15 V (b) 30 V (c) 45 V (d) 60 V

4.4.4.4 Effect of Wire Feed

Furthermore, it is evident from Fig. 4.9 that wire feed rate of 8 m/min surprisingly lowers kerf width and beyond that it widens slightly again at 10 m/min. This behavior is similar for all the selected alloys. It can be observed that variation of kerf width at both 4 m/min and 6 m/min are negligible and it narrows down at 8 m/min. The reason behind such sudden reduction in kerf width at 8 m/min is due to increased wire tension at higher wire feed rate. Increased wire tension results in less wire vibration hence narrower kerf width. However, at higher wire feed rate 10 m/min, abrupt wire vibration came into play and widened the kerf. Tosun et al. (2004) also observed similar behavior. This emphasizes the need for proper wire feed selection in maintaining narrow kerf width.

4.4.5 Taguchi Analysis - Recast Layer Thickness

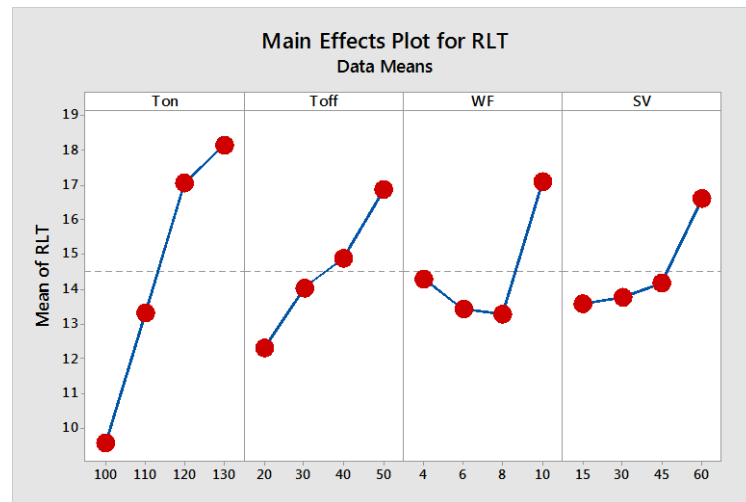


Figure 4.12. Effects plot for Recast Layer Thickness

Table 4.13. Response table for means of RLТ

| Level | T _{on} | T _{off} | WF | SV |
|-------|-----------------|------------------|-------|-------|
| 1 | 9.58 | 12.32 | 14.31 | 13.58 |
| 2 | 13.34 | 14.05 | 13.42 | 13.77 |
| 3 | 17.06 | 14.91 | 13.31 | 14.19 |
| 4 | 18.16 | 16.87 | 17.12 | 16.61 |
| Delta | 8.58 | 4.55 | 3.82 | 3.02 |
| Rank | 1 | 2 | 3 | 4 |

4.4.5.1 Effect of Pulse on Time

Nature of electrical discharge in WEDM process is determined by the input process parameters of WEDM process. During this process, some of the molten material from the wire electrode also deposits over machined surface in microscopic level (Simao et al., 2003). On the other hand, some of the molten workpiece material re-deposits due to rapid solidification that occurs due to continuous supply of dielectric fluid that instantly quenches the molten material (Aspinwall et al., 2003). Recast layer thickness was found to increase with increasing pulse on duration (T_{on}). Since longer pulse on time implicates more discharge spark impingement on workpiece surface for a given spark cycle, at higher discharge energy more molten material will be available for re-solidification and will add further to increase thickness of recast layer. As the discharge energy increases, subsequent electrical sparks penetrate further into the subsurface depth of workpiece material and plays a major role in altering the sub-

surface material property. Effect of pulse on duration on recast layer thickness is evident from the effects plot as shown in Figure 4.12 and is applicable for all the selected alloys. However, ANOVA results indicate that pulse off time has more influence on recast layer thickness increment along with servo voltage compared to pulse on time. Since pulse on time directly influences amount of discharge sparks received by the workpiece, taguchi analysis indicates pulse on time for selected parameter levels. Therefore, a higher delta value can be observed for pulse on time on affecting recast layer thickness as tabulated in Table 4.13.

4.4.5.2 Effect of Pulse off Time

Recast layer thickness is the assimilation of re-solidified molten material over one another layer of material which was found to increase with increasing pulse off duration. As the pulse off duration extends from 20 μs to 50 μs , more time was available for re-solidification that resulted in increment of recast layer thickness in case of all the selected alloys and can be observed in effects plot presented in Figure 4.12. SEM Figure 4.13(a-d) showed the effect of increasing pulse off duration on recast layer thickness for TNC11.

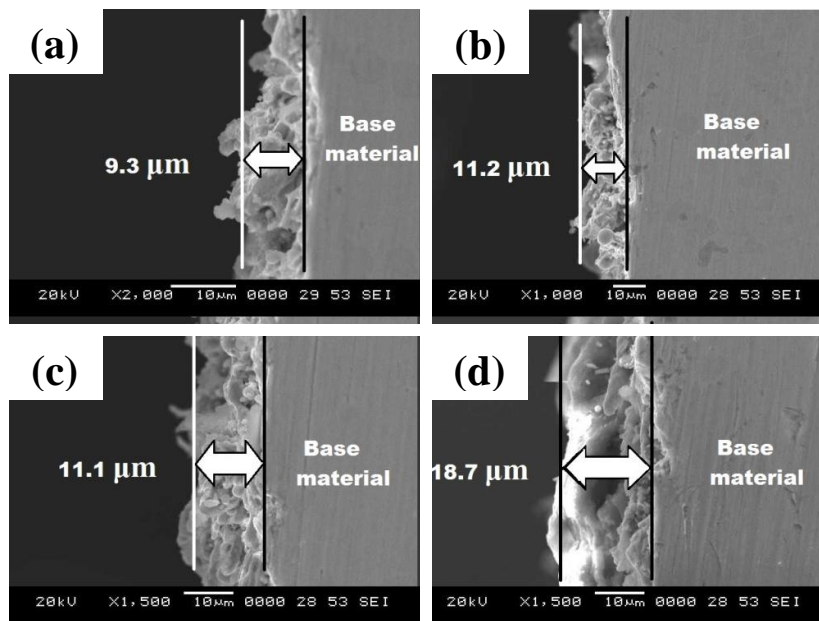


Fig. 4.13. Recast Layer Thickness at T_{off} : (a) 20 μs (b) 30 μs (c) 40 μs (d) 50 μs

4.4.5.3 Effect of Servo Voltage

It was observed in all the cases that an increase in servo voltage increased recast layer thickness. Increase in recast layer thickness from 15 V to 45 V was found quite minor. However, beyond 45 V recast layer thickness increases due to increased ionization of dielectric fluid which results in extreme discharge sparks on either side of the wire electrode. As the wire tends to maintain a more wider gap at higher servo voltage it results in a more intense sparking condition on the other side. As a result the wire electrode vibrates laterally to influence material removal on either side and results in more intense discharge conditions and hence increased recast layer thickness. Also, higher servo voltage results in widespread nature of electrical discharge that leads to abrupt local melting of workpiece material. This leads to uneven machined surface and is evident from Fig. 4.14. Beyond 30 V, the machined surface becomes uneven and influence of intense electrical discharge can be seen in Figure 4.14(c) and 4.14(d) which can be attributed to higher servo voltage that generated high intensity discharges which penetrated the workpiece surface and created numerous voids and irregularities. This resulted in overall increment of recast layer thickness and is observed for all the selected alloys. Rupajati et al. (2014) also noticed and reported similar behavior and concluded to implement lower value of servo voltage for better surface characteristics.

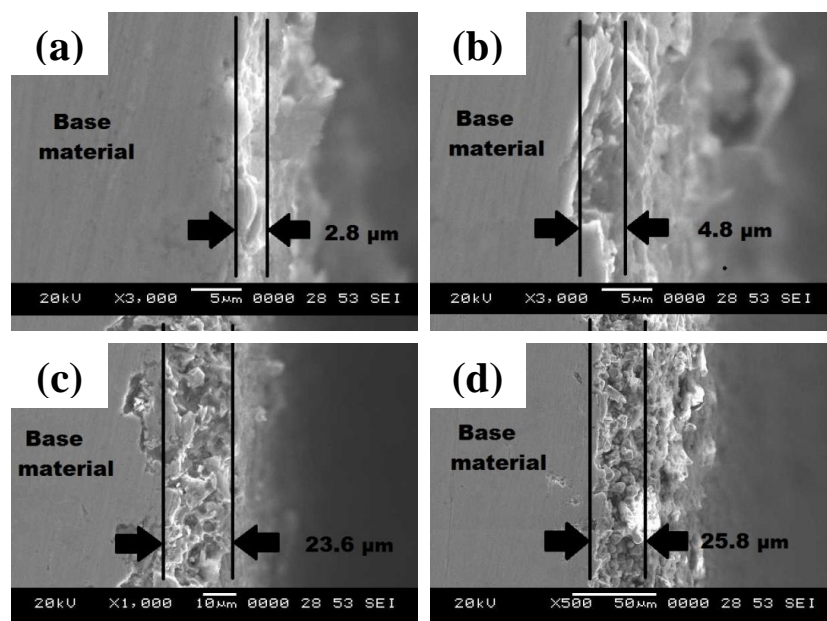


Fig. 4.14. Recast Layer Thickness at S / : (a) 15 V (b) 30 V (c) 45 V (d) 60 V

4.4.5.4 Effect of Wire Feed

Overall effect of entire range of wire feed rate values are minimal as along the entire range of wire feed rate values, net effect is negligible. The trend of results is similar for all the selected TiNiCu alloys. However, effect of wire feed on recast layer thickness is negligible at lower values 4 m/min and 6 m/min, but it reduces at 8 m/min and beyond that it increases. This is due to increased flushing of dielectric into the machining zone and abrupt vibration of wire electrode that contributed in faster re-solidification of molten material, hence thicker recast layer. However, higher wire feed rate contributed in abrupt vibration of wire that swept some molten material along with it. Therefore, combination of the above mentioned phenomena restricted abrupt variation in recast layer thickness at higher wire feed rate. It should also be noted that apparent effect of wire feed rate is less comparable to other parameters when recast layer thickness is concerned and such insignificant behavior is also confirmed by Hasçalık and Çaydaş (2004) during their study of machining AISI D5 tool steel using WEDM. However, it has been observed that for TNC11-13, 8m/min yields lowest recast layer thickness but for TNC21-23, 6 m/min yields lowest recast layer thickness. This implies that proper compensation should be applied while machining such intermetallic alloys.

4.5 ANALYSIS OF WEDM RESPONSES - MATERIAL REMOVAL RATE AND SURFACE ROUGHNESS

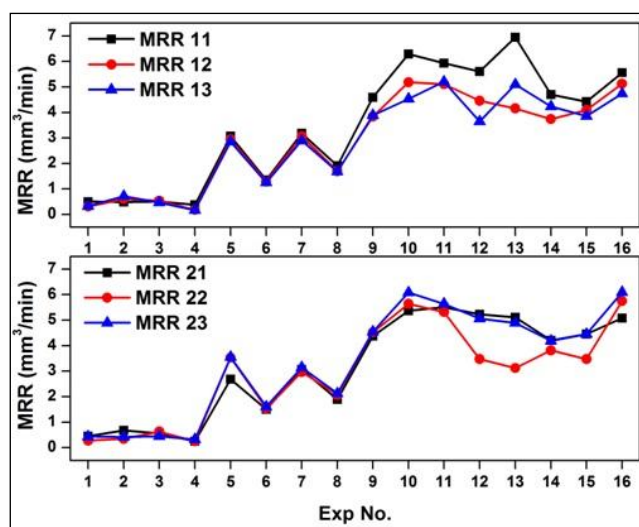


Fig. 4.15. Material Removal Rate of L16 experimental trial for Alloy Set 1 and 2

Figure 4.15 indicates material removal rate of alloy set 1 and 2 for Taguchi's L16 orthogonal experimental trials. It can be observed from the figure that MRR gradually increases as discharge energy increases at experimental trials having longer pulse on duration. Trend of results exhibited in the graph for both alloy sets show similarity. However, variation in MRR of the alloys under similar machining conditions (mainly observed at higher discharge energy settings) for experimental trials beyond 9 is due to varying thermal conductivity (Hsieh et al., 2009). Variation in thermal conductivity of TiNiCu shape memory alloys can be attributed to change in percentage composition of each element as established by Ramachandran et al. (2013, 2015). Such variation was also observed for machined surface roughness as can be seen in Figure 4.16. In case of surface roughness, trend of results also exhibit similarity. It can be noted that at higher discharge energy parameter machined surface roughness surges which also justifies proportional relation between material removal rate and surface roughness. Soni et al. (2017) established during optimization of wire electro discharge machining parameters while machining TiNiCo shape memory alloys that material removal rate and surface roughness cannot be optimized simultaneously as a single objective and hence employed multi-objective optimization using grey relational analysis. In case of MRR, higher divergence in response values were observed beyond eighth experimental run which shows that thermal conductivity becomes effectively influential for this machining response at higher discharge conditions.

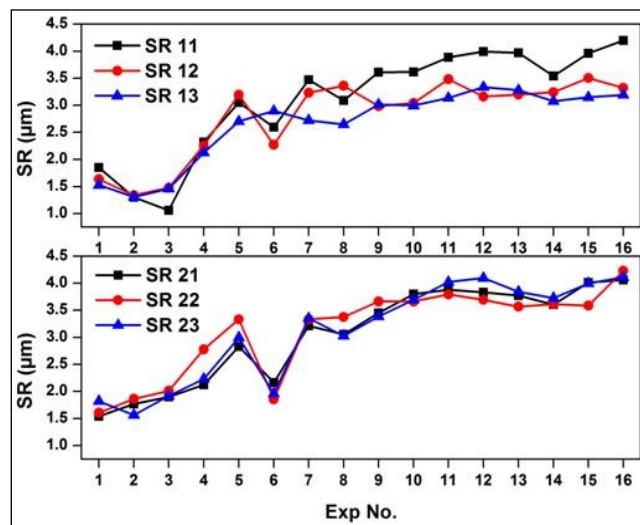


Fig. 4.16. Surface Roughness of L16 experimental trial for Alloy Set 1 and 2

4.6 ANALYSIS OF WEDM RESPONSES - SURFACE MICROHARDNESS AND SURFACE MORPHOLOGY

4.6.1 Surface Microhardness

Microhardness of WEDM-ed surface vary due to metallurgical changes that take place during machining, which is mainly due to formation of recast layer that is associated with generation of residual stresses (Soni et al., 2017). Residual stresses are generated on the machined surface due to intense thermal exposure caused due to electrical discharge and subsequent non-uniform dielectric quenching. This phenomenon leads to uneven distribution of stress generation leading to altered surface characteristics. However, it is imperative to observe the machined surface microhardness because it constrains the shape recovery of the machined component (Sun et al., 2012). Therefore, attempt has been made to grasp the effect of WEDM process parameters on machined surface microhardness of TiNiCu shape memory alloys. WEDM-ed surface exhibits a higher hardness due to the presence of recast layer. In a study, it was noted that metallurgical structure of recast layer varies widely even within a small zone. Also, chemical composition of recast layer changes drastically if the top layer is compared with the layer closer to workpiece matrix (Manjaiah et al., 2014). In our previous study, it was confirmed that recast layer consists of several oxide phases (TiO_2 , NiTiO_3) that occurs due to reaction of workpiece material with oxygen released due to dielectric breakdown. Along with oxide phases, CuZn and NiZn phases were also reported by Soni et al. (2017) which was believed to have migrated from wire electrode material. Presence of various phases has been associated with higher hardness of machined surface compared to the base material which was found to have influenced the base material upto a depth of 100 μm (Huang et al., 2004). As cast base material microhardness is tabulated in Table 4.14 and its deviation from parent value is represented in Figure 4.17 and 4.18.

Table 4.14. As cast material microhardness of prepared TiNiCu alloys

| Alloy symbol | Composition (at%) | Micro-hardness (~Hv) |
|--------------|--|----------------------|
| TNC11 | $\text{Ti}_{50}\text{Ni}_{40}\text{Cu}_{10}$ | 280 |
| TNC12 | $\text{Ti}_{45}\text{Ni}_{45}\text{Cu}_{10}$ | 480 |

| | | |
|-------|--|-----|
| TNC13 | Ti ₄₀ Ni ₅₀ Cu ₁₀ | 560 |
| TNC21 | Ti ₅₀ Ni ₃₅ Cu ₁₅ | 305 |
| TNC22 | Ti ₅₀ Ni ₃₀ Cu ₂₀ | 315 |
| TNC23 | Ti ₅₀ Ni ₂₅ Cu ₂₅ | 335 |

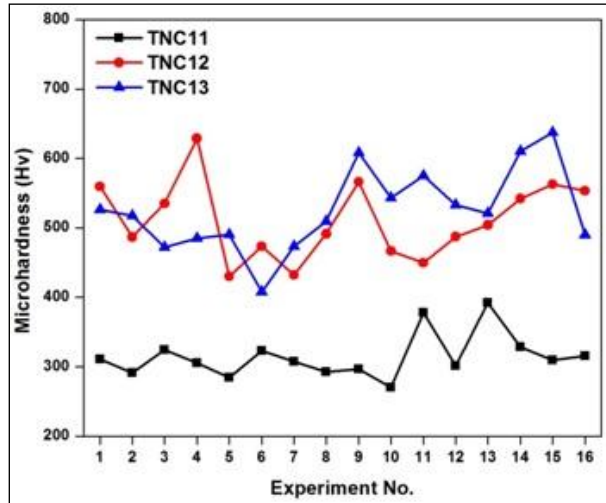


Figure 4.17. Machined surface microhardness of TNC11, TNC12 and TNC13

From Figure 4.17 it can be seen that for TNC11, TNC12 and TNC13 low machined surface microhardness was recorded around experimental run 5 and 6. Pulse on duration for this range was 110 μ s. So, it can be considered that for homologous TiNiCu alloys 110 μ s pulse on duration yields low machined surface microhardness which is desirable for intricate applications and valid for these three alloys and 100 μ s pulse on duration for TNC21, TNC22 and TNC23. It can be observed from Table 4.14 that microhardness of TNC11 is 50-60% lower compared to TNC12 and TNC13, which is due to lower nickel content compared to its counterparts (TNC12 and TNC13). The justification of such behavior was also reported in a recent work (Tosun et al., 2004) where it was noted that microhardness of TiNiCu alloys increases with increasing Cu content that replaces Ni. They have attributed such behavior to formation of precipitates like Ti(Ni, Cu)₂ in TiNiCu alloy system. In our case, Ti content was replaced by higher Ni content which lead to formation of Ni-rich precipitates (CuNi, TiNi₃). In a study by Shankar and Sellamuthu (2015), Ni was found to increase average hardness of Cu-Sn-Ni alloy. These Ni-rich precipitates that contributed in higher material hardness were also present in recast layer as it is a part of workpiece material. These Ni-rich precipitates along with oxide phases contributed

to high machined surface microhardness. Especially at higher pulse energy experimental runs, higher microhardness were observed. This is due to formation of more oxides and CuZn-NiZn phases caused due to powerful spark impingement at higher energy settings (9-16 experimental runs). It can be observed in Figure 4.17 and 4.18 that beyond experimental run 9, machined surface microhardness follows an incremental trend which justifies aforementioned discussion.

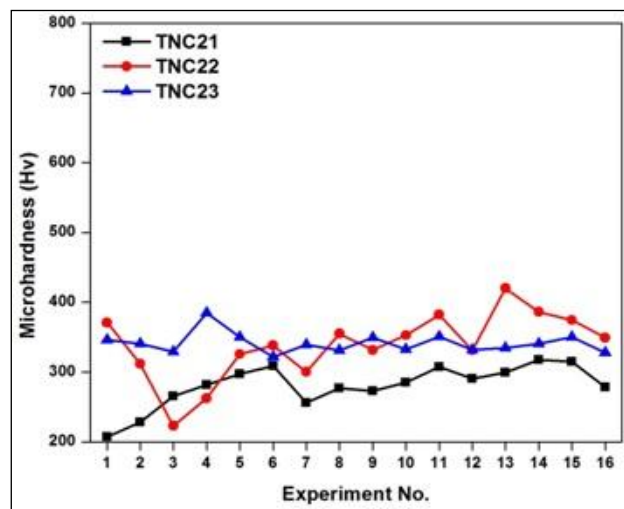


Figure 4.18. Machined surface microhardness of TNC21, TNC22 and TNC23

Higher machined surface microhardness indicates formation of an exterior hard shell around the WED machined component which will hinder proper shape recovery during reverse martensitic transformation and therefore is not desirable. More the machined surface microhardness is close to bulk material hardness suitable is the component for shape memory applications. Figure 4.19 demonstrates the effect of high machined surface microhardness on shape recovery action of WED machined components. Recast layer has higher microhardness compared to its base material. MH1, MH2,...MH7 are points at cross section of machined surface which correspond to microhardness values. MH1 and MH2 indicates machined surface microhardness which we have discussed in this section. In general it is observed that microhardness decreases with decreasing height from machined surface. Effect of machined surface microhardness have similar effect on shape recoverability as shown for recast layer thickness. A harder exterior shell will restrain total shape recovery (Case 2) whereas a softer shell will facilitate shape recovery (Case 1) which is depicted in Figure 4.19.

Therefore, we have aimed at indicating parameter levels which result in low machined surface microhardness as these factors will eventually determine the quality of the part to be produced using WEDM process.

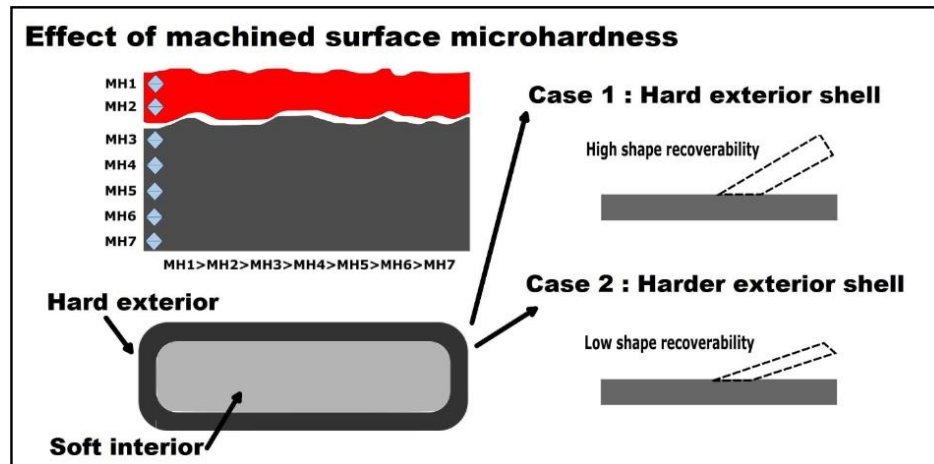


Figure 4.19. Effect of machined surface microhardness on shape recovery

4.6.2 Surface Morphology

4.6.2.1 Effect of Discharge Energy on Surface Morphology

Surface morphology is obtained through imaging system using high resolution microscopes, in this study scanning electron microscope was used to identify key features of the machined surfaces. Features of machined surface determines its quality and integrity and can be used to qualitatively determine better machined surface conditions. Nature of machined surface morphology depends on discharge energy during wire electro discharge machining. Duty factor ($T_{on}/T_{on}+T_{off}$) can be used to characterize nature of discharge energy as higher duty factor resembles higher discharge energy and lower duty factor resembles lower discharge energy. In this study based on design of experiments duty factor varies from 0.66 to 0.86. For the ease of understanding machined surface morphology at four different duty factor settings (0.66, 0.78, 0.81 and 0.84) of fourth, sixth, eleventh and fourteenth experimental run are shown in Figure 4.20.

Figure 4.20(a-d) represents scanning electron micrographs exhibiting machined surface morphology at different discharge conditions. Wire electro discharge

machined surface consists of lot of debris which is a resultant of instant resolidification of spark melted debris. During spark erosion process (WEDM) entire melted material is not removed from the parent workpiece. Due to presence of a dielectric medium some of the melted material quenches instantly and solidifies on the machined surface forming a layer of oxidized material also known as recast layer or white layer (Klocke et al., 2016). Micro globules, micro voids, resolidified debris are few features of wire electro discharge machined surface which in turn contributes to average surface roughness. From Figure 4.20a and 4.20b it can be seen that size of micro globules vary as well as apparent micro voids are more on the latter. Presence of more micro voids indicate more intense discharge conditions. Therefore, micro voids are more in number and hence more prominent in machined surfaces as shown in Figure 4.20c and 4.20d. From Figure 4.16 it is evident that resultant surface roughness of experimental run 4 is more than experimental run 6 which is also confirmed by surface morphology features of Figure 4.20a and 4.20b. It is to be observed in Figure 4.20b that there are ample melt free zones (marked with white circle) which are less in Figure 4.20a. Such melt free zones result in lower surface roughness (Roy and Sanna Yellappa, 2019). Features of machined surface as shown in Figure 4.20c and 4.20d are almost similar and hence exhibit surface roughness as observed from Figure 4.16. It is evident that machining parameters influence discharge condition which controls features of machined surface morphology. Until now influence of only electrical parameters pulse on time, pulse off time, servo voltage and wire feed are discussed on machined surface morphology of WEDMed TiNiCu shape memory alloys. However, there are other electrical parameters such as peak current and peak voltage and non-electrical parameters like flushing pressure and flushing direction also have effect on machined surface morphology and is discussed in upcoming sections.

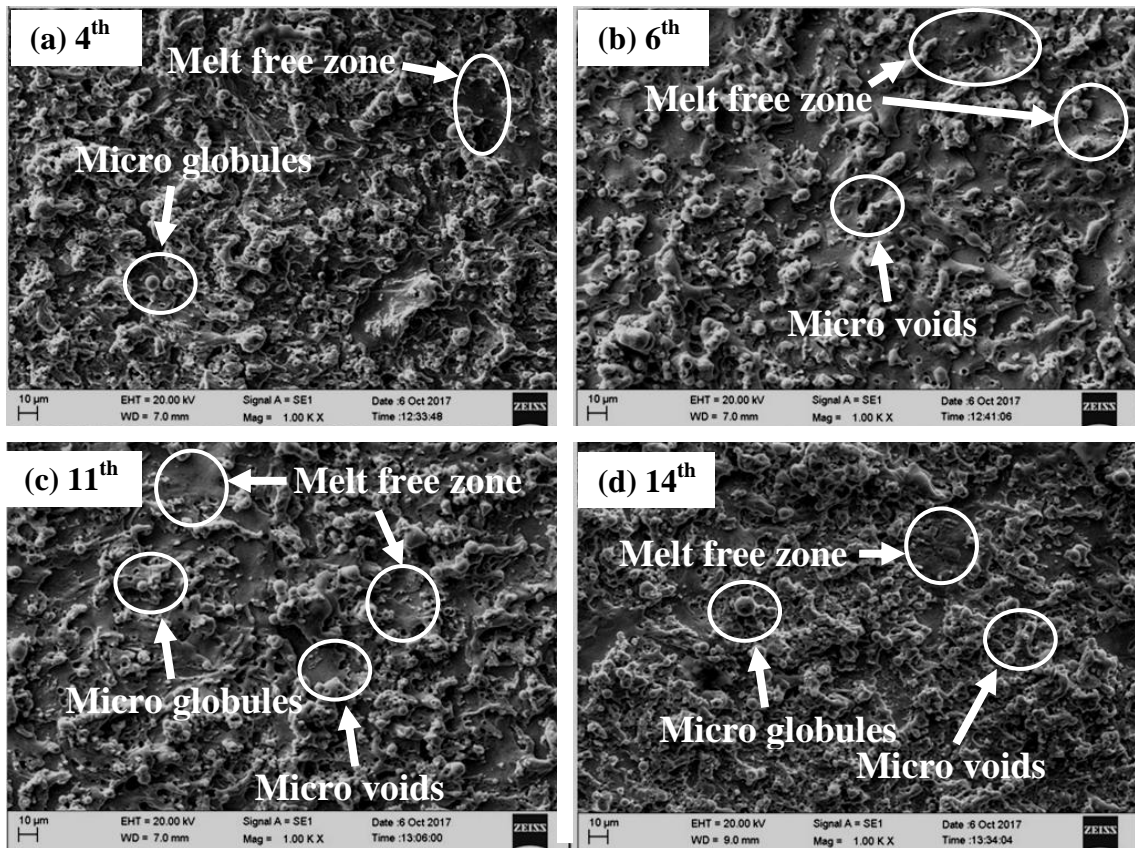


Figure 4.20. Surface morphology at (a) 4th (b) 6th (c) 11th and (d) 14th experimental run

4.6.2.2 Effect of Peak current and Peak voltage on Surface Morphology

A machined surface having minimum debris, defects and roughness is more desirable in order to obtain superior machining surface. Literature footprint on effect of peak current and peak voltage on machined surface morphology is very less and hence investigation on effect of peak current and peak voltage on machined surface morphology was done. WEDM technique is an electro-thermal production process where a 250 μm diameter wire electrode bombards the workpiece with avalanche of electrons i.e. sparking and causes melting of material. Material removal mechanism in WEDM being a thermal process leads to an unique "coral reef" surface morphology (Li et al., 2014). Machining parameters such as T_{on} , T_{off} , SV, WF etc. controls the duration of discharge, spark gap and controls flushing of machining zone to maintain efficient machining conditions. Peak current (I_p) and pulse peak voltage (V_p) on the other hand controls the intensity and nature of discharge that takes place in machining zone.

Table 4.15. Experimental Results

| Experimental Run | I_p (Amps) | V_p (Volts) | Ra (μm) | Rz (μm) |
|------------------|--------------|---------------|----------------------|----------------------|
| 1 | 1.39 | 58 | 2.39 | 18.23 |
| 2 | 1.33 | 54 | 2.71 | 17.01 |
| 3 | 1.28 | 53 | 2.91 | 18.24 |
| 4 | 0.85 | 32 | 1.3 | 9.34 |
| 5 | 0.84 | 30 | 1.4 | 8.77 |
| 6 | 0.82 | 28.5 | 1.48 | 9.58 |
| 7 | 0.92 | 31 | 1.02 | 7.62 |
| 8 | 0.89 | 29.6 | 1.03 | 8.02 |
| 9 | 0.87 | 29 | 1.23 | 10.01 |
| 10 | 1.41 | 60 | 2.73 | 16.79 |
| 11 | 1.38 | 57 | 2.78 | 17.13 |
| 12 | 1.36 | 55 | 2.87 | 18.34 |
| 13 | 0.77 | 36 | 1.21 | 9.34 |
| 14 | 0.75 | 30 | 1.42 | 9.41 |
| 15 | 0.74 | 28 | 1.52 | 11.14 |
| 16 | 0.76 | 28 | 1.1 | 8.26 |
| 17 | 0.74 | 27 | 1.17 | 10.05 |
| 18 | 0.73 | 25 | 1.31 | 11.02 |

Previous experimental investigations reveal that WEDM parameters T_{on} - pulse on time 110 μs , T_{off} - pulse off time 30 μs , 45 volts servo voltage (SV) and 6 m/min wire feed rate (WF) results in suitable material removal rate, surface roughness, kerf width and recast layer thickness (Roy et al., 2017; Roy and Narendranath, 2018; Roy and Narendranath, 2018a). Based on previous results as discussed earlier, T_{on} , T_{off} , SV and WF were kept constant throughout the experimentation process. Stock software of the WEDM equipment represents different values of peak current (I_p) and pulse peak voltage (V_p) in terms of bits and does not provide specific values, therefore a digital storage oscilloscope Tektronix TPS2012B was used to find out their mean values. Based on machine capability I_p and V_p can be varied in six and three levels respectively. Therefore, a simple factorial design of experiment consisting 18 experimental runs were used to investigate the effect of I_p and V_p on machined surface morphology (see Table 4.15). Table 4.15 shows mean values of I_p and V_p as recorded from the oscilloscope.

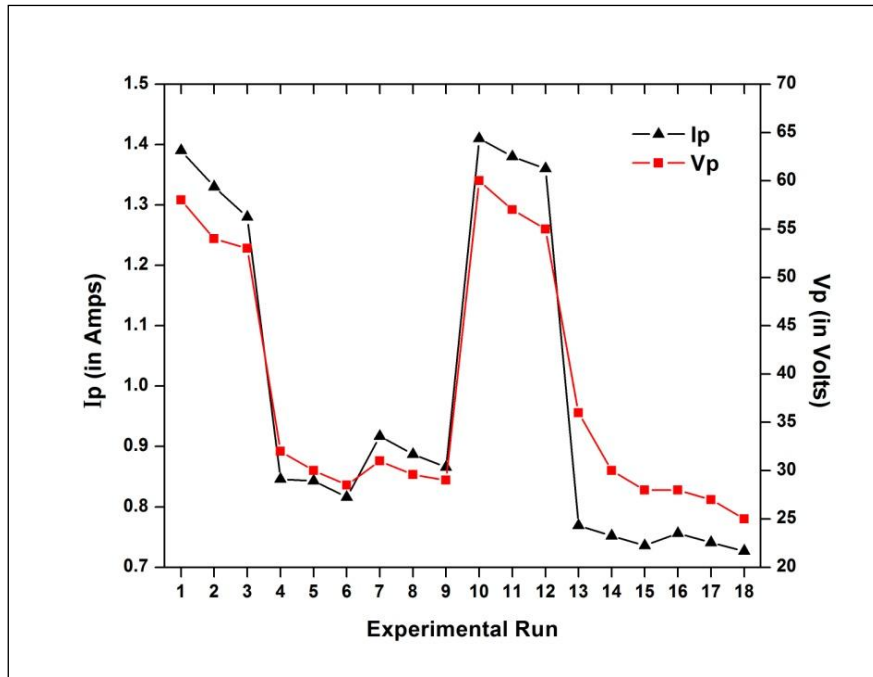


Figure 4.21. I_p and V_p for all experimental runs

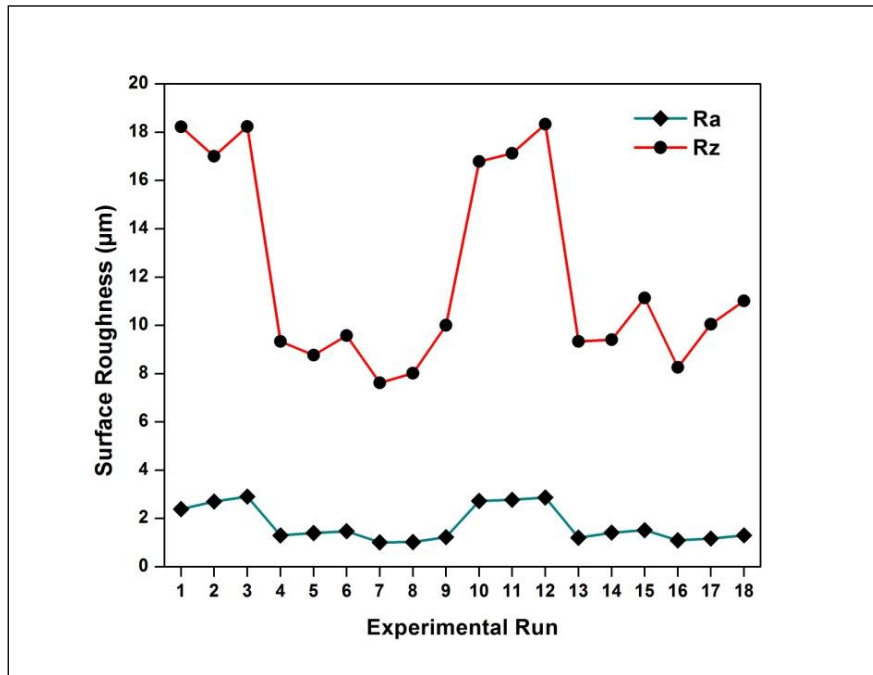


Figure 4.22. Average surface roughness (R_a) and depth (R_z)

Figure 4.21 corresponds to the values of I_p and V_p graphically where it can be seen that trials 1,2,3 and 10,11,12 have higher peak current and peak voltage compared to other trials. Subsequently average surface roughness and depth are approximately 50% higher at these experimental trials as can be seen from graph in Figure 4.22.

It can be seen from scanning electron micrographs of Figure 4.23 and 4.24 that trials 4-9 and 13-18 exhibit more or less similar machined surface morphology whereas 1-3 and 10-12 are similar. It can be inferred that trials 4-9 and 13-18 have more uniform machined surface conditions which is also apparent from R_a and R_z values in Figure 4.22. Introspection of the trend of trials reveal that surface roughness increases with increasing peak current and peak voltage. Highest surface roughness ($R_a : 2.91 \mu\text{m}$) was for 3rd experimental trial ($I_p : 1.28 \text{ A}$, $V_p : 53 \text{ V}$), whereas lowest recorded surface roughness ($R_a : 1.02 \mu\text{m}$) was for 7th experimental trial ($I_p : 0.917 \text{ A}$, $V_p : 31 \text{ V}$).

These results are in accordance with findings of researchers working with peak current (Chen et al., 2008; Hsieh et al., 2013). Close observation of 1st and 2nd experimental trial and their comparison with 3rd trial show that surface roughness increases slightly with a little decrease in peak current and peak voltage which opposes the general trend. The major reason behind this slight "rise" in average surface roughness can be attributed to rise in average surface depth value (R_z) and various features of machined surface which is the resultant of change in sparking conditions with varying I_p and V_p values.

Surface morphology of 3rd trial indicates higher number of micro-voids (marked with white circle) and melt free zones (marked with red area) compared to 1st trial (see Figure 4.23). Similar observation was noted for 10th and 13th trial (see Figure 4.24). Several micro voids can also be observed within melt free zones. Melt free zones signify absence of debris and micro-globules which results in sudden increase in surface depths. Such sudden increase in surface depths raises R_z value of the machined surface which in turn contributes in slight increment of average surface roughness.

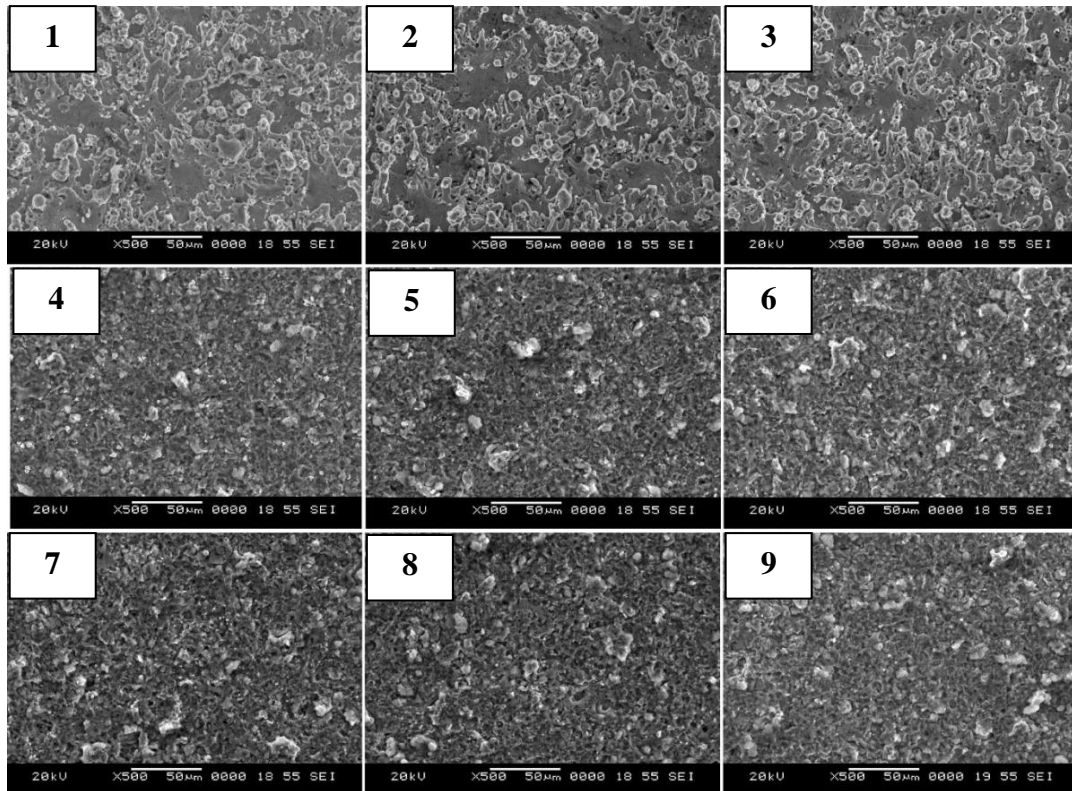


Figure 4.23. Surface morphology of experimental run 1-9

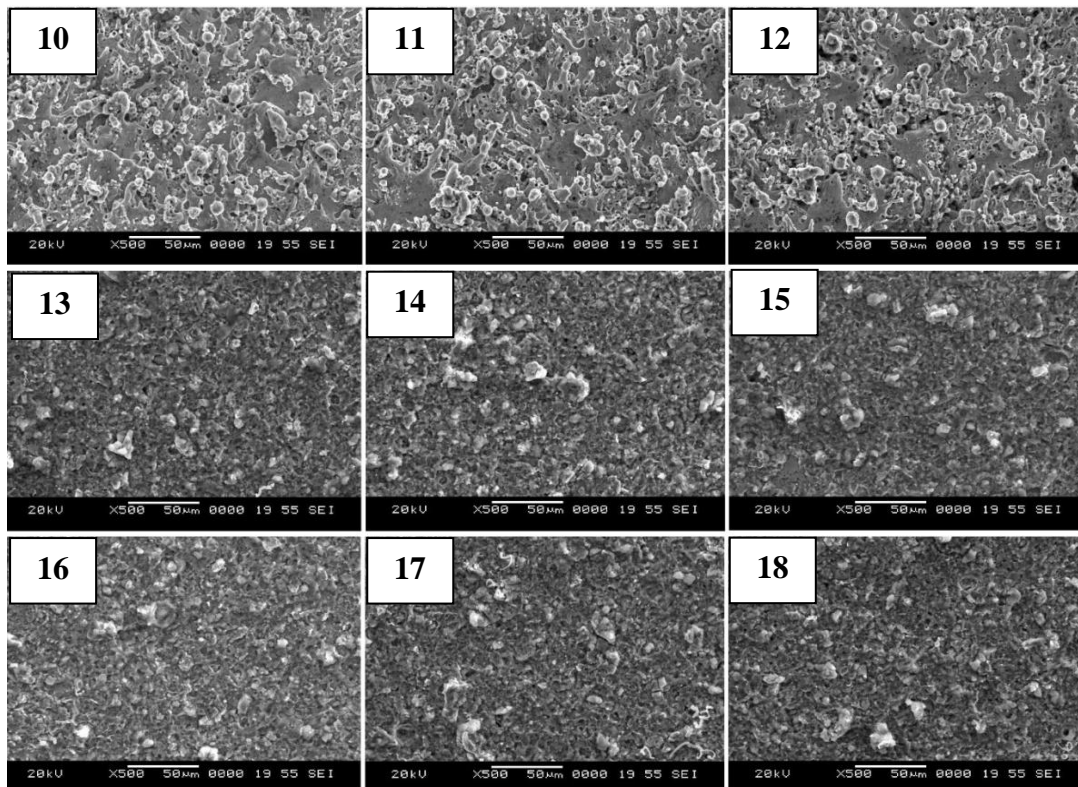


Figure 4.24. Surface morphology of experimental run 10-18

Although melt free zones are present for machined surfaces at slightly higher peak current and peak voltage settings, they contain lesser debris and micro-globules which is the reason behind slightly lower average surface roughness. Presence of more debris are also evident from micrographs of trial 4-9 and 13-18. More amount of debris can be seen on machined surface of trial 6, 9, 15, 18 compared to trial 4, 7, 13 and 16. As can be observed from scanning electron micrographs shown in Figure 4.23 and 4.24 of trial 4, 7, 13 and 16, there are no significant melt free zones, micro-voids and micro-globules, hence low average surface roughness (Ra) and surface depth (Rz) values. Few debris can be seen in all of these machined surfaces (marked with white box), but it should be noted that more debris are present at less intense discharge condition parameters indicating inefficient flushing condition post sparking. Micro-globules are another surface features of wire electro discharge machined surfaces whose size indicates the rate of dielectric quenching which is a consequence of post conditions of intense discharge conditions. Smaller micro-globules indicate faster quenching rate. Collapse of spark at the end of pulse on duration (T_{on}) is followed by the phenomenon which is precisely re-integration of dielectric fluid ions due to collapse of plasma channel and absence of potential difference. This phenomenon leads to disappearance of gas bubble causing formation of instantaneous vacuum field followed by a small scale shock wave (Abdullah and Shabgard, 2008). This determines the nature of intensity of debris removal from the freshly sparked surface. Stronger the vacuum due to collapse of gas bubble and plasma channel, stronger is the subsequent shock wave, hence a more efficient removal of debris from the machining zone. Since sparking conditions of trial 1 and 10 are slightly severe than trial 3 and 12, larger micro-globules can be seen for the latter (marked with white arrow). Presence of more micro-voids for the same can be justified with the spark profile of these trials as shown on Figure 4.25. These micrograph images of machined surface represent trial 1, 3, 10 and 12 respectively for a machining duration of 350 ms. Spark profiles (area shown with arrows indicating splatter direction) of trial 1 shows multiple superposition of resolidified material which also indicate more intense sparking for a given period of time whereas spark profile of trial 3 shows less intense and distributed discharge conditions. Since subsequent shock wave had less intensity therefore, more amount of debris and micro-voids can be seen on the machined surface. Spark profile of trial 10 and 12 further clarifies the need of intense discharge conditions for better debris

removal under similar machining conditions. Spark crater is almost indistinguishable for trial 10 which had severe sparking conditions (higher I_p and V_p), hence stronger shock wave resulting in better debris removal. On the contrary, spark crater of trial 12 proves inefficient removal of melted debris. Presence of a pockmark (marked with white box) further justifies this phenomenon. However, trend of results follow established norms as trial 10, 11 and 12 exhibits higher surface roughness compared to trial 1,2 and 3. Lower surface roughness of other experimental trials indisputably qualifies subsequent I_p and V_p levels for trim cut machining operations, especially 7th experimental trial.

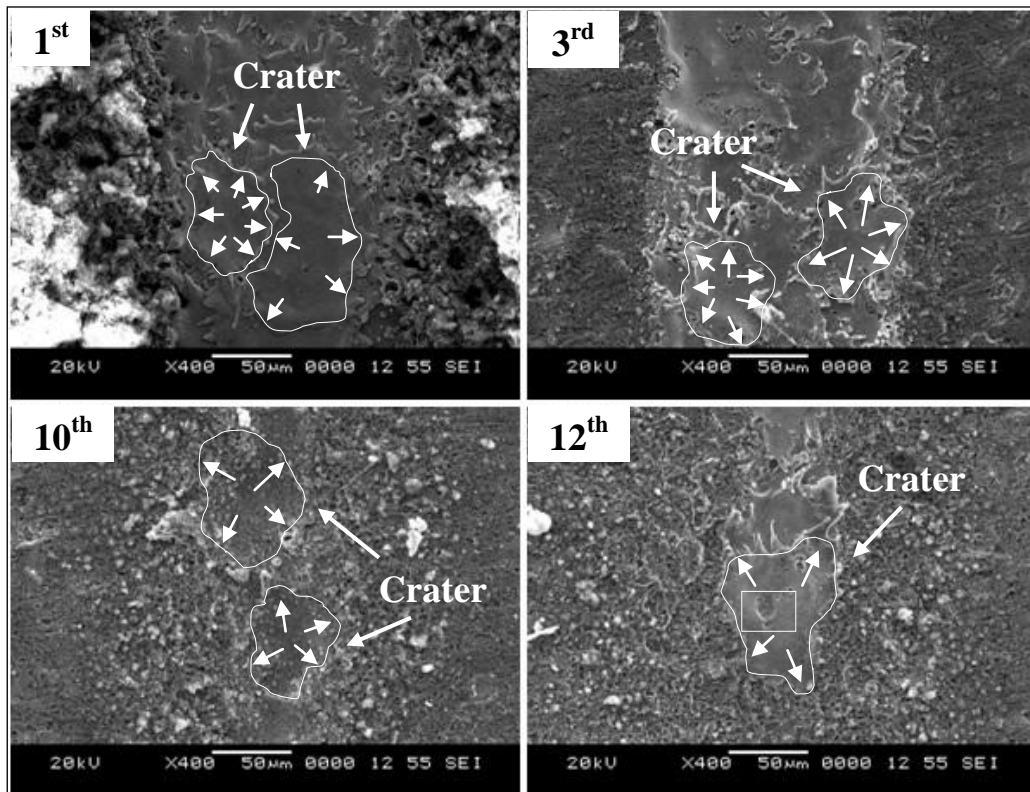


Figure 4.25. Spark profile of experimental trial 1st, 3rd, 10th and 12th

4.6.2.3 Effect of Flushing pressure and Direction on Surface Morphology

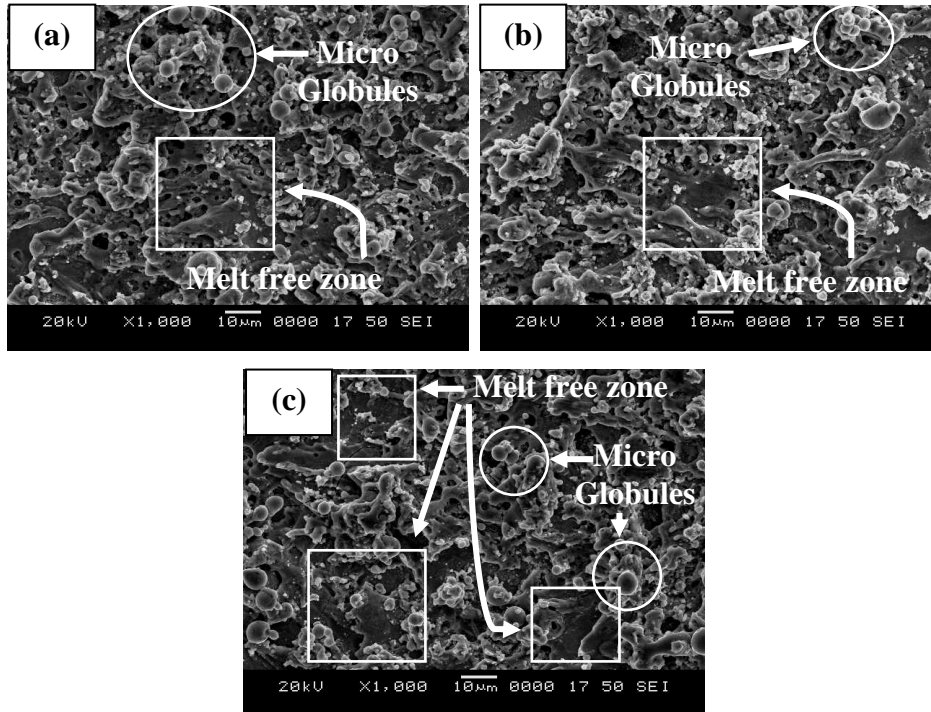


Figure 4.26. Machined surface morphology at (a) 49.03 (b) 98.06 and (c) 147.1 kPa flushing pressure for experimental run resembling higher discharge energy (22-24)

A separate set of experiments were performed to understand the effect of varying flushing pressure and direction on surface morphology of WEDM specimens (see Table 4.16). Results of all 27 experimental runs indicate that experimental run 7-9 has lowest whereas 22-24 has highest cutting speeds. Therefore, results involving these aforementioned experimental runs were considered for detailed discussion in this section. From the study, it was observed that presence of large size micro-globules are much more prominent at 49.03 kPa. Number of micro-globules were minimized at 98.06 kPa as seen in Figure 4.26b and appear again at 147.1 kPa but smaller in size as compared to Figure 4.26a and are indicated by circles. Micro-globules form due to dielectric quenching which is a result of slow quenching and inefficient flushing condition. Arooj et al. (2014) confirmed that large globules are the result of incomplete evaporation of workpiece material. Therefore, it is only typical to observe micro-globules of larger size at low flushing pressure level and smaller micro-globules at higher level of flushing pressure. Absence of any significant globules as

seen in Figure 4.26b on samples machined at 98.06 kPa imply efficient flushing condition for the given parameter set. Also, at 147.1 kPa flushing pressure, the recast surface without debris is visible compared to 49.03 kPa and are indicated by rectangular boxes. This shows that at higher flushing pressure levels, efficient removal of molten debris is possible. Regardless of indications of efficient flushing conditions, micro-cracks are present on machined surfaces at higher level of discharge energy and can be observed in Figure 4.26(a-c). Figure 4.27(a-c) represent micrograph of machined surface of experimental run 7-9 where no significant micro-cracks were observed.

Table 4.16. L27 experimental run

| Experimental Run | T_{on} (μs) | T_{off} (μs) | Flushing Pressure (kPa) | Cutting Speed (mm/min) |
|-------------------------|----------------------------|-----------------------------|--------------------------------|-------------------------------|
| 1 | 110 | 30 | 49.03 | 1.493 |
| 2 | 110 | 30 | 98.06 | 1.629 |
| 3 | 110 | 30 | 147.1 | 1.818 |
| 4 | 110 | 40 | 49.03 | 0.992 |
| 5 | 110 | 40 | 98.06 | 1.028 |
| 6 | 110 | 40 | 147.1 | 0.986 |
| 7 | 110 | 50 | 49.03 | 0.327 |
| 8 | 110 | 50 | 98.06 | 0.328 |
| 9 | 110 | 50 | 147.1 | 0.326 |
| 10 | 115 | 30 | 49.03 | 2.141 |
| 11 | 115 | 30 | 98.06 | 2.237 |
| 12 | 115 | 30 | 147.1 | 2.096 |
| 13 | 115 | 40 | 49.03 | 0.707 |
| 14 | 115 | 40 | 98.06 | 0.698 |
| 15 | 115 | 40 | 147.1 | 0.695 |
| 16 | 115 | 50 | 49.03 | 1.825 |
| 17 | 115 | 50 | 98.06 | 1.789 |
| 18 | 115 | 50 | 147.1 | 1.838 |
| 19 | 120 | 30 | 49.03 | 1.519 |
| 20 | 120 | 30 | 98.06 | 1.572 |
| 21 | 120 | 30 | 147.1 | 1.597 |
| 22 | 120 | 40 | 49.03 | 3.521 |
| 23 | 120 | 40 | 98.06 | 3.876 |
| 24 | 120 | 40 | 147.1 | 3.891 |
| 25 | 120 | 50 | 49.03 | 1.869 |
| 26 | 120 | 50 | 98.06 | 1.842 |
| 27 | 120 | 50 | 147.1 | 1.855 |

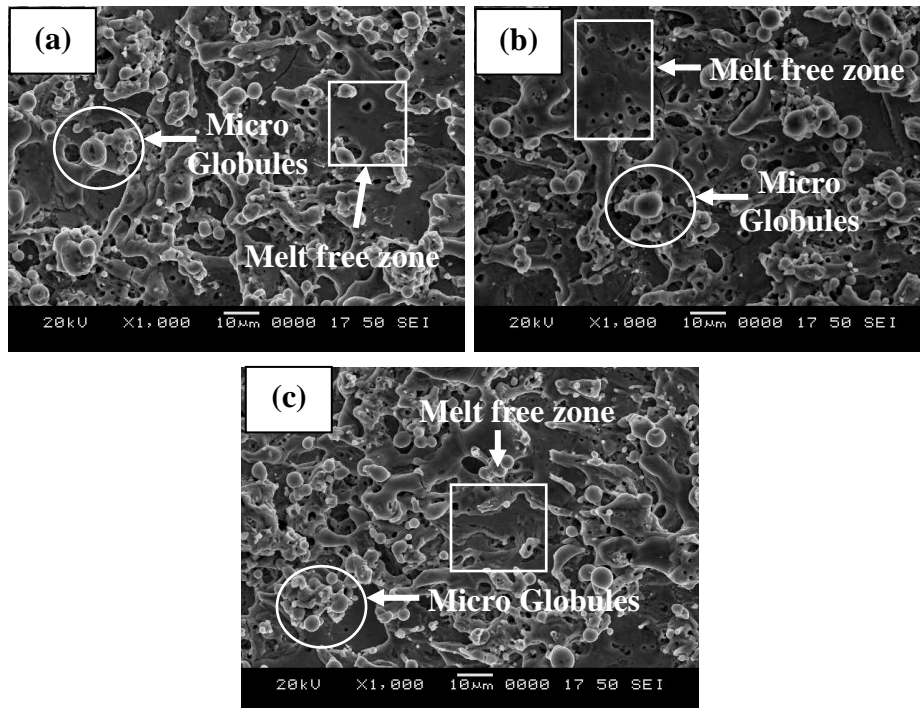


Figure 4.27. Machined surface morphology at (a) 49.03 (b) 98.06 and (c) 147.1 kPa flushing pressure for experimental run resembling higher discharge energy (7-9)

However, at low discharge condition machined surface consists lesser debris particles and is evident from the micrographs depicted in Figure 4.27(a-c). Machined surfaces shown in Figure 4.26(a-c) have more debris compared to Figure 4.27(a-c) due to which recast layer is visible only at few zones as highlighted with rectangular boxes in Figure 4.26(a-c). However, recast surface is visible and is more prominent for experimental run 7-9 as can be seen in Figure 4.27. Presence of lesser debris particles at lower discharge condition as shown in Figure 4.27(a-c) is due to efficient flushing of molten particles from the machining zone. At the aforementioned discharge condition, discharge pulse duration lasted 10 μ s less compared to experimental run representing higher discharge energy which contributed in removal of higher quantity of debris and thus machined surface is comparatively cleaner. However, presence of micro-globules is more at 98.06 kPa flushing pressure and increases at 147.1 kPa, which is due to abrupt wire vibration resulted from higher flushing pressure that lead to uneven sparking and consequently produced non-uniform localized heating. Such non-uniform localized heating created unfavorable sparking condition and more micro-globules are observed as a result of incomplete melting and fast quenching

effect (Sharma et al., 2016; Sharma et al., 2015). Therefore, flushing pressure should be adjusted at a nominal intensity based on the level of process parameter values.

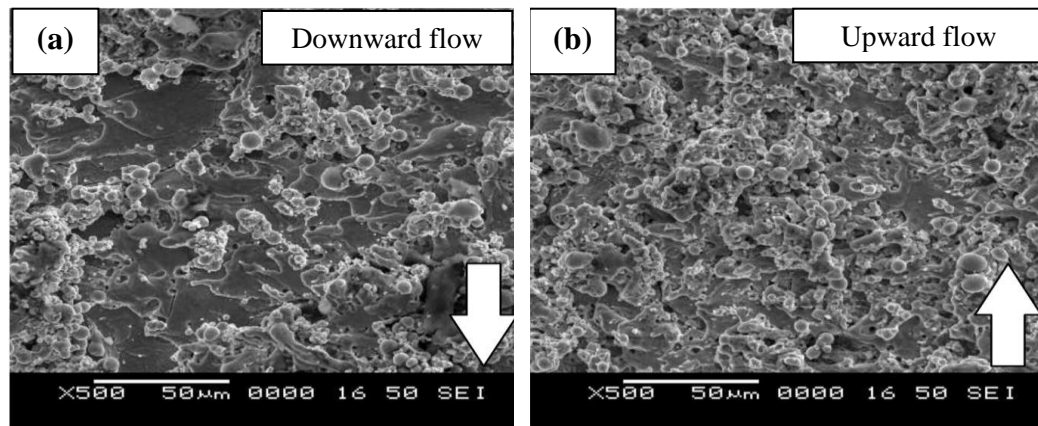


Figure 4.28. Surface morphology at (a) Downward and (b) Upward flushing direction

To study the effect of flushing direction on surface morphology, parameter representing higher discharge energy was used and 147.1 kPa flushing pressure was implemented. Figure 4.28a represents the machined surface morphology when only the top nozzle was operational and Figure 4.28b represents the machined surface morphology when only the bottom nozzle was operational. The direction of dielectric flow is indicated in Figure 4.28(a-b) with arrows. The difference in machined surface morphology is evident from the micrographs in Figure 4.28(a-b). Presence of micro-globules is lesser in downward direction flow than upward direction flow. Surface machined with downward direction flow have lesser debris compared to upward direction flow. The reason behind such behavior can be attributed to variation in flushing condition. When only top nozzle was operational, dielectric jet was able to penetrate closer to machining zone as it was running parallel to wire electrode in the same direction. Therefore, more molten debris was flushed from the machining zone. But when only bottom nozzle was operational, not only it was flushing in opposite direction of wire electrode but was also acting against gravity and was not efficient enough to spill out enough molten debris hence higher quantity of micro-globule formation was observed.

4.7 ANALYSIS OF WEDM RESPONSES - KERF WIDTH AND RECAST LAYER

Figure 4.29 and 4.31 represents average kerf width value and recast layer thickness for all 96 experiments conducted combining 6 alloy sets respectively. It is evident from these graphs that both kerf width and recast layer thickness are least at experimental run 1-3 as they have least discharge energy conditions. Trend of result indicate that kerf width increases as discharge energy increases however it is rising and lowering in a periodical manner across L16 experimental trials. Figure 4.30 illustrates that lower kerf width is a result of low discharge energy leading to more accurate machined profile indicated by inner area compared to programmed profile which is indicated by outer area. However, lower discharge energy conditions also indicate a slower machining rate. Periodical drop can be observed for 5th, 7th, 10th and 14th experimental run. This trend in result can be attributed to combination of higher wire feed rate whilst lower servo voltage settings (Roy and Narendranath, 2018a).

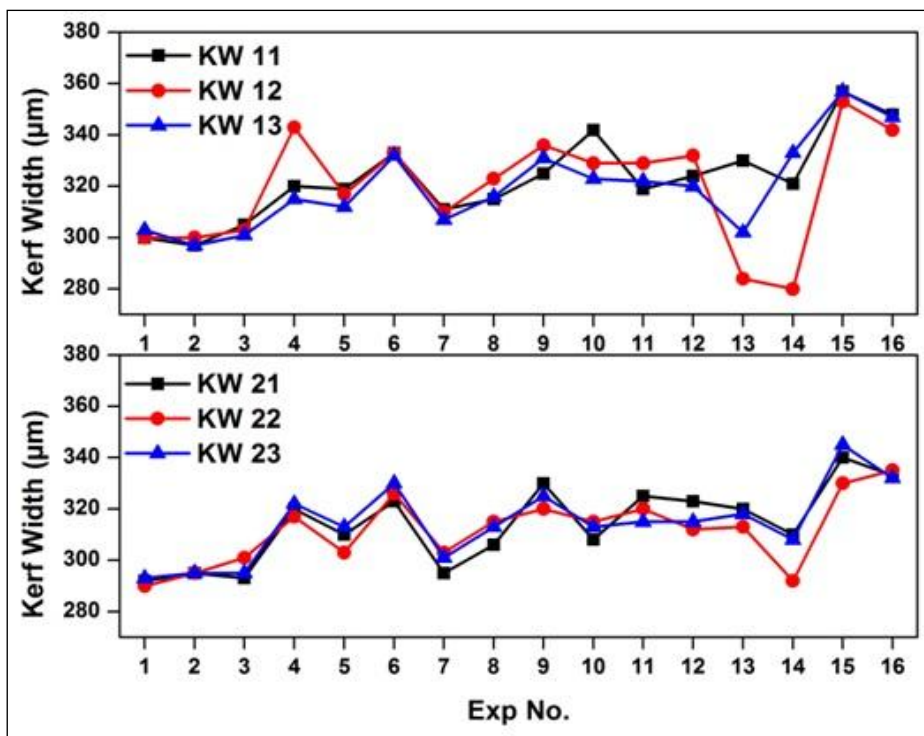


Figure 4.29. Kerf Width of L16 experimental trial for Alloy Set 1 and 2

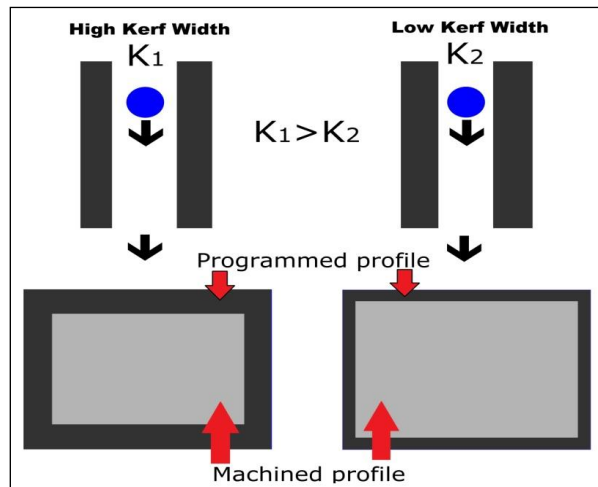


Figure 4.30. Effect of Kerf Width on machined profile

Recast layer thickness was found to be least at low discharge energy conditions as melted material available for resolidification were also less under such conditions. At higher discharge energy settings average recast layer thickness also increases owing to more amount of melted material. Similar to kerf width, periodical rise and drop were also observed in this case. Very thick recast layer thickness was observed for 4th experimental run even though a low material removal rate was registered for this trial. Such increment in recast layer thickness even at low discharge energy settings is due to a high pulse off time and combination of high wire feed rate and servo voltage which ensured enough time for resolidification of melted debris (Roy and Narendranath, 2018). Resulting machined surface also supports the observation as it exhibited higher surface roughness as seen in Figure 4.16, higher machined surface microhardness shown in Figure 4.17 and 4.18 and irregular surface morphology and more amount of debris is observed (marked with circle) as shown in Figure 4.32 where compositionally different alloys such as TNC11 and TNC23 exhibited difference in recast layer thickness which supports the study conducted by Hsieh et al. (2009) and Roy and Narendranath (2018).

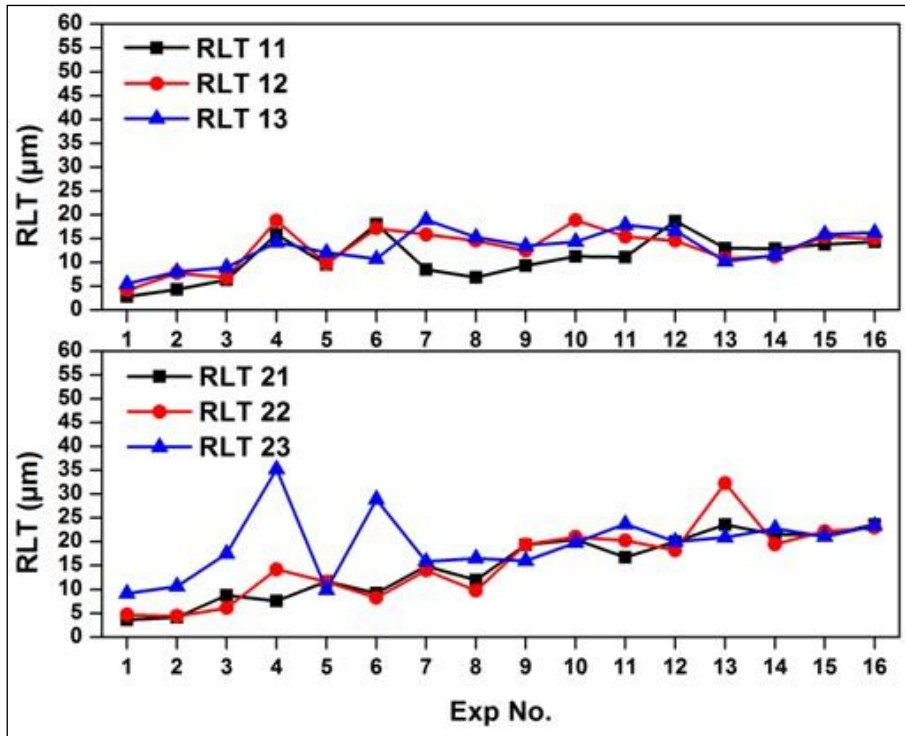


Figure 4.31. RLT of L16 experimental trial for Alloy Set 1 and 2

Under similar machining conditions, TNC11 and TNC23 exhibit varying recast layer thickness as can be seen in Figure 4.32a and 4.32c, similarly Figure 4.32b and 4.32d. Homologous alloys as experimented in this study, if exhibits thicker recast layer under similar machining conditions indicate a lower thermal conductivity. A material having higher thermal conductivity would transfer the heat from sparking to nearby material hence melted material would be less. However, material having comparatively lower thermal conductivity would melt more material due to impinging sparks and hence result will more material available for resolidification which directly influences recast layer thickness. Therefore, two significant spike in recast layer thickness can be observed for TNC23 at 4th and 6th experimental trials.

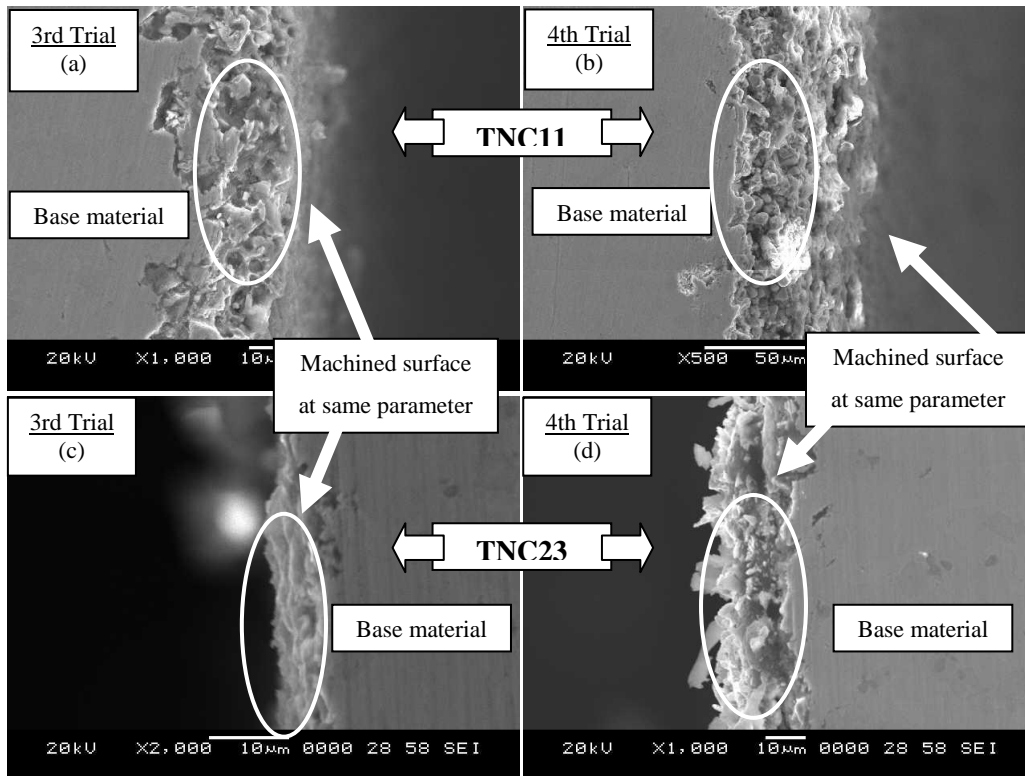


Figure 4.32. Recast layer thickness comparison (a,b) TNC11 (c,d) TNC23

4.8 VARIATION IN WEDM RESPONSES DUE TO HOMOGENIZATION

After vacuum arc melting these alloys were homogenized for 1 hour at 500°C. After homogenization of the alloys (TNC11, TNC12 and TNC13) they were subjected to wire electro discharge machining. Variation in machining responses due to homogenization was observed for all the alloys. Variation in material removal rate, surface roughness, kerf width and recast layer thickness are reported below.

4.8.1 Effect of homogenization on Material Removal Rate

In this section effect of homogenization on MRR is reported. During initial experimentation we have observed reduced kerf width of homogenized samples which led us to adopt a different methodology for MRR evaluation. The kerf width profile of a WEDM slit (schematic in Figure 4.33) was considered in this study.

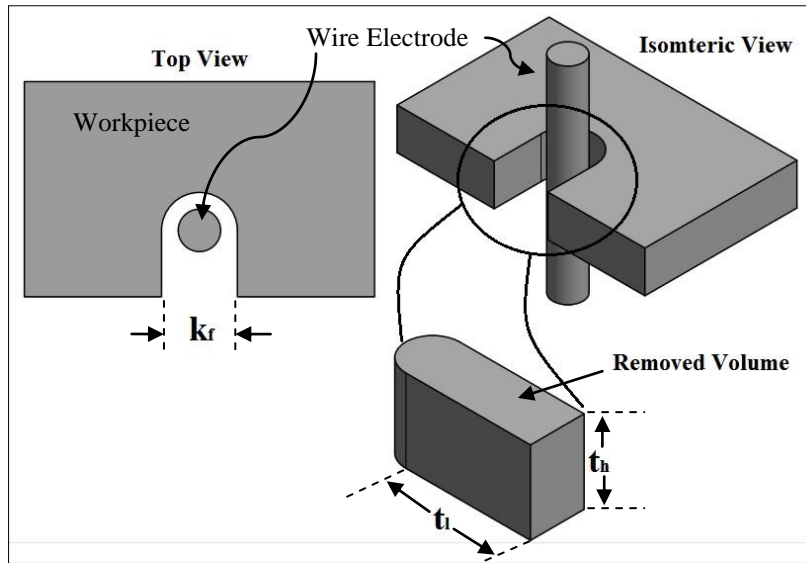


Figure 4.33. Kerf width profile

To evaluate MRR (volumetric) following equation was implemented:

$$MRR = \frac{[(t_l \times t_h \times k_f) + \frac{\pi}{2} \times (\frac{k_f}{2})^2 \times t_h]}{T} \text{ (mm}^3/\text{min)}$$

Where,

t_l = travel length (mm)

t_h = workpiece thickness (mm)

k_f = kerf width (mm)

T = time taken for the travel length (minutes)

Based on above equation MRR of homogenized and non-homogenized (as cast) alloys were evaluated and results are tabulated in Table 4.17. Respective plots are depicted in Figure 4.34.

Table 4.17. MRR of Homogenized and Non-Homogenized samples (in mm³/min)

| Exp No. | Homogenized | | | Non-Homogenized | | |
|---------|-------------|-------|-------|-----------------|-------|-------|
| | MRR11 | MRR12 | MRR13 | MRR11 | MRR12 | MRR13 |
| 1 | 0.84 | 0.84 | 0.84 | 0.34 | 0.53 | 0.42 |
| 2 | 1.62 | 1.15 | 1.35 | 0.42 | 0.49 | 0.51 |
| 3 | 1.18 | 1.07 | 1.111 | 0.62 | 0.69 | 0.71 |
| 4 | 0.32 | 0.35 | 0.36 | 0.34 | 0.29 | 0.33 |
| 5 | 3.23 | 3.76 | 4.02 | 2.27 | 3.51 | 4.01 |
| 6 | 1.21 | 1.23 | 1.25 | 1.47 | 1.42 | 1.73 |
| 7 | 1.47 | 1.58 | 1.87 | 3.09 | 2.63 | 2.89 |
| 8 | 1.79 | 1.76 | 2.19 | 2.03 | 2.08 | 2.31 |
| 9 | 4.62 | 4.79 | 4.91 | 3.05 | 4.21 | 5.23 |

| | | | | | | |
|-----------|------|------|------|------|------|------|
| 10 | 4.82 | 6.15 | 6.38 | 6.37 | 6.14 | 6.36 |
| 11 | 3.85 | 5.58 | 6.11 | 6.19 | 6.41 | 6.19 |
| 12 | 2.73 | 3.66 | 4.89 | 5.64 | 5.49 | 5.73 |
| 13 | 4.96 | 4.79 | 5.09 | 5.02 | 5.28 | 5.26 |
| 14 | 5.27 | 4.88 | 4.95 | 5.15 | 5.36 | 5.46 |
| 15 | 4.67 | 4.76 | 4.88 | 4.95 | 4.71 | 5.06 |
| 16 | 5.75 | 6.23 | 6.56 | 6.35 | 6.13 | 6.25 |

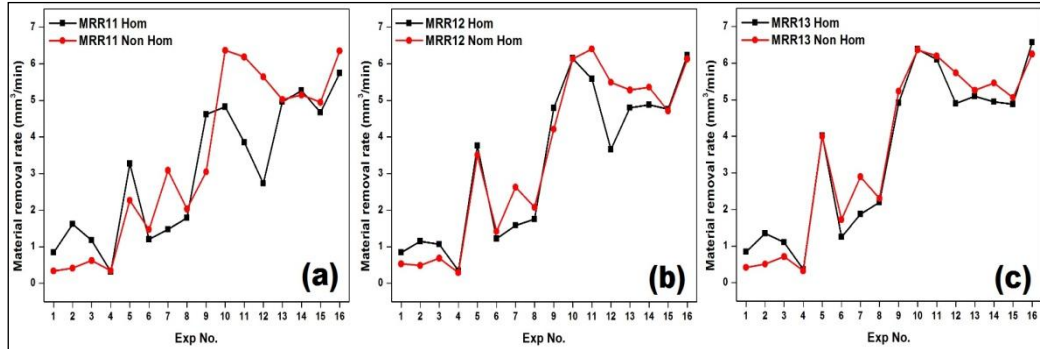


Figure 4.34. MRR L16 plots for homogenized and non-homogenized samples

From Figure 4.34(a-c) it can be seen that MRR of homogenized samples in most of the cases for a given experimental trial (out of 16 experimental trials) is lesser than non-homogenized samples. However, it can be seen from Figure 4.34(c) that variation in MRR for homogenized sample (TNC13) is close to non-homogenized sample (TNC13). But such variation is more prominent in case of TNC11 (Figure 4.34a). Homogenization leads to more uniform crystal structure compared to as cast melt and therefore leads to increased thermal conductivity, the result of which is more prominent for TNC11 (from Figure 4.34a). Reduced MRR of homogenized TNC11 alloy compared to as cast alloy indicating this change. However, during previous discussion in section 4.5 it was concluded that as cast TNC11 has lower thermal conductivity compared to as cast TNC12 and TNC13. In this case, it can be seen that difference in MRR experimental values for as cast TNC12 and TNC13 and homogenized TNC12 and TNC13 is not significant which implies negligible change in thermal conductivity of these alloys. From our previous discussion it is clear that homologous alloys (TNC11, TNC12 and TNC13) subjected to similar machining conditions (or parameters) and exhibiting reduced MRR indicates higher thermal conductivity. At higher thermal conductivity, the material will transfer the local heating caused by sparking to the nearby matrix of the material. Hence less than usual

melting will take place in the machining zone. This indicates that homogenization leads to increased thermal conductivity which is a result of uniform melt and grain structure. This leads to more efficient conduction of heat across the material compared to as cast material (which has preferably a heterogeneous melt compared to its homogenized counterpart). Investigation by Zhao et al. (2016) reveals that homogenization heat treatment leads to formation of ternary phases, which improves thermal and electrical conductivity of Al-Mg-Si alloy and WEDM results by Hsieh et al. (2009, 2013) supports findings of the current investigation.

4.8.2 Effect of homogenization on Surface Roughness

Table 4.18. SR of Homogenized and Non-Homogenized samples (in μm)

| Exp No. | Homogenized | | | Non-Homogenized | | |
|---------|-------------|------|------|-----------------|------|------|
| | SR11 | SR12 | SR13 | SR11 | SR12 | SR13 |
| 1 | 1.87 | 1.6 | 1.5 | 1.85 | 1.63 | 1.53 |
| 2 | 1.35 | 1.38 | 1.29 | 1.30 | 1.34 | 1.3 |
| 3 | 1.01 | 1.05 | 1.1 | 1.06 | 1.47 | 1.46 |
| 4 | 1.20 | 0.79 | 1.01 | 2.32 | 2.26 | 2.13 |
| 5 | 1.53 | 1.86 | 1.75 | 3.05 | 3.2 | 2.7 |
| 6 | 2.3 | 1.84 | 2.12 | 2.59 | 2.3 | 2.89 |
| 7 | 2.6 | 2.23 | 2.05 | 3.48 | 3.2 | 2.72 |
| 8 | 2.12 | 2.28 | 1.98 | 3.09 | 3.36 | 2.6 |
| 9 | 2.25 | 1.86 | 1.87 | 3.61 | 2.99 | 3.01 |
| 10 | 2.43 | 2.18 | 2.09 | 3.62 | 3.04 | 2.9 |
| 11 | 2.6 | 2.12 | 1.95 | 3.89 | 3.48 | 3.14 |
| 12 | 2.8 | 2.3 | 2.45 | 3.99 | 3.16 | 3.33 |
| 13 | 2.68 | 2.8 | 2.6 | 3.97 | 3.19 | 3.28 |
| 14 | 2.74 | 2.3 | 2.1 | 3.54 | 3.2 | 3.08 |
| 15 | 2.65 | 2.5 | 2.35 | 3.96 | 3.5 | 3.15 |
| 16 | 2.95 | 2.21 | 2.41 | 4.2 | 3.32 | 3.19 |

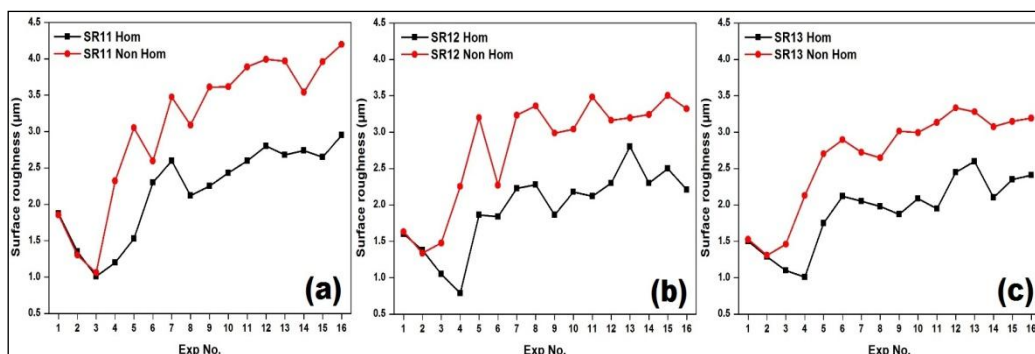


Figure 4.35. SR L16 plots for homogenized and non-homogenized samples

Table 4.18 represents surface roughness of machined surfaces of homogenized and non-homogenized (as cast) TNC11, TNC12 and TNC13 for L16 experimental trials. Figure 4.35(a-c) indicates the variation in machined surface roughness for TNC11, TNC12 and TNC13 with and without homogenization. From Figure 4.35 it is evident that surface roughness of homogenized samples are lower than their as cast counterparts. Trend of increased surface roughness with increasing pulse energy (discharge energy) is applicable for both as cast and homogeneous melt. However, reduced surface roughness due to homogenization further justifies rationalization given in previous section (effect of homogenization on MRR). Increased thermal conductivity leads to smaller crater formation and readily dislodgeable re-solidified melted debris which leads to lower surface roughness. This happens due to faster conduction of heat in high thermal conductivity material due to which impact of spark discharge (which creates a crater) has weaker effect on machined surface and creates smaller, shallow craters which results in lower surface roughness. Figure 4.35(a) represents surface roughness of TNC11 (homogenized and non-homogenized). It can be seen that variation in surface roughness at low discharge energy (experimental trial 1-3) is low which indicates that impact of low discharge energy has similar effect on homogenized and as cast material. Similar behavior was observed for TNC12 and TNC13 and can be observed in Figure 4.35(b) and 4.35(c). Figure 4.36 shows surface morphology of machined surface for as cast and homogenized samples where it can be seen that sample machined after homogenization treatment has lesser amount of debris and minimum micro-voids which contribute in lower surface roughness. For the ease of understanding and clarity, machined surface defects such as micro-voids and micro-cracks are marked in as cast machined micrograph. Findings by Nasr et al. (2007) while investigating on effect of workpiece thermal properties on machining results bear analogy with current findings. Finally, it can be concluded from the above results that surface roughness reduces due to homogenization under similar machining conditions for a given material (in our case TNC11, TNC12 and TNC13). This can be attributed to enhanced thermal conductivity due to uniform melt due to homogenization treatment of these alloys. Although surface roughness reduces, decreased MRR in previous section could be detrimental in certain cases. However,

reduced surface roughness of homogenized sample implies superior surface quality compared to as cast material.

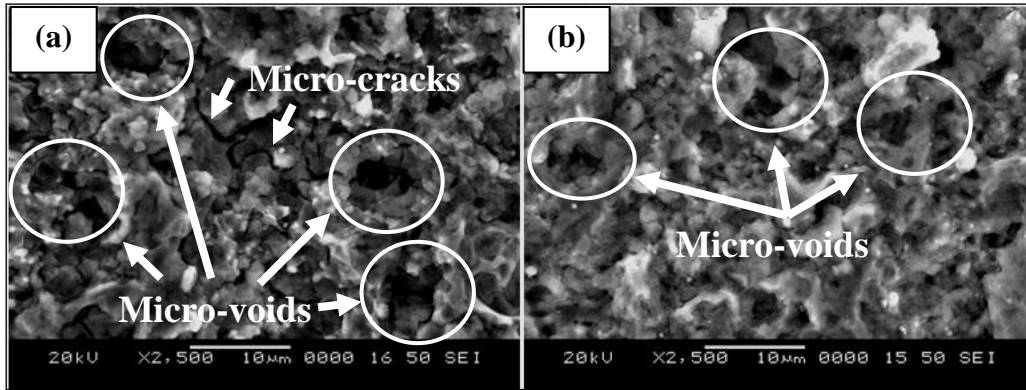


Figure 4.36. Machined surface morphology of TNC11 (a)As cast (b)Homogenized

4.8.3 Effect of homogenization on Kerf Width

Table 4.19. KW of Homogenized and Non-Homogenized samples (in μm)

| Exp No. | Homogenized | | | Non-Homogenized | | |
|---------|-------------|------|------|-----------------|------|------|
| | KW11 | KW12 | KW13 | KW11 | KW12 | KW13 |
| 1 | 305 | 313 | 308 | 300 | 300 | 303 |
| 2 | 294 | 306 | 302 | 297 | 300 | 297 |
| 3 | 323 | 328 | 318 | 305 | 303 | 301 |
| 4 | 300 | 305 | 300 | 320 | 343 | 315 |
| 5 | 335 | 336 | 326 | 319 | 317 | 312 |
| 6 | 292 | 301 | 297 | 333 | 333 | 332 |
| 7 | 285 | 291 | 290 | 311 | 310 | 307 |
| 8 | 282 | 289 | 295 | 315 | 323 | 316 |
| 9 | 313 | 306 | 315 | 325 | 336 | 331 |
| 10 | 320 | 322 | 320 | 342 | 329 | 323 |
| 11 | 313 | 317 | 315 | 319 | 329 | 322 |
| 12 | 325 | 320 | 323 | 324 | 332 | 320 |
| 13 | 326 | 290 | 310 | 330 | 284 | 302 |
| 14 | 324 | 310 | 326 | 321 | 280 | 333 |
| 15 | 344 | 339 | 340 | 357 | 353 | 357 |
| 16 | 331 | 332 | 333 | 348 | 342 | 347 |

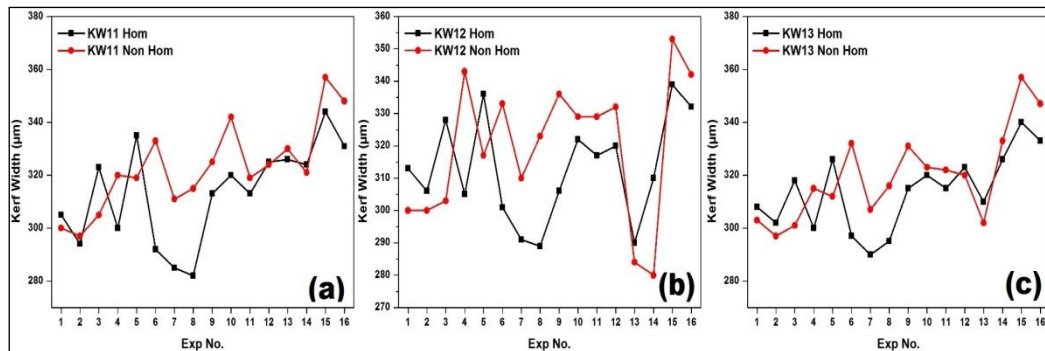


Figure 4.37. KW L16 plots for homogenized and non-homogenized samples

Table 4.19 represents kerf width of L16 experimental runs for homogenized and as cast TNC11, TNC12 and TNC13 whereas Figure 4.37(a-c) shows KW plots, although an increased kerf width was observed for certain experimental runs, overall behavior of KW along entire L16 experimental runs indicate that homogenized samples exhibit lower kerf width compared to their as cast counterparts. This phenomenon can be explained by discussion performed in the previous two sections. Increased thermal conductivity of homogenized alloys lead to lower melting of material from the machined surface and hence narrow width of cut (kerf width, KW). Whereas for as cast material more material could be removed for a similar machining condition, for homogenized material (having higher thermal conductivity) lesser material could be melt and leads to narrow kerf formation. Lower kerf indicates higher dimensional accuracy. Therefore, it can be concluded from this section that homogenization of TNC11, TNC12 and TNC13 could help in reducing dimensional accuracy as it leads to narrow kerf formation. Based on results obtained from machining of these alloys (homogenized and as cast) experimental run 7 and 8 provides lowest kerf width whereas MRR and SR have nominal values. Figure 4.38 shows kerf width of experimental run 4. This trial was chosen so as to understand the extent of influence of varying thermal conductivity on machining behavior even at low discharge energy machining conditions. These micrographs show the top view of the kerf of as cast and homogenized samples where it can be seen that more amount of resolidified debris (marked with arrow) are present at the kerf boundary for the as cast sample. This phenomenon proves that as cast material has a lower thermal conductivity due to which more amount of melted debris were formed under similar machining conditions

whereas homogenized sample has lower amount of debris available for resolidification being thermally more conductive, hence lower kerf width. Behavior of kerf width variation is similar to findings by Khan (2011) and Zhao et al. (2016) where it was found that higher thermal conductivity of the workpiece material leads to lower material removal rate and improved profile accuracy.

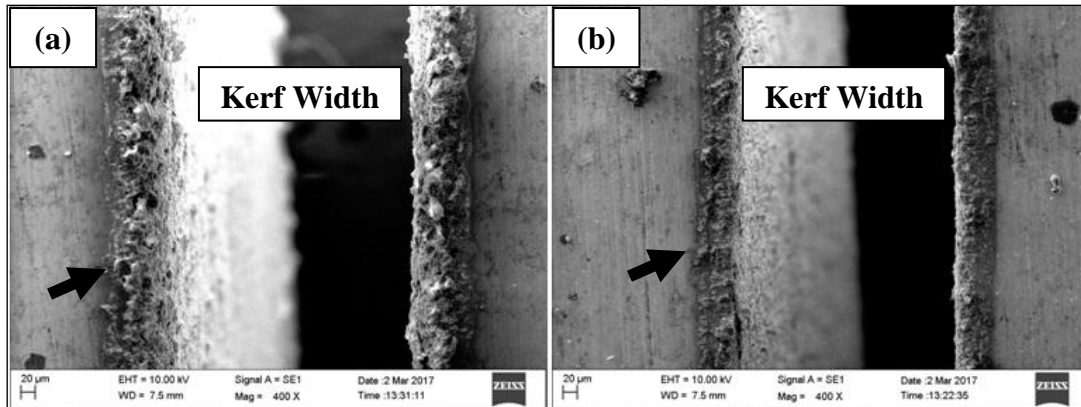


Figure 4.38. Kerf width of : (a) As cast and (b) Homogenized sample

4.8.4 Effect of homogenization on Recast Layer Thickness

Table 4.20. RLT of Homogenized and Non-Homogenized samples (in μm)

| Exp No. | Homogenized | | | Non-Homogenized | | |
|---------|-------------|-------|-------|-----------------|-------|-------|
| | RLT11 | RLT12 | RLT13 | RLT11 | RLT12 | RLT13 |
| 1 | 8.9 | 10.5 | 13.2 | 2.9 | 4.2 | 5.5 |
| 2 | 12.1 | 9.6 | 10.5 | 4.3 | 7.8 | 8.0 |
| 3 | 9.4 | 11.2 | 12.6 | 6.4 | 6.8 | 9.0 |
| 4 | 14.9 | 12.6 | 13.3 | 15.9 | 18.8 | 14.2 |
| 5 | 17.1 | 17.3 | 17.8 | 9.6 | 9.7 | 12.1 |
| 6 | 8.9 | 7.8 | 7.2 | 18.0 | 17.2 | 10.8 |
| 7 | 8.1 | 9.1 | 8.7 | 8.5 | 15.9 | 18.9 |
| 8 | 8.2 | 7.6 | 9.1 | 6.9 | 14.6 | 15.3 |
| 9 | 15.2 | 15.5 | 16.1 | 9.4 | 12.5 | 13.5 |
| 10 | 19.5 | 13.5 | 17.5 | 11.3 | 18.9 | 14.4 |
| 11 | 12.9 | 15.2 | 15.3 | 11.1 | 15.4 | 17.9 |
| 12 | 15.6 | 13.8 | 14.3 | 18.7 | 14.6 | 16.7 |
| 13 | 14.2 | 13.2 | 12.9 | 12.9 | 10.9 | 10.2 |
| 14 | 16.3 | 14.4 | 16.8 | 12.9 | 11.2 | 11.5 |
| 15 | 18.9 | 13.8 | 18.1 | 13.8 | 15.4 | 15.9 |
| 16 | 19.2 | 16.8 | 18.9 | 14.3 | 15.0 | 16.3 |

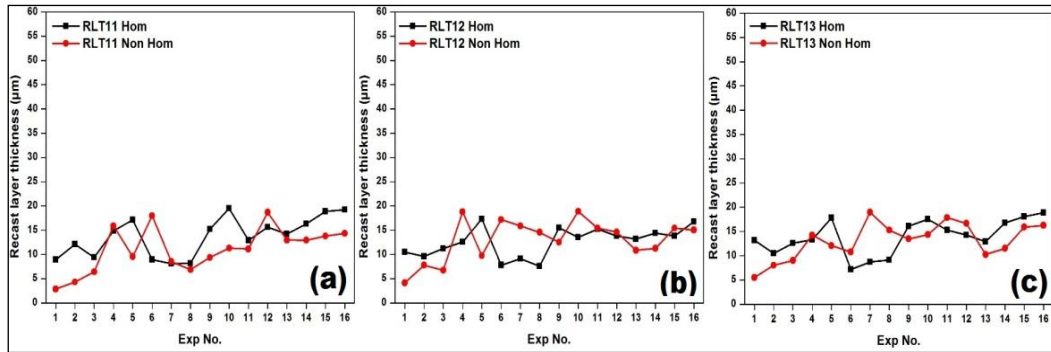


Figure 4.39. RLT L16 plots for homogenized and non-homogenized samples

L16 experimental values of recast layer thickness for homogenized and as cast alloys are tabulated in Table 4.20. Figure 4.39(a-c) represents RLT plots for all experiments. Although low RLT was observed for experimental 6-8, overall behavior of RLT for homogenized and as cast material show that RLT is more for homogenized samples. This is in correlation with the discussions made in the previous sections. Due to increased thermal conductivity of these alloys after homogenization, for a specific discharge energy lesser material was melt from the surface and most of the thermal energy was distributed to the core of the workpiece. This phenomenon leads to melting of material from within few microns from the machining surface but soon resolidifies due to quenching by dielectric medium of WEDM process. It can be seen from Figure 4.39(a-c) that at higher pulse energy settings (9-16 experimental runs) RLT varies a lot for as cast material. However, for homogenized material it can be seen that RLT variation at those parameters (9-16 experimental runs) are not as diverse as as-cast material. Therefore, it can be inferred from this section that although RLT increases due to homogenization treatment, at higher discharge energy it does not varies as par as it does during machining of as cast material. Also for experimental run 6-8 low RLT was noted which was lesser than as cast RLT. This happened due to combination of low duty factor and suitable servo voltage and wire feed rate as discussed in section 4.6.2.1 which indicates that for certain experimental runs low RLT can be achieved by homogenization.

Figure 4.40(a,b) shows recast layer thickness of as cast and homogenized sample of 6th experimental run for TNC11 alloy. It is clear that recast layer thickness of as cast sample is more than homogenized sample and influence of increased thermal

conductivity can be seen from voids that have formed under the recast layer for homogenized sample which is absent for the as cast sample indicating a defect free smooth sub surface layer. As discussed earlier, increased thermal conductivity of homogenized sample leads to more melting of subsurface material (few microns underneath) causing inflation of layers above in the form of micro voids leading to increased recast layer thickness. Therefore, presence of micro voids further confirms the above discussion and have been marked in Figure 4.40b for the ease of understanding.

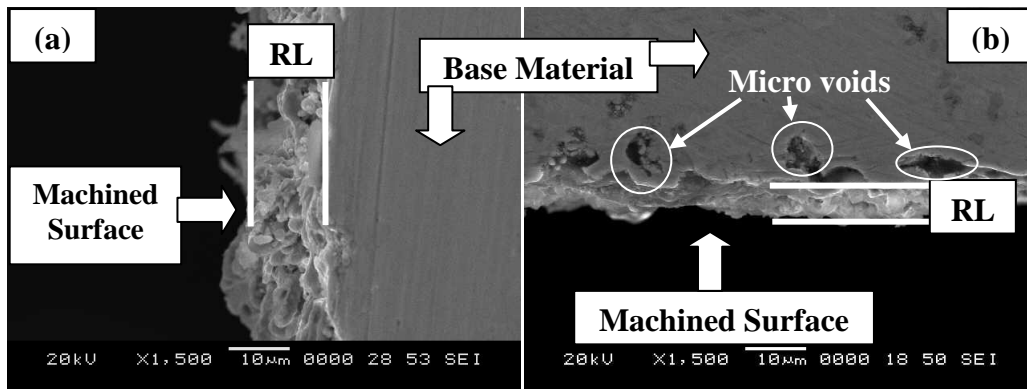


Figure 4.40. RLT of 6th experimental run for (a) As cast (b) Homogenized samples

4.9 IDENTIFICATION OF OPTIMUM MACHINED SURFACE MORPHOLOGY

Until now results of machining experimentation on TiNiCu shape memory alloys indicate that a particularly ideal machined surface morphology cannot be determined as there are several factors which influence its machined surface. Industry prefers a lower surface roughness where TiNiCu shape memory alloys find its applications mostly as sensors and actuators. These components when machined with WEDM must embrace suitable characteristics such as good machined surface, high dimensional accuracy and nominal flexibility. Each of the characteristics named above relates to machined surface morphology, kerf width and machined surface microhardness during WEDM of TiNiCu shape memory alloys. This section therefore attempts to identify suitable range of machining parameters which will yield suitable surface roughness, kerf width and machined surface microhardness to carry out further experimentation on machined surface morphology using Box Behnken design

of experiments. Box Behnken design of experiment fits ideally for the current objective as it will generate higher order response surfaces (end result being micrographs of machined surface) with the help of fewer experimental runs compared to factorial design of experiments. Since odd number of levels were identified for this study on the later stage, it became more relevant for this study due to its rotatable design. Further elaboration is given in the upcoming section.

4.9.1 Identification of suitable machining parameters yielding desirable response

Analysis of Variance and Taguchi Analysis from section 4.4 shows that Pulse on time (T_{on}), Pulse off time (T_{off}) and Servo voltage (SV) have significant influence on Material Removal Rate (MRR), Surface Roughness (SR), Kerf Width (KW) and Recast Layer Thickness (RLT). Therefore, it is imperative to implement T_{on} , T_{off} and SV for investigation of machined surface morphology using Box Behnken design of experiments.

Results of section 4.5 reveals that although material removal rate surges beyond 7th experimental run, surface roughness increases which is not desirable. Therefore, T_{on} of 110 μ s and below will yield lower surface roughness. Since lowest T_{on} used is 100 μ s, an intermediate value of 105 μ s has been considered for Box Behnken experimentation. Section 4.6 and 4.7 also exhibit that beyond 7th experimental run, machined surface microhardness, kerf width and recast layer thickness surge which affect shape recoverability and part accuracy of a WEDMed component. Scanning electron micrographs of machined surface for experimental run 4th, 6th, 11th and 14th show that 6th experimental run has least surface roughness, reason being combination of lower discharge energy and higher servo voltage value (60 V). Effects plot in section 4.4.3 indicates that surface roughness does not varies much between 15 V to 45 V and drops instantly at 60 V. Therefore, range of servo voltage value in this study has been set between 45 V to 60 V with an intermediate value of 52 V. It was also found that T_{off} has significant influence on recast layer thickness during WEDM of TiNiCu shape memory alloys. Shorter T_{off} indicates thinner recast layer formation and hence 20 to 30 μ s have been selected for machined surface morphology study along

with an intermediate value of 25 μs . Finally, variable parameters for the current study are listed in Table 4.21 given below.

Table 4.21. Selected parameter and their range for Box Behnken experimentation

| Parameter Name | Level 1 | Level 2 | Level 3 |
|-------------------------------------|-------------------|-------------------|-------------------|
| Pulse on time (T_{on}) | 100 μs | 105 μs | 110 μs |
| Pulse off time (T_{off}) | 20 μs | 25 μs | 30 μs |
| Servo voltage (SV) | 45 Volts | 52 Volts | 60 Volts |

4.9.2 Box Behnken - Design of Experiment

Based on rules of Box Behnken design of experiments all variables are significant and are chosen as discussed in the previous section. For a three factor - three level experimental design Box Behnken technique in Minitab software recommends experimental runs as shown in Table 4.22. Experimental run order and standard order are kept different in order to minimize error due to repetitive parameters. Randomization of experimental run minimizes such errors.

Table 4.22. DOE using Box Behnken technique for surface morphology experiments

| Experimental Run Order | Experimental Run Standard Order | T_{on} | T_{off} | SV | Duty Factor |
|------------------------|---------------------------------|-----------------|------------------|----|-------------|
| 1 | 15 | 110 | 25 | 60 | 0.81 |
| 2 | 4 | 105 | 30 | 45 | 0.77 |
| 3 | 11 | 110 | 20 | 52 | 0.85 |
| 4 | 12 | 105 | 25 | 52 | 0.81 |
| 5 | 6 | 105 | 25 | 52 | 0.81 |
| 6 | 14 | 100 | 20 | 52 | 0.83 |
| 7 | 7 | 105 | 25 | 52 | 0.81 |
| 8 | 2 | 110 | 30 | 52 | 0.79 |
| 9 | 8 | 100 | 30 | 52 | 0.77 |
| 10 | 9 | 110 | 25 | 45 | 0.81 |
| 11 | 5 | 105 | 20 | 60 | 0.84 |
| 12 | 1 | 105 | 30 | 60 | 0.78 |

| | | | | | |
|----|----|-----|----|----|------|
| 13 | 13 | 100 | 25 | 45 | 0.8 |
| 14 | 3 | 100 | 25 | 60 | 0.8 |
| 15 | 10 | 105 | 20 | 45 | 0.84 |

Based on generated parameter sets as shown in Table 4.22, WEDM experimentation was carried out. Machined surfaces were studied using scanning electron microscope to identify nature of surface morphology using scanning electron micrographs. Obtained images were investigated thoroughly to identify variation in surface morphology due to variation in parameter which in turn helped in identifying suitable parameter levels to perform efficient wire electro discharge machining of TiNiCu shape memory alloys.

4.9.3 Surface Morphology of Machined Surface using Box Behnken DOE

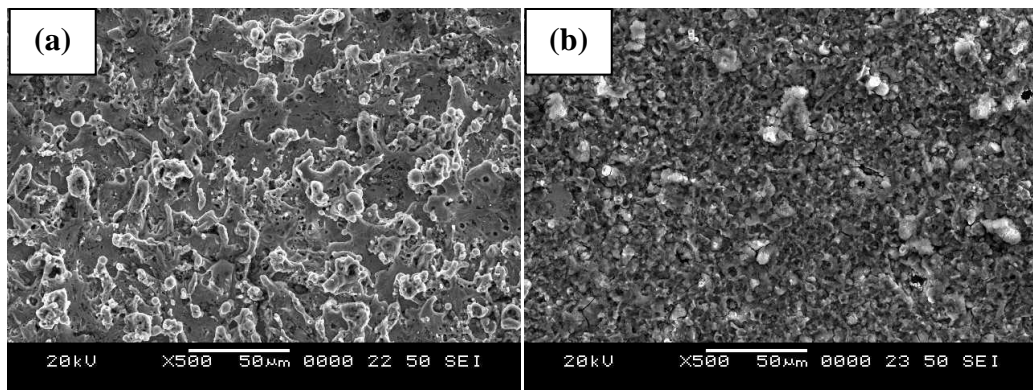


Figure 4.41. (a) Coral reef surface morphology (b) Optimum surface morphology

Based on observations made previously and from scanning electron micrographs of machined surfaces as discussed in section 4.6.2, it is evident that machined surfaces which are not exhibiting coral reef morphology are 4th, 8th and 9th experimental run. These surfaces indicate lower surface roughness compared to other experimental trials. Experimental trials leading to coral reef morphology consists of more resolidified debris and globules which contribute in higher surface roughness. Figure 4.41 displays surface morphology of experimental trial 12th and 8th to indicate difference between coral reef morphology and optimum machined surface morphology as obtained through this investigation. Input process parameters of 4th, 8th

and 9th experimental run are tabulated in Table 4.23 and scanning electron micrographs are presented in Figure 4.42.

Table 4.23. Input process parameters resulting suitable machined surface morphology

| Experimental Run | T _{on} (μs) | T _{off} (μs) | SV (Volts) | Surface Roughness (μm) |
|------------------|----------------------|-----------------------|------------|------------------------|
| 4 th | 105 | 30 | 45 | 1.16 |
| 8 th | 100 | 30 | 52 | 1.25 |
| 9 th | 110 | 25 | 45 | 1.34 |

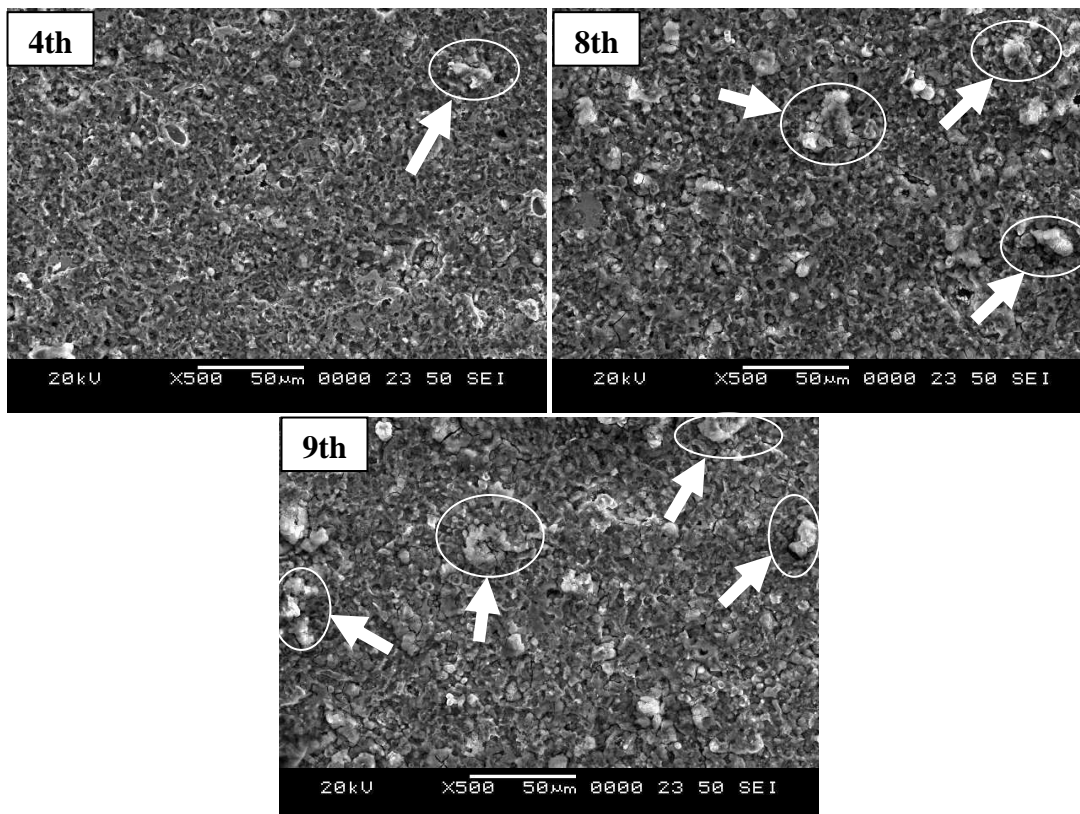


Figure 4.42. Scanning electron micrograph of optimum machined surface morphology

From the micrographs it can be seen that all three optimum machined surface morphology have similar features and represent optimum surface morphology as depicted in Figure 4.41b. However, from surface roughness tabulated in Table 4.23 it can be seen that 4th experimental run has least surface roughness. After close observation it can be seen that machined surface of 8th and 9th experimental run have more amount of debris deposited which justifies higher surface roughness recorded during investigation. Such debris are very low in case of machined surface of 4th

experimental run. Thus, T_{on} - 105 μ s, T_{off} - 30 μ s and SV - 45 Volts can be used as suitable input process parameters to generate optimum machined surface morphology during wire electro discharge machining of TiNiCu shape memory alloys.

4.10 SUMMARY

- Microstructural and XRD study of vacuum arc melted TiNiCu shape memory alloys indicate presence of TiNiCu, NiTi and TiCu phases. Sharp exothermic and endothermic peaks were observed only for alloys having equal molar ratio of Ti:Ni+Cu=1:1 during calorimetric analysis, where $Ti_{50}Ni_{25}Cu_{25}$ has least thermal hysteresis of around 6°C.
- Microhardness analysis of TiNiCu shape memory alloys reveal that for fixed Cu content alloys i.e. TNC11, TNC12 and TNC13, 10 at% increase in Ni and 10 at% drop in Ti leads to 100% rise in microhardness. For fixed Ti content alloy i.e. TNC21, TNC22 and TNC23, 10 at% increase in Cu and 10 at% drop in Ni leads to around 10% rise in microhardness.
- ANOVA and Taguchi analysis reveal that T_{on} has highest influence on MRR (91.43%), SR (88.64%) and RLT (22.59%) whereas SV has higher degree of influence on KW (46.27%) compared to T_{on} .
- Analysis of WEDM responses obtained through Taguchi's DOE shows that MRR, SR and RLT surges 1881.67%, 57.5% and 35% respectively by average due to increase in duty factor from 0.67 to 0.86, whereas KW drops around 5% by average.
- Homogenization of as cast TiNiCu shape memory alloys lead to maximum reduction in MRR, SR, KW and RLT by approximately 52%, 50%, 12% and 51% respectively.
- It was found that suitable machined surface morphology can be obtained at low to medium discharge energy settings, low peak current of 0.92 Amps and peak voltage of 31 Volts, higher flushing pressure (between 98.06 to 147.1 kPa) having downward direction flow at T_{on} - 105 μ s, T_{off} - 30 μ s, SV - 45 Volts.

CHAPTER 5

PREDICTION AND OPTIMIZATION OF WEDM RESPONSES

5.1 INTRODUCTION

In the present work artificial neural network (ANN) model is developed to predict machining responses of TiNiCu shape memory alloys machined using Wire EDM. As discussed in section 4.4, response data of TNC11 and TNC23 were chosen based on suitable characteristics they possess as a functional material. WEDM is a non-linear and highly stochastic process and it is not practical to implement theoretical models to predict machining responses. Therefore, attempt has been made in this section to develop a feed forward back propagation neural network armed with Levenberg-Marquardt training algorithm which can learn the complex physical process of WEDM in terms of real machining data. After the neural network was trained successfully, it was used to predict WEDM responses namely MRR, SR, KW and RLT using target input process parameters. Upto 6% prediction error was observed using the trained network. From the trained network, weights and biases were used to formulate fitness functions for each WEDM responses in order to perform optimization using genetic algorithm technique.

5.2 DEVELOPMENT OF SUITABLE NEURAL NETWORK

After input and output of ANN model were decided, selection of suitable network parameters was carried out. Since ANN model is a construct of nodal properties such as weights, bias, number of neurons, input layer, hidden layer, output layer etc, it is important to select suitable and proper network parameters for efficient mapping. Proper selection of network configuration is important because it influences learning time, data handling, program size etc. If a certain network model is too complex for a problem in hand which is very simple, then it would be wasteful to spend hours on training the network. Another such example consists of unnecessary number of

neurons which in turn increases calculation time and researchers find it difficult to arrive at simple solution within stipulated period of time which also impose complications like system over-clocking and RAM failure of the computer. Therefore, in this section we have emphasized on selection of optimum network parameters for successful ANN modeling.

Firstly, it is imperative to convert real machining data into "compute friendly" form which will be more convenient for the network to understand. This procedure is known as normalization of data and is a very critical step during neural network development where input and output values are converted to suitable values ranging from 0 to 1. Of the two chosen alloys, input process parameters, material removal rate, surface roughness, kerf width and recast layer thickness data were normalized using equations 3.4-3.6. Normalized inputs and outputs are tabulated in Table 5.1 and 5.2 respectively. After machining data were normalized other network parametric aspects such as neuron configuration, transfer function and training algorithm were also investigated based on trend of data.

Table 5.1. Normalized input process parameters

| Exp. No. | Raw Data | | | | Normalized Data | | | |
|----------|-----------------|------------------|----|----|-----------------|------------------|------|-----|
| | T _{on} | T _{off} | SV | WF | T _{on} | T _{off} | SV | WF |
| 1 | 100 | 20 | 4 | 15 | 0.77 | 0.4 | 0.25 | 0.4 |
| 2 | 100 | 30 | 6 | 30 | 0.77 | 0.6 | 0.5 | 0.6 |
| 3 | 100 | 40 | 8 | 45 | 0.77 | 0.8 | 0.75 | 0.8 |
| 4 | 100 | 50 | 10 | 60 | 0.77 | 1 | 1 | 1 |
| 5 | 110 | 20 | 6 | 45 | 0.85 | 0.4 | 0.75 | 0.6 |
| 6 | 110 | 30 | 4 | 60 | 0.85 | 0.6 | 1 | 0.4 |
| 7 | 110 | 40 | 10 | 15 | 0.85 | 0.8 | 0.25 | 1 |
| 8 | 110 | 50 | 8 | 30 | 0.85 | 1 | 0.5 | 0.8 |
| 9 | 120 | 20 | 8 | 60 | 0.92 | 0.4 | 1 | 0.8 |
| 10 | 120 | 30 | 10 | 45 | 0.92 | 0.6 | 0.75 | 1 |
| 11 | 120 | 40 | 4 | 30 | 0.92 | 0.8 | 0.5 | 0.4 |
| 12 | 120 | 50 | 6 | 15 | 0.92 | 1 | 0.25 | 0.6 |
| 13 | 130 | 20 | 10 | 30 | 1 | 0.4 | 0.5 | 1 |
| 14 | 130 | 30 | 8 | 15 | 1 | 0.6 | 0.25 | 0.8 |
| 15 | 130 | 40 | 6 | 60 | 1 | 0.8 | 1 | 0.6 |
| 16 | 130 | 50 | 4 | 45 | 1 | 1 | 0.75 | 0.4 |

Table 5.2. Normalized output process responses

| Exp. No. | MRR11 | MRR23 | SR11 | SR23 | KW11 | KW23 | RLT11 | RLT23 |
|----------|-------|-------|-------|-------|-------|-------|-------|-------|
| 1 | 0.019 | 0.019 | 0.748 | 0.899 | 0.95 | 1 | 1 | 1 |
| 2 | 0.017 | 0.017 | 0.923 | 1 | 1 | 0.962 | 0.908 | 0.943 |
| 3 | 0.019 | 0.023 | 1 | 0.862 | 0.867 | 0.962 | 0.777 | 0.681 |
| 4 | 0 | 0 | 0.598 | 0.739 | 0.1 | 0.442 | 0.179 | 0 |
| 5 | 0.411 | 0.559 | 0.365 | 0.438 | 0.633 | 0.615 | 0.578 | 0.971 |
| 6 | 0.149 | 0.223 | 0.511 | 0.845 | 0.4 | 0.288 | 0.044 | 0.241 |
| 7 | 0.427 | 0.489 | 0.231 | 0.299 | 0.767 | 0.846 | 0.643 | 0.744 |
| 8 | 0.232 | 0.313 | 0.352 | 0.426 | 0.7 | 0.615 | 0.746 | 0.716 |
| 9 | 0.642 | 0.733 | 0.187 | 0.285 | 0.533 | 0.385 | 0.591 | 0.736 |
| 10 | 0.901 | 0.999 | 0.185 | 0.165 | 0.25 | 0.615 | 0.468 | 0.591 |
| 11 | 0.846 | 0.922 | 0.099 | 0.036 | 0.633 | 0.577 | 0.479 | 0.441 |
| 12 | 0.796 | 0.821 | 0.065 | 0.006 | 0.55 | 0.577 | 0 | 0.582 |
| 13 | 1 | 0.793 | 0.073 | 0.106 | 0.45 | 0.519 | 0.363 | 0.549 |
| 14 | 0.658 | 0.671 | 0.209 | 0.152 | 0.6 | 0.712 | 0.365 | 0.476 |
| 15 | 0.616 | 0.716 | 0.075 | 0.045 | 0 | 0 | 0.309 | 0.543 |
| 16 | 0.789 | 1 | 0 | 0 | 0.15 | 0.25 | 0.277 | 0.455 |

Network configuration of a neural network can be defined by number of input, hidden and output layer and number of neurons each of these layers consist. In this study four input and four output responses were selected. Inputs are pulse on time (T_{on}), pulse off time (T_{off}), servo voltage (SV) and wire feed (WF). Output responses are material removal rate (MRR), surface roughness (SR), kerf width (KW) and recast layer thickness (RLT). Therefore, input and output layers consist of four neurons each. Based on equations 3.11 and 3.12, four inputs and four outputs can lead to maximum nine and minimum four neurons in the hidden layers of the neural network. After initial study it was found that although one hidden layer network configuration (4-4-4) significantly decreased training time, but poor correlation coefficient were obtained for training (R_{train}), validation ($R_{validation}$) and testing ($R_{testing}$). R-value indicates correlation coefficient and in this study three different R-values namely R_{train} , $R_{validation}$ and $R_{testing}$ were used combined to determine predictive efficiency of trained model. From Table 5.3 it can be observed that R-value of network 4-4-4 is better compared to 4-4-4. If correlation coefficient (R) is closer to 1, it indicates better mapping

conditions. After one more hidden layer was introduced in the neural network, significant improvement was observed in the correlation coefficient. Then trials were carried out to find the optimum neurons in the hidden layer with two hidden layers.

Table 5.3. R-value of different ANN architectures

| Sl. No. | Network Architecture | R_{train} | $R_{\text{validation}}$ | R_{testing} |
|---------|----------------------|--------------------|-------------------------|----------------------|
| 1. | 4-4-4 | 0.88 | 0.69 | 0.51 |
| 2. | 4-4-4-4 | 0.91 | 0.92 | 0.87 |
| 3. | 4-5-5-4 | 0.871 | 0.98 | 0.98 |
| 4. | 4-6-6-4 | 0.80 | 0.97 | 0.58 |
| 5. | 4-7-7-4 | 0.95 | 0.69 | -0.09 |
| 6. | 4-8-8-4 | 0.85 | 0.81 | 0.86 |
| 7. | 4-9-9-4 | 0.89 | 0.98 | 0.89 |

With increasing number of neurons, R-value improves. Even though 4-7-7-4 indicates better R_{training} value compared to other network architectures, its R_{testing} value indicates a negative gradient, hence not acceptable. Likewise, even though R_{testing} value of 4-5-5-4 is more than 4-9-9-4, R_{training} value of 4-9-9-4 exceeds it and hence indicates better mapping characteristics. This should also be noted that all R values represented in Table 5.3 are after first training run. After several training iterations R-value improves for 4-9-9-4 architecture and surpasses efficiency of other architectures. After network architecture has been decided (4-9-9-4), extensive investigation was carried out to decide suitable transfer function which has better predictive capability.

Transfer functions are also known as activation functions which are used to establish the mathematical relationship between input and output. A neural network can be designed with various transfer functions depending on the kind of data fed to the model. Generally transfer functions are sigmoid in nature but it may change depending on the kind of relation input and output of ANN model shares. Most widely used transfer functions are log-sigma (LS), pure-linear (PL) and tan-sigma (TS). It was found through extensive trial and error iterations that efficient training and prediction capability of ANN model can be affected by the selective use of transfer functions. To maintain uniformity in process, these transfer functions were

applied to all the neurons. Thereafter, MRR, SR, KW and RLT of alloy TNC11 were predicted using these transfer functions. The efficiency of these transfer functions to enhance the predictive quality of the network model can be clearly seen from the prediction graphs depicted in Figure 5.1(a-l).

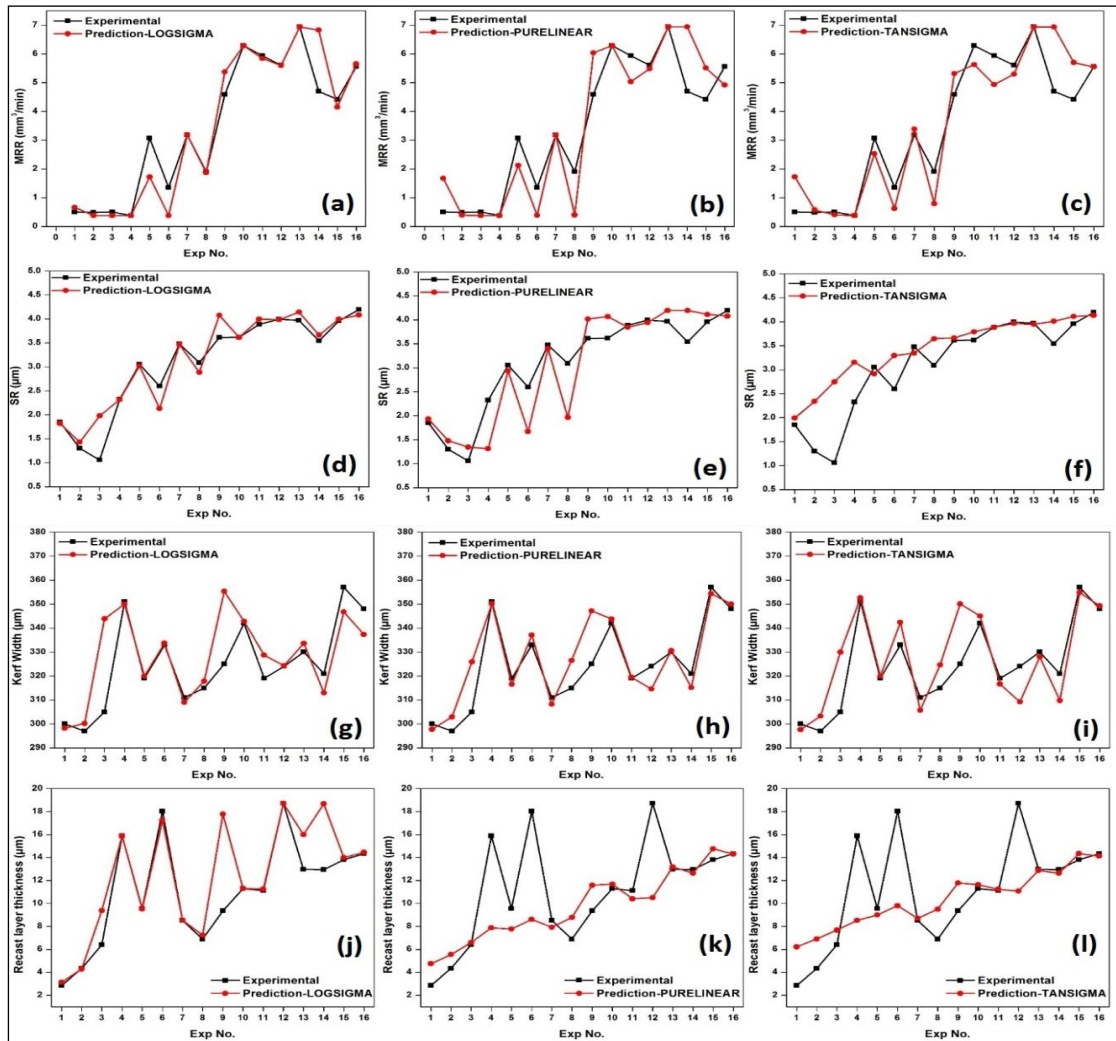


Figure 5.1. Experimental and prediction of (a-c)MRR (d-f)SR (g-i)KW (j-l)RLT

Prediction values of each experimental run has been plotted alongside the experimental value by incorporating three different transfer functions namely, log-sigma, pure-linear and tan-sigma. Figure 5.1(a-c) exhibits prediction plot for MRR, Figure 5.1(d-f) for SR, Figure 5.1(g-i) for KW and Figure 5.1(j-l) for RLT. It can be observed that LS transfer function yields better capability for prediction of MRR compared to PL and TS. Similar behavior is observed for SR and RLT prediction.

Even though these transfer functions yield similar curve fitting in case of KW, PL exhibits most accurate prediction behavior compared to LS and TS. It is obvious that prediction error is very high in all of the above instances of MRR, SR, KW and RLT. However, importance of proper transfer function selection is evident. It is to be noted that training of the network using log-sigma module was stopped after 15th cycle. For pure-linear and tan-sigma, training was stopped after 22nd and 40th cycle respectively. This shows that even after pure-linear and tan-sigma transfer function embedded network models were trained for more cycles, they failed to deliver accurate prediction. However, log-sigma function yielded better results compared to pure-linear and tan-sigma. Correlation coefficient (R) of the network model for each transfer function is tabulated in Table 5.4. From Table 5.4 it is evident that by using Log-sigma transfer function during training stage, better correlation and higher performance can be achieved. In case of training, validation and testing phases, log-sigma yielded better fitting compared to pure-linear and tan-sigma transfer functions.

Table 5.4 Training performance chart using different transfer functions

| Training performance variables | LOG-SIGMA | PURE-LINEAR | TAN-SIGMA |
|--|------------------|--------------------|------------------|
| Training coefficient (R_{train}) | 0.99 | 0.91 | 0.91 |
| Validation coefficient ($R_{\text{validation}}$) | 0.99 | 0.92 | 0.94 |
| Testing coefficient (R_{testing}) | 0.99 | 0.98 | 0.95 |
| Performance | 0.00226 | 0.0175 | 0.0169 |
| Gradient | 0.0144 | 0.0661 | 0.0809 |
| Mu (Training gain) | 0.001 | 0.001 | 0.001 |
| Epoch | 4 | 39 | 17 |
| Validation checks | 4 | 39 | 17 |

Finally it was concluded that log-sigma (LS) was found suitable transfer function for modelling and prediction of MRR, SR and RLT whereas pure-linear was suitable for KW prediction and were used in further investigation. Thereafter, effort has been put to apply suitable training algorithm to the neural network. Training algorithms are used in ANN to minimize the error that is generated during ongoing training phase of the neural network. Weights and bias are constantly updated during training process using the training algorithm. This update of weights and biases helps to establish better mapping or training of the neural network by reducing the error. Since Wire

EDM process is a non-linear process it is of utmost importance to minimize the errors which generates after activation of the neuron. This error is processed in terms of a error function through training algorithm and subsequently weights and biases are updated slightly so as to reduce the error until it reaches a minimum allowable limit. Levenberg-Marquardt training algorithm was used in this study for its ability to map non-linear relations. This training algorithm was supported in a study by Conde et al. (2018) due to its fast learning rate and accuracy. Figure 5.2 indicates the training algorithm in action.

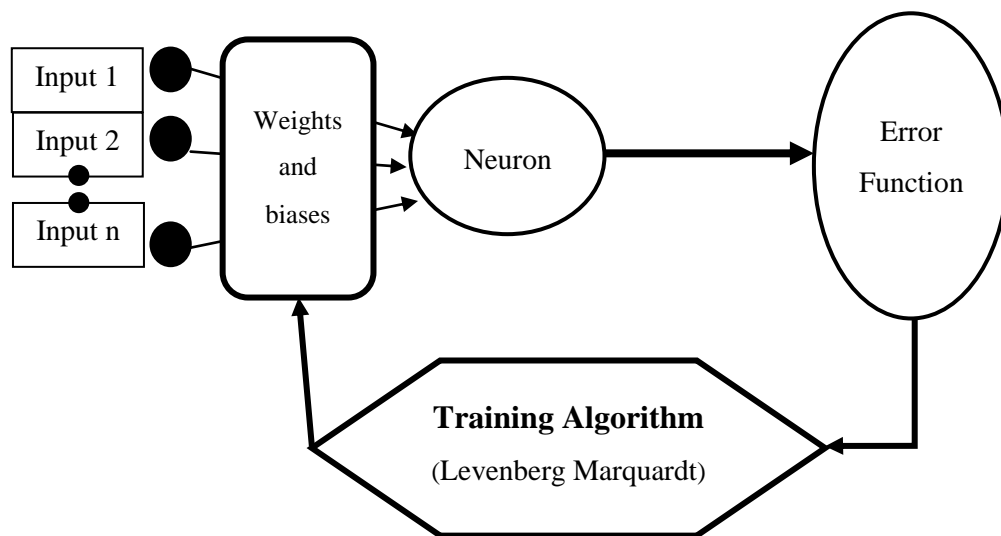


Figure 5.2. Training algorithm updating weight and bias to minimize error

Based on the trend of input and output of the network, training parameters were optimized. Training parameters used to optimize the neural network are epochs, goal, minimum gradient, maximum fails, mu, mu decrease and mu increase. Role of these parameters are briefly explained below :

Epochs - Number of iterations to done before network training is stopped.

Goal - Network function used to define the performance of the trained network.

Minimum gradient - Minimum performance gradient value of the network.

If this value becomes too small, training is stopped as continued training is unlikely to produce any significant improvements.

Maximum fails - Maximum number of validation checks before training is stopped.

Stopping of validation checks indicate network is avoiding error accumulation.

Mu - This training parameter works as a blending factor.

The greater it is the more weight is given to gradient descent learning and a small step size. The smaller it is the more weight is given to large step size. Mostly used with Levenberg-Marquardt algorithm.

Mu decrease - Amount to decrease mu after an unsuccessful step in training with the Levenberg-Marquardt training algorithm.

Mu increase - Amount to increase mu after a successful step in training with the Levenberg-Marquardt training algorithm.

After the development of an efficient neural network was completed, training of the network was carried out to find suitable R values. After network reached good correlation coefficient, training was stopped and prediction was carried out and subsequent results are discussed in the upcoming section.

5.3 PREDICTION OF WEDM RESPONSES

After successful training of the artificial neural network it is expected to provide suitable prediction results. By training the neural network, relationship between inputs and outputs were mapped in terms of weights, biases, training and learning functions. In this study, four input sets were selected based on duty factor. Duty factor is the ratio of discharge duration to discharge cycle. This factor represents energy dissipation factor during sparking in Wire EDM process. In this case duty factor ranges from 0.66 to 0.86. These four input parameter sets were chosen based on four intermediate values between the range, which are 0.75, 0.78, 0.81 and 0.84. Table 5.5 represents the four sets chosen for testing of the trained neural network for predictive study. Figure 5.3 and 5.4 indicates the comparison of experimental and predicted responses of these chosen input sets.

Table 5.5 Input sets chosen for testing

| Sl. No. | Duty Factor | T _{on} (μs) | T _{off} (μs) | SV (Volts) | WF (m/min) |
|---------|-------------|----------------------|-----------------------|------------|------------|
| 1. | 0.75 | 110 | 20 | 45 | 6 |
| 2. | 0.78 | 110 | 30 | 60 | 4 |
| 3. | 0.81 | 120 | 40 | 30 | 4 |
| 4. | 0.84 | 130 | 30 | 15 | 8 |

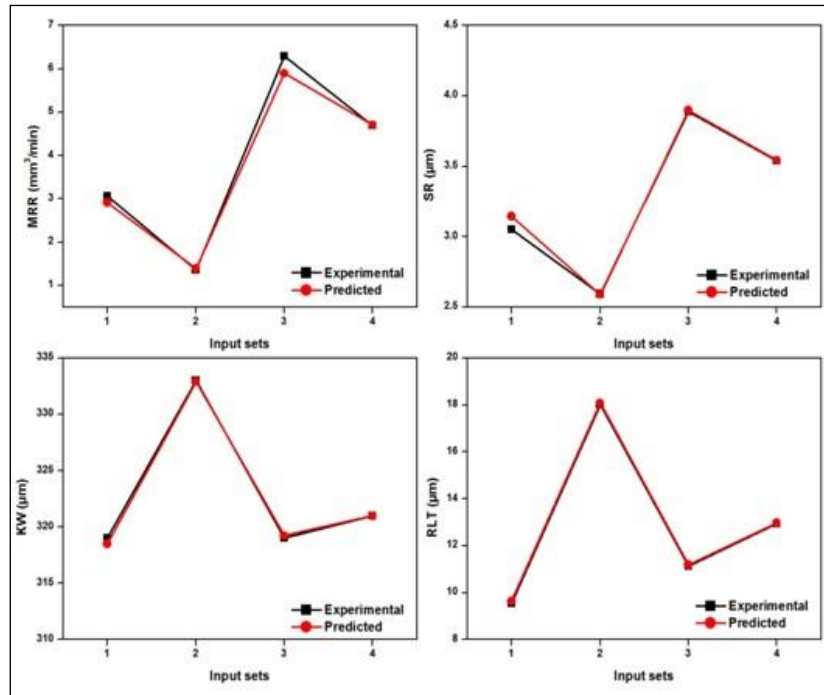


Figure 5.3. Experimental and predicted values of responses of TNC11

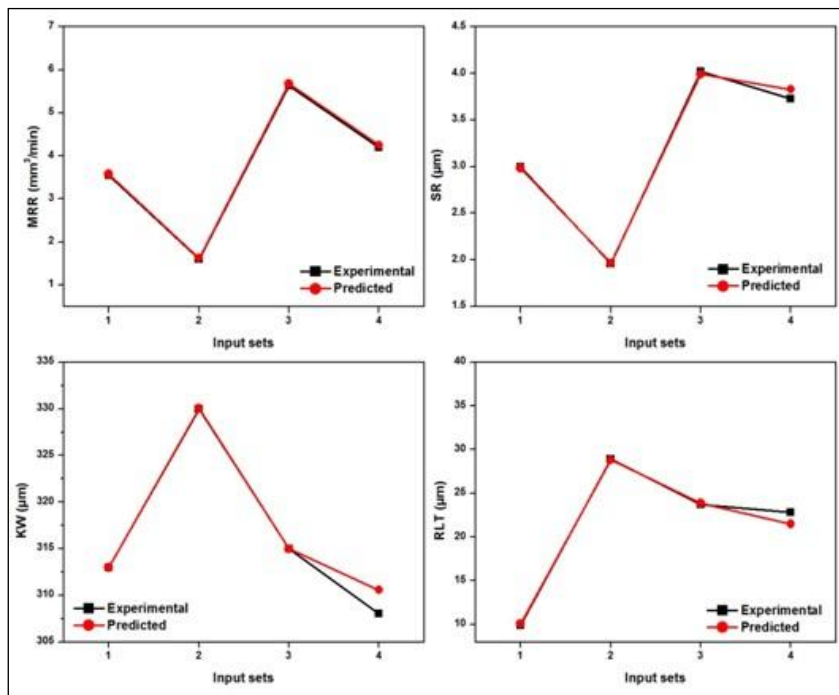


Figure 5.4. Experimental and predicted values of responses of TNC23

Percentage absolute errors associated with prediction of response for TNC11 and TNC23 are tabulated in Table 5.6 and 5.7 respectively. Percentage prediction error is given by the equation 5.1.

$$\% \text{ Error (prediction)} = \left| \frac{(\text{Experimental value} - \text{Predicted value})}{\text{Experimental value}} \right| \times 100 \quad (5.1)$$

Table 5.6. Percentage prediction error of TNC11

| Sl. No. | Duty Factor | Response | TNC11 | | (%) Error |
|---------|-------------|----------|--------------|-----------|--------------|
| | | | Experimental | Predicted | |
| 1. | 0.75 | MRR | 5.93 | 5.89 | 0.63 |
| | | SR | 3.89 | 3.89 | 0.22 |
| | | KW | 319 | 319.22 | 0.07 |
| | | RLT | 11.13 | 11.18 | 0.55 |
| 2. | 0.78 | MRR | 1.36 | 1.39 | 2.81 |
| | | SR | 2.59 | 2.58 | 0.21 |
| | | KW | 333 | 332.92 | 0.021 |
| | | RLT | 18.02 | 18.09 | 0.35 |
| 3. | 0.81 | MRR | 4.69 | 4.71 | 0.08 |
| | | SR | 3.54 | 3.54 | 0.04 |
| | | KW | 321 | 320.97 | 0.01 |
| | | RLT | 12.94 | 12.97 | 0.28 |
| 4. | 0.84 | MRR | 3.07 | 2.92 | 4.96 |
| | | SR | 3.05 | 3.15 | 3.06 |
| | | KW | 319 | 318.51 | 0.16 |
| | | RLT | 9.56 | 9.65 | 0.96 |

Table 5.7. Percentage prediction error of TNC23

| Sl. No. | Duty Factor | Response | TNC23 | | (%) Error |
|---------|-------------|----------|--------------|-----------|--------------|
| | | | Experimental | Predicted | |
| 1. | 0.75 | MRR | 5.64 | 5.67 | 0.56 |
| | | SR | 4.02 | 3.99 | 0.72 |
| | | KW | 315 | 314.97 | 0.01 |
| | | RLT | 23.72 | 23.86 | 0.55 |
| 2. | 0.78 | MRR | 1.61 | 1.62 | 0.91 |
| | | SR | 1.96 | 1.96 | 0.16 |
| | | KW | 330 | 330.02 | 0.01 |
| | | RLT | 28.93 | 28.81 | 0.42 |
| 3. | 0.81 | MRR | 4.1891 | 4.25 | 1.51 |
| | | SR | 3.726 | 3.83 | 2.76 |
| | | KW | 308 | 310.58 | 0.84 |
| | | RLT | 22.81 | 21.48 | 5.86 |
| 4. | 0.84 | MRR | 3.55 | 3.57 | 0.61 |
| | | SR | 2.99 | 2.98 | 0.49 |
| | | KW | 313 | 313.01 | 0.001 |
| | | RLT | 9.93 | 10.07 | 1.51 |

From the results it is evident that ANN efficiently maps input and output of WEDM process and can predict output responses with very low percentage error as low as

0.001% and as high as 5.86% (marked bold in Table 5.6 and 5.7) which is well within allowable limit. Soni et al. (2018) reported similar observation while predicting WEDM responses MRR and SR. (Therefore, ANN prediction of WEDM responses for TiNiCu shape memory alloys exhibit suitability for its adoption as a powerful predictive tool. Since the trained neural network at its current condition performs low error predictions of WEDM responses, its weights and biases for involved neurons and layers are used to generate fitness function to conduct optimization of WEDM responses using genetic algorithm. Upcoming section discusses in detail about steps followed and final fitness function for selected WEDM responses.

5.4 DEVELOPMENT OF GENETIC ALGORITHM FITNESS FUNCTION

Artificial neural network learns the non-linear relationship between input and output, in this case of WEDM's in terms of weights and biases assigned to each neuron and layers associated with the network. Figure 5.5 illustrates a straightforward and basic nature of weights and bias coupled between two layers in a neural network. Where dark circles indicate neurons from input layer and white circles indicate neurons from 1st hidden layer. w_1, w_2, w_3 and w_4 represent weights assigned to 1st neuron of the hidden layer connecting neurons from input layer and b_1 represents bias added to the hidden layer. Assignment of weights and bias depend on transfer function used and training algorithm incorporated. Signal emitted by 1st neuron (y) is represented by equation 5.2.

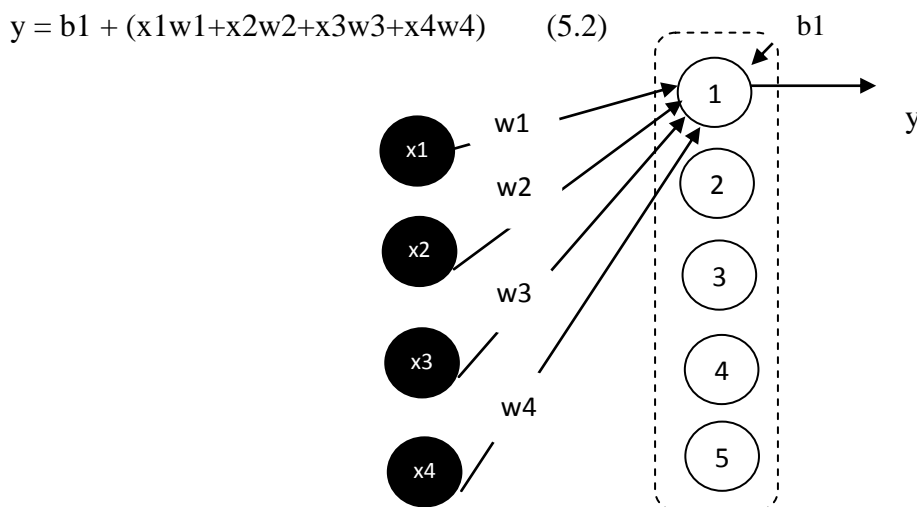


Figure 5.5. Weight and bias distribution

Following this expression, final signal that is delivered by output layer for each WEDM response represents the function in terms of weights and bias which in turn can be used as fitness function for multi objective optimization using genetic algorithm. Fitness function for material removal rate, surface roughness, kerf width and recast layer thickness for TNC11 and TNC23 are given below.

$$y(1) = \text{MRR}_{11} = 26.53 + 82.57 * x(1) - 8.29 * x(2) - 23.05 * x(3) + 7.26 * x(4);$$

$$y(2) = \text{SR}_{11} = -14.93 - 43.93 * x(1) - 3.26 * x(2) + 18.87 * x(3) + 2.88 * x(4);$$

$$y(3) = \text{KW}_{11} = -31.25 - 36.06 * x(1) + 0.51 * x(2) + 1.92 * x(3) - 46.82 * x(4);$$

$$y(4) = \text{RLT}_{11} = 30.01 - 34.42 * x(1) - 33.50 * x(2) + 15.54 * x(3) + 29.17 * x(4);$$

$$y'(1) = \text{MRR}_{23} = 67.14 + 89.42 * x(1) - 26.79 * x(2) + 27.59 * x(3) - 18.48 * x(4);$$

$$y'(2) = \text{SR}_{23} = -66.29 - 137.39 * x(1) + 1.55 * x(2) - 20.71 * x(3) + 2.34 * x(4);$$

$$y'(3) = \text{KW}_{23} = 22.82 - 64.01 * x(1) - 32.39 * x(2) - 12.68 * x(3) - 38.26 * x(4);$$

$$y'(4) = \text{RLT}_{23} = -36.82 + 15.41 * x(1) + 12.23 * x(2) + 18.57 * x(3) - 69.84 * x(4);$$

Where $y(1)$, $y(2)$, $y(3)$ and $y(4)$ represent material removal rate (MRR), surface roughness (SR), kerf width (KW) and recast layer thickness (RLT) and $x(1)$, $x(2)$, $x(3)$ and $x(4)$ represent pulse on time (T_{on}), pulse off time (T_{off}), servo voltage (SV) and wire feed (WF) respectively. Expressions with apostrophe (') represent WEDM responses for TNC23 alloy. These functions are obtained after adding weights and bias for all the layers and are considered as fitness function for optimizing WEDM responses and is discussed in the next section.

5.5 OPTIMIZATION OF WEDM RESPONSES

Objective of the present work is to find optimum input process parameters to get maximum material removal rate (MRR), minimum surface roughness (SR), kerf width (KW) and recast layer thickness (RLT). To perform optimization of a particular response variable using genetic algorithm technique, a fitness function or a non-linear function is required which expresses that response variable in terms of influencing input variables. In this case each of WEDM responses namely MRR, SR, KW and RLT are expressed in terms of T_{on} , T_{off} , SV and WF as shown in mathematical expressions in section 5.5.

At first constraints of these functions are to be determined first to make sure solutions provided after selection, crossover and mutation satisfies proper fitness value. Fitness value is the net output of each fitness function whose maximization and minimization is determined by the value of input constraints. Here constraint bounds (minimum and maximum) are set in terms of normalized values of inputs as tabulated in Table 5.1 and are formulated as follows:

$$0.7 \leq T_{on} \leq 1$$

$$0.4 \leq T_{off} \leq 1$$

$$0.4 \leq SV \leq 1$$

$$0.25 \leq WF \leq 1$$

Multi objective optimization function $y(1)$ and $y'(1)$ will be minimized automatically by genetic algorithm approach which is not desirable. However, for other response functions namely $y(2)$, $y(3)$, $y(4)$, $y'(2)$, $y'(3)$ and $y'(4)$, minimization is expected. Therefore, to avoid minimization of MRR, fitness functions $y(1)$ and $y'(1)$ are inversed as follows:

$$y(1) = \frac{1}{26.53+82.57*x(1)-8.29*x(2)-23.05*x(3)+7.26*x(4)};$$

$$y'(1) = \frac{1}{67.14+89.42*x(1)-26.79*x(2)+27.59*x(3)-18.48*x(4)};$$

Firstly, GA generates a set of coded chromosomes containing input process parameters such as pulse on time, pulse off time, servo voltage and wire feed. Then fitness value of the first population is calculated using chromosome values of the fitness function, also known as objective function. Selection operator selected as "tournament" also known as reproduction operator makes more copies of suitable population (in this case suitable WEDM responses). Thereafter, crossover factor is implied to determine improved sets of new solutions which is set at 0.8 in this study. The new solutions obtained until this point are combined with initial population to sort them as per their dominance which is determined by pareto-optimal front. Dominance of every solution is compared with every other solution using following rule:

Objective 1 (i) > Objective 2 (j) and Objective 2 (i) ≥ Objective 2 (j);

Or Objective 1 (i) ≥ Objective 1 (j) and Objective 2 (i) > Objective 2 (j); where $i \neq j$

Where i and j are chromosome numbers.

If aforementioned rules are satisfied, then solution i is marked as more dominant compared to j, or else it is marked as non-dominating. These solutions are classified as non-dominated fronts or pareto-optimal fronts having different ranks. Based on superiority of pareto-optimal fronts, which is determined by value of distance measure function, known as distance crowding function in MATLAB. The genetic algorithm was implemented using *optimtool* command and coding in MATLAB and selected parameters are tabulated in Table 5.8.

Table 5.8. Parameters settings used in GA multi objective optimization

| GA Parametric Operator | Option Used |
|----------------------------------|-------------------------|
| Population | Double vector (size 50) |
| Creation function | Uniform |
| Selection | Tournament (size 2) |
| Reproduction crossover fraction | 0.8 |
| Mutation function | Adaptive feasible |
| Crossover function | Constraint dependent |
| Migration function (direction) | Forward |
| Migration fraction | 0.2 |
| Migration interval | 20 |
| Distance measure function | Distance crowding |
| Pareto front population fraction | 0.8 |
| Hybrid function | fgoalattain |

After multi-objective genetic algorithm was performed following aforementioned procedures, based on distance measure function optimized WEDM input process parameters are tabulated in Table 5.9 and 5.10.

Table 5.9. Optimized WEDM input parameters for TNC11

| Responses | Parameters | | | |
|-----------|-----------------|------------------|----|----|
| | T _{on} | T _{off} | WF | SV |
| MRR | 130 | 25 | 4 | 60 |
| SR | 100 | 50 | 4 | 60 |
| KW | 120 | 25 | 4 | 60 |
| RLT | 100 | 20 | 4 | 15 |

Table 5.10. Optimized WEDM input parameters for TNC23

| Responses | Parameters | | | |
|-----------|-----------------|------------------|----|----|
| | T _{on} | T _{off} | WF | SV |
| MRR | 130 | 20 | 10 | 15 |
| SR | 100 | 50 | 4 | 60 |
| KW | 120 | 50 | 10 | 60 |
| RLT | 100 | 20 | 4 | 60 |

It can be observed that optimized WEDM input process parameters are not same for TNC11 and TNC23 as based on discussion in section 4.4 and 4.5, due to variation in physical properties of these alloys and results are in accordance with findings by Sahu et al. (2019). Slight variation in set of parameters is in accordance with results obtained in previous chapter and shows that genetic algorithm has successfully optimized material removal rate, surface roughness, kerf width and recast layer thickness.

5.7 SUMMARY

From results obtained in section 5.2 and 5.3 it is clear that with proper training of artificial neural network, behavior of input-output factors of complex systems like WEDM can be mapped even though they are non-linear in nature. Although error is bound to exist, prediction of output responses of Wire EDM process can be performed.

- Trained ANN model successfully predicted responses like material removal rate, surface roughness, kerf width and recast layer thickness with percentage error as low as 0.001% and as high as 5.86% which are within allowable limit.
- Multi objective optimization of WEDM responses using genetic algorithm reveals that 0.84 and 0.86 duty factor yields higher MRR for TNC11 and TNC23 respectively. Since TNC23 has a higher thermal conductivity than

TNC11, a higher duty factor is in agreement with previous results. $100 \mu\text{s } T_{\text{on}}$ and $50 \mu\text{s } T_{\text{off}}$ resulting to 0.67 duty factor was found suitable to achieve lower surface roughness. $120 \mu\text{s } T_{\text{on}}$ and $25 \mu\text{s } T_{\text{off}}$ for TNC11 and $120 \mu\text{s } T_{\text{on}}$ and $50 \mu\text{s } T_{\text{off}}$ for TNC23 was found suitable for narrow kerf width whereas $100 \mu\text{s } T_{\text{on}}$ and $20 \mu\text{s } T_{\text{off}}$ was confirmed as optimized parameters for a thinner recast layer for both TNC11 and TNC23 respectively.

CHAPTER 6

CONCLUSION AND FUTURE SCOPE

6.1 CONCLUSIONS

In this study of TiNiCu shape memory alloys $Ti_{50}Ni_{40}Cu_{10}$ (TNC11), $Ti_{45}Ni_{45}Cu_{10}$ (TNC12), $Ti_{40}Ni_{50}Cu_{10}$ (TNC13) and $Ti_{50}Ni_{35}Cu_{15}$ (TNC21), $Ti_{50}Ni_{30}Cu_{20}$ (TNC22), $Ti_{50}Ni_{25}Cu_{25}$ (TNC23) prepared using vacuum arc melting are subjected to wire electro discharge machining. Due to variation in physical properties, these homologous alloys exhibited variation in machining responses also. Several aspects of machining responses are studied in this investigation along with its prediction and optimization and thereafter following conclusions were drawn.

- Microstructural and XRD study of vacuum arc melted TiNiCu shape memory alloys indicate presence of TiNiCu, NiTi and TiCu phases. Sharp exothermic and endothermic peaks were observed only for alloys having equal molar ratio of Ti:Ni+Cu=1:1 during calorimetric analysis, where $Ti_{50}Ni_{25}Cu_{25}$ has least thermal hysteresis of around 6°C.
- Microhardness analysis reveals that for TNC11, TNC12 and TNC13 alloys, 10 at% increase in Ni and 10 at% lowered Ti content leads to 100% rise in microhardness. For TNC21, TNC22 and TNC23, 10 at% increase in Cu and 10 at% lowered Ni content leads to only around 10% rise in microhardness.
- ANOVA and Taguchi analysis reveal that T_{on} has highest influence on MRR (91.43%), SR (88.64%) and RLT (22.59%) whereas SV has higher degree of influence on KW (46.27%) compared to T_{on} .
- Analysis of WEDM responses obtained through Taguchi's DOE shows that MRR, SR and RLT surges 1881.67%, 57.5% and 35% respectively by average due to increase in duty factor from 0.67 to 0.86, whereas KW drops around 5% by average.

- Homogenization of as cast TiNiCu shape memory alloys lead to maximum reduction in MRR, SR, KW and RLT by approximately 52%, 50%, 12% and 51% respectively.
- It was found that suitable machined surface morphology can be obtained at low to medium discharge energy settings, low peak current of 0.92 Amps and peak voltage of 31 Volts, higher flushing pressure (between 98.06 to 147.1 kPa) having downward direction flow at T_{on} - 105 μ s, T_{off} - 30 μ s, SV - 45 Volts.
- Developed artificial neural network successfully predicted WEDM responses where highest percentage error recorded was 5.86% and lowest percentage error recorded was 0.001%.
- Multi objective optimization of WEDM responses using genetic algorithm reveals that 0.84 and 0.86 duty factor yields higher MRR for TNC11 and TNC23 respectively. Since TNC23 has a higher thermal conductivity than TNC11, a higher duty factor is in agreement with previous results. 100 μ s T_{on} and 50 μ s T_{off} resulting to 0.67 duty factor was found suitable to achieve lower surface roughness. 120 μ s T_{on} and 25 μ s T_{off} for TNC11 and 120 μ s T_{on} and 50 μ s T_{off} for TNC23 was found suitable for narrow kerf width whereas 100 μ s T_{on} and 20 μ s T_{off} was confirmed as optimized parameters for a thinner recast layer for both TNC11 and TNC23 respectively.

6.2 FUTURE SCOPE OF WORK

Even though much has been covered on wire electro discharge machining characteristics of TiNiCu shape memory alloys in this investigation, there are several aspects which can be considered for future study. Some of those aspects are listed below.

- Material removal mechanism of wire electro discharge machining process is directly influenced by dielectric medium and flushing conditions. Hence, future investigation can be carried out in improving nature of dielectric fluid and flushing conditions.

- Kerf width at top surface and bottom surface of a workpiece are never same and therefore requests further investigation on optimizing these conditions so as to obtain a more precise machined profile.
- Recast layer thickness can be reduced if quenching of melting material can be done instantaneously. Therefore, future investigation regarding temperature of dielectric fluid can be carried out to obtain a thinner recast layer.
- The effect of wire electrode material and its life is an important aspect in WEDM. Hence, further research is required in this area.

REFERENCES

Abbasi, M., Kermanpur, A., & Emadi, R. (2015). "Effects of Thermo-Mechanical Processing on the Mechanical Properties and Shape Recovery of the Nanostructured Ti₅₀Ni₄₅Cu₅ Shape Memory Alloy". *Proc. Mater. Sci.*, 11, 61-66.

Abdullah, A., & Shabgard, M. R. (2008). "Effect of ultrasonic vibration of tool on electrical discharge machining of cemented tungsten carbide (WC-Co)". *Int. J. Adv. Manuf. Technol.*, 38(11-12), 1137-1147.

Ahlers, M. (1986). "Martensite and equilibrium phases in Cu-Zn and Cu-Zn-Al alloys." *Prog. Mater. Sci.*, 30, 135-186.

Ali, M., AbuZaiter, A., Schlosser, C., Bycraft, B., & Takahata, K. (2014). "Wireless displacement sensing of micromachined spiral-coil actuator using resonant frequency tracking." *Sensors*, 14(7), 12399-12409.

Andhare, A. B., & Jithin, E. V. (2015). Analysis of Wire Vibration in Wire Electric Discharge Machining Process. *J. Vib. Eng. Technol*, 3(5), 627-635.

Arooj, S., Shah, M., Sadiq, S., Jaffery, S. H. I., & Khushnood, S. (2014). "Effect of Current in the EDM Machining of Aluminum 6061 T6 and its Effect on the Surface Morphology". *Arab. J. Sci. Eng.*, 39(5), 4187-4199.

Aspinwall, D. K., Dewes, R. C., Lee, H. G., Simao, J., & McKeown, P. A. (2003). "Electrical discharge surface alloying of Ti and Fe workpiece materials using refractory powder compact electrodes and Cu wire". *CIRP Annals*, 52(1), 151-156.

Assarzadeh, S., & Ghoreishi, M. (2008). "Neural-network-based modeling and optimization of the electro-discharge machining process". *Int. J. Adv. Manuf. Technol.*, 39(5-6), 488-500.

Biffi, C. A., & Tuissi, A. (2017). "Nitinol laser cutting: microstructure and functional properties of femtosecond and continuous wave laser processing." *Smart Mater. Struct.*, 26(3), 035006.

Bobbili, R., Madhu, V., & Gogia, A. K. (2013). "Effect of wire-EDM machining parameters on surface roughness and material removal rate of high strength armor steel". *Mater Manuf Process.*, 28(4), 364-368.

Buehler, W.J., Gilfrich, J.V., Wiley, R.C. (1963), "Effect of low-temperature phase changes on mechanical properties of alloys near composition TiNi." *Int. J. Appl. Phys.*, 34, 1475-1477.

Busch J.D., Johnson A.D., Lee C.H., Stevenson D.A. (1990). "Shape-memory properties in Ni-Ti sputter-deposited film." *Int. J. Appl. Phys.*, 68, 6224.

Cai, M., Fu, Y. Q., Sanjabi, S., Barber, Z. H., & Dickinson, J. T. (2007). "Effect of composition on surface relief morphology in TiNiCu thin films". *Surf. Coat. Tech.*, 201(12), 5843-5849.

Çaydaş, U., & Hascalık, A. (2008). "A study on surface roughness in abrasive waterjet machining process using artificial neural networks and regression analysis method". *J. Mater. Process. Technol.*, 202(1-3), 574-582.

Chakraborty, S., Dey, V., & Ghosh, S. K. (2015). "A review on the use of dielectric fluids and their effects in electrical discharge machining characteristics". *Precis. Eng.*, 40, 1-6.

Chen, C. H., Wang, H. K., & Wu, S. K. (2018). "A study on the crystallization behavior of amorphous Ti50Ni25Cu25 shape memory ribbon by X-ray diffraction measurement". *Intermetallics*, 93, 347-354.

Chen, C. H., Wu, S. K., & Wang, H. K. (2018). "Transformational and pseudoelastic characteristics of melt-spun Ti₅₀Ni₂₅Cu₂₅ shape memory ribbon crystallized and aged at a low temperature". *J. Alloys Compd.*, 753, 655-663.

Chen, H. C., Lin, J. C., Yang, Y. K., & Tsai, C. H. (2010). "Optimization of wire electrical discharge machining for pure tungsten using a neural network integrated simulated annealing approach". *Expert Syst. Appl.*, 37(10), 7147-7153.

Chen, S. L., Hsieh, S. F., Lin, H. C., Lin, M. H., & Huang, J. S. (2008). "Electrical discharge machining of a NiAlFe ternary shape memory alloy". *J. Alloys Compd.*, 464(1-2), 446-451.

Conde, A., Arriandiaga, A., Sanchez, J. A., Portillo, E., Plaza, S., & Cabanes, I. (2018). "High-accuracy wire electrical discharge machining using artificial neural networks and optimization techniques". *Robot CIM-Int Manuf.*, 49, 24-38.

Craciunescu, C. M., Li, J., & Wuttig, M. (2003). "Constrained martensitic transformations in TiNiCu films". *Thin Solid Films*, 434(1-2), 271-275.

Di, S., Chu, X., Wei, D., Wang, Z., Chi, G., & Liu, Y. (2009). "Analysis of kerf width in micro-WEDM". *Int. J. Mach. Tools Manu.*, 49(10), 788-792.

Du, H., & Fu, Y. (2004). "Deposition and characterization of Ti_{1-x}(Ni,Cu)_x shape memory alloy thin films". *Surf. Coat. Tech.*, 176(2), 182-187.

Duerig, T. W., & Pelton, A. R. (1994). "Ti-Ni shape memory alloys". *Materials properties handbook: titanium alloys*, 1035-1048.

Ebisu, T., Kawata, A., Okamoto, Y., Okada, A., & Kurihara, H. (2018). "Influence of Jet Flushing on Corner Shape Accuracy in Wire EDM". *Procedia CIRP*, 68, 104-108.

El-Bagoury, N., & Nofal, A. (2010). "Microstructure of an experimental Ni base superalloy under various casting conditions". *Mat. Sci. Eng. A-Struct.*, 527(29-30), 7793-7800.

El-Hofy, H. (2005). "Advanced machining processes: nontraditional and hybrid machining processes". McGraw Hill, New York.

Falvo, A. (2008). "Thermomechanical characterization of Nickel-Titanium Shape Memory Alloys", Ph.D. Thesis, University of Calabria, Rende, Italy.

Frotscher, M., Kahleyss, F., Simon, T., Biermann, D., & Eggeler, G. (2011). "Achieving small structures in thin NiTi sheets for medical applications with water jet and micro machining: a comparison." *J. Mater. Eng. Perform.*, 20(4-5), 776-782.

Fu, C. H., Liu, J. F., Guo, Y. B., & Zhao, Q. Z. (2016). "A comparative study on white layer properties by laser cutting vs. electrical discharge machining of Nitinol shape memory alloy". *Procedia CIRP*, 42, 246-251.

Fu, Y., & Du, H. (2003). "RF magnetron sputtered TiNiCu shape memory alloy thin film". *Mat. Sci. Eng. A-Struct.*, 339(1-2), 10-16.

Fu, Y., Du, H., Zhang, S., & Gu, Y. (2005). "Stress and surface morphology of TiNiCu thin films: effect of annealing temperature". *Surf. Coat. Tech.*, 198(1-3), 389-394.

Gallardo Fuentes, J. M., Gümpel, P., & Strittmatter, J. (2002). "Phase change behavior of nitinol shape memory alloys". *Adv. Eng. Mater.*, 4(7), 437-452.

Gao, Y., Pu, Z. J., Wu, K. H. (1997). "TEM studies of NiTi-Hf and NiTi-Zr high temperature shape memory alloys." Proceedings of the Second International

Conference on the Shape Memory and Superelastic Technologies, Asilomar Conference Center, Pacific Grove, USA, 83-88.

Gao, Z. Y., Sato, M., & Ishida, A. (2015). "Microstructure and shape memory behavior of annealed $Ti_{44.5}Ni_{55.5-x}Cu_x$ ($X=15.3-32.8$) thin films with low Ti content". *J. Alloys Compd.*, 619, 389-395.

Gargarella, P., Pauly, S., Song, K. K., Hu, J., Barekar, N. S., Khoshkhoo, M. S., Kerscher, E. (2013). "Ti-Cu-Ni shape memory bulk metallic glass composites". *Acta Mater.*, 61(1), 151-162.

Ghadimi, M., Shokuhfar, A., Zolriasatein, A., & Rostami, H. R. (2013). "Morphological and structural evaluation of nanocrystalline NiTiCu shape memory alloy prepared via mechanical alloying and annealing". *Mater. Lett.*, 90, 30-33.

Gil, F. J., Solano, E., Pena, J., Engel, E., Mendoza, A., & Planell, J. A. (2004). "Microstructural, mechanical and cytotoxicity evaluation of different NiTi and NiTiCu shape memory alloys". *J. Mater. Sci.: Mater. Med.*, 15(11), 1181-1185.

Goodlet, A., & Koshy, P. (2015). "Real-time evaluation of gap flushing in electrical discharge machining". *CIRP Annals*, 64(1), 241-244.

Goryczka, T., & Van Humbeeck, J. (2006). "Characterization of a NiTiCu shape memory alloy produced by powder technology". *J. Achiev. Mater. Manuf. Eng.*, 17(1-2), 65-68.

Goswami, A., & Kumar, J. (2014). "Investigation of surface integrity, material removal rate and wire wear ratio for WEDM of Nimonic 80A alloy using GRA and Taguchi method". *Engineering Science and Technology, an International Journal*, 17(4), 173-184.

Guo, Y., Klink, A., Fu, C., & Snyder, J. (2013). "Machinability and surface integrity of Nitinol shape memory alloy". *CIRP Annals*, 62(1), 83-86.

Guo, Z. N., Lee, T. C., Yue, T. M., & Lau, W. S. (1997). "A study of ultrasonic-aided wire electrical discharge machining". *J. Mater. Process. Technol.*, 63(1-3), 823-828.

Haas, P., Pontelandolfo, P., & Perez, R. (2013). "Particle hydrodynamics of the electrical discharge machining process. Part 1: Physical considerations and wire EDM process improvement". *Procedia CIRP*, 6, 41-46.

Habib, S. (2017). "Optimization of machining parameters and wire vibration in wire electrical discharge machining process". *Mech. Adv. Mater. Mod. Process.*, 3(1), 3.

Haenschke, T., Davis, C. L., & Attallah, M. M. (2013). "Influence of the microstructural inhomogeneities on the martensite-to-austenite phase transformation temperatures in TiNiCu-based shape-memory alloys". *Mater. Chem. Phys.*, 141(1), 272-277.

Hargovind, S., Narendranath, S., & Ramesh, M. R. (2019). "Advanced machining of TiNiCo shape memory alloys for biomedical applications". *Emerg. Mater. Res.*, 1-8.

Hasçalık, A., & Çaydaş, U. (2004). "Experimental study of wire electrical discharge machining of AISI D5 tool steel". *J. Mater. Process. Technol.*, 148(3), 362-367.

He, W. J., Min, G. H., Yin, Y. S., & Tolochko, O. (2009). "Martensitic transformation and mechanical properties of Ti-rich Ti-Ni-Cu melt-spun ribbon". *T Nonferr. Metal Soc.*, 19(6), 1464-1469.

Hill, D. J., & Minsker, B. S. (2010). "Anomaly detection in streaming environmental sensor data: A data-driven modeling approach". *Environ. Modell. Softw.*, 25(9), 1014-1022.

Hoh, D. J., Hoh, B. L., Amar, A. P., Wang, M. Y. (2009). "Shape memory alloys: metallurgy, biocompatibility, and biomechanics for neurosurgical applications." *Oper. Neurosurg.*, 64(suppl_5), ons199-ons214.

Hori, K., Namazu, T., Inoue, S. (2010). "Effect of Cu content on the shape memory behavior of Ti–Ni–Cu alloy thin films prepared by triple-source dc magnetron sputtering." *Thin Solid Films*, 518(21), S26-S28.

Hsieh, S. F., Chen, S. L., Lin, H. C., Lin, M. H., & Chiou, S. Y. (2009). "The machining characteristics and shape recovery ability of Ti–Ni–X (X= Zr, Cr) ternary shape memory alloys using the wire electro-discharge machining." *Int. J. Mach. Tool Manufact.*, 49(6), 509-514.

Hsieh, S. F., Hsue, A. W., Chen, S. L., Lin, M. H., Ou, K. L., & Mao, P. L. (2013). "EDM surface characteristics and shape recovery ability of $Ti_{35.5}Ni_{48.5}Zr_{16}$ and $Ni_{60}Al_{24.5}Fe_{15.5}$ ternary shape memory alloys". *J. Alloys Compd.*, 571, 63-68.

Huang, C. A., Tu, G. C., Yao, H. T., & Kuo, H. H. (2004). "Characteristics of the rough-cut surface of quenched and tempered martensitic stainless steel using wire electrical discharge machining". *Metallurgical and Materials Transactions A*, 35(4), 1351-1357.

Humbeeck, J.V. and Stalmans, R. (1998). "Characteristics of shape memory alloys." *Shape Memory Materials*, K. Otsuka and C.M. Wayman, eds., Cambridge University Press, 149-183.

Hung, C. H., Chang, F. Y., Chang, T. L., Chang, Y. T., Huang, K. W., & Liang, P. C. (2015). "Micromachining NiTi tubes for use in medical devices by using a femtosecond laser". *Opt. Laser Eng.*, 66, 34-40.

Hwang C.M., Wayman C.M. (1983). "Phase transformations in TiNiFe, TiNiAl and TiNi alloys." *Scr. Mater.*, 17(11), 1345-1350.

Ikram, A., Mufti, N. A., Saleem, M. Q., & Khan, A. R. (2013). "Parametric optimization for surface roughness, kerf and MRR in wire electrical discharge machining (WEDM) using Taguchi design of experiment". *Journal of Mechanical Science and Technology*, 27(7), 2133-2141.

Ishida A, Takei A, Miyazaki S. (1993). "Shape memory thin film of Ti-Ni formed by sputtering." *Thin Solid Films*, 228, 210.

Ishida, A., Sato, M., & Gao, Z. (2014). "Effects of Ti content on microstructure and shape memory behavior of $Ti_xNi_{(84.5-x)}Cu_{15.5}$ ($x= 44.6-55.4$) thin films". *Acta Mater.*, 69, 292-300.

Ishida, A., Sato, M., & Gao, Z. Y. (2013). "Properties and applications of TiNiCu shape-memory-alloy thin films". *J. Alloys Compd.*, 577, S184-S189.

Ishida, A., Sato, M., & Ogawa, K. (2008). "Microstructure and shape memory behavior of annealed Ti-36.8 at.% Ni-11.6 at.% Cu thin film". *Mat. Sci. Eng. A-Struct.*, 481, 91-94.

Ishida, A., Sato, M., Ogawa, K., & Yamada, K. (2006). "Shape memory behavior of Ti-Ni-Cu thin films". *Mat. Sci. Eng. A-Struct.*, 438, 683-686.

James, R.D. and Hane, K.F. (2000). "Martensitic transformations and shape-memory materials". *Acta Mater.*, 48(1), 197-222.

Jani J.M., Leary M., Subic A., Gibson M.A. (2014). "A review of shape memory alloy research, applications and opportunities." *Mater. Des.*, 56, 1078-1113.

Jiang, H. J., Ke, C. B., Cao, S. S., Xiao, M. A., & Zhang, X. P. (2013). "Phase transformation and damping behavior of lightweight porous TiNiCu alloys fabricated by powder metallurgy process". *T Nonferr. Metal Soc.*, 23(7), 2029-2036.

Kajiwara, S. (1999). "Characteristics features of shape memory effect and related transformation behavior in Fe-based alloys." *Mat. Sci. Eng. A-Struct.*, 273-275, 67-88.

Karthik, G., Kashyap, B., & Prabhu, T. R. (2017). "Processing, properties and applications of Ni-Ti-Fe shape memory alloys". *Mat. Today: Proceedings*, 4(2), 3581-3589.

Kawata, A., Okada, A., Okamoto, Y., & Kurihara, H. (2017). "Influence of nozzle jet flushing on wire breakage in 1st-cut wire EDM from start hole". In *Key Eng. Mater.* (Vol. 749, pp. 130-135). Trans Tech Publications.

Kaya, E., & Kaya, İ. (2019). "A review on machining of NiTi shape memory alloys: The process and post process perspective". *Int. J. Adv. Manu. Tech.*, 100(5-8), 2045-2087.

Kaynak, Y., Karaca, H. E., Noebe, R. D., & Jawahir, I. S. (2013). "Tool-wear analysis in cryogenic machining of NiTi shape memory alloys: A comparison of tool-wear performance with dry and MQL machining". *Wear*, 306(1-2), 51-63.

Kaynak, Y., Karaca, H. E., Noebe, R. D., & Jawahir, I. S. (2013). "Analysis of tool-wear and cutting force components in dry, preheated, and cryogenic machining of NiTi shape memory alloys". *Procedia CIRP*, 8, 498-503.

Kaynak, Y., Robertson, S. W., Karaca, H. E., & Jawahir, I. S. (2015). "Progressive tool-wear in machining of room-temperature austenitic NiTi alloys: The influence of cooling/lubricating, melting, and heat treatment conditions". *J. Mater. Process. Technol.*, 215, 95-104.

Kaynak, Y., Tobe, H., Noebe, R. D., Karaca, H. E., & Jawahir, I. S. (2014). "The effects of machining on the microstructure and transformation behavior of NiTi alloy". *Scr. Mater.*, 74, 60-63.

Khan, A. A. (2011). "Role of heat transfer on process characteristics during electrical discharge machining". *Developments in heat transfer*, 21, 417-435.

Kim J.I., Liu Y., Miyazaki S. (2003). "Ageing-induced two-stage R-phase transformation in Ti–50.9at.%Ni." *Acta Mater.*, 52(2), 487-499.

Kim, Y. W., Lee, S. H., & Nam, T. H. (2007). "Microstructure modifications of Ti–Ni–Cu shape memory alloy strips fabricated by arc melt overflow process". *Phys. Scr.*, 2007(T129), 245.

Klocke, F., Hensgen, L., Klink, A., Ehle, L., & Schwedt, A. (2016). "Structure and composition of the white layer in the wire-EDM process". *Procedia CIRP*, 42, 673-678.

Knowles, K.M. and Smith, D.A. (1981). "The crystallography of the martensitic transformation in equiatomic nickel-titanium." *Acta Mater.*, 29, 101-110.

Kong, M. C., Axinte, D., & Voice, W. (2011). "Challenges in using waterjet machining of NiTi shape memory alloys: An analysis of controlled-depth milling." *J. Mater. Process. Technol.*, 211(6), 959-971.

Kong, M. C., Axinte, D., & Voice, W. (2011). "An innovative method to perform maskless plain waterjet milling for pocket generation: a case study in Ti-based superalloys". *Int. J. Mach. Tool. Manu.*, 51(7-8), 642-648.

Kong, M. C., Srinivasu, D., Axinte, D., Voice, W., McGourlay, J., & Hon, B. (2013). "On geometrical accuracy and integrity of surfaces in multi-mode abrasive waterjet machining of NiTi shape memory alloys". *CIRP Annals*, 62(1), 555-558.

Konishi, T., Okada, A., Okamoto, Y., & Kurihara, H. (2015). "Effect of Tilting Jet Flushing Nozzle on Wire EDM Performance". *Int. J. Electr. Mach.*, 20, 3-8.

Kuriakose, S., & Shunmugam, M. S. (2005). "Multi-objective optimization of wire-electro discharge machining process by non-dominated sorting genetic algorithm". *J. Mater. Process. Technol.*, 170(1-2), 133-141.

Lee J.H, Nam T.H, Ahn H.J, Kim Y.W. (2006). "Shape memory characteristics and superelasticity of Ti-45Ni-5Cu alloy ribbons." *Mat. Sci. Eng. A-Struct*, 438-440, 691-694.

Lee, E. S., & Shin, T. H. (2011). "An evaluation of the machinability of nitinol shape memory alloy by electrochemical polishing." *J. Mech. Sci. Tech.*, 25(4), 963.

Lee, E. S., Shin, T. H., Kim, B. K., & Baek, S. Y. (2010). "Investigation of short pulse electrochemical machining for groove process on Ni-Ti shape memory alloy." *International Journal of Precision Engineering and Manufacturing*, 11(1), 113-118.

Lee, S. H., & Li, X. P. (2001). "Study of the effect of machining parameters on the machining characteristics in electrical discharge machining of tungsten carbide". *J. Mater. Process. Technol.*, 115(3), 344-358.

Li, C., Nikumb, S., & Wong, F. (2006). "An optimal process of femtosecond laser cutting of NiTi shape memory alloy for fabrication of miniature devices." *Opt Laser Eng*, 44(10), 1078-1087.

Li, H. F., Qiu, K. J., Zhou, F. Y., Li, L., & Zheng, Y. F. (2016). "Design and development of novel antibacterial Ti-Ni-Cu shape memory alloys for biomedical application". *Scientific reports*, 6, 37475.

Li, L., Wei, X. T., & Li, Z. Y. (2014). "Surface integrity evolution and machining efficiency analysis of W-EDM of nickel-based alloy". *Appl. Surf. Sci.*, 313, 138-143.

Liao, Y. S., Huang, J. T., & Chen, Y. H. (2004). "A study to achieve a fine surface finish in Wire-EDM". *J. Mater. Process. Technol.*, 149(1-3), 165-171.

Liao, Y. S., Huang, J. T., & Su, H. C. (1997). "A study on the machining-parameters optimization of wire electrical discharge machining". *J. Mater. Process. Technol.*, 71(3), 487-493.

Liu, J. F., Li, L., & Guo, Y. B. (2014). "Surface integrity evolution from main cut mode to finish trim cut mode in W-EDM of shape memory alloy". *Appl. Surf. Sci.*, 308, 253-260.

Liu, Y., Xie, Z. L., Tong, Y. X., & Lim, C. W. (2006). "Properties of rapidly annealed Ti₅₀Ni₂₅Cu₂₅ melt-spun ribbon". *J. Alloys Compd.*, 416(1-2), 188-193.

Lo, Y. C., Wu, S. K., & Horng, H. E. (1993). "A study of B2 \leftrightarrow B19 \leftrightarrow B19' two-stage martensitic transformation in a Ti₅₀Ni₄₀Cu₁₀ alloy". *Acta. Mater.*, 41(3), 747-759.

Lo, Y. C., Wu, S. K., & Wayman, C. M. (1990). "Transformation heat as a function of ternary Pd additions in $Ti_{50}Ni_{50-z}Pd_z$ alloys with x: 20~50 at.%". *Acta Mater.*, 24(8), 1571-1576.

Löbel, R., Thienhaus, S., Savan, A., & Ludwig, A. (2008). "Combinatorial fabrication and high-throughput characterization of a Ti–Ni–Cu shape memory thin film composition spread". *Mat. Sci. Eng. A-Struct*, 481, 151-155.

Ma, X. Z., Zhang, L., Cao, G. H., Lin, Y., & Tang, J. (2007). "Electrochemical micromachining of nitinol by confined-etchant-layer technique". *Electrochim. Acta*, 52(12), 4191-4196.

Mabe, J., Cabell, R., Butler, G. (2005). "Design and control of a morphing chevron for takeoff and cruise noise reduction". Proc., 26th Annual AIAA Aeroacoustics Conference, Monterey, C.A., 1-15.

Machado, L. G., & Savi, M. A. (2003). "Medical applications of shape memory alloys." *Braz. J. Med. Biol. Res.*, 36(6), 683-691.

Mahapatra, S. S., & Patnaik, A. (2007). "Optimization of wire electrical discharge machining (WEDM) process parameters using Taguchi method". *Int. J. Adv. Manuf. Tech.*, 34(9-10), 911-925.

Makenzi, M. M., & Ikua, B. W. (2014, December). "A review of flushing techniques used in electrical discharge machining". In *Proceedings of Sustainable Research and Innovation Conference* (pp. 162-165).

Maki, T. (1998). "Ferrous shape memory alloys." *Shape Memory Materials*, K Otsuka and C.M. Wayman, eds., Cambridge University Press, 117-126.

Manjaiah, M., Narendranath, S., & Akbari, J. (2014). "Optimization of wire electro discharge machining parameters to achieve better MRR and surface finish". *Proc. Mater. Sci.*, 5, 2635-2644.

Manjaiah, M., Narendranath, S., & Basavarajappa, S. (2016). "Wire electro discharge machining performance of TiNiCu shape memory alloy". *Silicon*, 8(3), 467-475.

Manjaiah, M., Narendranath, S., Basavarajappa, S. (2014). "Review on non-conventional machining of shape memory alloys." *T Nonferr. Metal Soc.*, 24(1), 12-21.

Manjaiah, M., Narendranath, S., Basavarajappa, S., & Gaitonde, V. N. (2018). "Investigation on material removal rate, surface and subsurface characteristics in wire electro discharge machining of $Ti_{50}Ni_{50-x}Cu_x$ shape memory alloy". *P I Mech. Eng L-J Mat.*, 232(2), 164-177.

Manjaiah, M., Narendranath, S., Basavarajappa, S., & Gaitonde, V. N. (2015). "Effect of electrode material in wire electro discharge machining characteristics of $Ti_{50}Ni_{50-x}Cu_x$ shape memory alloy". *Precis. Eng.*, 41, 68-77.

Manoj, I. V., Joy, R., & Narendranath, S. (2019). Investigation on the Effect of Variation in Cutting Speeds and Angle of Cut During Slant Type Taper Cutting in WEDM of Hastelloy X. *Arab J Sci Eng*, 1-11.

Manoj, I. V., Joy, R., Narendranath, S., & Nedelcu, D. (2019, August). Investigation of machining parameters on corner accuracies for slant type taper triangle shaped profiles using WEDM on Hastelloy X. In *IOP Conf Ser Mater Sci Eng* (Vol. 591, No. 1, p. 012022). IOP Publishing.

Mathew, B., & Babu, J. (2014). "Multiple process parameter optimization of WEDM on AISI304 using Taguchi grey relational analysis". *Proc. Mater. Sci.*, 5, 1613-1622.

Mathew, B., Benkim, B. A., & Babu, J. (2014). "Multiple Process Parameter Optimization of WEDM on AISI304 Using Utility Approach". *Proc. Mater. Sci.*, 5, 1863-1872.

Matveeva, N. M., Pushin, V. G., Shelyakov, A. V., & Bykovskii, Y. U. (1997). "Influence of crystallization conditions on structure and shape memory effect in amorphous alloys of TiNi-TiCu system". *Fizika Metallov i Metallovedenie (Russia)*, 83(6), 82-92.

Melton, K.R. (1999). "General applications of shape memory alloys and smart materials." *Shape Memory Materials*,. K. Otsuka, C.M. Wayman, eds., Cambridge University Press, 91-100.

Middleton, L.A., Kennon, N.F. and Dunne, D.P. (1985). "Martensitic Transformation in Nitinol." *Metallography*, 17, 61-72.

Morakabati, M., Kheirandish, S., Aboutalebi, M., Taheri, A. K., & Abbasi, S. M. (2010). "The effect of Cu addition on the hot deformation behavior of NiTi shape memory alloys". *J. Alloys Compd.*, 499(1), 57-62.

Motemani, Y., Tan, M. J., White, T. J., & Banas, A. (2011). "Evolution of structural, surfacial and mechanical properties of titanium–nickel–copper thin films during rapid thermal annealing". *Surf. Coat. Tech.*, 205(10), 3147-3157.

Müller, F., & Monaghan, J. (2000). "Non-conventional machining of particle reinforced metal matrix composite." *Int. J. Mach. Tools Manuf.*, 40(9), 1351-1366.

Müller, F., & Monaghan, J. (2001). "Non-conventional machining of particle reinforced metal matrix composites". *J. Mater. Process. Technol.*, 118(1-3), 278-285.

Muniappan, A., Thiagarajan, C., & Somasundaram, S. (2017). "Optimization of kerf width obtained in WEDM of aluminum hybrid composite using Taguchi method". *ARPJ. Eng. Appl. Sci.*, 12, 382-388.

Munz, M., Risto, M., & Haas, R. (2013). "Specifics of flushing in electrical discharge drilling". *Procedia CIRP*, 6, 83-88.

Murty, B. S., Rao, M. M., & Ranganathan, S. (1995). "Differences in the glass-forming ability of rapidly solidified and mechanically alloyed Ti-Ni-Cu alloys". *Mat. Sci. Eng. A-Struct*, 196(1-2), 237-241.

Nakayama H., Tsuchiya K., Umemoto M. (2001). "Crystal refinement and amorphisation by cold rolling in TiNi shape memory alloys." *Scripta Mater.*, 44, 1781–1785.

Nam, T. H., Park, S. M., Kim, T. Y., & Kim, Y. W. (2005). "Microstructures and shape memory characteristics of Ti–25Ni–25Cu (at.%) alloy ribbons". *Smart Mater. Struct.*, 14(5), S239.

Nam, T. H., Saburi, T., Kawamura, Y., & Shimizu, K. I. (1990). "Shape Memory Characteristics Associated with the B2-B19 and B19-B19' Transformations in a Ti-40Ni-10Cu (at.%) Alloy". *Mater. Trans., JIM*, 31(4), 262-269.

Naresh, H., Bharath, H. S., & Prashantha, S. (2017). "The Influence of Alloying Constituent Fe on Mechanical Properties Of NiTi Based Shape Memory Alloys". *Mater. Today: Proceedings*, 4(10), 11251-11259.

Nasr, M., Ng, E. G., & Elbestawi, M. (2007). "Effects of workpiece thermal properties on machining-induced residual stresses-thermal softening and conductivity". *P. I. Mech. Eng. B. J. Eng.*, 221(9), 1387-1400.

Nourbakhsh, F., Rajurkar, K. P., Malshe, A. P., & Cao, J. (2013). "Wire electro-discharge machining of titanium alloy". *Procedia CIRP*, 5, 13-18.

Otsuka, K., Ren, X. (2005). "Physical metallurgy of Ti-Ni based shape memory alloys." *Prog. Mater. Sci.*, 50, 511-678.

Parashar, V., Rehman, A., Bhagoria, J. L., & Puri, Y. M. (2010). "Kerfs width analysis for wire cut electro discharge machining of SS 304L using design of experiments". *Indian Journal of Science and Technology*, 3(4), 369-373.

Pradhan, M. K. (2012). "Determination of optimal parameters with multi response characteristics of EDM by response surface methodology, grey relational analysis and principal component analysis". *Int. J. Manuf. Tech. Manag.*, 26(1-4), 56-80.

Pramanik, A., & Basak, A. K. (2018). "Sustainability in wire electrical discharge machining of titanium alloy: Understanding wire rupture". *J. Clean. Prod.*, 198, 472-479.

Puri, A. B., & Bhattacharyya, B. (2003). "An analysis and optimisation of the geometrical inaccuracy due to wire lag phenomenon in WEDM". *Int. J. Mach. Tool. Manufact.*, 43(2), 151-159.

Puri, A. B., & Bhattacharyya, B. (2005). "Modeling and analysis of white layer depth in a wire-cut EDM process through response surface methodology". *The Int. J. Adv. Manuf. Technol.*, 25(3-4), 301-307.

Ramachandran, B., Chen, C. H., Chang, P. C., Kuo, Y. K., Chien, C., & Wu, S. K. (2015). "Thermal and transport properties of as-grown Ni-rich TiNi shape memory alloys". *Intermetallics*, 60, 79-85.

Ramachandran, B., Tang, R. C., Chang, P. C., Kuo, Y. K., Chien, C., & Wu, S. K. (2013). "Cu-substitution effect on thermoelectric properties of the TiNi-based shape memory alloys". *J. Appl. Phy.*, 113(20), 203702.

Ramakrishnan, R., & Karunamoorthy, L. (2008). "Modeling and multi-response optimization of Inconel 718 on machining of CNC WEDM process". *J. Mater. Process. Technol.*, 207(1-3), 343-349.

Rao, T. B., & Krishna, A. G. (2014). "Selection of optimal process parameters in WEDM while machining Al7075/SiCp metal matrix composites". *The Int. J. Adv. Manuf. Technol.*, 73(1-4), 299-314.

Ren, M. H., Wang, L., Xu, D., & Cai, B. C. (2000). "Sputter-deposited Ti–Ni–Cu shaped memory alloy thin films". *Mater. Des.*, 21(6), 583-586.

Roy, A., & Narendranath, S. (2018). "Effect of spark gap voltage and wire electrode feed rate on machined surface morphology during Wire EDM process". *Mater. Today: Proceedings*, 5(9), 18104-18109.

Roy, A., & Narendranath, S. (2018). "Impact of variation in wire electro discharge machining responses of homologous TiNiCu shape memory alloys for smart applications: an experimental investigation". *Mater. Res. Express*, 5(12), 125701.

Roy, A., & Sanna Yellappa, N. (2019). "Influence of dielectric flushing conditions during WEDM of TiNiCu shape memory alloys". *Emerg. Mater. Res.*, 8(3), 376-386.

Roy, A., Nath, S. N., & Nedelcu, D. (2017). "Experimental Investigation on variation of output responses of as cast TiNiCu shape memory alloys using wire EDM". *Int. J. Mod. Manu. Technol.*, 9(1), 90-101.

Rupajati, P., Soepangkat, B. O. P., Pramujati, B., & Agustin, H. C. (2014). "Optimization of recast layer thickness and surface roughness in the wire EDM process of AISI H13 tool steel using Taguchi and fuzzy logic". In *Appl. Mech. Mater.* (Vol. 493, pp. 529-534). Trans Tech Publications.

Saburi T. (1989). "Structure and mechanical behavior of Ti-Ni shape memory alloys." *Proc. MRS International Meeting on Advanced Materials*, 9, 77-91.

Saburi T. (1998). "Ti–Ni shape memory alloys." *Shape memory material*,. Otsuka and C.M. Wayman, eds., Cambridge University Press, 49-97.

Saburi, T., Takagaki, T., Nenno, S., & Koshino, K. (1988, May). "Mechanical Behavior of Shape Memory Ti--Ni--Cu Alloys". In *Proceedings of the MRS International Meeting on Advanced Materials*. (Vol. 9, pp. 147-152).

Sahu, S. N., Murmu, S. K., & Nayak, N. C. (2019). "Multi-objective Optimization of EDM Process with Performance Appraisal of GA based Algorithms in Neural Network Environment". *Mater. Today: Proceedings*, 18, 3982-3997.

Saravanan, M., Kumar, A. V., Kannan, V. N., & Thangaiyah, I. S. (2017). "Optimization of process parameters during wire electrical discharge machining of Ti Gr 2 for improving corner accuracy". *Mater. Today: Proceedings*, 4(2), 2105-2113.

Schulze, H. P., & Schätzing, W. (2013). "Influences of different contaminations on the electro-erosive and the electrochemical micro-machining". *Procedia CIRP*, 6, 58-63.

Shankar, K. V., & Sellamuthu, R. (2015). "Determination of the effect of nickel content on hardness, optimum aging temperature and aging time for spinodal bronze alloys cast in metal mould". In *Appl. Mech. Mater.* (Vol. 813, pp. 597-602). Trans Tech Publications.

Sharma, P., Chakradhar, D., & Narendranath, S. (2016). Effect of wire diameter on surface integrity of wire electrical discharge machined Inconel 706 for gas turbine application. *J. Manuf. Process.*, 24, 170-178.

Sharma, P., Chakradhar, D., & Narendranath, S. (2015). Evaluation of WEDM performance characteristics of Inconel 706 for turbine disk application. *Mater. Des.*, 88, 558-566.

Shelyakov, A. V., Sitnikov, N. N., Menushenkov, A. P., Korneev, A. A., Rizakhanov, R. N., & Sokolova, N. A. (2013). "Fabrication and characterization of amorphous-crystalline TiNiCu melt-spun ribbons". *J. Alloys Compd.*, 577, S251-S254.

Shelyakov, A., Sitnikov, N., Khabibullina, I., Tabachkova, N., Fominski, V., & Andreev, N. (2019). "Effect of high-rate annealing on microstructure, martensitic transformation and shape memory behavior of TiNiCu melt-spun ribbons". *Mater. Lett.*, 248, 48-51.

Shi, P., Yang, D. Z., Shen, H. M., & Chen, F. X. (2000). "Effects of aging on martensitic transformation of Ti50Ni25Cu25 shape memory alloy". *Mater. Des.*, 21(6), 521-524.

Shiva, S., Palani, I. A., Paul, C. P., Mishra, S. K., & Singh, B. (2016). "Investigations on phase transformation and mechanical characteristics of laser additive manufactured TiNiCu shape memory alloy structures". *J. Mater. Process. Technol.*, 238, 142-151.

Simao, J., Lee, H. G., Aspinwall, D. K., Dewes, R. C., & Aspinwall, E. M. (2003). "Workpiece surface modification using electrical discharge machining". *Int. J Mach Tool Manu.*, 43(2), 121-128.

Singh, A. K., Mahajan, R., Tiwari, A., Kumar, D., & Ghadai, R. K. (2018, June). "Effect of Dielectric on Electrical Discharge Machining: A Review". In *IOP Conference Series: Materials Science and Engineering* (Vol. 377, No. 1, p. 012184). IOP Publishing.

Sivaprakasam, P., Hariharan, P., & Gowri, S. (2014). "Modeling and analysis of micro-WEDM process of titanium alloy (Ti-6Al-4V) using response surface approach". *Engineering Science and Technology, an International Journal*, 17(4), 227-235.

Soni, H., Narendranath, S., & Ramesh, M. R. (2018). "ANN and RSM Modeling Methods for Predicting Material Removal Rate and Surface Roughness during WEDM of Ti₅₀Ni₄₀Co₁₀ Shape Memory Alloy". *Advances in Modelling and Analysis A*, 54, 435-443.

Soni, H., Narendranath, S., & Ramesh, M. R. (2018). "Experimental Investigation on Effects of Wire Electro Discharge Machining of Ti₅₀Ni₄₅Co₅ Shape Memory Alloys". *Silicon*, 10(6), 2483-2490.

Soni, H., Sannayellappa, N., & Rangarasaiah, R. M. (2017). "An experimental study of influence of wire electro discharge machining parameters on surface integrity of TiNiCo shape memory alloy". *J. Mater. Res.*, 32(16), 3100-3108.

Sun, L., Huang, W. M., Ding, Z., Zhao, Y., Wang, C. C., Purnawali, H., & Tang, C. (2012). "Stimulus-responsive shape memory materials: a review". *Mater. Des.*, 33, 577-640.

Surya, V. R., Kumar, K. V., Keshavamurthy, R., Ugrasen, G., & Ravindra, H. V. (2017). "Prediction of machining characteristics using artificial neural network in wire EDM of Al7075 based In-situ Composite". *Mater. Today: Proceedings*, 4(2), 203-212.

Sutou, Y., Omori, T., Yamauchi, K., Ono, N., Kainuma, R., & Ishida, K. (2005). "Effect of grain size and texture on pseudoelasticity in Cu–Al–Mn-based shape memory wire". *Acta Mater.*, 53(15), 4121-4133.

Tanjilul, M., Ahmed, A., Kumar, A. S., & Rahman, M. (2018). "A study on EDM debris particle size and flushing mechanism for efficient debris removal in EDM-drilling of Inconel 718". *J. Mater. Process. Technol.*, 255, 263-274.

Tarng, Y. S., Ma, S. C., & Chung, L. K. (1995). "Determination of optimal cutting parameters in wire electrical discharge machining". *Int. J Mach Tool Manu.*, 35(12), 1693-1701.

Theisen, W., & Schuermann, A. (2004). "Electro discharge machining of nickel–titanium shape memory alloys". *Mat Sci Eng A: Struct*, 378(1-2), 200-204.

Thillaivanan, A., Asokan, P., Srinivasan, K. N., & Saravanan, R. (2010). "Optimization of operating parameters for EDM process based on the taguchi method and artificial neural network". *International Journal of engineering science and technology*, 2(12), 6880-6888.

Tomozawa, M., Kim, H. Y., Yamamoto, A., Hiromoto, S., & Miyazaki, S. (2010). "Effect of heat treatment temperature on the microstructure and actuation behavior of a Ti–Ni–Cu thin film microactuator". *Acta Mater.*, 58(18), 6064-6071.

Tosun, N., Cogun, C., & Tosun, G. (2004). "A study on kerf and material removal rate in wire electrical discharge machining based on Taguchi method". *J. Mater. Process. Technol.*, 152(3), 316-322.

Tung, A. T., Park, B. H., Liang, D. H., & Niemeyer, G. (2008). "Laser-machined shape memory alloy sensors for position feedback in active catheters." *Sens. Actuator A Phys.*, 147(1), 83-92.

Ugrasen, G., Ravindra, H. V., Prakash, G. N., & Keshavamurthy, R. (2014). "Process optimization and estimation of machining performances using artificial neural network in wire EDM". *Procedia materials science*, 6, 1752-1760.

Walker J.A., Gabriel K.J., Mehregany M. (1990). "Thin-film processing of TiNi shape memory alloy." *Sens. Actuator A Phys.*, 21(1-3), 243-246.

Wang, Y. Q., Zheng, Y. F., Cai, W., & Zhao, L. C. (1999). "The tensile behavior of Ti₃₆Ni₄₉Hf₁₅ high temperature shape memory alloy". *Scr. Mater.*, 40(12), 1327-1331.

Wang, Z. G., Zu, X. T., & Huo, Y. (2005). "Effect of heating/cooling rate on the transformation temperatures in TiNiCu shape memory alloys". *Thermochim. Acta*, 436(1-2), 153-155.

Wang, Z. G., Zu, X. T., Dai, J. Y., Fu, P., & Feng, X. D. (2003). "Effect of thermomechanical training temperature on the two-way shape memory effect of TiNi and TiNiCu shape memory alloys springs". *Mater. Lett.*, 57(9-10), 1501-1507.

Wang, Z. G., Zu, X. T., Feng, X. D., Zhu, S., Dai, J. Y., Lin, L. B., & Wang, L. M. (2002). "Study of two-way shape memory extension spring of narrow hysteresis TiNiCu shape memory alloys". *Mater. Lett.*, 56(3), 284-288.

Wax, S., Fischer, G., Sands, R. (2003). "The past, present and future of DARPA's investment strategy in smart materials". *J. Miner. Met. Mater. Eng.*, 55(12), 17-23.

Wegener, K., Kliuev, M., & Baumgart, C. (2018). "Fluid Dynamics in Electrode Flushing Channel and Electrode-Workpiece Gap During EDM Drilling". In *Proceedings of the 19th ISEM Conference (ISEM-XIX)* (Vol. 68, pp. 254-259). Elsevier.

Wei Z.G., Sandstrom, Miyazaki S. (1998). "Shape-memory materials and hybrid composites for smart systems: Part I Shape-memory materials". *J Mater Sci*, 33-15, 37-43.

Weinert, K., & Petzoldt, V. (2004). "Machining of NiTi based shape memory alloys". *Mat Sci Eng A: Struct*, 378(1-2), 180-184.

Weinert, K., & Petzoldt, V. (2008). "Machining NiTi micro-parts by micro-milling". *Mat Sci Eng A: Struct*, 481, 672-675.

Weinert, K., Petzoldt, D., Kotter, D. (2004). "Turning and Drilling of NiTi Shape Memory Alloys". *CIRP Ann-Manuf. Techn.*, 53(1), 65-68.

Weinert, K., Petzoldt, V., & Buschka, M. (2002). "Machining properties of an austenitic NiTi shape memory alloy". *J. Prod. Eng., Vol. IN1*, 9-12.

Wong, Y. S., Lim, L. C., & Lee, L. C. (1995). "Effects of flushing on electro-discharge machined surfaces". *J. Mater. Process. Technol.*, 48(1-4), 299-305.

Wu, M.H. (1990). "Cu-Based Shape Memory Alloys". *Engineering Aspects of Shape Memory Alloys*, T.W. Duerig, K.N. Melton, D. Stöckel and C.M. Wayman, eds., Butterworth-Heinemann Ltd., 69-95.

Xie, Z. L., Cheng, G. P., & Liu, Y. (2007). "Microstructure and texture development in Ti50Ni25Cu25 melt-spun ribbon". *Acta Mater.*, 55(1), 361-369.

Yue, X., Yang, X., & Kunieda, M. (2018). "Influence of metal vapor jets from tool electrode on material removal of workpiece in EDM". *Precis. Eng.*, 53, 278-288.

Zarnetta, R., Kneip, S., Somsen, C., & Ludwig, A. (2011). "High-throughput characterization of mechanical properties of Ti–Ni–Cu shape memory thin films at elevated temperature". *Mat Sci Eng A: Struct*, 528(21), 6552-6557.

Zhao, Q., Qian, Z., Cui, X., Wu, Y., & Liu, X. (2016). "Influences of Fe, Si and homogenization on electrical conductivity and mechanical properties of dilute Al–Mg–Si alloy". *J Alloy Compd*, 666, 50-57.

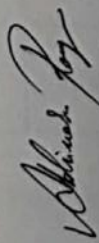
Zheng, H. X., Mentz, J., Bram, M., Buchkremer, H. P., & Stöver, D. (2008). "Powder metallurgical production of TiNiNb and TiNiCu shape memory alloys by combination of pre-alloyed and elemental powders". *J Alloy Compd*, 463(1-2), 250-256.

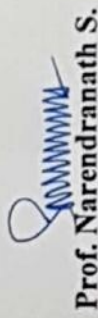
Zinelis, S. (2007). "Surface and elemental alterations of dental alloys induced by electro discharge machining (EDM)". *Dent Mater*, 23(5), 601-607.

LIST OF PUBLICATIONS BASED ON PHD RESEARCH WORK

| Sl. No. | Title of the Paper | Authors | Name of the Journal / Conference / Symposium, Vol., No., Pages | Month & Year of Publication | Category * |
|---------|--|---|--|-----------------------------|------------|
| 1 | Experimental investigation on variation of output responses of as cast TiNiCu shape memory alloys using Wire EDM. | Abhinaba Roy, Narendranath S., Dumitru Nedelcu | International Journal of Modern Manufacturing Technologies | June, 2017 | 1 |
| 2 | Impact of variation in wire electro discharge machining responses of homologous TiNiCu shape memory alloys for smart applications: an experimental investigation | Abhinaba Roy, Narendranath S. | Materials Research Express | Sept, 2018 | 1 |
| 3 | Effect of spark gap voltage and wire electrode feed rate on machined surface morphology during Wire EDM process | Abhinaba Roy, S. Narendranath | Materials Today : Proceedings | Oct, 2018 | 1 |
| 4 | Influence of dielectric flushing conditions during WEDM of TiNiCu shape memory alloys | Abhinaba Roy, S. Narendranath | Emerging Materials Research | Sep, 2019 | 1 |
| 5 | Effect of peak current and peak voltage on machined surface morphology during WEDM of TiNiCu shape memory alloys | Abhinaba Roy, S. Narendranath, Alokesh Pramanik | Journal of Mechanical Science and Technology | Oct, 2019 | 2 |
| 6 | Study of wire electro discharge machining accuracy of TiNiCu shape memory alloys through kerf analysis | Abhinaba Roy, S. Narendranath | International Conference on Precision, Meso, Micro and Nano Engineering (COPEN-10) | Dec, 2017 | 3 |
| 7 | An empirical view on accuracy and machinability of TiNiCu shape memory alloys during wire electro discharge machining | Abhinaba Roy, S. Narendranath | National Conference on Advanced Materials, Manufacturing and Metrology (NCAMMM-2018) | Feb, 2018 | 3 |

Category 1 : Journal paper, full paper reviewed 2 : Journal paper, Abstract reviewed 3 : Conference/Symposium paper, full paper reviewed 4 : Conference/Symposium paper, abstract reviewed 5 : others (including papers in Workshops, NITK Research Bulletins, Short notes etc.)


Abhinaba Roy
 (Research Scholar)


Prof. Narendranath S.
 (Research Guide)

BIO-DATA

1. Name : Abhinaba Roy
2. Father's Name : Ajit Kumar Roy
3. Date of Birth : 07/09/1989
4. Nationality : Indian
5. Marital Status : Married
6. Address :



(Permanent Address)

S/o. Dr. Ajit Kumar Roy
Maternate, Badurtali Lane
Krishnanagar, Agartala
Tripura (West), Tripura
India - 799001

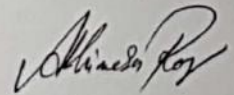
(Present Address)

M005, Manufacturing Laboratory
Department of Mechanical Engg.
National Institute of Technology Karnataka
Surathkal, Mangalore, Dakshina Kannada
Karnataka, India - 575025

7. Mobile Number : +91-7022384560/6362897802
8. Email-ID : er.abhi.roy@gmail.com/roy.abhinaba89@gmail.com
9. Educational Qualification :

| Qualification | College | University | Year of Passing | CGPA |
|--------------------------------------|---|---|-----------------|------|
| Ph.D. (Mechanical Engineering) | National Institute of Technology Karnataka | National Institute of Technology Karnataka | 2020 | 7.5 |
| M.Tech (Manufacturing Technology) | National Institute of Technology Agartala | National Institute of Technology Agartala | 2014 | 8.35 |
| B.Tech (Mechanical Engineering) | Kalinga Institute of Industrial Technology, Bhubaneswar | KIIT (Deemed to be University) | 2012 | 7.3 |

I declare that the above information is true and correct to best of my knowledge.


(Abhinaba Roy)